



Mechanism and kinetics of the reaction between liquid sodium and nuclear fuel of future fast neutron reactors

Concettina Andreello

► To cite this version:

Concettina Andreello. Mechanism and kinetics of the reaction between liquid sodium and nuclear fuel of future fast neutron reactors. Other. Université de Lyon, 2020. English. NNT : 2020LYSEM027 . tel-03537842

HAL Id: tel-03537842

<https://theses.hal.science/tel-03537842>

Submitted on 20 Jan 2022

HAL is a multi-disciplinary open access archive for the deposit and dissemination of scientific research documents, whether they are published or not. The documents may come from teaching and research institutions in France or abroad, or from public or private research centers.

L'archive ouverte pluridisciplinaire **HAL**, est destinée au dépôt et à la diffusion de documents scientifiques de niveau recherche, publiés ou non, émanant des établissements d'enseignement et de recherche français ou étrangers, des laboratoires publics ou privés.



N°d'ordre NNT : 2020LYSEM027

THESE de DOCTORAT DE L'UNIVERSITE DE LYON

opérée au sein de
l'Ecole des Mines de Saint-Etienne

Ecole Doctorale N° 488
Sciences, Ingénierie, Santé

Spécialité de doctorat : Génie des procédés

Soutenue publiquement le 07/12/2020, par :
Concettina ANDRELLO

Mécanisme et cinétique de la réaction entre le sodium liquide et le combustible nucléaire des futurs réacteurs à neutrons rapides

Mechanism and kinetics of the reaction between liquid sodium and nuclear fuel of future fast neutron reactors

Devant le jury composé de :

GUÉNEAU, Christine
WOUTERS, Yves
WALLEZ, Gilles
KONINGS, Rudy J.M.
AÏT ABDERRAHIM, Hamid
FAVERGEON, Loïc
DESGRANGES, Lionel
FREIS, Daniel

Expert senior, CEA Saclay
Professeur, Univ. Grenoble Alpes
Professeur, CNRS – Chimie ParisTech
Professeur, TU Delft, JRC-Karlsruhe
Professeur, UCL, SCK-CEN
Professeur, ENSM, Saint-Etienne
Expert senior, CEA, Cadarache
Scientific Officer, JRC-Karlsruhe

Présidente
Rapporteur
Rapporteur
Examineur
Examineur
Directeur de thèse
Co-directeur de thèse
Co-directeur de thèse

Spécialités doctorales	Responsables :	Spécialités doctorales	Responsables
SCIENCES ET GENIE DES MATERIAUX MECANIQUE ET INGENIERIE GENIE DES PROCÉDES SCIENCES DE LA TERRE SCIENCES ET GENIE DE L'ENVIRONNEMENT	K. Wolski Directeur de recherche S. Drapier, professeur F. Gruy, Maître de recherche B. Guy, Directeur de recherche D. Grailliot, Directeur de recherche	MATHEMATIQUES APPLIQUEES INFORMATIQUE SCIENCES DES IMAGES ET DES FORMES GENIE INDUSTRIEL MICROELECTRONIQUE	O. Roustant, Maître-assistant O. Boissier, Professeur JC. Pinoli, Professeur N. Absi, Maître de recherche Ph. Lalevée, Professeur

EMSE : Enseignants-chercheurs et chercheurs autorisés à diriger des thèses de doctorat (titulaires d'un doctorat d'État ou d'une HDR)

ABSI	Nabil	MR	Génie industriel	CMP
AUGUSTO	Vincent	MR	Génie industriel	CIS
AVRIL	Stéphane	PR	Mécanique et ingénierie	CIS
BADEL	Pierre	MA(MDC)	Mécanique et ingénierie	CIS
BALBO	Flavien	PR	Informatique	FAYOL
BASSEREAU	Jean-François	PR	Sciences et génie des matériaux	SMS
BATTON-HUBERT	Mireille	PR	Sciences et génie de l'environnement	FAYOL
BEIGBEDER	Michel	MA(MDC)	Informatique	FAYOL
BLAYAC	Sylvain	MA(MDC)	Microélectronique	CMP
BOISSIER	Olivier	PR	Informatique	FAYOL
BONNEFOY	Olivier	PR	Génie des Procédés	SPIN
BORBELY	Andras	MR(DR2)	Sciences et génie des matériaux	SMS
BOUCHER	Xavier	PR	Génie Industriel	FAYOL
BRODHAG	Christian	DR	Sciences et génie de l'environnement	FAYOL
BRUCHON	Julien	MA(MDC)	Mécanique et ingénierie	SMS
CAMEIRAO	Ana	MA(MDC)	Génie des Procédés	SPIN
CHRISTIEN	Frédéric	PR	Science et génie des matériaux	SMS
DAUZERE-PERES	Stéphane	PR	Génie Industriel	CMP
DEBAYLE	Johan	MR	Sciences des Images et des Formes	SPIN
DEGEORGE	Jean-Michel	MA(MDC)	Génie industriel	Fayol
DELAFOSSSE	David	PR0	Sciences et génie des matériaux	SMS
DELORME	Xavier	MA(MDC)	Génie industriel	FAYOL
DESRAYAUD	Christophe	PR	Mécanique et ingénierie	SMS
DJENIZIAN	Thierry	PR	Science et génie des matériaux	CMP
BERGER-DOUCE	Sandrine	PR	Sciences de gestion	FAYOL
DRAPIER	Sylvain	PR	Mécanique et ingénierie	SMS
DUTERTRE	Jean-Max	MA(MDC)		CMP
EL MRABET	Nadia	MA(MDC)		CMP
FAUCHEU	Jenny	MA(MDC)	Sciences et génie des matériaux	SMS
FAVERGEON	Loïc	CR	Génie des Procédés	SPIN
FEILLET	Dominique	PR	Génie Industriel	CMP
FOREST	Valérie	MA(MDC)	Génie des Procédés	CIS
FRACZKIEWICZ	Anna	DR	Sciences et génie des matériaux	SMS
GARCIA	Daniel	MR(DR2)	Sciences de la Terre	SPIN
GAVET	Yann	MA(MDC)	Sciences des Images et des Formes	SPIN
GERINGER	Jean	MA(MDC)	Sciences et génie des matériaux	CIS
GOEURLOT	Dominique	DR	Sciences et génie des matériaux	SMS
GONDRAN	Natacha	MA(MDC)	Sciences et génie de l'environnement	FAYOL
GONZALEZ FELIU	Jesus	MA(MDC)	Sciences économiques	FAYOL
GRAILLOT	Didier	DR	Sciences et génie de l'environnement	SPIN
GROSSEAU	Philippe	DR	Génie des Procédés	SPIN
GRUY	Frédéric	PR	Génie des Procédés	SPIN
HAN	Woo-Suck	MR	Mécanique et ingénierie	SMS
HERRI	Jean Michel	PR	Génie des Procédés	SPIN
KERMOUCHE	Guillaume	PR	Mécanique et Ingénierie	SMS
KLOCKER	Helmut	DR	Sciences et génie des matériaux	SMS
LAFOREST	Valérie	MR(DR2)	Sciences et génie de l'environnement	FAYOL
LERICHE	Rodolphe	CR	Mécanique et ingénierie	FAYOL
MALLIARAS	Georges	PR	Microélectronique	CMP
MOLIMARD	Jérôme	PR	Mécanique et ingénierie	CIS
MOUTTE	Jacques	CR	Génie des Procédés	SPIN
NAVARRO	Laurent	CR		CIS
NEUBERT	Gilles			FAYOL
NIKLOVSKI	Jean-Pierre	Ingénieur de recherche	Mécanique et ingénierie	CMP
NORTIER	Patrice	PR	Génie des Procédés	SPIN
O CONNOR	Rodney Philip	MA(MDC)	Microélectronique	CMP
PICARD	Gauthier	MA(MDC)	Informatique	FAYOL
PINOLI	Jean Charles	PR	Sciences des Images et des Formes	SPIN
POURCHEZ	Jérémy	MR	Génie des Procédés	CIS
ROUSSY	Agnès	MA(MDC)	Microélectronique	CMP
ROUSTANT	Olivier	MA(MDC)	Mathématiques appliquées	FAYOL
SANAUR	Sébastien	MA(MDC)	Microélectronique	CMP
SERRIS	Eric	IRD		FAYOL
STOLARZ	Jacques	CR	Sciences et génie des matériaux	SMS
TRIA	Assia	Ingénieur de recherche	Microélectronique	CMP
VALDIVIESO	François	PR	Sciences et génie des matériaux	SMS
VIRICELLE	Jean Paul	DR	Génie des Procédés	SPIN
WOLSKI	Krzysztof	DR	Sciences et génie des matériaux	SMS
XIE	Xiaolan	PR	Génie industriel	CIS
YUGMA	Gallian	CR	Génie industriel	CMP

Supervision and Funding

The PhD studies presented in this manuscript have been supervised by Prof. Loïc Favergeon, Professor of Process design at the Département of Procédés de Transformations des Solides et Instrumentation (PTSI) / Laboratoire Georges Friedel at the Ecole Nationale Supérieure des Mines de Saint-Etienne, Dr. Lionel Desgranges from Commissariat à l’Energie Atomique et aux énergies alternatives, Centre de Cadarache, Département d'Etudes des Combustibles, Service d’analyses d’Elaboration, d’Expérimentations et d’Examens des combustibles and Dr. Daniel Freis from Joint Research Centre-Karlsruhe, Directorate G- Nuclear Safety and Security, Nuclear Fuel Safety Unit.

The research was carried out for 7 months at CEA Cadarache, DEN/DEC/SA3E/LAMIR, and for 2 years and 3 months at JRC-Karlsruhe.

Funding for the PhD studentship were provided by the CINNA project of CEA and partially by the ENEN+ project (funding from the EURATOM, Research and Training programme H2020, grant agreement N° 755576).

Acknowledgement

I wish to thank Pr. Loïc Favergeon, for accepting me as Ph.D. candidate at Ecole de Mines and for his continuous support while performing these studies.

I also wish to thank Dr. Lionel Desgranges and Dr. Daniel Freis for their excellent advice and all the time invested in discussing with me the results.

I am also very grateful to Rudy Konings for giving me the possibility to perform this research project in his research group. My acknowledgements to Beatrice Teisseire and Isabelle Moysan for welcoming me in their unit.

I also wish to thank Rachel and Thomas for introducing and guiding me through the “surface science” world, for their support and encouragements. I am grateful for our scientific discussions around the results, coming with more questions than answers at the end.

This work would not be possible without the technical help of Herwin, Co, Patrick, Sebastian and Daniele B. Thanks for helping me with sample preparations and especially for the effort in opening/cut the capsules.

I owe my sincere gratitude to Bert, Markus, Toto, Oliver and Jerome not only for being amazing colleagues, but also great friends. I will always be grateful for all the times you all helped me, supporting my crazy ideas on the lamellae preparation and spent a lot of time with me acquiring images.

I wish to thank Corine Farnaud for helping me with the French administrative procedures and, above of all, for giving me her warm support. To Petra Strube a big thank for facilitating the organization of my German period.

I would like to thank my friend and office mate Jean Francois for encouraging me even during the stressful moments. I very special thanks to the Female Football team, and in particular, to our coach Herwin, not only for his endurance, but also for being an amazing friend.

My heartfelt thanks to Lorenza, Jessica, Jone, Eider and Giovanna for the time they spent with me and for sharing unforgettable moments. I would like to thank Mari, Simo, Walter, Marco, Davide, Alessandro, Laetitia, Pauline, Tommaso, Gully, Ema, Luca L., Luca B. and Wirginia for the nice time together.

I am thankful to my lovely family for supporting and giving me their unconditioned love. Thanks to my Mum, Laura, and my Dad, Carmelo. Thanks to my nephews, Manuel and Alessandro, for making me happy with their bright smiles.

Finally, I have no words to thank the most important person, my husband. Thank you for being present even when thousands of kilometers are between us.

Table of Contents

List of figures	ix
List of Tables.....	xvii
Abbreviations	xix
Notations	xxi
Résumé	xxiv
Introduction	xl
Introduction	xl
1 Background and state of the art.....	- 1 -
1.1 Sodium cooled Fast reactors: past experience and new concept design.....	- 1 -
1.2 Sodium-fuel interaction	- 3 -
1.2.1 Out-of-pile experience.....	- 5 -
1.2.1.1 Compatibility tests between UO_2 and liquid sodium.....	- 5 -
1.2.1.2 Compatibility tests between PuO_2 and liquid sodium.....	- 6 -
1.2.1.3 Compatibility tests between $(\text{U,Pu})\text{O}_2$ and liquid sodium	- 7 -
1.2.2 Irradiation experience.....	- 8 -
1.2.2.1 Experimental Breeder Reactor-II	- 9 -
1.2.2.2 Belgium Reactor-2	- 11 -
1.2.2.3 SILOE	- 12 -
1.2.2.4 Rapsodie and Phénix	- 13 -
1.2.2.5 Dounreay Fast Reactor.....	- 14 -
1.2.2.6 The influence of the Joint Oxide Gain.....	- 17 -
1.2.3 Internal storage experience.....	- 18 -
1.3 Conclusions	- 18 -
2 Heterogeneous kinetics and mechanisms modelling.....	- 20 -
2.1 Description of the reaction	- 20 -
2.2 Nucleation and growth.....	- 22 -
2.2.1 Principles for the growth modelling.....	- 23 -
2.2.1.1 Modelling of the space function	- 25 -
2.2.1.2 Modelling of the reactivity.....	- 27 -
2.3 Requirements for the modelling	- 29 -
2.3.1 Thermodynamic aspects	- 29 -
2.3.1.1 Oxygen solubility in liquid sodium.....	- 30 -
2.3.1.2 Na-U-Pu-O system.....	- 32 -
2.3.1.3 Na-U-O system	- 33 -

2.3.1.4	Comparison of Na-U-Pu-O and Na-U-O systems	- 36 -
2.3.2	Kinetic aspects.....	- 37 -
2.3.3	Sodium diffusion	- 41 -
2.4	Conclusion	- 42 -
3	Research objectives	- 43 -
4	Experimental and characterization methods	- 45 -
4.1	Surface studies	- 45 -
4.2	Interaction tests using closed capsule	- 48 -
4.2.1	Sample preparation.....	- 49 -
4.2.1.1	UO ₂ samples	- 49 -
4.2.1.2	U _{1-x} Pu _x O ₂ pellets	- 51 -
4.2.2	Imposed oxygen potential	- 55 -
4.2.3	Sodium niobate buffer preparation.....	- 56 -
4.3	Experimental set-up	- 57 -
4.4	Characterization methods	- 59 -
4.4.1	X-ray Photoelectron Spectroscopy	- 59 -
4.4.2	X-ray Diffraction	- 61 -
4.4.2.1	Grazing Incidence X-ray Diffraction	- 63 -
4.4.3	Scanning Electron Microscopy	- 64 -
4.4.3.1	Energy Dispersive X-ray Spectroscopy	- 65 -
4.4.4	Focus Ion Beam.....	- 65 -
4.4.5	Transmission Electron Microscopy (TEM).....	- 66 -
5	Surface studies.....	- 67 -
5.1	Reference studies	- 67 -
5.1.1	Reference of metallic sodium and sodium oxide	- 67 -
5.1.2	Reference of uranium oxidation state.....	- 69 -
5.1.3	Stability of UO _{2+x} films	- 70 -
5.2	Interaction studies.....	- 71 -
5.2.1	Deposition of metallic sodium on stoichiometric UO ₂ at room temperature	- 71 -
5.2.2	Deposition of metallic sodium on UO _{2+x} ($0 \leq x \leq 1$) at room temperature ...	- 72 -
5.2.3	Formation of a ternary compound and its phase identification	- 74 -
5.2.4	Oxidation by molecular oxygen	- 77 -
5.3	Conclusion	- 78 -
6	Compatibility tests.....	- 82 -
6.1	Introduction	- 82 -

6.2	Reaction products characterization.....	- 84 -
6.2.1	Phase identification	- 84 -
6.2.2	Elemental composition	- 86 -
6.2.3	Influence of the crystallographic orientation.....	- 87 -
6.2.3.1	Surface with the $\langle 111 \rangle$ crystal lattice direction	- 87 -
6.2.3.2	Surface with the $\langle 001 \rangle$ crystal lattice direction	- 89 -
6.2.3.3	Polycrystalline sample	- 90 -
6.2.3.4	Cross section	- 91 -
6.2.4	Diffusion species	- 92 -
6.3	Excess of oxygen	- 93 -
6.4	Conclusions	- 95 -
7	Kinetic studies: imposed oxygen potential.....	- 97 -
7.1	Introduction	- 97 -
7.1.1	Compatibility tests with imposed oxygen potential	- 97 -
7.2	Characterization.....	- 98 -
7.2.1	Sodium niobate buffer.....	- 98 -
7.2.2	Reaction product: characterization and phase identification.....	- 99 -
7.2.2.1	X-Ray Diffraction	- 99 -
7.2.2.2	EDX	- 103 -
7.2.2.3	Transmission Electron Microscopy	- 106 -
7.2.2.4	Morphology and cross section view.....	- 107 -
7.2.3	Geometrical model and instantaneous nucleation.....	- 108 -
7.2.4	Sense of development of the reaction product	- 110 -
7.2.5	Rate determining step.....	- 113 -
7.3	Conclusions	- 115 -
8	MOX kinetic studies.....	- 118 -
8.1	Introduction	- 118 -
8.2	Compatibility tests.....	- 119 -
8.2.1	Characterizations	- 119 -
8.3	Kinetics tests: Imposed oxygen potential	- 122 -
8.3.1	Characterization	- 122 -
8.3.1.1	X-ray radiography	- 122 -
8.3.1.2	XRD	- 124 -
8.3.2	SEM.....	- 127 -
8.3.3	EDX.....	- 129 -

8.3.4	Rate determining step.....	- 130 -
8.4	Conclusion	- 132 -
9	Modelling of the reaction mechanism	- 136 -
9.1	Experimental data for the modelling	- 136 -
9.1.1	UO ₂ vs MOX for modelling	- 138 -
9.2	Modelling of the reaction mechanism	- 139 -
9.3	Conclusion	- 146 -
10	Conclusions	- 147 -
10.1	General conclusions	- 147 -
10.2	Future perspectives	- 148 -
	Conclusions	- 150 -
	Conclusions Générales	- 150 -
	Perspectives	- 151 -
	Annex: Concentration of oxygen dissolved in liquid sodium	- 153 -
	Annex: Na-O system	- 155 -
	Annex: Na-Pu-O system.....	- 157 -
	Annex: Additional information on the Na-U-O system	- 159 -
	Annex: Detailed calculations of geometrical	- 161 -
	Annex: XPS studies of sodium and sodium oxide	- 163 -
	Annex: Heterogeneous MOX.....	- 165 -
	Bibliography.....	- 169 -

List of figures

Figure 1: Core layout of ASTRID and internal storage position (green positions) [6] - 2 -

Figure 2: Left: fresh UO_2 sample. Middle: UO_2 after interaction with sodium [15] Right: formation of a loose surface layer after the interaction between liquid sodium containing sodium oxide and stoichiometric UO_2 [23] (as polished). - 6 -

Figure 3: Cross-section view (as polished) of $\text{U}_{0.8}\text{Pu}_{0.2}\text{O}_2$ samples after the interaction with liquid sodium, for 48h at 1173 K [19]. Left: sample with $\text{O/M}=1.960$ showing absence of reaction. Middle: sample with $\text{O/M}=1.970$ showing the Na_3MO_4 layer at the surface and at the grain boundaries. Right: sample with $\text{O/M}=1.995$ showing the Na_3MO_4 layer at the surface and at the grain boundaries. - 7 -

Figure 4: Reaction product location as function of the dissociation temperature. Rearranged from [22]. Left: after 6 days with the reaction product at a distance from the centreline of $r=0.8$. Right: after 65 days with the reaction product at the pellet rim. - 10 -

Figure 5: Non-demounted failed fuel assembly tested in BR-2 [32], before and after cleaning. The breach is clearly oriented outward to the coolant channel indicating that the cause of the rupture can be attributed to the high internal gas pressure caused by very high heat rating. - 11 -

Figure 6: Failed pin in SILOE reactor from [21]. Left: view of the hot spot position showing the maximum thickness of the reaction layer at the hot spot. Middle: view of the upper part of the breach showing a near uniform reaction layer at the pellet rim. Right: view of the upper intact pin showing the sodium penetration and the reaction layer at the pellet rim. - 12 -

Figure 7: Comparison of two different failed fuel pins. Left: failed pin in which no fuel was lost. Right: failed pin in which fuel loss was reported. - 14 -

Figure 8: Failed pin in DFR, with two breaches, from [12]. Detailed view of one wide crack at the upper end and one smaller crack at the lower end of the fuel column. - 15 -

Figure 9: JOG formation due to the chemical evolution of Mixed-Oxide Fuel [38] and fission product formation behavior in Fast Breeder Reactors (FBR). Detailed view of the JOG [39] morphology after post irradiation examination of a fuel pin. - 17 -

Figure 10: Different reactional zone. A represents the initial solid and B the formed phase after the reaction. - 22 -

Figure 11: Isotropic and anisotropic growth. A represents the initial solid and B the formed phase after the reaction. - 25 -

Figure 12: Inward and outward development. A represents the initial solid and B the formed phase after the reaction. - 25 -

Figure 13: Oxygen solubility in liquid sodium. Comparison between the available equations in literature. - 31 -

Figure 14: Section of the phase diagram Na-U-Pu-O and Na-U-O systems at 1000 K [18]- 32 -

Figure 15: Oxygen potential thresholds for the formation of Na-U-O ternary phases, adapted from [80]. C_0 lines correspond to the potential of sodium containing a concentration of C_0 ppm of oxygen. - 34 -

Figure 16: Oxygen potential thresholds for the formation Na_3UO_4 and $Na_3U_{1-x}Pu_xO_4$ and the correspondent oxygen concentration in liquid sodium in wppm. - 37 -

Figure 17: Kinetic curve for out-of-pile experimental tests. Left: Kinetic curves over a broad range of fuel composition and initial O/M ratio [20]. Right: Kinetic curves for the reaction between pure sodium and $(U_{0.7}Pu_{0.3})O_2$ in the temperature range 500-800 °C [16]. - 38 -

Figure 18: Measured diameter variation of the reaction product formation from out-of-pile and in-pile experiments [12]. The values were obtained for large and small hole-type (CEA values) defects. - 40 -

Figure 19: Surface analysis Labstation at JRC-Karlsruhe - 46 -

Figure 20: Preparation chamber. Left: view of the thin film preparation chamber. Right: detailed view of the chamber with the uranium oxide source on. - 47 -

Figure 21: Left: surface treatment chamber. Right: Characterization chamber with the view of XPS device. - 48 -

Figure 22: Left: Dry glovebox for the handling of reactive metallic sodium. Right: Detailed view of metallic sodium in mineral oil. - 48 -

Figure 23: Left: Minor actinides cell equipped with tele-manipulators. Right: view of the calcination furnace for MOX and sodium interaction studies. - 49 -

Figure 24: Single crystal surface view. Left: Rough surface after the cut. Right: Fine-polished surface. - 50 -

Figure 25: UO_2 pellets after the sintering. Left: surface view. Right: cross section view. - 51 -

Figure 26: Mixed oxide powder fabrication. - 51 -

Figure 27: XRD pattern of the sintered MOX showing the formation of a single phase with a lattice parameter of 5.446 Å. - 53 -

Figure 28: Plot of the lattice parameter as function of the Pu/(U+Pu) ratio according to Vegard's law and the calculated value, corresponding to stoichiometric $U_{0.68}Pu_{0.32}O_{2.00}$. - 53 -

Figure 29: Ceramography of Fresh MOX. The sample showed the presence of fabrication faults. - 54 -

Figure 30: View of the near surface zone of fresh MOX. Presence of open grain boundaries. - 54 -

Figure 31: Oxygen potential thresholds for the formation of Na-U-O ternary phases. Oxygen levels in liquid sodium (C_0) and oxygen potential imposed by the Na_3NbO_4 buffer (Blue line). - 55 -

Figure 32: XRD pattern of the Na_3NbO_4 buffer for stabilization of the oxygen potential. View of the disks after pressing. - 56 -

Figure 33: Left: Calcination furnace for the interaction tests between UO_2 and sodium. Right: detailed view of the capsule before the interaction test. - 57 -

Figure 34: Two design of the capsule for interaction tests. Left: Capsule design with two chambers and sample position; Right: Capsule design with a unique chamber and sample position. - 58 -

Figure 35: View of a cut capsule after the interaction. Due to the tightness, the capsule was cut by saw. Left: capsule fixed on the support for the cut. Middle: view of the excess of sodium after the interaction. Right: dissolution of the sodium excess with Ethanol. - 59 -

Figure 36: Basic components of a monochromatic XPS system. Right: schematic diagram of photoelectron process. - 60 -

Figure 37: Left: Visualization of the Bragg's law for X-ray diffraction. d_{hkl} is the distance between two adjacent planes, θ is the angle of incidence, also called Bragg angle. Black circles represent atoms. Right: schematic representation of the $\theta/2\theta$ diffraction. - 62 -

Figure 38: View of the sample and sample holder for XRD measurement. Left: UO_2 single crystal as mounted on a silicon sample holder. Right: view of the sample ready for the XRD measurement. - 63 -

Figure 39: Focus Ion Beam installed in the glove box for the analysis of high-radioactive materials. The glovebox is still under preparation. - 66 -

Figure 40: Na-1s core-level spectra with equalized peak intensities. Left: after deposition of metallic sodium followed by oxidation with molecular oxygen. Right: after deposition of metallic sodium followed by oxidation using atomic oxygen. - 68 -

Figure 41: Uranium 4f core level X-ray Photoemission Spectra recorded for U(IV) (left, green), U(V) in U_2O_5 (middle, red), and U(VI) (right, blue). - 69 -

Figure 42: Heat treatment of UO_3 thin film under UHV showing the progressive reduction to UO_2 - 71 -

Figure 43: Comparison between the normalized U-4f, O-1s, Na-1s and valence-band spectra before and after deposition of about two nm of sodium on UO_2 at room temperature - 72 -

Figure 44: Successive depositions of metallic sodium on UO_3 at room temperature, which resulted in a complete reduction of UO_3 into UO_2 . - 73 -

Figure 45: U-4f, O-1s and Na-1s spectra at various temperatures for the studies of the ternary compound formation. - 75 -

Figure 46: Effect of temperature on Na/ UO_3 followed by valence band spectra (left) and energy of the 5f peak and its FWHM (right). - 75 -

Figure 47: Left: Reciprocal Space Mapping (RSM) of the NaUO_3 phase produced in this study. Right: Corresponding GIXRD pattern of the NaUO_3 phase. - 76 -

Figure 48: U4f, Na1s and O1s core level spectra after oxidation by molecular oxygen at 673 K of the film of sodium on stoichiometric uranium oxide - 77 -

Figure 49: U4f, Na1s and O1s core level spectra after oxidation by molecular oxygen at 673 K of the film of sodium on hyper-stoichiometric uranium oxide - 78 -

Figure 50: NaUO_3 film obtained in the present study compared to $\text{Ba}_2\text{U}_2\text{O}_7$ and NaUO_3 bulk - 79 -

Figure 51: Thermodynamic of sodium deposition on stoichiometric and hyper-stoichiometric uranium oxide at room T - 80 -

Figure 52: U4f core spectra for the oxidation by molecular at 673 K after deposition of sodium on stoichiometric uranium oxide UO_2 . - 81 -

Figure 53: U4f core spectra for the oxidation by molecular at 673 K after deposition of sodium on hyper-stoichiometric uranium oxide UO_{2+x} . - 81 -

Figure 54: XRD of the single crystal 001 after oxidation in air at 350 °C for 1 h. Red: UO_2 and Black: U_3O_7 . The sample was slightly oxidation to U_3O_7 - 83 -

Figure 55: Characteristic XRD pattern of the single crystal having the surface well oriented on the $\{001\}$ direction (NAINT4). Red index: UO_2 phase. Black index: Na_3UO_4 phase. - 85 -

Figure 56: Left: Ring diffraction pattern from the corrosion phase with a cubic crystal structure. Right: Crystal planes and interplanar spacing by Miller indices. - 86 -

Figure 57: Example of a characteristic EDX spectrum reordered on the sample surface and the table with the corresponding element composition in weight % (w%) and atomic % (A%).- 87 -

Figure 58: Comparison between the initial (a) and the corroded (b) surface of the single crystal $\langle 111 \rangle$ (NAINT1). - 88 -

Figure 59: XRD of the single crystal with the $\langle 111 \rangle$ crystal lattice direction (NAINT1) and details of the ring diffraction of the UO_2 bulk and the Na_3UO_4 phase - 89 -

Figure 60: Comparison between the initial (a) and the corroded (b) surface of the single crystal $\langle 001 \rangle$ (NAINT4). - 90 -

Figure 61: Corroded surface of the single crystal $\langle 001 \rangle$ (NAINT2). - 90 -

Figure 62: Comparison between the initial (left) and the corroded (right) surface of the polycrystalline sample. - 91 -

Figure 63: Cross-section view of the samples after the interaction with liquid sodium for 50h at 800°C . Left: single crystal 001 Middle: single crystal 111 Right: polycrystalline - 92 -

Figure 64: EDX line-scan across the boundary bulk-new phase. No diffusion of sodium into the UO_2 bulk was measured. The geometrical size of the beam is close to $1.5\text{-}2\mu\text{m}$ and leads to a not well defined border with the new phase. - 93 -

Figure 65: Single crystal after 50h interaction at 1073 K with liquid sodium containing sodium oxide. Left: tilted view of the sample surface showing the presence of a uniform corroded layer. Right: top view of the corroded surface. - 94 -

Figure 66: Polycrystalline sample after 50h interaction at 800°C with liquid sodium containing sodium oxide. Left: tilted view of the sample surface showing the presence of a uniform corroded layer. Right: top view of the corroded surface. - 94 -

Figure 67: Left: Uranium bulk. Middle: interface between the bulk and the corrosion layer. Right: Corrosion layer - 95 -

Figure 68: XRD of the sodium niobate buffer after the interaction tests. The insert shows how the buffer looked like after the interaction. - 99 -

Figure 69: GIXRD on single crystal after 24 hours of interaction. Presence of uranium oxide bulk and two additional phases, NaUO_3 and Na_3UO_4 , were detected. - 100 -

Figure 70: Interpretation of the different peak, which appeared in the GIXRD pattern. - 102 -

Figure 71: EDX mapping on cross section lamellae. (1) View of the lamellae and the corresponding phases. (2) Uranium mapping. (3) Sodium mapping. (4) Oxygen mapping. (5) Platinum mapping. - 104 -

Figure 72: EDX line scan performed on the FIB-lamellae. Normalized individual intensity results from the uranium oxide bulk to the platinum protection layer. - 105 -

Figure 73: Left: View of the lamella for TEM analysis. Right: High resolution TEM at the interface between the bulk, UO_2 , and the corrosion layer. - 106 -

Figure 74: Comparison of high resolution (upper) and diffraction pattern (bottom) images obtained by TEM. Left: corrosion layer. Middle: interface between the bulk and the corrosion layer. Right: uranium oxide bulk. - 107 -

Figure 75: Morphology changes after sodium exposure. Left: Initial uranium oxide single crystal fine-polished. Right: Characteristic morphology of the uranium oxide after exposure to liquid sodium. - 107 -

Figure 76: Cross section view of the corrosion layer. Evolution with time from 12 to 192 hours of interaction, from left to right. - 108 -

Figure 77: Visual inspection of the samples before and after the reaction with liquid sodium. Upper: Unreacted sample. Bottom: From left to right: reacted samples after 12, 24 and 48 hours. - 109 -

Figure 78: Surface roughness evaluation by confocal laser scanning profilometer of the initial sample surface (left) and of the reacted surface (right) of NAIN7. - 110 -

Figure 79: Sense of development of a solid phase. Illustration of both outward and inward growth and the correspondent mobile interface. Blue squares represent the markers. - 111 -

Figure 80: Platinum marker for the study of the sense of development. Left: top view of the platinum marker with the corresponding dimensions. Right: cross section view of the platinum mark for the determination of the sense of development. - 111 -

Figure 81: Platinum markers. Left: Reference marker on unreacted sample. Middle: After 12 hours of interaction with liquid sodium. Right: After 24 hours of interaction with liquid sodium. - 112 -

Figure 82: Detailed view of the corrosion layer after 192 hours of interaction. Potential void formation at the internal interface in support to the outward growth assumption. - 112 -

Figure 83: Fit of the experimental point at 12, 24, 48 and 96 hours of interaction. - 114 -

Figure 84: Fit of the experimental point at 12, 24, 48, 96 and 192 hours of interaction and corresponding law as function of time. - 114 -

Figure 85: Comparison between the general law given in literature [89] and UO_2 results. - 115 -

<i>Figure 86: Section of the oxygen potential thresholds for the formation of the NaUO_3 and Na_3UO_4 ternary phases. Green line: oxygen potential imposed in the sodium interaction tests.</i>	- 116 -
<i>Figure 87: Identified phases through XRD and EDX analyses.</i>	- 117 -
<i>Figure 88: XRD pattern on MOX after 50 hour interaction</i>	- 119 -
<i>Figure 89: Surface view of the MOX after sodium interaction</i>	- 120 -
<i>Figure 90: Cross section view of the MOX sample after sodium exposure</i>	- 121 -
<i>Figure 91: Fractured surface of mixed oxide pellet after 50 hours of sodium interaction-</i>	121 -
<i>Figure 92: X-ray radiography of the capsule after sodium interaction at 973K. Left: before interaction Middle: after 12 hours of sodium interaction. Right: after 192 hours of interaction.</i>	- 122 -
<i>Figure 93: View of the samples after the recovery. Top left: NAIN14. Top right: NAIN15. Bottom left: NAIN16. Bottom right: NAIN17.</i>	- 124 -
<i>Figure 94: XRD pattern of the moisture Na_3NbO_4 and reduced mixed oxide. Black: Na_3NbO_4. Red: $(\text{U,Pu})\text{O}_{1.99}$</i>	- 125 -
<i>Figure 95: View of faults on the pellet surface after sodium interaction at 973 K. Right: NAIN17. Right: NAIN16.</i>	- 127 -
<i>Figure 96: Scanning electron micrograph of a fracture surface of mixed oxide pellet. Appearance of a corrosion layer confined at the pellet periphery.</i>	- 128 -
<i>Figure 97: Comparison between an internal fracture surface which did not come into direct contact with sodium (left) and an internal surface exposed to sodium (right) during the interaction test.</i>	- 128 -
<i>Figure 98: EDX spectrum of mixed oxide after sodium interaction</i>	- 129 -
<i>Figure 99: Fit of the experimental point at 24, 48 and 96 hours of interaction at 973 K.</i>	- 131 -
<i>Figure 100: Fit of the experimental point at 24, 48, 96 and 192 hours at 973 K.</i>	- 131 -
<i>Figure 101: Comparison between the experimental data obtained for interaction tests between UO_2 (black line) and MOX (red line) with liquid sodium at the beginning of the reaction.-</i>	132 -
<i>Figure 102: Comparison between the experimental data obtained for interaction tests between UO_2 (black line) and MOX (red line) with liquid sodium for long-period reaction.</i>	- 133 -

Figure 103: Comparison between the experimental result of the present study and data in literature. - 134 -

Figure 104: Comparison between the experimental result of the present study and data in literature. - 134 -

Figure 105: Schematic illustration of the interaction studies at 298 K. Left: deposition of metallic sodium on stoichiometric uranium oxide. Right: deposition of metallic sodium on hyper-stoichiometric uranium oxide - 137 -

Figure 106: Oxygen threshold for the formation of trisodium uranoplutonate. Blue line: oxygen potential imposed in this study. Yellow line: oxygen potential expected in internal storage. - 138 -

Figure 107: Schematic view of the proposed reaction mechanism. Diffusion zone, external and internal interface are indicated to localize where the steps take place. - 141 -

Figure 108: Experimental data and modelling fit. The modelling describes in a precise manner the beginning of the reaction and it is conservative over the long-term. - 145 -

Figure 109: Na-O phase diagram [62] - 155 -

Figure 110: Na-Pu-O phase diagram from [53] - 157 -

Figure 111: Calculated Na-U-O phase diagram at ~600°C from [80] - 159 -

Figure 112: Na-1s spectra obtained on Au after oxidation with atomic and molecular oxygen, on stoichiometric UO_2 , on stoichiometric UO_2 with molecular oxygen and on UO_{2+x} . - 164 -

Figure 113: SEM of Heterogeneous MOX - 165 -

Figure 114: RAMAN Mapping heterogeneous MOX - 166 -

List of Tables

<i>Table 1: Main proprieties comparison of MO_2 and Na_3MO_4 ($M=\text{U}, \text{Pu}$)</i>	- 4 -
<i>Table 2: Summary of the main results of failed fuel pin tests under irradiation</i>	- 16 -
<i>Table 3: Geometrical factor G_D for rate determining step of diffusion</i>	- 24 -
<i>Table 4: Expressions of the molar space function S_m [41]</i>	- 26 -
<i>Table 5: Structural proprieties of Na-U-Pu-O compounds</i>	- 33 -
<i>Table 6: Summary of structural proprieties of Na-U-O compounds</i>	- 35 -
<i>Table 7: Calculated chemical diffusion coefficients of sodium at different temperature</i>	- 41 -
<i>Table 8: MOX sample designations and basic data</i>	- 52 -
<i>Table 9: Binding energy of metallic sodium and sodium oxide in this study</i>	- 68 -
<i>Table 10: Binding energy of U(IV), U(V) and U(VI)</i>	- 70 -
<i>Table 11: Summary of the results of the interaction between pure sodium and stoichiometric uranium oxide</i>	- 71 -
<i>Table 12: Summary of the results of the progressive deposition of metallic sodium on hyper-stoichiometric uranium oxide</i>	- 73 -
<i>Table 13: Summary of the results at various temperatures for the studies of the ternary compound formation</i>	- 74 -
<i>Table 14: Test matrix for corrosion resistance tests</i>	- 83 -
<i>Table 15: Summary of the XRD results</i>	- 85 -
<i>Table 16: Test matrix for kinetic studies</i>	- 98 -
<i>Table 17: Measured and calculated values of the trisodium uranate phase</i>	- 101 -
<i>Table 18: Elemental composition measured by EDX</i>	- 103 -
<i>Table 19: Test matrix for MOX-sodium interaction tests (compatibility and kinetic studies).</i>	- 118 -
<i>Table 20: Summary of the sample recovery after each interaction</i>	- 123 -

<i>Table 21: MOX lattice parameter after sodium interaction at 973 K</i>	- 126 -
<i>Table 22: Summery of the phases in the Na-O system</i>	- 156 -
<i>Table 23: Structural proprieties of Na-Pu-O compounds</i>	- 158 -
<i>Table 24: Calculated oxygen potential thresholds of sodium uranate formation [73]</i>	- 159 -
<i>Table 25: Thermodynamic data of the Na-U-O system</i>	- 160 -

Abbreviations

ALARA	As Low As Reasonably Achievable
ANL	Argonne National Laboratory
ASTRID	Advanced Sodium Technology Reactor for Industrial Demonstration
BE	Binding Energy
BOL	Beginning Of Life
BR-2	Belgium Reactor-2
CEA	Commissariat à l’Energie Atomique et aux énergies alternatives
CHA	Concentric Hemispherical Analyzer
DC	Direct Current
DFR	Dounreay Fast Reactor
DND	Delayed Neutron Detection
EBR-II	Experimental Breeder Reactor-II
ECR	Electron Cyclotron Resonance
EDX	Energy Dispersive X-ray
EELS	Electron Energy-Loss Spectroscopy
EMSE	Ecole nationale supérieure des Mines de Saint-Etienne
EOL	End Of Life
FARO	Furnace And Release Oven
FIB	Focus Ion Beam
FCCI	Fuel Cladding Chemical Interaction
FCMI	Fuel Cladding Mechanical Interaction
FCI	Fuel Coolant Interaction
FWHM	Full Width at Half Maximum
GIXRD	Grazing Incidence X-Ray Diffraction
HRTEM	High Resolution Transmission Electron Microscope
JOG	Joint Oxide Gain
JRC	Joint Research Centre
MA	Minor Actinides
MOX	Mixed OXide, (U,Pu)O ₂
O/M	Oxygen to Metal ratio
R&D	Research and Development
RSM	Reciprocal Space Mapping
SEM	Scanning Electron Microscopy

SFR	Sodium cooled Fast Reactor
SFRP	Sodium Fuel Reaction Product
TEM	Transmission Electron Microscope
UHV	Ultra-High Vacuum
XPS	X-ray Photoelectron Spectroscopy
XRD	X-Ray Diffraction

Notations

a	lattice parameter (\AA)
at %	atomic percent
\AA	Angström
A	solid reactant
A_M	atomic impurities
B	solid product
C_O	oxygen concentration (ppm)
ΔC	difference of concentration of the diffusing species (mol m^{-3})
D	diffusion coefficient ($\text{m}^2 \text{s}^{-1}$)
E_a	apparent activation energy (J mol^{-1})
e_0	initial half-thickness of a plate particle (m)
fcc	face centered cubic
G_D	geometrical factor
G_i	gas phase
ΔG_{O_2}	oxygen potential thresholds of formation (J mol^{-1})
h	length of a cylindrical particle (m)
J	diffusion flux ($\text{mol m}^2 \text{s}^{-1}$)
J	Joule
k	rate constant (s^{-1})
k_0	frequency factor
K	Kelvin
l_0	constant length (=1m)
m	meter
mol	mole
n_A	amount of solid reactant at time t (mol)
n_B	amount of solid product at time t (mol)
n_i	amount of intermediate species (mol)
n_0	initial amount of solid reactant (mol)
Na	Sodium

N_0	initial number of particles
O	Oxygen
ppm	part per million
Pu	Plutonium
Q	activation energy (J mol^{-1})
r_e	external radius of a particle (m)
r_i	internal radius of a particle (m)
r_0	initial radius of a particle (m)
R	ideal gas constant ($=8.314 \text{ J K}^{-1} \text{ mol}^{-1}$)
s_0	initial surface area of a particle (m^2)
S	surface area of the reactional zone (m^2)
S_m	space function ($\text{m}^2 \text{ mol}^{-1}$)
t	time (s)
T	temperature (K)
U	Uranium
V	Volume (m^3)
V_X	vacancy
w %	weight percent
wppm	weight part per million
X_i	interstitial element
z	expansion coefficient
α	fractional extent of the powder
β_i	arithmetic stoichiometric number of reactant
ν_B	stoichiometric coefficient related to solid product
ν_{G_i}	stoichiometric coefficient related to gas G_i
ν_s	areic rate ($\text{mol m}^{-2} \text{ s}^{-1}$)
ξ	extent of reaction (mol)
\Re	rate of reaction
ϕ	areic reactivity of growth ($\text{mol m}^{-2} \text{ s}^{-1}$)

Résumé

Pour satisfaire les besoins en énergie du futur, une nouvelle génération de réacteurs nucléaires, dénommée GEN-IV, fait l'objet de recherches avec l'objectif d'atteindre les plus haut standards de sûreté, de performances économiques et de développement durable. Parmi les concepts étudiés, les réacteurs à neutrons rapides refroidis au sodium bénéficient d'un important retour d'expérience tant du point de vue des résultats de recherche que de l'exploitation industrielle.

Un des concepts prometteurs pour ces futurs réacteurs à neutrons rapides s'articule autour d'un flot nucléaire compact sans barillet de stockage du combustible nucléaire, comme cela était le cas dans les réacteurs français, Phénix et Superphénix. Eliminer le barillet, et ses 20 tonnes de sodium, réduit significativement le risque de réaction sodium-air et minimise la manutention des assemblages combustibles. Dans cette configuration, les assemblages de combustible utilisé seront placés dans une zone dédiée de la cuve réacteur (position verte dans la Figure 1) tout au long de leur période d'entreposage. Toutefois, cette zone dédiée devra aussi accueillir des aiguilles défectueuses.

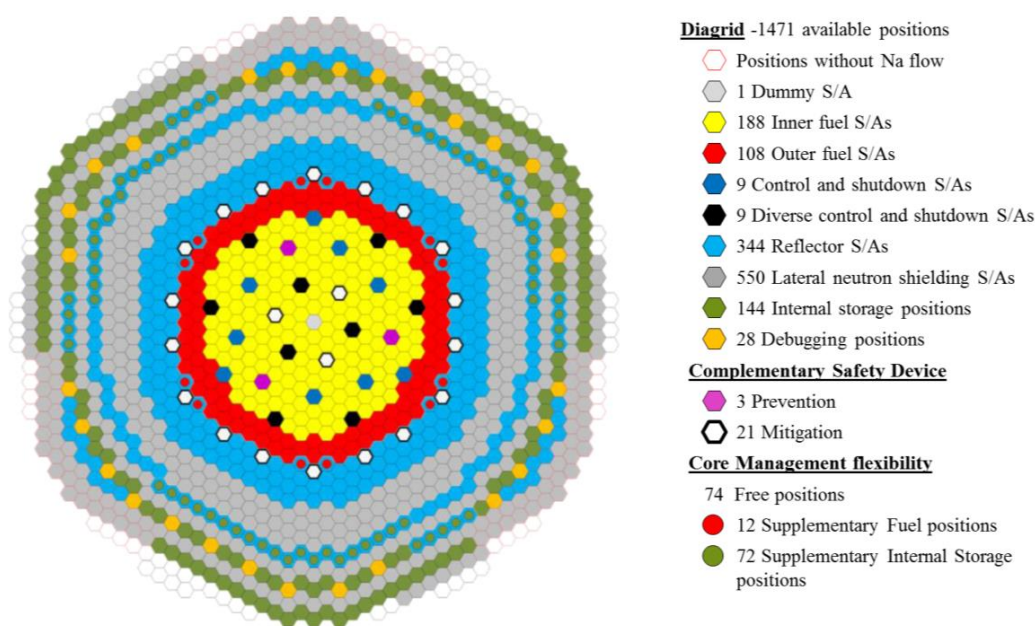


Figure 1: Cœur de ASTRID, projet réacteur à neutrons rapides porté par le CEA.

Une aiguille est considérée comme défectueuse lorsqu'une brèche existe dans la gaine (

Figure 2), ce qui conduit au relâchement des produits de fission volatils. Dans les réacteurs rapides actuels, les systèmes de détections sont suffisamment performants pour détecter ce relâchement au plus tôt, et arrêter le réacteur dès l'apparition d'une aiguille défectueuse.

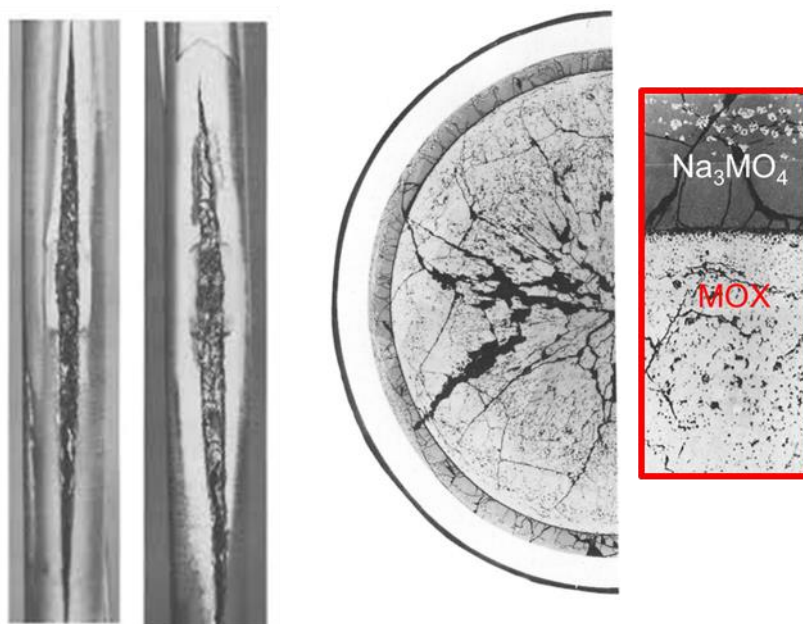


Figure 2: aiguille défectueuse, gauche vue d'ensemble, milieu demi-coupe radiale, droite zoom sur l'interface combustible-produit de corrosion

Le sort des aiguilles défectueuses reste toutefois une question ouverte dans le concept sans barillet. En effet, lorsqu'une aiguille défectueuse est en contact avec le sodium, une réaction chimique se produit entre le sodium et le combustible nucléaire, un oxyde mixte de plutonium et d'uranium (dénommé MOX). Des essais en réacteur ont démontré que cette réaction conduisait essentiellement à la formation du composé Na_3MO_4 (où $M=U$ ou Pu), qui a une densité (autour de 5,6) presque deux fois plus faible que celle du MOX (autour de 10,9). Cette densité plus faible du produit de corrosion induit des déformations sur la gaine, qui peuvent éventuellement provoquer le relâchement de matière fissile dans le cœur du réacteur.

Les futurs réacteurs de GEN-4 se doivent d'avoir un haut niveau de sûreté, ce qui conduit à une stratégie de « cœur propre », c'est-à-dire un niveau de contamination en matière fissile du circuit primaire aussi bas que possible. De manière à satisfaire cette exigence dès la conception, il est indispensable de savoir de quelle période de temps on dispose avant qu'une aiguille défectueuse en stockage interne ne se dégrade suffisamment pour conduire à la dissémination de matière fissile. On ne peut répondre à cette question qu'avec une prédiction fiable de la cinétique de réaction entre le combustible oxyde et le sodium liquide.

Dans ce travail, on a choisi une méthodologie de prédiction basée sur une modélisation mécaniste de la réaction MOX-Sodium. Cette méthodologie s'appuie sur le formalisme de la cinétique hétérogène, car nous avons à faire à une réaction solide (MOX) – liquide (sodium). Le formalisme de la cinétique hétérogène prend en compte les mécanismes de germination et croissance, eux-mêmes subdivisés en plusieurs étapes élémentaires. La cinétique de la réaction s'écrit alors en fonction de la contribution de chacune de ces étapes élémentaires.

Appliqué au cas de la réaction MOX-sodium, le formalisme de la cinétique hétérogène nous demandera de répondre aux questions suivantes :

- 1- Quels sont les produits de réactions qui se forment dans les conditions réelles de stockage interne ? et quelles sont les propriétés de leurs défauts ponctuels impliqués dans les étapes élémentaires ?
- 2- A-t-on une germination instantanée ?
- 3- Quelles sont les espèces impliquées dans les étapes élémentaires, et leur chemin de diffusion ?
- 4- Existe-il une étape élémentaires limitante qui déterminerait la cinétique de la réaction ?

La littérature nous fournit certaines réponses mais pas toutes. En effet, même si le système U-Pu-O-Na a été largement étudié du point de vue thermodynamique, la cinétique de la réaction MOX-sodium reste en grande partie inexplorée. On ne recense en effet que deux études majeures sur ce sujet datant des années 1970-80.

Du point de vue thermodynamique, on considère généralement que la réaction MOX-sodium en réacteur conduit à la formation d'un composé analogue à l'uranate de tri-sodium. Même si le système ternaire U-O-Na a fait lui aussi l'objet de nombreuses investigations, les mécanismes de formation de ce composé ainsi que l'état d'oxydation de l'uranium dans ce composé sont toujours débattus. Par ailleurs, l'exploration du système U-Pu-O-Na n'étant pas achevée, l'extrapolation au cas réel ne peut se faire sans hypothèses ad-hoc.

Du point de vue cinétique, la littérature ne fournit que des données éparses sur la réaction du combustible oxyde avec le sodium liquide.

Des tests ont été réalisés en réacteur dans lesquels on a mesuré l'augmentation du diamètre d'une aiguille défectueuse en fonction du temps. Ce changement de diamètre a été attribué au gonflement dû à la formation du produit de corrosion moins dense. Le peu de résultats obtenus a été utilisé pour proposer des lois de gonflement de la gaine. Une loi très générale est donnée ci-dessous :

$$\frac{\Delta d}{d} \% \approx 1.6t^{0.25} \quad (1)$$

Des tests hors réacteur ont confirmé que la réaction se produisait avec une cinétique de type parabolique (Figure 35). Ces résultats ont justifié que l'on considère que la cinétique de réaction soit contrôlée par un mécanisme de diffusion. L'hypothèse d'une étape limitante due à la diffusion du sodium dans la couche de corrosion a été proposée, sans que, cependant, rien ne vienne l'étayer.

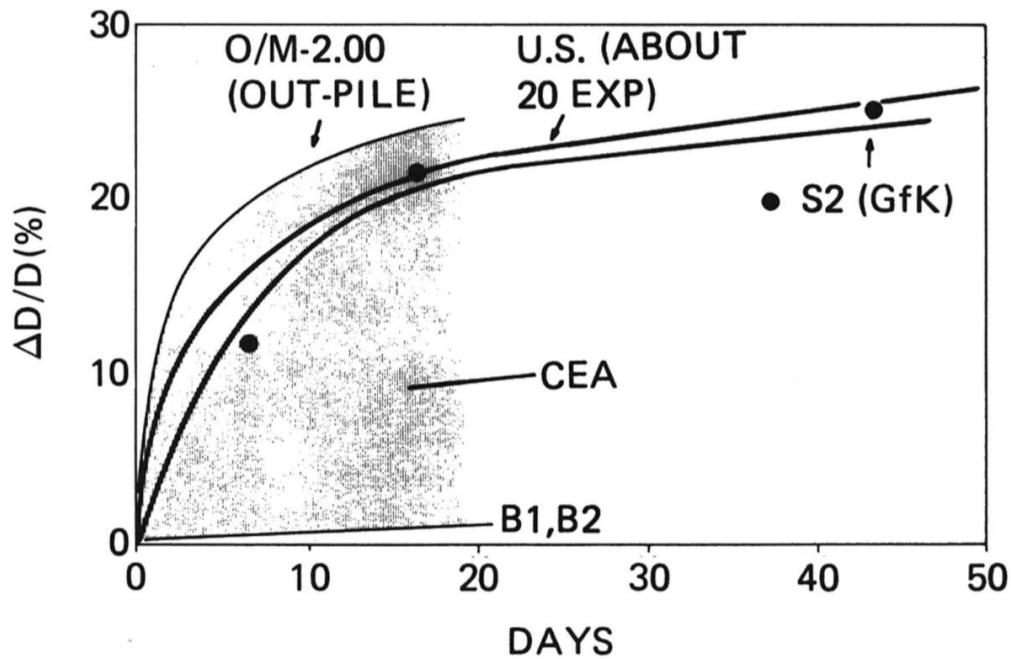


Figure 3: Measured diameter variation of the reaction product formation from out-of-pile and in-pile experiments [12]. The values were obtained for large and small hole-type (CEA values) defects.

Pour construire une modélisation prédictive de la réaction combustible-sodium, cette étude a été organisée de la manière suivante :

1. Obtenir des informations sur les mécanismes réactionnels avec un système sur lequel il est aisé de mettre en œuvre des méthodes de caractérisation sophistiquées, c'est à dire étudier la réaction UO_2 -sodium plutôt que la réaction MOX -sodium. Sur ce système étudier les questions suivantes
 - a. Quel est le degré d'oxydation de l'uranium dans le produit de corrosion
 - b. Quel est le mécanisme de germination et comment se forme le produit de corrosion
 - c. Quelle est la cinétique de croissance, avec une attention toute particulière sur type de croissance et son étape limitante
2. Vérifier comme le comportement de l' UO_2 peut être extrapolé à celui du MOX .
3. Proposer, à partir de cette analyse, des hypothèses raisonnables pour construire un modèle cinétique.

Cette démarche théorique s'est concrétisée par la démarche expérimentale suivante :

- i. des études de surface pour déterminer le degré d'oxydation de l'uranium dans la couche de corrosion (point 1.a). Pour ce faire, on a réalisé des couches minces d'oxyde d'uranium sous ultravide que l'on a fait réagir avec du sodium. La caractérisation de ces couches a été réalisée par XPS, car cette méthode est l'une des plus performantes pour des déterminer l'état d'oxydation d'un atome.

- ii. des test de compatibilité, c'est-à-dire des tests dans lesquels l'oxyde est le sodium sont mis en contact dans une capsule étanche contenant une quantité donnée d'oxygène, pour étudier le mécanisme de germination (point 1.b). Ces tests ont aussi permis l'analyse de la couche de corrosion au tout début de la réaction.
- iii. Des études cinétiques, c'est-à-dire des tests dans lesquels l'oxyde est le sodium sont mis en contact dans une capsule étanche où on impose un potentiel oxygène donné, pour étudier le mécanisme de croissance.

Les tests de compatibilité et les études cinétiques ont été réalisées avec de l' UO_2 , mais aussi avec du MOX enrichi à environ 30%, pour établir comment les mécanismes réactionnels pourraient être transposés de l' UO_2 au MOX.

Pour connaître le degré d'oxydation de l'uranium dans la couche de corrosion, des couches minces d'oxyde d'uranium et d'uranate de sodium ont été réalisées sous ultravide, puis soumises à différents environnements. Il en ressort que le sodium métallique tend à réduire l'oxyde d'uranium sur-stœchiométrique et que l'uranium peut être stabilisé sous la seule forme +5 lors d'un traitement thermique. Ce dernier point montre clairement que, en condition de stockage interne les produits de corrosion se formeront préférentiellement avec un degré d'oxydation +5, plutôt qu'avec un degré d'oxydation supérieur qui est observé pour certains composés ternaires U-Na-O. De plus, le sodium réduit le trioxyde d'uranium en formant, à température ambiante, $\text{Na}_2\text{O} + \text{UO}_{2+x}$, et, à haute température, un composé ternaire, ce qui permet de conclure à l'existence de mécanismes de diffusion thermiquement activés qui contribuent à la formation de la couche de corrosion. Une fois formé, le composé ternaire sera stable jusqu'à au moins 973K.

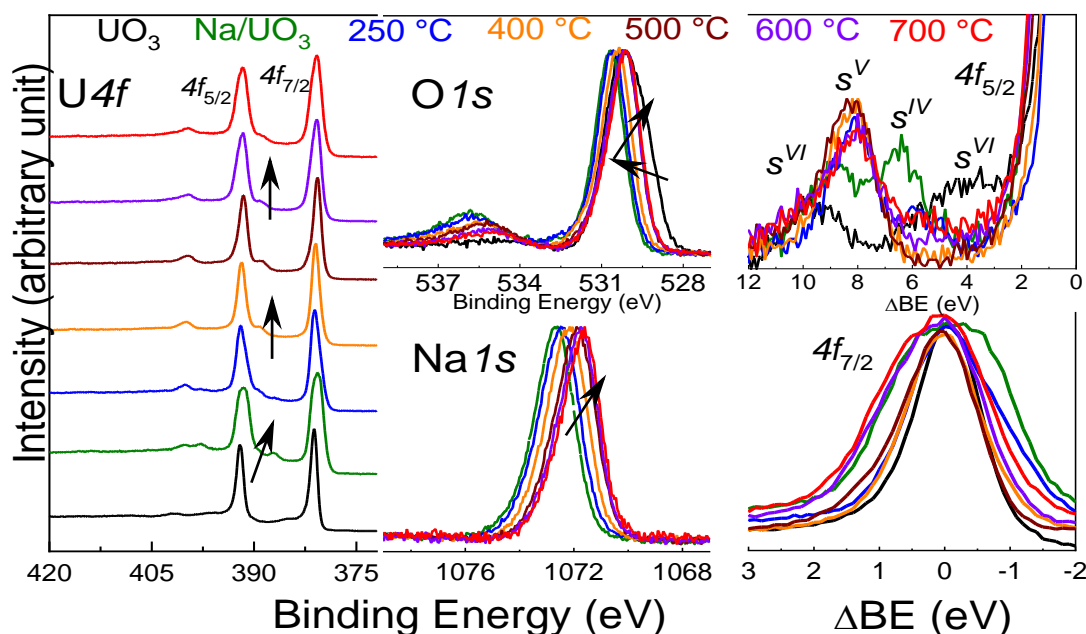


Figure 4: U-4f, O-1s and Na-1s spectra at various temperatures for the studies of the ternary compound formation.

Les tests de compatibilité, en capsules étanches avec un contenu en oxygène constant, ont confirmé le mécanisme de germination instantanée lors de la réaction dioxyde d'uranium-sodium liquide. Le produit de corrosion se forme uniformément en couvrant toute la surface de l'échantillon, que la concentration en oxygène initiale soit élevée ou faible.

Même si cette surface peut présenter des morphologies différentes en fonction de l'orientation cristallographique des grains sous-jacents, l'épaisseur de la couche de corrosion ne montre pas de dépendance en fonction de l'orientation des grains ou de leur taille (dans la plage 5-20 μ m). Elle ne montre pas de différence non plus suivant que l'échantillon soit un mono ou un polycristal. Nous en avons déduit que la cinétique de réaction ne dépendait pas de l'orientation, ni de la taille des grains de l'oxyde. La couche de corrosion n'était pas complètement adhérente au substrat UO_2 . Ce manque d'adhérence pourrait provenir soit du mécanisme réactionnel lui-même, ou bien de la préparation de l'échantillon avant les examens. Ce type de comportement a déjà été reporté par Mignanelli et al pour la réaction entre du sodium liquide et de l' UO_2 .

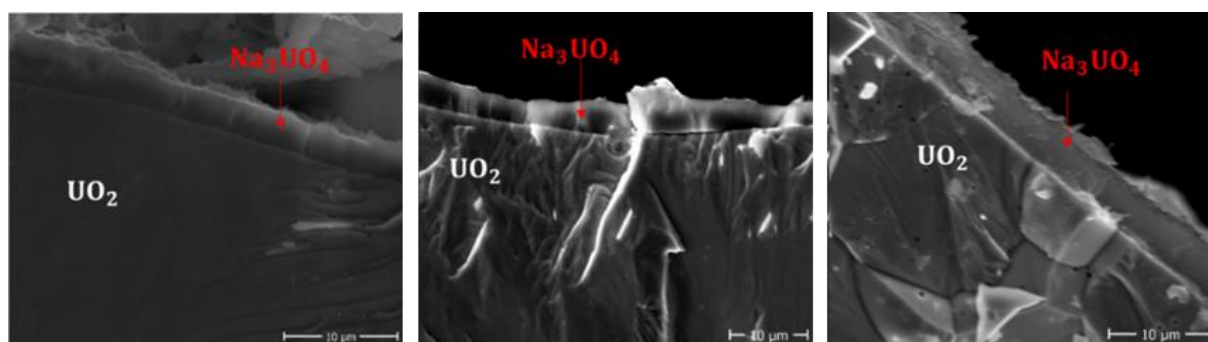


Figure 5: Cross-section view of the samples after the interaction with liquid sodium for 50h at 800°C. Left: single crystal 001 Middle: single crystal 111 Right: polycrystalline

L'absence de diffusion du sodium dans l' UO_2 a été mise en évidence avec des mesures par EDX. Les examens MEB ont permis de mieux caractériser la morphologie de la couche de corrosion. Cette dernière apparaît comme une couche uniforme répartie sur toute la surface de l'échantillon initial. Sa forme ne dépend pas de la quantité d'oxygène disponible initialement, même si son épaisseur augmente avec cette quantité d'oxygène. La présence d'oxygène additionnel dans le sodium initial n'a pas conduit la désintégration des échantillons, même à forte teneur en oxygène. Ce résultat diffère de la couche de corrosion lâche ou encore de la désintégration de l'échantillon qui ont pu être observés dans certains articles.

Après 50 heures à 1073K, on obtient une couche d'uranate de trisodium Na_3UO_4 formée sur l' UO_2 en présence de sodium contenant de l'ordre de 10 ppm d'oxygène dissous, conformément aux résultats de la littérature. Le paramètre de maille de cette phase mesurée par diffraction X est proche des valeurs de la littérature. La symétrie cubique et la valeur du paramètre de maille ont aussi été confirmés par des mesures MET. L'examen MET a aussi permis de mettre en évidence la croissance préférentielle de l'uranate de trisodium suivant son axe (111). Cette orientation préférentielle a aussi été mise en évidence par diffraction X sur monocristal que le monocristal d' UO_2 soit orienté (111) ou (100).

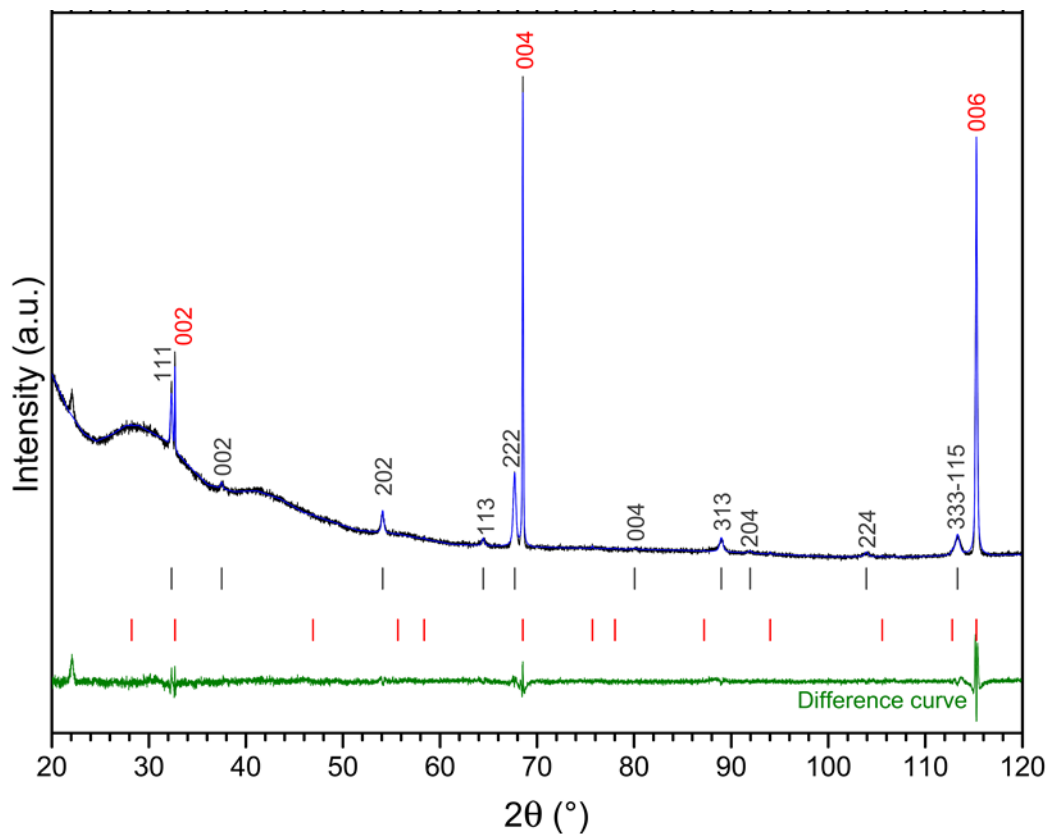


Figure 6: Characteristic XRD pattern of the single crystal having the surface well oriented on the $\{001\}$ direction (NAINT4). Red index: UO_2 phase. Black index: Na_3UO_4 phase.

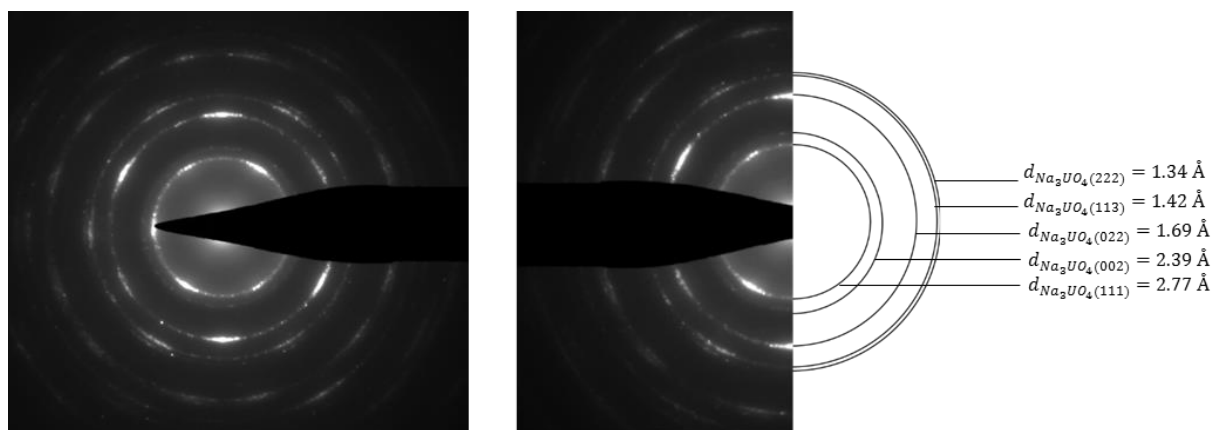


Figure 7: Left: Ring diffraction pattern from the corrosion phase with a cubic crystal structure. Right: Crystal planes and interplanar spacing by Miller indices.

Les études cinétiques ont été menées au moyen d'une capsule étanche, conçue spécifiquement pour ce travail, où on dispose du dioxyde d'uranium, du sodium et un tampon REDOX. La présence du tampon REDOX permet d'imposer dans la capsule un potentiel oxygène connu, qui varie en fonction de la température. Pour une température donnée, la réaction était arrêtée à des temps d'interaction différents, la couche de corrosion caractérisée en fonction du temps d'interaction.

Les observations faites sur la couche de corrosion formée au cours de ces essais nous a permis d'identifier pour la première fois :

1. Un mécanisme de croissance externe pour la couche de corrosion, ce qui implique que l'espèce diffusante contrôlant la cinétique de croissance doit être le cation uranium, considération qui n'avait jamais été envisagée précédemment
2. La formation d'une couche de corrosion composée de deux phases chimiques différentes pour un potentiel oxygène proche de celui des conditions de stockage interne, ce qui, là aussi, n'avait jamais été considéré auparavant, et qui ouvre la question de l'existence de deux phases dans la couche de corrosion formée avec du MOX, en réacteur cette fois-ci.

La caractérisation de la couche de corrosion a été réalisée par diffraction des rayons X en incidence rasante (GIXRD) à l'Institut de Mathématique et de Physique de Prague. Cette technique permet une caractérisation de l'extrême surface d'un solide, ce qui s'est avéré pertinent pour notre cas. L'analyse du diffractogramme a permis d'identifier deux phases chimiques différentes :

1. L'uranate de tri-sodium, Na_3UO_4 , avec un paramètre de maille de $4.78(6) \text{ \AA}$ une structure cubique simple.
2. L'uranate de sodium, NaUO_3 , avec des paramètres de maille de $a=7.83(1) \text{ \AA}$, $b=7.45(1) \text{ \AA}$ et $c=6.78(1) \text{ \AA}$.

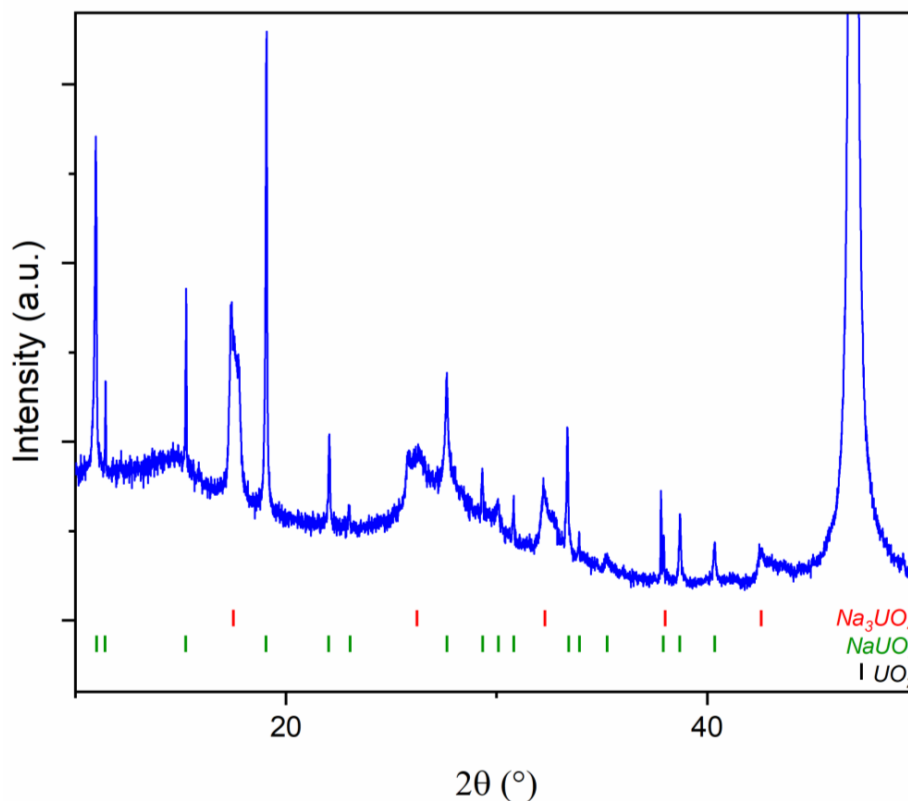


Figure 8: GIXRD on single crystal after 24 hours of interaction. Presence of uranium oxide bulk and two additional phases, NaUO_3 and Na_3UO_4 , were detected.

Une lame FIB a été fabriquée à la surface de l'un échantillon d' UO_2 monocristallin de manière à englober la couche de corrosion et son interface avec le substrat UO_2 . Une mesure EDX le long d'une ligne sur cette lame a été effectuée pour identifier les différents flux d'espèces chimiques. Les résultats, présentés dans la Figure 9, confirment l'absence de diffusion du sodium dans l' UO_2 . Le sodium n'est effectivement détecté que hors de l' UO_2 . Les profils DEX vont aussi apparaître l'existence de deux phases chimiques différentes dans la couche de corrosion. Ces phases forment des couches uniformes parallèles à la surface de l' UO_2 initial. La phase la plus proche de l' UO_2 est aussi celle qui est la plus riche en sodium. En cohérence avec les résultats de diffraction, cette phase, la plus proche de l' UO_2 et la plus riche en sodium, serait l'uranate de tri-sodium, Na_3UO_4 , alors que l'autre phase serait l'uranate de sodium NaUO_3 , plus pauvre en sodium et au contact du sodium.

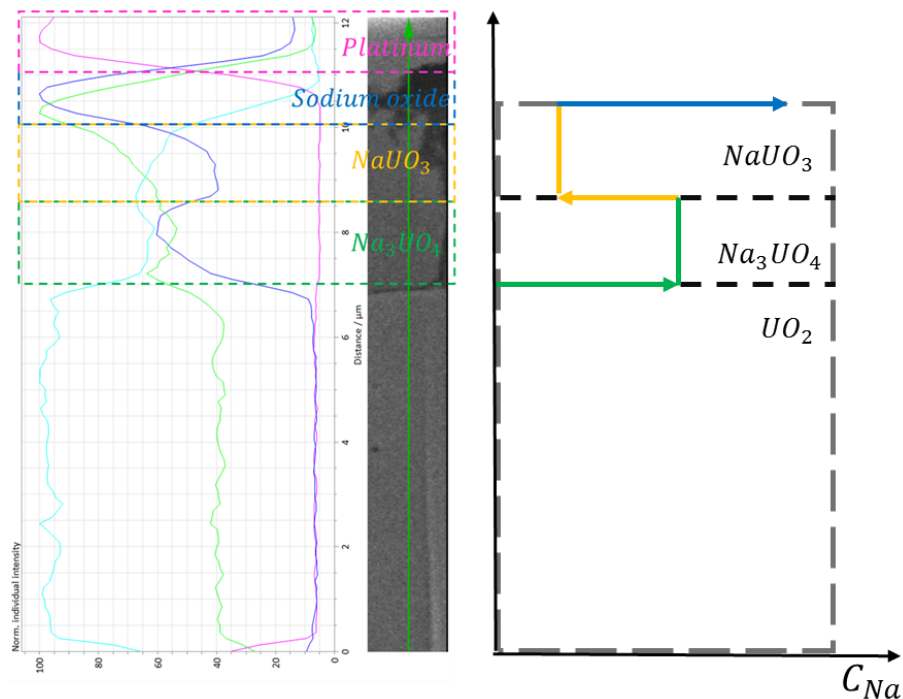


Figure 9: EDX line scan performed on the FIB-lamellae. Normalized individual intensity results from the uranium oxide bulk to the platinum protection layer.

La formation de deux phase différentes, dans les conditions de notre test, est cohérente avec les données thermodynamiques disponibles. Comme illustré sur la Figure 10, Le potentiel imposé par le tampon REDOX au cours de ces essais se situe en effet dans une zone biphasée, NaUO_3 et Na_3UO_4 , du diagramme de phase. La formation de ces deux composés est donc attendue dans des conditions d'équilibre thermodynamiques, et éventuellement des conditions locales d'équilibre thermodynamique.

Ce résultat nous amène considérer deux nouvelles questions pertinentes pour la sûreté d'un stockage interne dans un futur réacteur à neutrons rapides.

La première question porte sur la nature des produits de corrosion qui sont effectivement formés dans les conditions réacteur : peut-on se contenter de considérer une seule phase chimique dans les produits de corrosion sachant que nos résultats expérimentaux montrent l'existence de deux phases chimiques différentes, NaUO_3 et Na_3UO_4 . En effet, les conditions thermodynamiques dans lesquelles nos essais à potentiels imposé ont été réalisées sont très proches des conditions attendues en réacteur.

La seconde question porte sur notre capacité à transposer des résultats obtenus avec le système Na-U-O dans le système Na-U-Pu-O nécessairement plus complexe. Si cette transposition est faite de manière brutale, alors il faudrait aussi considérer deux phases dans le système Na-U-Pu-O. Néanmoins, si on se reporte à la littérature pour les valeurs les plus élevées en potentiel oxygène pour lesquelles on observe la formation de l'uranoplutonate de tris-sodium, une concentration en plutonium proche de 30% ou supérieure serait suffisante pour stabiliser la seule phase uranoplutonate de tris-sodium dans des conditions réacteurs. Malheureusement, le seuil exact en potentiel oxygène pour le passage d'un système mono à biphasé est mal connu, ce qui fait peser de fortes incertitudes sur notre capacité à faire des prédictions dans le système Na-U-Pu-O.

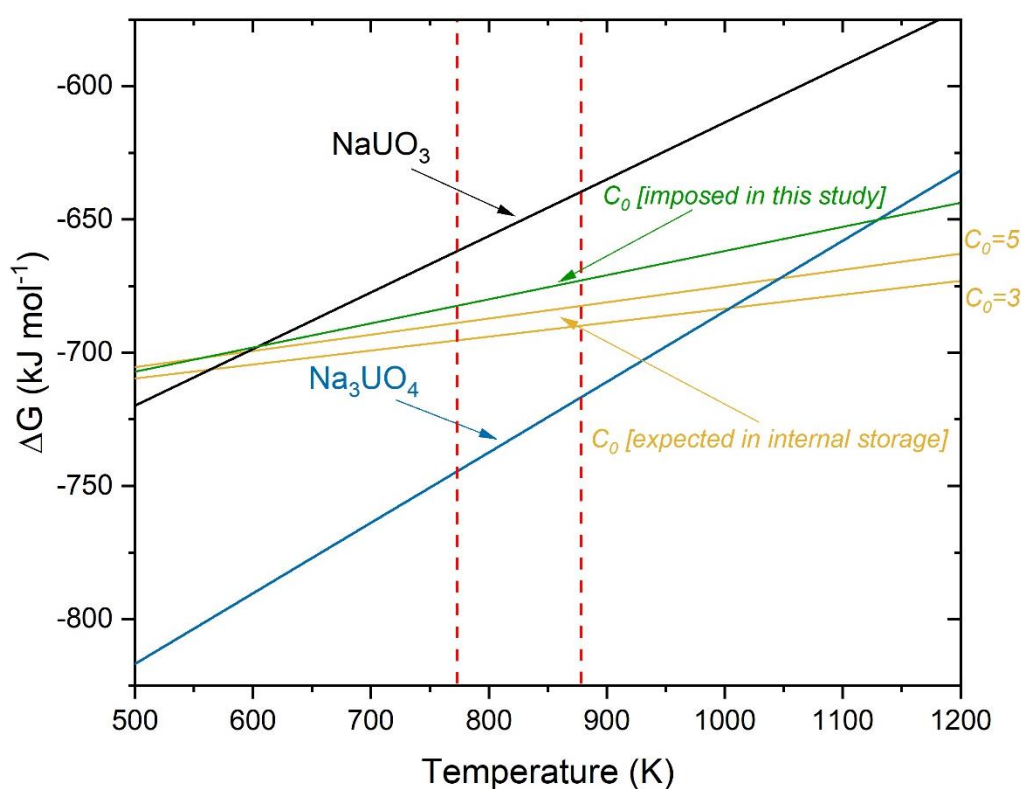


Figure 10: Section of the oxygen potential thresholds for the formation of the NaUO_3 and Na_3UO_4 ternary phases. Green line: oxygen potential imposed in the sodium interaction tests.

Pour savoir si la réaction UO_2 +sodium se développait avec un mécanisme de croissance interne ou externe, nous avons utilisé des marqueurs déposés sur la surface d'un monocristal d' UO_2 avant la mise en contact avec du sodium, et observé leur position après le développement de la

couche de corrosion. La comparaison de la position de la surface initiale avant et après réaction a été effectuée en superposant, sur l'image obtenue après réaction, le profil de la surface avant réaction (ligne verte sur la Figure 11).

Dans tous les cas, nous avons observé une croissance externe, c'est à dire que la couche de corrosion s'est développée par-dessus la surface initiale. Sur deux échantillons, on a observé une couche de corrosion qui s'étendait aussi légèrement sous la surface initiale. Mais cette faible pénétration, de l'ordre 0.2 and 0.5 μm , pourrait aussi être un artéfact expérimental, soit lors de la préparation du marqueur, soit lors de la mesure.

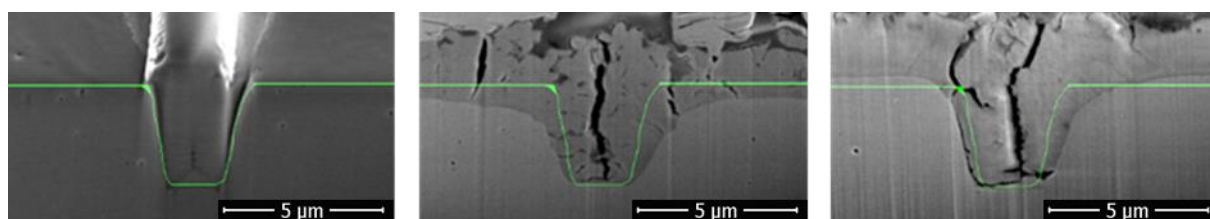


Figure 11: Platinum markers. Left: Reference marker on unreacted sample. Middle: After 12 hours of interaction with liquid sodium. Right: After 24 hours of interaction with liquid sodium.

L'épaisseur de la couche de corrosion a été mesurée en fonction de la durée de l'interaction UO_2 +sodium à haute température, pour caractériser la cinétique de réaction. La mesure de la couche de corrosion a été réalisée en plusieurs endroits sur le même échantillon pour obtenir une valeur moyenne. L'évolution de l'épaisseur de la couche de corrosion suit une forme parabolique en fonction du temps, comme cela est montré sur la Figure 12.

Comme nous avons mesuré la couche de corrosion formée sur une surface plane, la forme parabolique de l'épaisseur de la couche de corrosion en fonction du temps est une indication claire d'une cinétique de corrosion contrôlée par un mécanisme de diffusion. Cette observation est cohérente avec la littérature pour la réaction MOX +sodium avec du MOX irradié ou non. Cette littérature attribue toutefois l'étape de diffusion limitante à la diffusion du sodium dans la couche de corrosion. Nos résultats sont en désaccord avec cette hypothèse, car nous n'observons pas de diffusion du sodium dans l' UO_2 et, plus important, nous avons un mécanisme de croissance externe. Ce dernier point met clairement en évidence le fait qu'il faut considérer l'étape limitante comme une étape limitante de diffusion de l'uranium, sous forme interstitielle ou lacunaire.

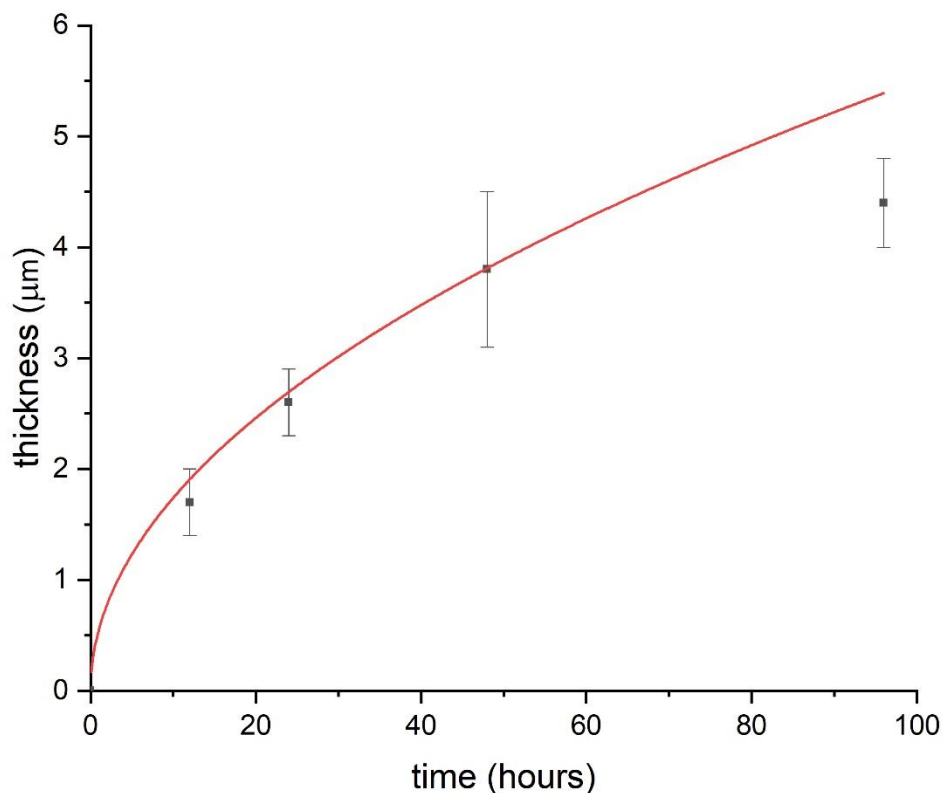


Figure 12: Fit of the experimental point at 12, 24, 48 and 96 hours of interaction.

Les expériences utilisant du MOX étaient destinées à être comparées avec celles utilisant de l' UO_2 . Cela n'a pu être possible pour ce qui concerne l'étude structurale du produit de réaction MOX+sodium, car ce dernier s'est amorphisé, vraisemblablement pendant les phases d'entreposage en contact avec de la vapeur d'eau. Les analyses avec le MEB ont malgré tout montré l'existence d'une couche de corrosion. Il conviendra à l'avenir de développer une méthodologie qui permette la caractérisation structurale de cette couche de corrosion et son attribution éventuelle à de l'uranoplutonate de trisodium.

Les mesures par diffraction X ont cependant montré que le substrat MOX avait été réduit pendant la réaction. La détermination du paramètre de maille du MOX, par la simulation des pics de diffraction avec l'option full-pattern matching, donne des valeurs plus élevées que celle du MOX stœchiométrique. Ces valeurs sont associées à un rapport O/(U+Pu) de 1,99 pour des temps d'interactions de moins de 24 heures et de 1,98 pour des temps d'interactions plus longs, ce qui correspond à une réduction progressive du MOX avec le temps d'interaction.

L'examen au MEB des échantillons le long de surfaces de fracture a permis d'apporter des informations clés sur la couche de corrosion. On observe ainsi la formation d'une couche de corrosion uniforme couvrant l'intégralité de la surface de la pastille MOX (Figure 14). L'épaisseur de cette couche ne dépend pas de l'orientation cristallines des grains sous-jacents. La couche de corrosion est clairement observable grâce une séparation nette du substrat. La

pénétration du sodium le long des joints de grains est visible sous la forme d'une phase foncée, que l'on peut aussi observer dans certains pores.

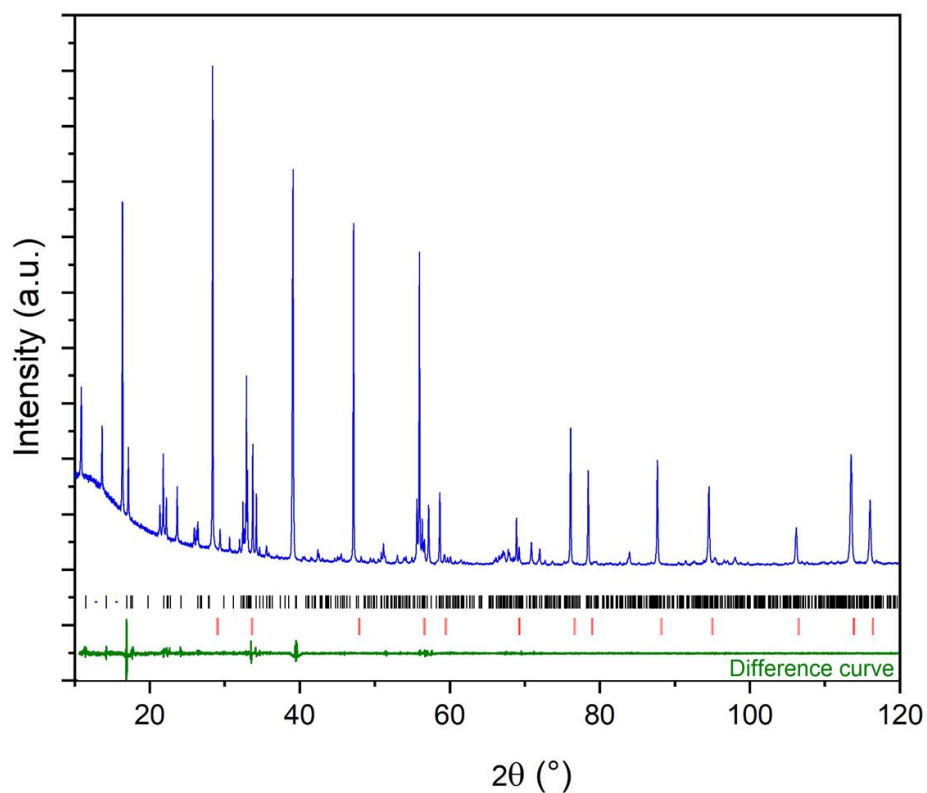


Figure 13: XRD pattern of the moisture Na_3NbO_4 and reduced mixed oxide. Black: Na_3NbO_4 . Red: $(\text{U,Pu})\text{O}_{1.99}$

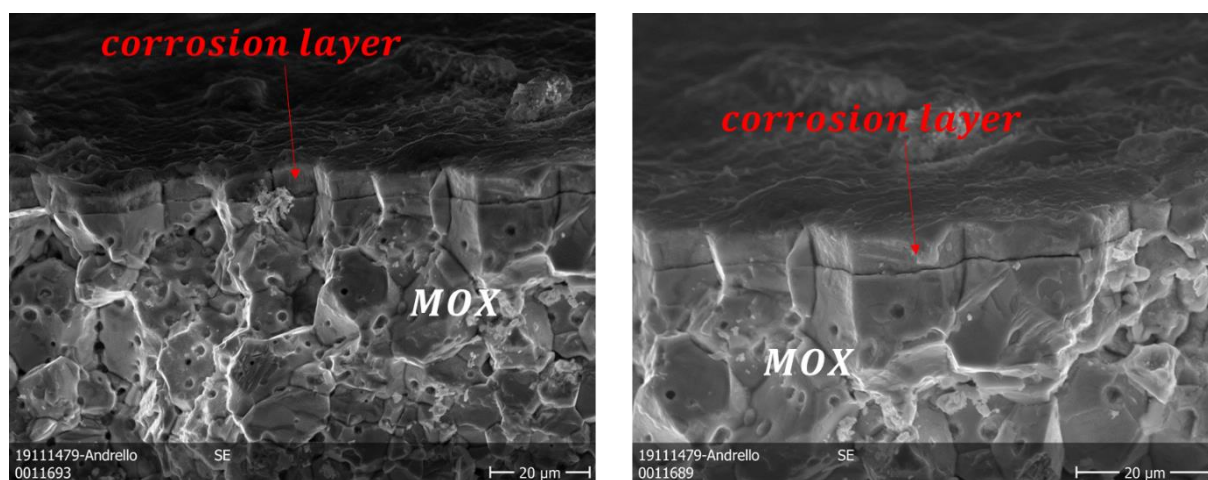


Figure 14: Cross section view of the MOX sample after sodium exposure

Les mesures expérimentales de l'épaisseur de la couche de corrosion ont été ajustées avec un modèle numérique, pour ce qui concerne la couche de corrosion superficielle uniquement. A ce stade, nous ne prendrons pas en compte la corrosion le long des joints de grains qui nécessitent une méthodologie de caractérisation spécifique. D'une manière équivalente à ce qui a été observé pour l' UO_2 , la cinétique de réaction suit une évolution parabolique, comme présenté sur la Figure 15., signe d'une cinétique de corrosion contrôlée par une étape limitante de diffusion. Si on fait abstraction de la propagation de la réaction de corrosion le long des joints de grains, l' UO et le MOX se comportent de manière similaire avec le sodium liquide.

La Figure 16 présente la comparaison entre les résultats expérimentaux de cette étude et ceux de la littérature. La courbe bleue correspond à la loi générale proposée par Craig et al. Nos données obtenues à 973K sont en bon accord avec la loi proposée par Craig. Ce bon accord conforte la validité de nos observations et de notre méthodologie.

La comparaison entre la morphologie des pastilles avant et après interaction a permis de mettre en évidence le rôle du procédé de fabrication des pastilles MOX sur leur tenue à la corrosion par le sodium. La présence de joints de grains « ouverts » ou de fissures avant la réaction agit comme autant de chemins par lesquels le sodium vas pouvoir aisément diffuser. De cette manière le sodium peut pénétrer au cœur de la pastille et les faire éclater lors qu'il réagit avec l'oxyde pour former des phases moins denses.

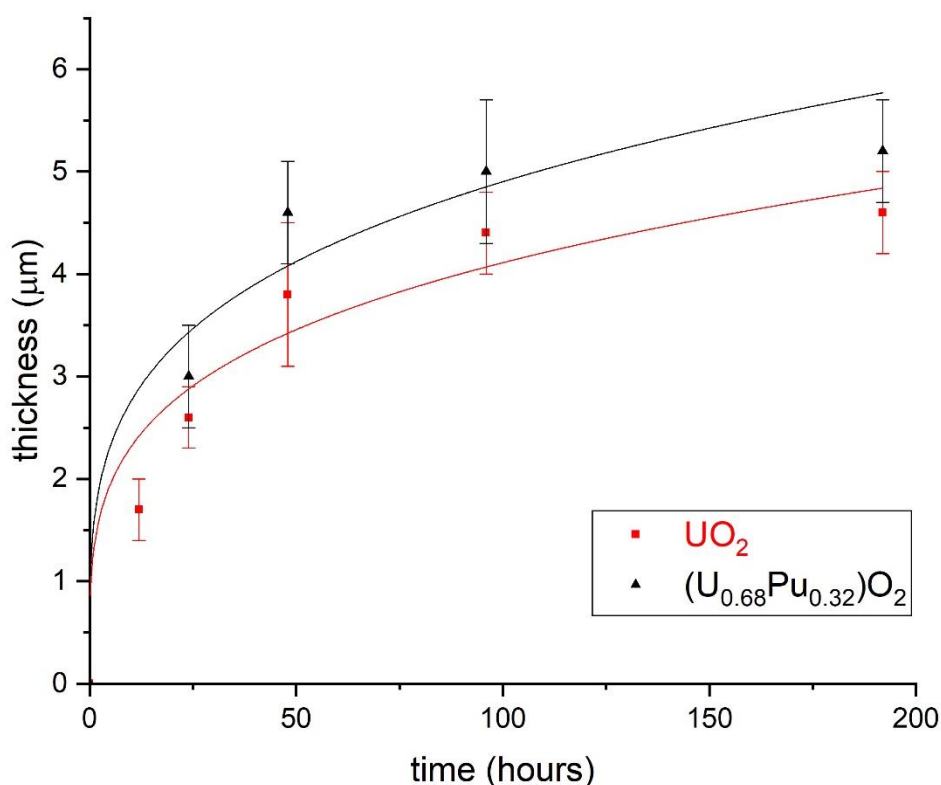


Figure 15: Comparison between the experimental data obtained for interaction tests between UO_2 (black line) and MOX (red line) with liquid sodium for long-period reaction.

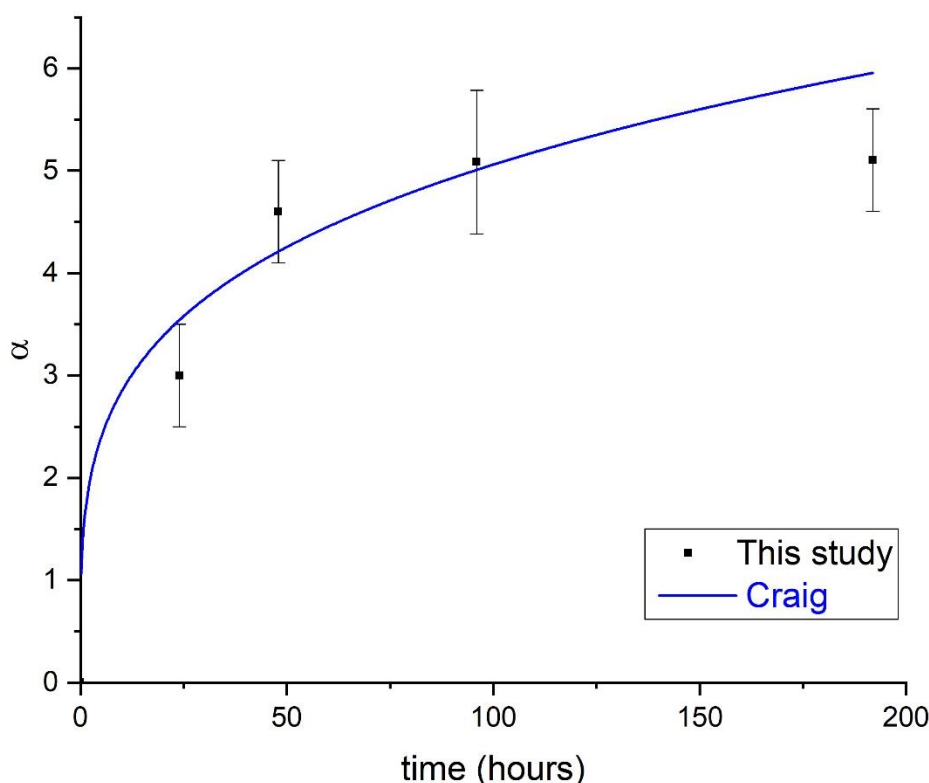


Figure 16: Comparison between the experimental result of the present study and data in literature.

Grâce aux observations expérimentales obtenues dans ce travail, et en considérant que UO_2 et MOX se comportent de manière équivalente, un mécanisme réactionnel a été proposé pour la formation de la couche de corrosion externe.

Ce mécanisme inclut les étapes suivantes :

1. Adsorption dissociative de l'oxygène O_2 sur la surface externe, i.e. la surface de Na_3UO_4 ;
2. Adsorption du sodium, Na, sur la même interface;
3. Création de nouvelles mailles de Na_3UO_4 à la surface externe de Na_3UO_4 et création de lacunes d'uranium;
4. Diffusion de l'uranium via un mécanisme lacunaire de la surface interne UO_2 - Na_3UO_4 vers la surface externe de la couche de Na_3UO_4 ; et diffusion de l'oxygène au travers de la couche de Na_3UO_4 vers la surface externe via un mécanisme interstitiel ;
5. Réaction à l'interface interne avec la création de lacune d'oxygène dans l' UO_2 et formation d'atomes d'oxygène dans les sites interstitiels de la phase Na_3UO_4 phase,
6. Réaction à l'interface interne avec la création de lacune d'oxygène dans l' UO_2 et formation d'atomes d'uranium dans les sites de la phase Na_3UO_4 ;
7. Réaction d'annihilation des lacunes d'uranium et d'oxygène, qui devrait conduire à la formation progressive de cavités l' UO_2 .

La résolution du système d'équations associées à chaque étape de ce mécanisme permet d'obtenir l'expression suivante pour le taux d'avancement de la réaction :

$$\frac{d\alpha}{dt} = \phi S_m = \frac{V_{mA} l_0 k_0}{ze_0^2} \frac{1}{\alpha} \exp\left(-\frac{E_{app}}{RT}\right) P_{O_2}^{1/2} \left(1 - \frac{P_{O_2,eq}^{1/2}}{P_{O_2}^{1/2}}\right)$$

Par construction ce modèle décrit une cinétique strictement parabolique. Il est adapté pour décrire les résultats expérimentaux au début de la réaction, puis il fournit une valeur conservative de la couche de corrosion pour les temps plus élevés. En ce sens, il est adapté à une prédiction sûre de la cinétique de corrosion dans la mesure, la couche de corrosion effectivement formée ne sera jamais plus épaisse que celle prédite par le modèle.

Le travail de thèse présenté ici a permis d'acquérir de nouvelles données expérimentales et de proposer une première modélisation de la cinétique de corrosion qui méritera d'être améliorée par la suite.

Le modèle cinétique a été construit pour décrire la formation d'une couche de corrosion monophasée à la surface de l'oxyde en s'appuyant sur les observations expérimentales apportées par ce travail, à savoir :

1. Le produit de corrosion contient des atomes d'uranium à l'état d'oxydation (V);
2. La germination est instantanée et la cinétique peut être décrite par le mécanisme de croissance uniquement;
3. L'étape limitante est une étape de diffusion
4. La croissance suit un mécanisme de croissance externe, ce qui implique une étape limitante de diffusion de l'uranium.

Le modèle inclut l'influence de la pression partielle en oxygène et de la température, ce qui permettra de l'utiliser pour des études de sensibilité dans le cadre des études de conception d'un stockage interne. Néanmoins, il est nécessaire d'améliorer ce modèle pour pouvoir rendre compte de la corrosion aux joints de grains, et, le cas échéant, de l'existence d'une couche de corrosion biphasée.

Le travail expérimental de la thèse a permis de mettre en évidence deux faits originaux qui n'avaient jamais été ni observés ni discutés précédemment, c'est à dire :

1. La croissance externe de la couche de corrosion
2. La formation d'une couche de corrosion biphasée.

Ces nouveaux résultats nous ont aussi permis de critiquer certaines interprétations de la littérature, notamment l'attribution d'une étape limitante de diffusion du sodium. Nous avons en effet montré que nos résultats étaient plus cohérents avec une étape limitante de diffusion de l'uranium.

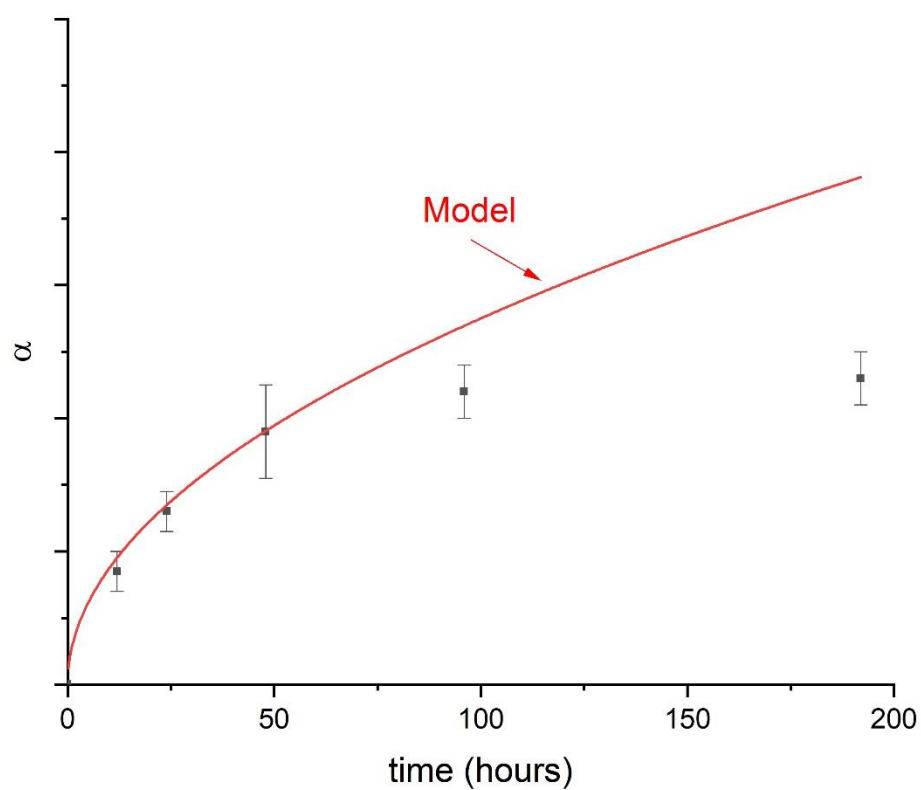


Figure 17: Experimental data and modelling fit. The modelling describes in a precise manner the beginning of the reaction and it is conservative over the long-term.

Introduction

In order to fulfil the energy needs for future generations, nuclear fast reactors are an option that is studied at institutions which are involved in nuclear research, such as the Commissariat à l'Energie Atomique et aux énergies alternatives (CEA), the Directorate for Nuclear Safety & Security of the European Commission's Joint Research Centre (JRC) and the Ecole nationale supérieure des Mines de Saint-Etienne (EMSE). To become actual reactors, the nowadays concepts have to prove their sustainability, economy and safety. In order to achieve these objectives, one option of future sodium cooled fast reactors consists in a compact nuclear island without an external sodium pool, as it existed in Phénix or Superphénix French fast reactors. Removing the sodium pool reduces the risk of air-sodium reaction and minimizes the handling of the fuel bundles. In this design, the spent fuel assemblies will be placed in a dedicated zone of the main reactor vessel during their storage period, waiting for the decay of residual heat to levels that are compatible with handling in air. However, this dedicated storage zone will also have to receive failed fuel pins for the same reason.

A failure occurs when the pin cladding is opened with a breach that leads to the release of volatile fission products. In current fast reactors, the detection systems are fast enough to promptly shutdown the reactor in the case a pin failure. The failed pins have to be removed from the core but cannot be unloaded out of the sodium pool immediately, because the decay heat needs to decrease to acceptable levels for dry storage first.

The main open question about the internal storage concerns the fate of failed fuel elements. When a failed fuel pin is in contact with sodium, a chemical reaction can occur between sodium and the Mixed OXide (MOX) fuel. The corrosion products formed by this reaction have lower densities than the fuel, leading to strains on the cladding that can possibly induce the release of fissile materials into the core. Under the clean core policy foreseen for a future nuclear reactor, dissemination of fissile matter has to be kept as low as possible in order to allow the reactor inspection and surveillance.

In the Phénix reactor, one year of internal storage of a failed fuel element did not lead to dissemination of fissile matter into the reactor system. However, this result alone is not sufficient to ensure the safe storage of failed elements during the expected storage time for the future fast reactors which will be about three years. Consequently, more information is needed to further support the internal storage feasibility.

In storage conditions, different scenarios can be proposed to describe the evolution of the failed fuel pin. Here we will focus on the scenario where sodium enters the fuel pin through a breach feeding the reaction between oxide fuel and liquid sodium, whose kinetics will be lower in storage conditions compared to in-core conditions. Thus, the formation of the less dense corrosion product could lead to further opening of the breach, similar to what happens in the failed pin during core operation but slower. For the design of a safe storage of failed fuel pins, it is mandatory to know how much time is needed before the cladding integrity is threatened by the formation of the corrosion product. In order to answer this question, the kinetics of the reaction between oxide fuel and liquid sodium in storage conditions need then to be accurately known.

One option for the determination of the kinetics of the fuel-sodium reaction could be performing several experiments under different experimental environments representative for internal storage with durations as long as 3 years. This method is obviously impossible in the timeframe of a Ph.D. thesis. This is the reason why was chosen a predictive methodology based on a mechanistic modelling of the sodium-oxide reaction.

This methodology uses the formalism of heterogeneous kinetics because the reaction occurs between a solid, the oxide fuel, and a liquid, the sodium. This formalism considers two processes: nucleation and growth. If each process obeys the same chemical equation, they follow different mechanism is made of successive steps. Writing a comprehensive modelling for the reaction would require having data describing both nucleation and growth processes. Some information is available in literature but not all.

This dissertation is concerned by the modelling made of the kinetics of the fuel-sodium reaction together with the experimental results gained in order to support this modelling. Most of the experiments were performed on UO_2 in order to develop a basic understanding of the reaction mechanism and to identify the reaction step, which is determining the overall kinetics. In addition, a series of complementary experiments were carried out on MOX in order to investigate if the principal kinetics are comparable to UO_2 and if the developed model could be applied to MOX.

The manuscript is organized as follows:

Chapter 1 reports the state of the art concerning the sodium-fuel interaction. Out-of-pile and in-pile experiences are described and some conclusions drawn by previous authors are summarized.

In Chapter 2, the basic notions of the heterogeneous kinetic theory are presented. Based on this theory, a set of data needed for the modelling of the reaction mechanism is listed. Moreover, the current data available in literature are reported.

Chapter 3 illustrates the objectives of this study as well as the structure and methodologies used to achieve these objectives.

The experimental method used to gain the needed data are described in Chapter 4: X-Ray Photoelectron Spectroscopy (XPS), X-Ray Diffraction (XRD) and Grazing Incidence X-Ray Diffraction (GIXRD), Scanning Electron Microscopy (SEM) and Energy Dispersive X-Ray Spectroscopy (EDX), Focus Ion Beam (FIB) and Transmission Electron Microscopy (TEM). The nuclear laboratories of JRC, where the experimental were performed, together with the sample preparation are also presented as well as the devices used for the sample characterizations and a brief recall to the physics.

In Chapter 5, the main objective is to understand the oxidation state of the corrosion layer, which forms due to the interaction sodium-fuel. For that, thin films were prepared under ultra-high vacuum on various substrates and their surfaces were studied by XPS.

Chapter 6 aims to investigate the nucleation process and to understand the main features of the sodium-fuel reaction such as a possible impact of the grain orientation or the penetration of

sodium through grain boundaries. For that, interaction tests in closed capsules, under different conditions were carried out using single crystal and polycrystalline samples of uranium oxide.

In Chapter 7, the main objective is to describe the growth process and particularly the sense of development of the corrosion layer as well as the nature of the rate-limiting step. For that, interaction tests at fixed oxygen potential were done by using a buffer.

In Chapter 8, the objective is to investigate the mixed oxide and sodium corrosion, in order to establish if mixed oxide behaves at the same manner of uranium oxide. For this, the same experiments performed with uranium oxide were repeated with MOX.

Chapter 9 describes a proposal for a reaction mechanism for growth, which matches the experimental observations. From the mechanism and in link with the experimental results, a kinetic law is proposed and compared to the experimental kinetic data. The modelling includes the influence of the oxygen partial pressure and the temperature and can be used for the design of the internal storage.

In Chapter 10, some general conclusion of the presented studies are given and some suggestion for further studies are proposed.

Introduction

Pour satisfaire les besoins en énergie des futures générations, les réacteurs nucléaires à neutrons rapides sont une option qui est étudiée dans les institutions impliquées dans la recherche sur le nucléaire, telles que le Commissariat à l'Energie Atomique et aux énergies alternatives (CEA), le « Directorate for Nuclear Safety & Security » du Joint Research Centre (JRC) de l'Union Européenne et l'Ecole nationale supérieure des Mines de Saint-Etienne (EMSE). Avant de pouvoir être fabriqué, les concepts étudiés aujourd'hui devront démontrer qu'ils atteignent les plus haut standards de sûreté, de performances économiques et de développement durable. Pour atteindre ces objectifs, une option pour les futurs réacteurs à neutrons rapides refroidis au sodium s'articule autour d'un îlot nucléaire compact sans barillet de stockage du combustible nucléaire, comme cela était le cas dans les réacteurs français, Phénix et Superphénix. Eliminer le barillet, et ses 20 tonnes de sodium, réduit significativement le risque de réaction sodium-air et minimise la manutention des assemblages combustibles. Dans cette configuration, les assemblages de combustible usé seront placés dans une zone dédiée de la cuve réacteur tout au long de leur période d'entreposage, en attendant que leur puissance résiduelle décroisse suffisamment pour permettre leur manipulation à l'air libre. Toutefois, cette zone dédiée devra aussi accueillir des aiguilles défectueuses pour les mêmes raisons.

Une aiguille est considérée comme défectueuse lorsqu'une brèche existe dans la gaine ce qui conduit au relâchement des produits de fission volatils. Dans les réacteurs rapides actuels, les systèmes de détections sont suffisamment performants pour détecter ce relâchement au plus tôt, et arrêter le réacteur dès l'apparition d'une aiguille défectueuse. Les aiguilles défectueuses doivent être déchargées du cœur mais ne peuvent pas être évacuées du sodium immédiatement, parce que leur puissance résiduelle doit décroître suffisamment pour qu'elles puissent être acceptées dans un stockage à sec.

Le sort des aiguilles défectueuses reste toutefois une question ouverte dans le concept sans barillet. En effet, lorsqu'une aiguille défectueuse est en contact avec le sodium, une réaction chimique se produit entre le sodium et le combustible nucléaire, un oxyde mixte de plutonium et d'uranium (dénommé MOX). Les produits de corrosion générés par cette réaction ont une densité plus faible que celle du combustible, qui peuvent éventuellement provoquer le relâchement de matière fissile dans le cœur du réacteur. La stratégie de « cœur propre » imposée aux futurs réacteurs nucléaires impose un niveau bas de contamination en matière fissile pour permettre les opérations d'inspection et de surveillance.

Dans le réacteur Phénix, on n'a pas observé de dissémination de matière fissile lors du stockage interne d'une aiguille défectueuse pendant une durée de un an. Cependant, ce résultat seul ne suffira pas à garantir la sûreté en stockage interne d'une aiguille défectueuse pour un futur réacteur rapide, dont la durée estimée est de trois ans. De ce fait, il est nécessaire de disposer de plus d'information pour assurer la faisabilité d'un stockage interne sûr.

En conditions de stockage interne, différents scénarii ont été proposés pour décrire l'évolution de l'aiguille défectueuse. Dans ce travail, nous ne nous intéresserons qu'au scénario dans lequel le sodium entre dans l'aiguille par une brèche et alimente la réaction combustible oxyde – sodium liquide, dont la cinétique sera plus faible en conditions de stockage interne que dans le cœur du réacteur. Ainsi, la formation de produits de corrosion moins dense pourrait conduire à une ouverture plus grande de la brèche de manière similaire à ce qui se passe dans le cœur du

réacteur mais avec une vitesse plus lente. Si on veut garantir la sûreté du stockage interne dès sa conception, il est indispensable de savoir de combien de temps on dispose avant que la gaine ne perde son intégrité par la formation des produits de corrosion. Pour répondre à cette question, on se doit de connaître avec précision la cinétique de la réaction entre le combustible oxyde et le sodium liquide.

On pourrait envisager de déterminer la cinétique de réaction combustible-sodium en réalisant plusieurs expériences dans des environnements représentatifs du stockage interne, et pour des durées d'au moins trois ans. Cette méthode est évidemment incompatible avec la durée d'une thèse. C'est pourquoi une méthodologie prédictive a été choisie sur la base d'une modélisation mécanistique de la réaction sodium-oxyde. Cette méthodologie s'appuie sur le formalisme de la cinétique hétérogène, car il s'agit d'une réaction entre un solide, le combustible oxyde, et un liquide, le sodium liquide. Ce formalisme considère deux processus : germination et croissance. Chacun de ces processus est composé d'étapes successives. L'écriture d'une modélisation complète pour une réaction implique de pouvoir décrire à la fois les processus de germination et croissance. Une partie des données nécessaires est disponible dans la littérature, mais pas tout.

L'objet de ce mémoire est la modélisation de la cinétique de réaction sodium-oxyde avec les résultats expérimentaux acquis en support de cette modélisation. La plupart des résultats expérimentaux ont été acquis sur du dioxyde d'uranium, UO_2 , avec l'objectif de comprendre les mécanismes réactionnels et d'identifier les étapes réactionnelles qui déterminent la cinétique d'ensemble. De plus, une série d'expériences complémentaires ont été réalisées avec du MOX pour savoir si les cinétiques de corrosion étaient comparables et si la modélisation pourrait être transposable de l' UO_2 au MOX.

Le manuscrit s'organise de la manière suivante :

Le chapitre 1 présente l'état de l'art sur la réaction oxyde-sodium. Les expériences réalisées hors et dans un réacteur nucléaire sont présentées et les conclusions auxquelles sont arrivés les auteurs sont résumées.

Dans le chapitre 2, on aborde les notions essentielles de la théorie de la cinétique hétérogène. On en déduit quelles données sont nécessaires pour la modélisation d'un mécanisme réactionnel. Les données disponibles dans la littérature sont présentées.

Le chapitre 3 présente les objectifs de cette étude, la structure et la méthodologie choisies pour atteindre ces objectifs.

Les méthodes expérimentales utilisées pour obtenir les données nécessaires sont décrites dans le chapitre 4 : X-Ray Photoelectron Spectroscopy (XPS), X-Ray Diffraction (XRD) and Grazing Incidence X-Ray Diffraction (GIXRD), Scanning Electron Microscopy (SEM) and Energy Dispersive X-Ray Spectroscopy (EDX), Focus Ion Beam (FIB) and Transmission Electron Microscopy (TEM). On présente aussi les laboratoires haute activité du JRC, où le travail expérimental a été réalisé, ainsi que la méthode de préparation des échantillons, les appareils de caractérisation utilisés et quelques rappels de physiques.

Dans le chapitre 5, on s'attache à déterminer l'état d'oxydation de l'uranium dans la couche de corrosion formée par l'interaction combustible-sodium. Pour ce faire, des couches minces ont été préparées sous ultravide sur des substrats divers et leur surface a été caractérisée par XPS.

Le chapitre 6 vise à étudier le processus de germination et à identifier les principales caractéristiques de la réaction oxyde – sodium, comme l'impact potentiel de l'orientation cristalline ou la pénétration du sodium le long des joints de grains. Pour ce faire des tests d'interaction en capsules étanches ont été réalisés dans différentes conditions en utilisant des mono ou des polycristaux de dioxyde d'uranium.

Dans le chapitre 7, on vise à décrire le processus de croissance, et plus particulièrement le sens du développement de la couche de corrosion ainsi que la nature de l'étape limitante. Pour ce faire, des tests d'interaction, avec un potentiel oxygène fixé, ont été réalisés en utilisant un tampon REDOX.

Dans le chapitre 8, on s'intéresse à la réaction entre le MOX et le sodium liquide, pour savoir si ce dernier se comporte de la même manière que le dioxyde d'uranium. Dans cette perspective, les mêmes expériences que celles réalisées avec le dioxyde d'uranium seront répétées avec le MOX.

Le chapitre 9 décrit une proposition pour le mécanisme de réaction de croissance cohérent avec les observations expérimentales. À partir de ce mécanisme et en cohérence avec les résultats expérimentaux, une loi cinétique est proposée et comparée aux données cinétiques expérimentales. La modélisation inclut l'influence de la pression partielle en oxygène ainsi que celle de la température et peut être utilisée pour des études de conception.

Dans le chapitre 10, on donne les conclusions générales de ce travail et de nouvelles pistes de recherche sont proposées.

1 Background and state of the art

Ce chapitre présente l'état de l'art sur la réaction oxyde-sodium. Après une rapide introduction sur la conception des réacteurs à neutrons rapides refroidis au sodium et leur retour d'expérience, les expériences d'interaction combustible-sodium réalisées hors et dans un réacteur nucléaire sont présentées et les conclusions auxquelles sont arrivés les auteurs sont résumées.

This chapter summarizes the state of the art in science and technology on the chemical interaction between oxide based nuclear fuels and liquid sodium reactor coolant. At the beginning, a brief summary of the Sodium cooled Fast Reactor (SFR) technology, followed by a more detailed presentation of the reaction between sodium and oxide fuel, is presented to give a comprehensive overview and to help the understanding of the application field and the importance of the fuel-sodium interaction phenomena for reactor safety. After this, the current status of the interaction data available in the literature is critically examined.

1.1 Sodium cooled Fast reactors: past experience and new concept design

In many countries, nuclear power plays a key role in the production of clean and sustainable energy. In order to improve the sustainability, economics, proliferation resistance & physical protection and, most important, the safety and reliability of future reactor systems, a new generation, namely Generation IV, of nuclear reactors is under research and development (R&D) worldwide. Reactors of Gen. IV shall comply with high safety standards as consequence of tougher regulations imposed after the Chernobyl (1986) and Fukushima-Daiichi (2011) accidents. Among the selected designs [1], the SFR is an attractive option since there is available relevant experimental and industrial experience. The SFR concept claims the highest technology maturity with a knowledge which extends through the design, construction, operation and decommissioning of prototype, demonstration and commercial reactors [2]. SFRs, indeed, count more than 400 reactor-years of operation experience worldwide, among which approximately 100 reactor-years of operation were acquired at industrial level [3]. The feedback from operation experience was very important to improve the SFR design, which can achieve all the goals imposed for the Gen. IV, especially in terms of safety. In Europe, the interest on the development of the SFR technology started in the early 1960s and continuous till today. France is particularly involved in these efforts thanks to the success of its SFR program in the past, starting with the experimental Rapsodie reactor, which lead to the construction and operation of the prototype Phénix reactor. The Phénix reactor not only provided electricity to the grid till 2009, but was also used to get unique data and experiences for the improvement of the design and safety of future SFRs. Several important safety tests were indeed performed during its operation. In general, the layout of SFR can be arranged in pool or loop type, where the difference is essentially the size of the reactor pressure vessel: large-size reactors are mainly pool-type, instead small-size reactors are loop-type [4]. An advantage of the pool design is the occurrence of natural circulation, which ensures the safe removal of the residual heat in case of loss of offsite power [3]. SFRs use liquid sodium as coolant, which provides several advantages including a high thermal conductivity and a large

heat capacity, which creates a large thermal inertia against overheating in case of loss of flow. In addition, sodium does not act as a moderator, which allows using a fast neutron spectrum with the advantage of a good neutron economy, enabling effective breeding and transmuting of long-lived radioactive elements into fission products with much shorter half-life [5]. This enables a significant reduction of the amount and long-term radiotoxicity of nuclear waste. Moreover, the primary system does not need to be pressurized since the high boiling point of sodium allows operating near to atmospheric pressure. However, sodium also has its drawbacks, mostly due to the high chemical reactivity with water and air. In France, the main SFR concept under R&D was until 2019 the Advanced Sodium Technology Reactor for Industrial Demonstration or ASTRID (©CEA, with the support of the industrial partners EDF and AREVA). The expected goal of ASTRID was the demonstration of the multi-recycling and transmutation of the uranium-plutonium fuel on an industrial scale together with the operability of SFRs for commercial power production.

The pre-conceptual design of ASTRID foresaw a pool-type primary circuit with a conical inner vessel (“redan”) [5] which allowed in-service inspection and repair access. The core was designed to accommodate the internal storage of spent and defective fuel pins at the core periphery. Figure 18 shows the ASTRID core layout. The fission power of the fuel assemblies in the internal storage position has to be much smaller than that of the decay heat [6] in order to avoid neutron coupling with the core. The main benefit of the internal storage is the elimination of an external sodium pool. The internal storage reduces the fuel handling time from 20 to 9 days [7], and it eliminates the sodium-water and sodium-air interaction risks associated to the external pool. The implementation of the internal storage has the drawback of fuel dissemination risk and, consequently, potential contamination of the primary system, due to the presence of defective fuel pins. On this respect, to safely assess the internal storage, studies on the coolant-fuel interaction are currently under development.

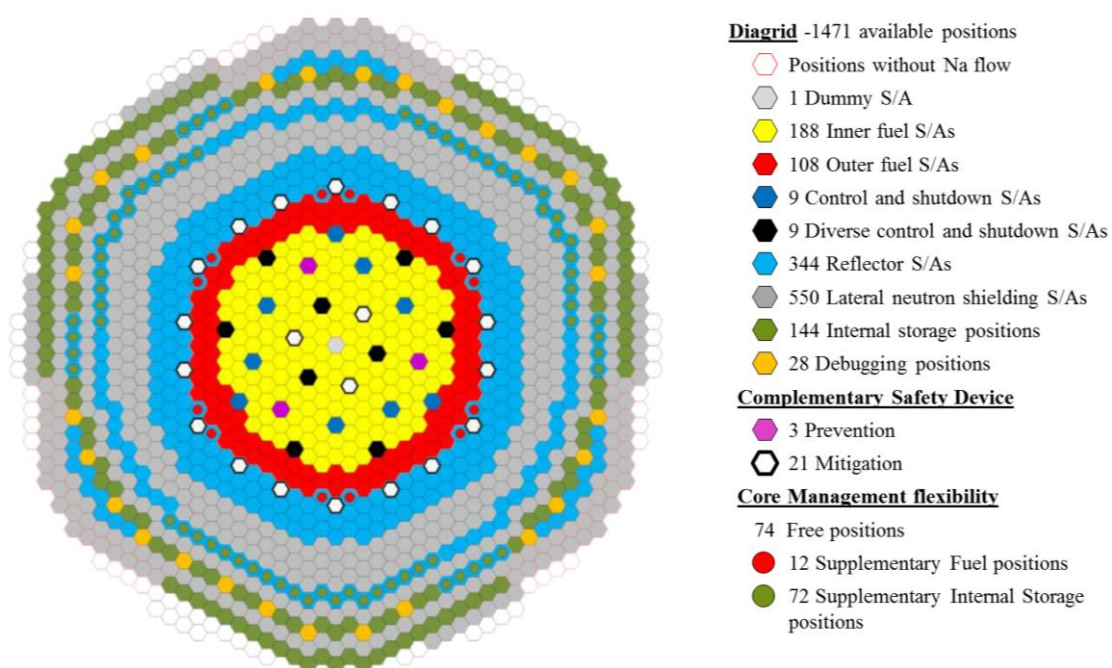


Figure 18: Core layout of ASTRID and internal storage position (green positions) [6]

1.2 Sodium-fuel interaction

A fuel pin failure is identified as the initiating event for the interaction between sodium and fuel, since the breach would allow the liquid sodium to enter the cladding with the consequence of fuel-sodium chemical reaction. In normal condition, fuel and coolant are physically separated by the cladding to prevent the release of gaseous and solid fission products into the primary system. However, the cladding can breach due to several reasons (fabrication defects, mechanical stress, etc.) which allows the physical contact between fuel and coolant. Long-term operation experience and continuous research on the evolution of cladding material and design led to the gradual reduction of in-core cladding ruptures to very low levels. Nevertheless, both in normal operation and accidental condition, cladding might fail. Three main fuel pin failure types [8] during the lifetime are identified, depending on the causes and the time of occurrence, as the following:

1. Beginning Of Life (BOL): caused by defects during the fuel pin fabrication (welding, material or fuel defects or premature pin corrosion). Usually occurs during the first ten days of operation. Improvements in cladding material and design have significantly reduced such type of failures (as demonstrated during Phénix reactor operation) [9].
2. Accidental: During an unexpected event, such as cooling failure or power fluctuations, cladding could fail at any time during the reactor cycle.
3. End Of Life (EOL): Generally occurs at high burn-up, due to mechanical and chemical interaction between fuel and cladding (FCMI and FCCI), radiation damage and high internal pressure (~7 MPa). These conditions make cladding susceptible to ruptures.

Even though rare, the occurrence of a pin failure has to be reliably detected within an acceptable time, to avoid severe consequences and to ensure the safe shut down of the reactor. Defective fuel pins are then removed from the core, before unacceptable amounts of fission products or fuel can contaminate the primary circuit. During the normal operation, two different types of failure are considered [10] for the detection:

1. Leak failure: The damage of the fuel pins is small and accompanied only by the emission of fission gases and volatile fission products. This failure can be detected by monitoring fission products in the cover gas (gas chromatography and gamma spectrometry). The reactor can continue to operate over weeks or months, as long as Delayed Neutron Detection (DND) failure is not developed.
2. DND failure: A larger damage of the fuel pin implies the exposure of the fuel to sodium, leading to their direct contact and dispersal of fuel into the primary circuit. In such a case, the DND system can detect traces of fuel in the primary circuit by the delayed neutron emission outside the core. Following the occurrence of the first DND, the neutron flux level, which initiates automatic reactor shutdown (SCRAM), can be expected within days to weeks.

The time between the gas signal and the DND signal depends on the breach size and the burnup. DND signals are efficient and sufficient to ensure a safe shutdown, as the experience has shown. This assessment is also supported by in-pile experiments [11]. As long as no DND signal is detectable, the coolant contamination by gaseous, volatile and soluble fission products can be

tolerated for normal operation [10]. Moreover, the experience highlighted that the fuel pin failure occurrence, during the normal operation, concerns much more the economic aspects [12], due to unplanned shutdown and inoperability of the reactor for days [13], and not safety issues. However, the long-term evolution, associated to the storage period of circa 3 years, of failed fuel pins and its consequence have still to be understood. The severe degradation of the failed pin, followed by fuel dissemination, is a complex phenomenon, which can lead to undesirable consequences. As a consequence of the sodium-fuel reaction product build up, the initial failure can propagate (longitudinal cracking) and allow more and more sodium to ingress and infiltrate the fuel, leading to further reaction swelling and potential fuel release from an increasing area of exposed fuel. The chemical interaction of sodium with mixed oxide (U,Pu)O₂ is an important factor in the behavior of failed fuel pins. The sodium-fuel incompatibility was indeed recognized since the early beginning of SFRs operation. The reaction leads to the formation of the so-called Fuel-Sodium Reaction Product (FSRP), which mainly consists of trisodium uranoplutonate (Na₃(U,Pu)O₄) [14, 15, 16, 17, 18].

As it will be seen later on the reaction of sodium with mixed oxide (U,Pu)O₂ can lead to many different compound; in the case of SFR reactor the chemical nature of the corrosion product is mainly determined by the oxygen potential of the sodium within the primary circuit. This oxygen potential is imposed by the oxygen concentration in the sodium and this latter has to be maintained in precise limits. It must not be too low in order to prevent corrosion by liquid metal sodium of the primary vessel steels, it must not be too high to prevent oxidation of these steels. A usual value for oxygen concentration in SFR sodium is about 5ppm.

Na₃(U,Pu)O₄ has very unfavourable physical proprieties, when compared to the starting fuel, such as a much lower density and thermal conductivity [19, 20], as reported in Table 1. The properties of the reaction product could then enhance pellet swelling, influencing the cladding integrity due to higher associated Fuel Cladding Mechanical Interaction (FCMI). The pin swelling results usually in a strong local swelling [21] in the defect zone, although a smaller uniform swelling proceeds along the intact cladding. Some authors [10] indicated the phenomenon of fuel-sodium reaction swelling as the primary driving force of the deterioration of the failed pins. Instead, some others [22], linked the deterioration to the weakness of the cladding due to the high burnup. This discrepancy needs still to be clarified.

Table 1: Main proprieties comparison of MO₂ and Na₃MO₄ (M=U,Pu)

Compound	Melting Temperature (K)	Density (g cm ⁻³)	Thermal conductivity (W m ⁻¹ K ⁻¹)
(U,Pu)O ₂	3000 ± 30*	10.99-11.08	1.7-5.4**
Na ₃ MO ₄	1693 ± 25	5.59-5.68	0.9-1.0**

*depending on Pu content and O/M ratio

**depending on T

Laboratory experiments, modelling and in-reactor tests are required to increase the knowledge on the behavior of failed fuel pins, which is necessary to manage the complexity of the

phenomena involved in the sodium-fuel reaction. One of the most important aspects in this context is the kinetics of the sodium-fuel reaction. The identification and quantification of the principal mechanisms governing the reaction kinetics can contribute fundamentally to the prediction of the evolution of the reaction inside the fuel pin and improve the understanding of the main causes, which govern the deterioration of breached pins and the potential fuel dissemination. A realistic kinetic model of the fuel-sodium reaction is then needed to interpret the reactor tests and to extrapolate the long-term evolution.

1.2.1 Out-of-pile experience

Although the thermodynamics of the sodium- fuel reaction are satisfactory known, the experience gained on the kinetics behavior is limited. Interaction tests between dense pellets and liquid sodium were performed between 1970 and 1990, with the main aim to support the understanding of the reaction product formation and evolution with time.

1.2.1.1 Compatibility tests between UO_2 and liquid sodium

Between 1980 and 1990, Mignanelli and Potter [15, 16, 17, 18] performed a numbers of out-of-pile tests, using both uranium oxide and mixed oxide samples in interaction with liquid sodium. The main objective of their work was to obtain new insights and a more detailed understanding of the sodium-fuel reaction. Uranium oxide pellets, having different stoichiometry, were firstly tested with pure liquid sodium, under isothermal conditions (in the temperature range 450-900°C) to determine the swelling as function of the oxygen available in the fuel pellet. As established by the thermodynamic investigations [14], it was proven that stoichiometric uranium oxide UO_2 does not react with pure sodium. The interaction between hyper-stoichiometric UO_{2+x} dense pellets and liquid sodium resulted in different degrees of pellet damage, from slight swelling to complete disintegration, depending on the initial O/M ratio. In some tests, the presence of an oxygen getter resulted in an overall reduction of the pellet swelling. The reaction usually started at the periphery of the pellet but was followed by sodium penetration along the grain boundaries and subsequent attack of the inner grain boundaries. In hyper-stoichiometric UO_{2+x} with x higher than 0.05 the reaction appeared fast and destructive, either at low and high temperature, and showed surface erosion with formation of cracks along a specific direction. Big grain sizes, which are characteristic of hyper-stoichiometric fuel, resulted in destructive behavior due to grain boundaries attack. Pellets with small grain size showed less severe effects [15]. The fabrication defects also enhanced the sodium penetration and attack along the cracks. Single crystals showed the formation of a Na_3UO_4 layer at the periphery and penetration of sodium, which caused cracks also along certain orientations and enhanced the rate of the reaction. At temperatures below 450°C strong destructive behavior was observed, which may be linked to the formation of the sodium oxide (Na_2O) compound at the grain boundaries. The latter, due to its greater expansion compared to Na_3UO_4 , can force the grains apart. However, the oxygen concentration and temperature in SFR, are far below those needed for the formation of sodium oxide.

Consequently, scenarios with formation of sodium oxide are not representative for SFR operation, and the destructive effect caused by the formation of sodium oxide does not need be accounted. In contrast to the reaction between hyper-stoichiometric UO_2 and pure liquid sodium, the reaction between stoichiometric UO_2 and sodium containing dissolved oxygen showed a non-destructive behavior and resulted in the formation of a layer less coherent than of those formed in the reaction between hyper-stoichiometric UO_{2+x} and pure sodium.

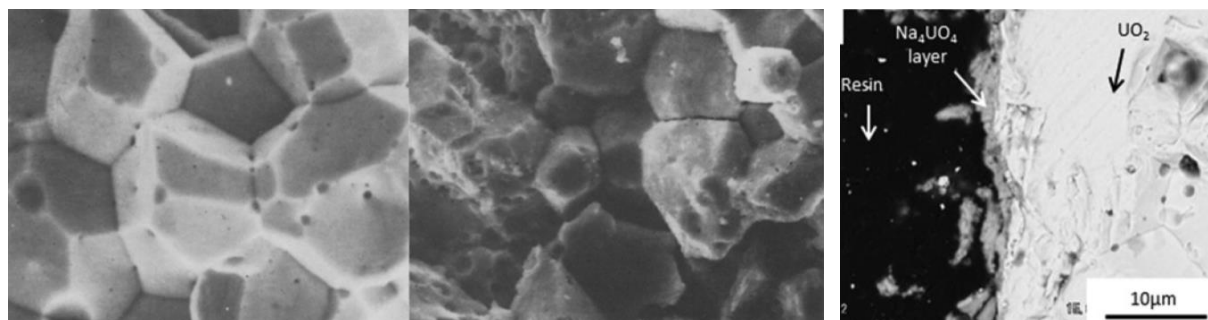


Figure 19: Left: fresh UO_2 sample. Middle: UO_2 after interaction with sodium [15] Right: formation of a loose surface layer after the interaction between liquid sodium containing sodium oxide and stoichiometric UO_2 [23] (as polished).

More recently, Matsunaga et al. [23] reported the effect of stoichiometric UO_2 in interaction with sodium containing sodium oxide at 500°C . They reported the formation of a loose layer at the pellet surface, in agreement with Mignanelli [15], but probably much more enhanced here due to the polishing procedure. The product layer showed a non-uniform thickness and the surface was in part uncovered, as reported in the right part of Figure 19. In contradiction to what was observed by Mignanelli and Potter [15], Matsunaga et al. reported the grain boundaries penetration by sodium even using stoichiometric UO_2 .

1.2.1.2 Compatibility tests between PuO_2 and liquid sodium

The sodium- PuO_2 reaction is poorly known. Only few interaction tests between pure plutonia (PuO_2) and liquid sodium are reported in literature and are used as limit cases to examine the influence of the Pu content on the extent of the reaction. Housseau et al. [20] reported the degree of swelling to be up to 45% in pure PuO_2 with an initial O/M ratio of 2, independently from the temperature. However, the evaluation of the swelling has to be considered with care due to the “de-cohesion” of the sample after the interaction. In contradiction to those results, Mignanelli et al. [16] reported a swelling of 100% in the case of pure stoichiometric plutonia and of 20% for $\text{PuO}_{1.87}$. In both cases, the significant swelling did not cause degradation or powdering of the samples. The threshold value, below which the reaction between plutonia and sodium does not take place, was reported to be an O/M ratio of 1.57 [20]. However, further investigations are needed to safely state the limit value and to achieve an accurate knowledge of the reaction between pure plutonia and liquid sodium.

1.2.1.3 Compatibility tests between (U,Pu)O₂ and liquid sodium

Blackburn et al. [19] performed several out-of-pile isothermal interaction tests between liquid sodium and MOX with the composition (U_{0.8}Pu_{0.2})O₂ for establishing the equilibrium O/M ratio of MOX as a function of temperature. All the tests were carried out for 48 hours in the temperature range between 700-900 °C. Figure 20 shows the cross-section view of the samples tested at 1173 K, as polished. The MOX matrix is light grey, the dark grey material is the reaction product and the dark circles in the MOX matrix are fuel porosity. Samples with an O/M ratio of 1.960 did not react with liquid sodium in the whole temperature range and it can be considered as the threshold below which sodium does not react with U_{0.8}Pu_{0.2}O₂, independently from the temperature. Samples with an O/M ratio of 1.970 showed the formation of the reaction product at the surface and poor formation at the grain boundaries. Obviously, the reaction was much greater at 1173 K than at 973 K. Finally, the samples with an O/M ratio of 1.995 clearly showed the formation of a thick surface reaction layer of Na₃MO₄ and the presence of a thinner reaction layer at the grain boundaries. As expected, the reaction rate is influenced by both the initial O/M ratio and temperature, confirming that higher oxygen content in the pellet, as well as higher temperature, increase the reaction rate. Unfortunately, there was no information reported on the sample preparation, which may have helped in a better understanding of the results. The formed layer at the surface of the sample with an O/M ratio of 1.970 showed a near uniform thickness, but almost detached from the bulk. Surprisingly, the layer of the sample with O/M ratio=1.995 exhibited less uniformity, which seems to be related to the different MOX grains. In both cases, the recovery and polish processes may have modified the real aspect of the reaction product, due to its well-known fragility.

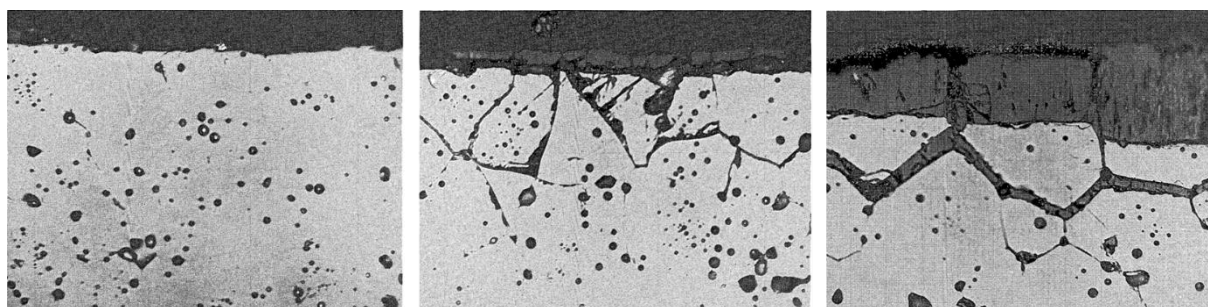


Figure 20: Cross-section view (as polished) of U_{0.8}Pu_{0.2}O₂ samples after the interaction with liquid sodium, for 48h at 1173 K [19]. Left: sample with O/M=1.960 showing absence of reaction. Middle: sample with O/M=1.970 showing the Na₃MO₄ layer at the surface and at the grain boundaries. Right: sample with O/M=1.995 showing the Na₃MO₄ layer at the surface and at the grain boundaries.

The threshold O/M value for the fuel-sodium reaction was determined from the weight increase of the pellets and resulted in the final O/M value of 1.95 when the initial O/M corresponded to 1.995. It is not surprising that the final O/M depends on both the Pu content of MOX and the temperature. Obviously, a higher Pu content and a higher reaction temperature will correspond to a lower final O/M ratio [24]. Instead, Caputi et al. [25] reported that for U_{0.75}Pu_{0.25}O_{2-x}, with x<0.04 the reaction between sodium and fuel will not occur, in agreement with Adamson et al.

[26], who reported a threshold value of an O/M ration equal to 1.96. Another investigative work on the reaction between (U,Pu)O₂ and liquid sodium was carried out by Mignanelli and Potter [16]. MOX samples with the composition of (U_{0.7}Pu_{0.3})O₂ were tested in the temperature range between 450 and 800 °C. The reaction between stoichiometric (U_{0.7}Pu_{0.3})O₂ and liquid sodium at 800 °C was almost completed in less than 18.5 hours. The reaction product Na₃MO₄ was formed at the surface and along the grain boundaries leading to a pellet swelling of circa 12% [16]. In the temperature range of 500-600 °C the reaction product formation was confined to the pellet rim. In agreement with the observations of Blackburn [19], at lower temperature, a slight sodium attack of the grain boundaries was detected, which did not allow getting quantitative data. As expected, the sample with an O/M ratio of 1.98 showed less swelling than the stoichiometric sample [16]. Surprisingly, the sample with an O/M ratio of 1.93 revealed a thin reaction product layer at the pellet surface. The latest sample was re-tested with excess of oxygen in liquid sodium, by using sodium oxide, and the reaction resulted in the formation of a powdery product on the surface of the pellet, with a volumetric pellet swelling of circa 6-7%.

1.2.2 Irradiation experience

Herein, the in-core fuel pin failures and the state of the fuel and cladding at the stage of the failure are discussed. These features are relevant because they establish the initial conditions of failed fuel pins in the internal storage. During the past operation of SFRs, the prediction of the consequences of the sodium-fuel interaction met high interest, mostly from an economic point of view, since the potential operation of the reactor with failed fuel pins, would avoid unplanned reactor shutdown. In general, in-pile tests and post irradiation examinations of failed pins demonstrated that the occurrence of pin failure did not influence the safety of the reactor [13]. Historically, in-pile tests on defective fuel pins were performed with the aim to test the efficiency of the pin failure detection systems [27], to ensure the safe shutdown, to determine the conditions under which the pin rupture occurred and to understand some of the major factors which might influence the fuel-sodium reaction. Except for spontaneous failure due to fabrication defects, the tests of failed fuel pins were usually made on pre-defected pins, or by overpassing the fuel pin design limits. Irradiation induces some change in the fuel matrix composition and properties, thereby it is important to couple the laboratory studies with the “real” sodium-fuel reaction, which occurs under irradiation conditions. Indeed, the degradation of failed fuel pins can be strongly influenced by the burn-up [22, 21]. Furthermore, the behaviour of failed fuel pins under active core conditions (450-550°C) has to be differentiated from those in the internal storage position, where fission rates are negligible and the coolant temperature is constant at about 500 °C. Table 2 summarises some of the performed tests and corresponding conclusions. The in-pile investigations, which are discussed hereinafter, are more specifically concerned with the available knowledge of the sodium-fuel interaction in the event of a cladding breach under normal operation conditions of SFRs.

1.2.2.1 *Experimental Breeder Reactor-II*

Experimental Breeder Reactor-II (EBR-II) was a pool type sodium-cooled fast reactor operated by Argonne National Laboratory (ANL) at the National Reactor Testing Station in Idaho. The reactor was designed as demonstrated plant and converted to irradiation facility in 1967. One of the missions of the reactor was to investigate inherently safe plant response and operational-reliability. The reactor core was used for testing fuels and materials providing information on the safety of SFR. Tests of run-beyond-clad breach were also performed to demonstrate and support the safety of continued operation of oxide fuel with breached cladding. Irradiation tests of 25 pre-defected pins, which contained mixed oxide ($U_{0.75}Pu_{0.25}O_{2-x}$ (with $0 < x < 0.06$), were performed during the Run-Beyond-Cladding-Breach (RBCB) program of EBR-II, in 1982. The theoretical density of the mixed oxide fuel was 92-94% and the peak linear powers were 30-68 kW/m. In detail, results of tests in the EBR-II suggest that, at low burn-up, the failed pins were capable to accommodate greater pellet swelling thanks to the ability of the cladding to expand. In these cases, the reaction product could act beneficially and protect open cracks without causing fuel release. However, when the cladding was weakened due to high burn-up, the reaction product caused additional breaches [22, 28], favouring further infiltration of sodium, which resulted in a severe degradation. In both cases, no appreciable amount of fuel was lost. The maximum diameter increase measured was 34%. Strain et al. [22] attributed the location of the reaction product formation to the dissociation temperature of the reaction product (1373 K). On the short-term, the reaction occurred inside the fuel and the reaction product formed at the grain boundaries and cracks at $r \sim 0.8$ (where r is the standardized radius of the pellet). The reaction progressively proceeded outwards to form a uniform layer between fuel and cladding (at $r \sim 0.9$). This can be explained by the temperature increase due to the presence of the reaction layer, which has a lower thermal conductivity compared to the fuel. The dissociation isotherm of the reaction product then moves outwards and in consequence the reaction layer too. Figure 21 illustrates this behavior. The reaction layer was confined to the outer region of the fuel [22, 29]. At high burn-up, fission product inclusions were present in the reaction layer, together with some remnant elements of the previous fuel-cladding chemical interaction. The fuel-sodium reaction seemed to occur quite rapidly, first by grain-boundary diffusion of sodium and then continued by consumption of fuel grains from the surface inwards [29]. Another example of pin failure in EBR-II came from an unintentional test where a fuel assembly was operated at very high cladding temperatures. The original test foresaw the assembly irradiation for circa 100 days under run beyond cladding breach mode, using fuel parameters similar to those for the Monju reactor. The peak cladding temperature was estimated to circa 1073 K for 26 days, among them 22 in the run beyond cladding breach mode [30]. The most damaged pin, showed a maximum diameter swelling at the mid-length of the largest breach, with a change of 10% and with an appreciable amount of fuel loss. Several additional small breaches were observed along the pin length. Reasonably, the development of the large breach can be thought of as imminent due to the extremely high temperature and perhaps locally exacerbated by fission gas released from the fuel. As a consequence, the fuel loss can be the result of this strong and direct contact between the unreacted fuel and sodium. Indeed, the post failure ceramography showed that the reaction product was not fully developed, probably due to the combination of a fast fuel loss and a slow reaction kinetics. In conditions under which the development of a narrow breach was slow, at temperatures below 650 °C in most of the tests in EBR-II, fuel loss was unlikely. In the latter case, the formation of the reaction product could act as protective layer against the

fuel release. The extent of the reaction product formation showed a maximum amount at the bottom end of the fuel column, with a thickness of circa 240 μm . Although there was a visible breach at the top end of the fuel column, no reaction product was observed. The lack of reaction product formation was attributed to the dissociation temperature [30], which should be approximately 800 $^{\circ}\text{C}$ in this specific case, in contradiction to what was reported before and with the temperature value indicated by out-of-pile experiments. Perhaps, the explanation of the lack of reaction product can be linked to the breach position or size, rather than to the temperature. However, in contradiction with out-of-pile [14, 18, 20] and some other in-pile [21, 12] experimental observations, a fuel pin with initial an O/M ratio of 1.96 showed a greater amount of reaction product than the one with an initial O/M ratio of 1.99. This probably indicates that the initial O/M ratio does not affect too much the extent of reaction product formation. Theoretically, the sodium can act as a source of oxygen to start the sodium-fuel reaction, but in mixed-oxide fuel the primary source of oxygen should be the fuel itself [12]. This means that the O/M ratio cannot be excluded a priori as influencing parameter for the reaction development. The previous results need to be further investigated to better understand the degree of influence of the initial O/M ratio on the reaction rate. In general, the formation of the reaction layer is strongly depended on the local conditions.

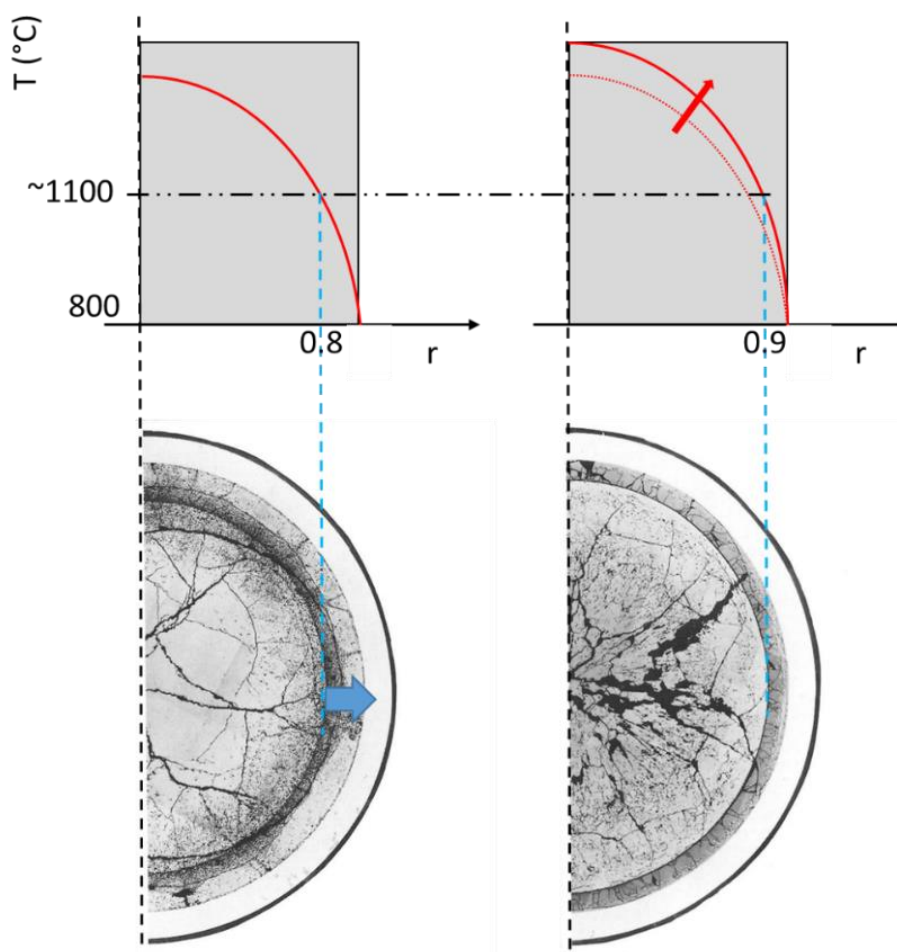


Figure 21: Reaction product location as function of the dissociation temperature. Rearranged from [22]. Left: after 6 days with the reaction product at a distance from the centreline of $r=0.8$. Right: after 65 days with the reaction product at the pellet rim.

1.2.2.2 Belgium Reactor-2

The Belgium Reactor-2 (BR-2) was commissioned in 1962 and is still operated as a materials testing reactor. The mission of this reactor is to contribute to warrant the safety of nuclear installations. In past experiences, BR-2 was used to test failed fuel pins of SFR.

Several irradiation tests were performed, mainly using fuel assemblies which contained $U_{0.8}Pu_{0.2}O_{2-x}$ ($0 < x < 0.01$), with different cladding types. Other types of fuel pins are here not deeply discussed, since they concerned channel blockage tests, through the melting of fuel pins.

In BR-2, fuel assemblies were irradiated under extreme conditions (high heat rating and high clad temperatures), in order to test the material behaviour and failure probability [12]. The fuel assemblies were also run after the failure detection in order to study the behaviour of failed pins running beyond failure. Figure 22 shows a non-demounted failed fuel assembly, before and after cleaning. The defects were oriented outward to the coolant channel indicating that the cause of the rupture can be probably attributed to the high internal gas pressure caused by very high heat rating. The diameter of the defected pin increased due to the sodium-fuel reaction. Indeed, a reaction layer of Na_3MO_4 was present along the whole active length with a maximum thickness of 500 μm at the hot spot. The layer thickness decreased to 100-200 μm at the fuel column ends and the maximum diameter increase was up to 30%. One of those pins revealed a several centimetre-long major crack at the hot spot, but no failure propagation occurred and no fuel was lost. At low burn-up, the investigated faults are self-limiting [31]. It was also demonstrated that the reaction layer formation is strongly dependent on the O_2 availability [21], as resulted from the performed test with high O_2 content.

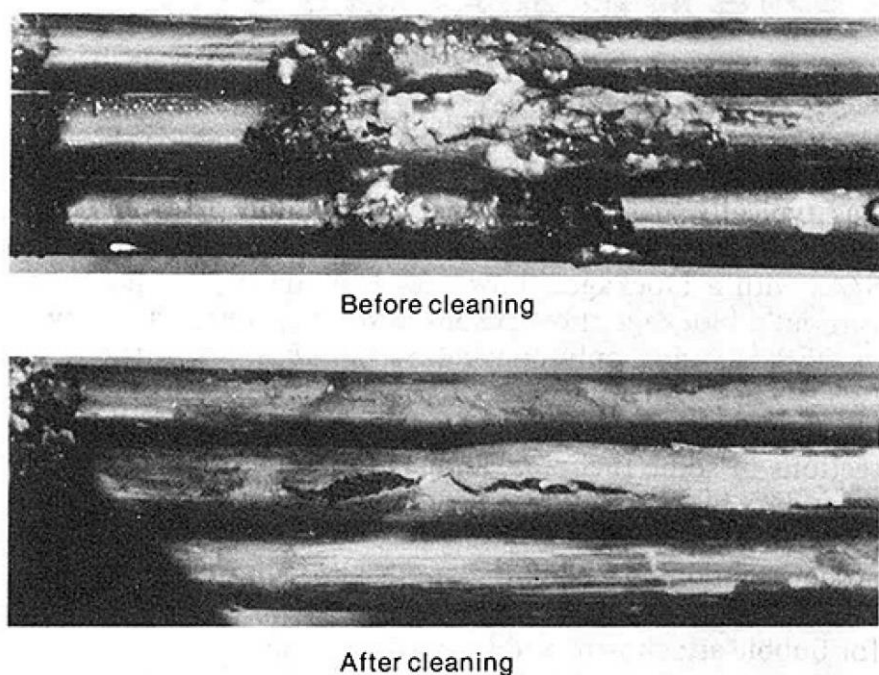
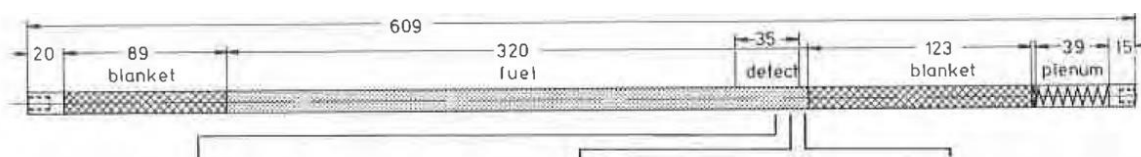


Figure 22: Non-demounted failed fuel assembly tested in BR-2 [32], before and after cleaning. The breach is clearly oriented outward to the coolant channel indicating that the cause of the rupture can be attributed to the high internal gas pressure caused by very high heat rating.

1.2.2.3 SILOE

SILOE reactor was an experimental reactor at Grenoble was a light water pool-type reactor characterized by a forced downstream water circulation. The reactor operated from 1963 to 1997 and was used mainly as material testing for irradiating materials and equipment.

Between 1975 and 1986, within a French-German irradiation program, various fuel pins were tested in the SILOE reactor [13, 28]. Among the tested fuel pins, fresh and pre-irradiated pins (in Rapsodie, Phenix and KNK II [28]), with artificial defects, were used. The reactor was operated with a single breached pin, under well-controlled conditions, to evaluate the pin behaviour beyond failure. The post failure analysis suggested that small defects need weeks before they can develop. The sodium would enter the pin and causes secondary effects only under power cycling conditions [13]. The presence of large artificial defects does not result in an excessive fuel loss (0 to 1500 mg [13]) and, obviously, the fuel loss increases with increasing open area of the breach. The reaction layer is usually formed in the originally open fuel-clad gap [28] and is present along the whole fuel column with a near-uniform thickness (of about 200µm [21]) and the maximum thickness at the hot spot. The results are in good agreement with those of BR-2, abovementioned. No pin-to-pin failure propagation was observed. Figure 23 shows the view of the defect region in three different longitudinal positions.



8. Pin Drawing of SILOE-S2

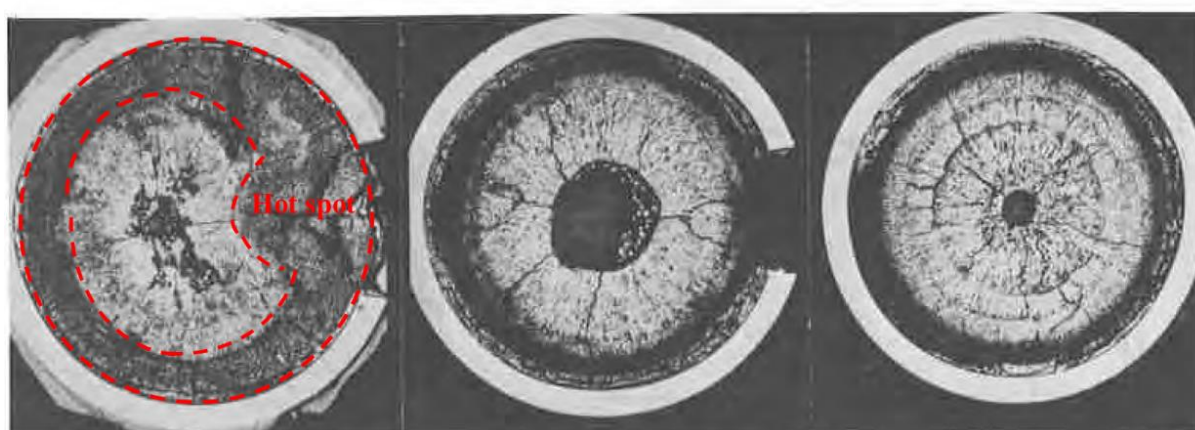


Figure 23: Failed pin in SILOE reactor from [21]. Left: view of the hot spot position showing the maximum thickness of the reaction layer at the hot spot. Middle: view of the upper part of the breach showing a near uniform reaction layer at the pellet rim. Right: view of the upper intact pin showing the sodium penetration and the reaction layer at the pellet rim.

1.2.2.4 *Rapsodie and Phénix*

Rapsodie and Phénix reactors belonged to sodium cooled fast reactor technology and were particularly useful in the achievement of wide knowledge on the safety of SFR. Rapsodie reactor was the first fast neutron research reactor at Cadarache using liquid sodium coolant. Numerous irradiation experiments were conducted in Rapsodie during its operation from 1967 to 1982. The main objective of the reactor was the development of steel cladding for sodium-cooled fast neutron reactors. The Phénix power reactor, located at the Marcoule nuclear site, was a small-scale prototype fast breeder reactor. The reactor was a pool-type sodium cooled fast breeder reactor and was operated from 1974 to 2009. Several tests also known as “end-of-life” tests related to safety issues were carried out, among which e.g. the risk of cladding failure and its impact on the reactor operation in safety.

Experiments in the Rapsodie and Phénix reactors showed a very low pin failure rate [12] compared to other SFRs. Since the 1970s, within a numbers of irradiation programs, several tests were performed in the Rapsodie and Phénix reactors, with the aim to investigate the evolution of failed fuel pins. Recently, Costin [9] collected and reviewed most of these in-pile test data. The post irradiation examinations of the different failed fuel pins showed usually the presence of a uniform thick reaction layer along the whole fuel column with a maximum thickness (in the worst case of circa 600-700 μm) at the hot spot. The layer thickness decreased down to 100 μm at the fuel column ends. In all cases, no breach propagation or secondary failures were observed. The sodium infiltration was found to be dependent on the defect size and position, as expected. A breach at the upper end of the fuel column represented the worst scenario since the sodium can potentially fill up the whole length of the fuel pin. Air infiltration during an irradiation test, in the Rapsodie reactor, allowed investigating the influence of the excess of oxygen in sodium. The amount of oxygen dissolved in sodium was estimated to exceed 200 ppm, but no influence on the reaction product formation was reported, in contradiction to the observations in BR-2 abovementioned. This aspect needs additional investigation and further understanding. Only one case of fuel loss was reported and was probably enhanced by the presence of a large breach size (longitudinal 44 cm). In this specific case, the fuel loss could be realistically attributed to the removal and dismantling operations, rather than to the core conditions. The comparison between failed fuel pins without and with fuel loss, reported in Figure 24, revealed two main differences: the presence of a uniform reaction layer in the first case, and contrarily a not fully developed reaction layer; in the second case with the presence of significant large cracks, which reach the central void, in agreement with the observed behavior in EBR-II. Tests on pin failed at the Beginning Of Life (BOL) revealed that the swelling of the pellet due to the reaction product can be accommodated by the cladding swelling, in agreement with the observations after the tests in EBR-II. The failures at that stage showed a slow evolution, needing tens of days before the reactor was shut down. Instead, in the case of rupture at the End Of Life (EOL), the closure of the gap, due to the pellet swelling, limited the reaction to the breach area, mitigating the reaction product formation. Here, the failure evolution was much faster than the one at BOL and the reactor shutdown was required within few hours.

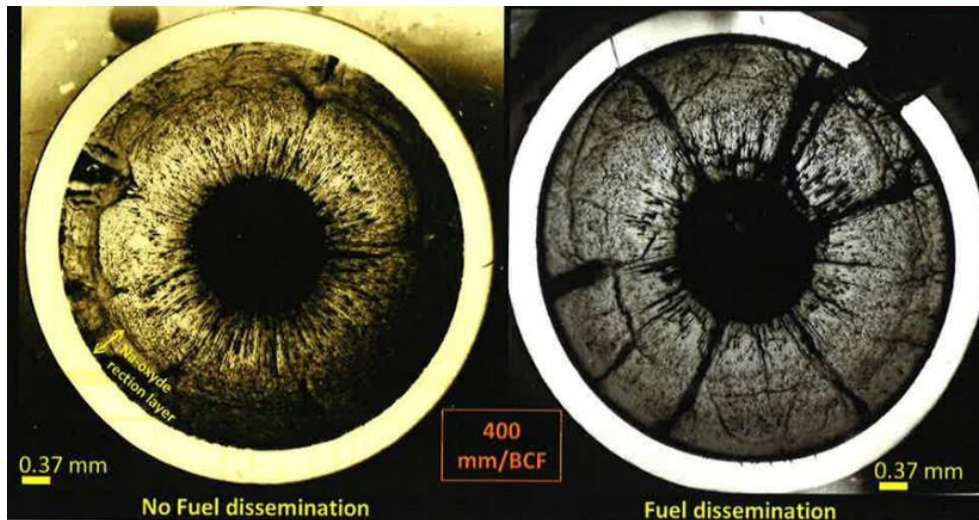


Figure 24: Comparison of two different failed fuel pins. Left: failed pin in which no fuel was lost. Right: failed pin in which fuel loss was reported.

1.2.2.5 Dounreay Fast Reactor

The Dounreay Fast Reactor (DFR) did not belong to the “pure” SFR technology and was unique for its combined down-flow NaK primary coolant and N₂ cover gas. The reactor showed a relatively high pin failure rate, which was actually attributed to gas entrainment caused by NaK down-flow [27], except for “a single fabrication batch where some impurities causing heavy internal corrosion remained in the pins during fabrication” [33].

Fuel bundles containing pre-defected fuel pins, with U_{0.8}Pu_{0.2}O_{1.98} and U_{0.7}Pu_{0.3}O_{2-x} (0.02 < x < 0.05), were used to test defective fuel pins behaviour. Figure 25 shows a failed pin in DFR, with two breaches, one wide crack at the upper and one smaller crack at the lower end of the fuel column. Nevertheless, the formation of the reaction product did not cause severe deterioration. The potassium reacts with the fuel to form a higher density compound than sodium uranate [32] and, therefore, NaK can interfere with the sodium uranate formation. Consequently, the pin damage might be far less than it would be in a sodium cooled reactor. Although fuel loss was observed, in most cases, the failed pins did not affect neighbouring ones, even when the failures were significant.

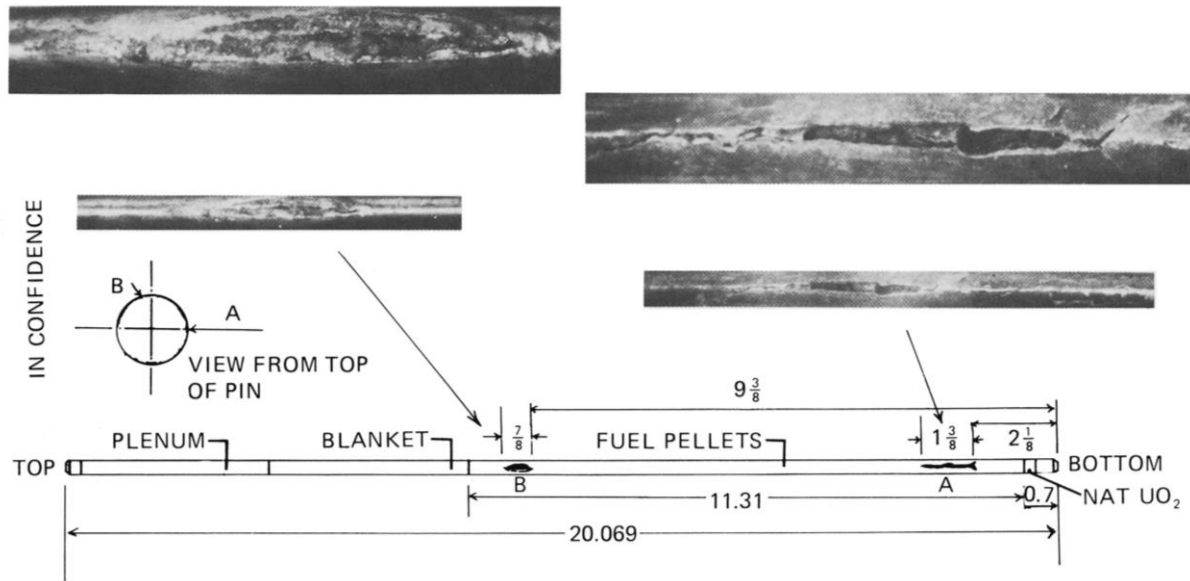


Figure 25: Failed pin in DFR, with two breaches, from [12]. Detailed view of one wide crack at the upper end and one smaller crack at the lower end of the fuel column.

Table 2: Summary of the main results of failed fuel pin tests under irradiation

Reference	Reactor	Main results
Strain [22]	EBR-II	Uniform layer at the pellet rim Temperature, burnup and O/M ratio influence on the FSRP location and morphology Secondary breaches and fuel dissemination in case of degraded or high temperature of cladding
Kleykamp [28] Weimar [21]	SILOE	Thicker layer at the hot spot Uniform layer at the pellet rim
Plitz [12] Weimar [21]	BR-2	Thicker layer at the hot spot Uniform layer at the pellet rim No failure propagation and no fuel loss
Costin [9]	PHENIX	Uniform layer at the pellet rim Observation of porous morphology of the fuel grains Only one case of fuel dissemination with large cracks
Costin [9]	RAPSODIE	In the case of EOL failure ROS limited to the breach area due to the closure of the gap High burn-up lead to a thicker layer formation when compared with non-irradiated fuel
Plitz [12] Warinner [32]	DFR	High failure rate was attributed to gas entrainment caused by NaK down-flow Formation of the reaction product did not cause severe deterioration

1.2.2.6 The influence of the Joint Oxide Gain

During reactor operation, the initial MOX fuel can undergo many changes due to the radiation damage induced by fission fragments and neutrons, temperature gradient across the pellet and the reactions between fuel and fission products. In addition, fuel and fission products can mechanically and chemically interact with the cladding material. The initial gap between the fuel pellet and the cladding is filled with inert helium gas. During irradiation, it is progressively filled up with fission gases, such as Xenon and Krypton, and becomes more and more closed as result of fuel pellet swelling. Under continuous irradiation, due to the strong temperature gradient, the fission products diffuse predominantly in radial direction, towards the cladding. At high burn-up, as result of the fission products accumulation at the pellet-cladding location, a so-called Joint Oxide Gain (JOG) layer is formed. Figure 26 shows the JOG formation due to the chemical evolution of Mixed-Oxide Fuel and a view of the JOG morphology after post irradiation examination of a fuel pin. Although the chemical composition of the JOG is well-known, the specific mechanism behind its formation is not yet fully-understood. Post irradiation examination by EPMA demonstrated that, among all the volatile and metallic precipitate fission products, the JOG is mainly constituted of Cs, Mo, I, Te and Ba [34, 35]. At high-burnup, molybdenum is present in the JOG, mostly in the oxidized state MoO_2 , MoO_3 or Cs_2MoO_4 . However, also some other phases such as CsI , Cs_2Te and Cs_2UO_4 [34, 36] were observed. The formation of these compounds, especially the molybdenum oxides, can act as buffer against the rise of the oxygen potential [16] and therefore the O/M ratio of the fuel is maintained close to 2.0 [37], despite the continuous release of oxygen due to the fission.

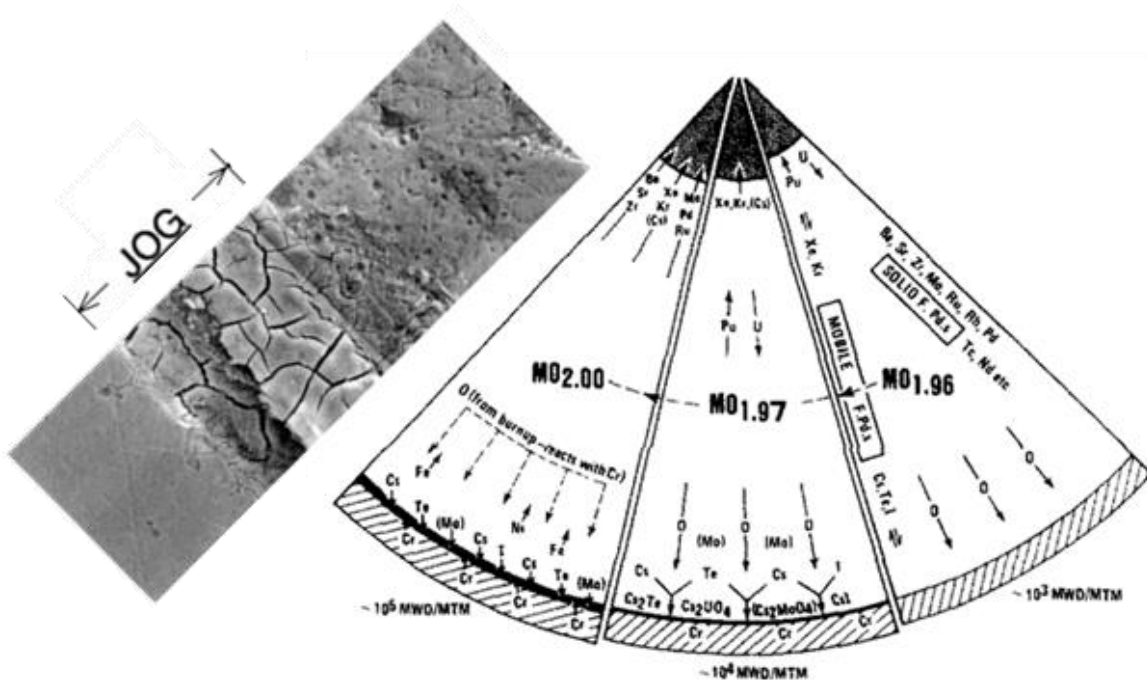


Figure 26: JOG formation due to the chemical evolution of Mixed-Oxide Fuel [38] and fission product formation behavior in Fast Breeder Reactors (FBR). Detailed view of the JOG [39] morphology after post irradiation examination of a fuel pin.

In the event of a pin failure, especially at high burn-up, sodium will react firstly with the JOG. The formation of cesium, sodium and molybdenum oxide phases was suggested [8] rather than cesium substitution by sodium in the main component of the JOG. Recently, the reaction between Cs_2MoO_4 , contained in the JOG, and sodium was confirmed and the reaction forms the phase $\text{Cs}_3\text{Na}(\text{MoO}_4)_2$ [40]. Moreover, the calculated oxygen potential threshold was reported slightly below that of Na_3UO_4 [40]. One could imagine that the presence of the JOG at the rim of the fuel pellet could delay the sodium infiltration into the fuel, at least temporarily. Nevertheless, the mechanism of the reaction between liquid sodium and JOG is still poorly understood and consequently its role on the long-term progression of the reaction cannot be stated.

1.2.3 Internal storage experience

Between 1982 and 1983, a long-time internal storage experiment was carried out in the Phénix reactor. This is, up to now, a unique long-term demonstration of the feasibility of the internal storage concept. The subassembly CPD 0409 was chosen as demonstrator, because the in-core pin failure had a slow evolution and was then well representative for a typical failed pin which will be stored in the internal storage. The fuel was a standard mixed oxide with a Pu/M ratio of 0.269 and the breach of the cladding was approximately 3.5 cm long. The narrow breach led to an exposed surface of the fuel in the order of mm^2 . The total storage period was 500 days, including 300 days during reactor operation. Even if the storage time was less than half of the required time for the complete cool down of the pins, some important features could be extrapolated. During the prolonged internal storage, the reaction product did not exhibit significant changes compared to the one observed in post failure analysis, indicating that most of the reaction should take place in the core. Most of the available oxygen in the fuel was probably consumed by the initial reaction, when the failed pin was still in the core and then subject to a significant fuel temperature and temperature gradient. With the flattening of the fuel temperature in the storage position, the oxygen migration in the fuel will be suppressed and the reaction evolution was controlled mainly by the oxygen impurities in the primary coolant. Under steady-state conditions, the deterioration of failed pins may only slowly proceed through fuel-sodium reaction. The reaction product should then evolve with a limited rate and should not cause undesirable effects, as suggested by the non-occurrence of a DND signal during the whole storage period.

1.3 Conclusions

Despite some uncertainties, out-of-pile and in-pile test are usually in good agreement in a wide range of investigations. However, the current understanding of the fuel-sodium reaction is based on few observations only. At the beginning of the reaction, when i.e. the failed pin is still in the active core, the factors which may strongly influence the extent of the reaction are the initial O/M ratio and Pu content in the fuel, as well as the burn-up, temperature gradient and oxygen content in liquid sodium. Some secondary factors such as type of defect and sodium speed can be also considered important at that stage. Under in-core conditions, the development of the

reaction product can be most probably linked to the fuel temperature. Although some uncertainties exist on the exact values of the dissociation and melting temperature of the reaction product and the O/M ratio required for the reaction, the location of the reaction product can be reasonably predicted on the base of the great fuel temperature gradient which places the formation of the reaction product to the outer radial region of the fuel. This simply means that the reaction product thickness is directly dependent on the steep temperature gradient and can explain the large reaction product layers found by post failure analysis. Moreover, in light of the in-pile experiments, it is reasonable to suppose that most of the reaction should take place in the stage of rupture and should not evolve dramatically if the failed pins are promptly removed from the core and placed in the storage facility. The experiment of the long-term storage in Phénix was conducted for about one year. This period of time did not completely cover the expected storage time of three years of the future sodium fast reactors and due to its uniqueness, does not allow extrapolating conclusive statements, but the successful results encourage further investigations.

2 *Heterogeneous kinetics and mechanisms modelling*

In the previous chapter was showed that the demonstration for the feasibility of a 3-year safe storage for future SFR has still to be made. The key parameter for this demonstration relies on the kinetics of the corrosion reaction between mixed oxide base fuels and liquid sodium. That is why this reaction kinetics has to be modelled in a predictive manner. In the present study, the formalism of heterogeneous kinetics was chosen in order to achieve this modelling. The empirical approach consisting in fitting experimental data could not be realized because of the 3-years duration of the representative experiments.

This chapter focuses on the description of the generalized approach used to model a reaction of a solid exposed to a reactive fluid. To interpret the kinetic data, the use of the chemical kinetic concepts will be extended to the heterogeneous reactions, specifying that the involved intermediates in heterogeneous reactions are adsorbed species and point defects. Indeed, the rates at which the products form are usually governed by interfacial and diffusion processes, both involving crystallographic defects. Three main assumptions are considered: the reaction is the result of the combination of surface nucleation and growth, the reaction occurs in steady-state conditions and the growth process is kinetically controlled by a single elementary step [41]. The aim of a kinetic model is to understand the reaction and to predict the evolution of the reaction rate as a function of time in a given temperature and pressure domain, taking into account the morphological characteristics of the solid which is transformed.

Dans ce chapitre 2, on aborde les notions essentielles de la théorie de la cinétique hétérogène. On en déduit quelles données sont nécessaires pour la modélisation d'un mécanisme réactionnel. Les données disponibles dans la littérature sont présentées.

2.1 *Description of the reaction*

In general, the transformation of a solid A (reactant) which produces another solid phase B on the surface of A, can be expressed by the following reaction balance:



where v_{G_i} and v_B are the algebraic stoichiometric coefficients of the fluid G_i and the solid phase B, respectively. At a given time, the extent of reaction ξ , with respect to the initial solid A and the produced solid B, can be written as:

$$\xi_A = n_0 - n_A(t) \quad (mol) \quad (3)$$

$$\xi_B = \frac{1}{v_B} n_B(t) \quad (\text{mol}) \quad (4)$$

where n_0 is the initial amount of A, n_A and n_B are the amounts of A and B at given time t , respectively. Consequently, the speed of conversion is:

$$r_A = \frac{d\xi_A}{dt} = -\frac{d(n_A)}{dt} \quad (\text{mol} \cdot \text{s}^{-1}) \quad (5)$$

$$r_B = \frac{d\xi_B}{dt} = \frac{1}{v_B} \frac{dn_B}{dt} \quad (\text{mol} \cdot \text{s}^{-1}) \quad (6)$$

For the evaluation of the state of the reaction, we can use the fractional extent α , which is an intensive parameter, without dimension. Its expression is given by:

$$\alpha_A = \frac{\xi_A}{n_0} = 1 - \frac{n_A}{n_0} \quad (7)$$

$$\alpha_B = \frac{\xi_B}{n_0} = \frac{n_B}{v_B n_0} \quad (8)$$

From which, the rate of the reaction can be derived:

$$\Re_A = \frac{d\alpha_A}{dt} = \frac{1}{n_0} \frac{d\xi_A}{dt} = \frac{r_A}{n_0} \quad (9)$$

$$\Re_B = \frac{d\alpha_B}{dt} = \frac{1}{n_0} \frac{d\xi_B}{dt} = \frac{r_B}{n_0} \quad (10)$$

Under the steady state approximation, no accumulation of intermediate species is possible, and consequently a general extent of the reaction can be defined independently of the solid phase:

$$\begin{aligned} \xi_A &= \xi_B = \xi \\ \frac{d\xi_A}{dt} &= \frac{d\xi_B}{dt} = \frac{d\xi}{dt} \end{aligned} \quad (11)$$

Finally, the fractional conversion and fractional conversion rate are then:

$$\alpha = \frac{\xi_A}{n_0} = 1 - \frac{n_A}{n_0} = \frac{\xi_B}{n_0} = \frac{n_B}{v_B n_0} \quad (12)$$

$$\frac{d\alpha}{dt} = \frac{1}{n_0} \frac{d\xi}{dt}$$

2.2 Nucleation and growth

The transformation of a solid phase into another solid phase occurs usually via two processes: nucleation and growth. The reaction always starts with the formation of a nucleus and the growth can be then reached only after the nucleation. Thereby, to achieve a complete understanding of the overall reaction, one needs to know both mechanisms. Even if extremely important, the nucleation process is not yet fully-understood [41]. The growth process is basically the growth of the nuclei which leads to the evolution of the formed phase through the “destruction” of the initial phase. Although nucleation and growth contribute to the same reaction and are represented by the same balance reaction, the two processes involve different reaction surfaces and mechanisms. In the case of reactions between a solid and a fluid, nucleation is a process which occurs on the surface of the solid and the speed of nuclei appearance depends on the free surface which is not yet transformed. The growth, instead, proceeds at the interfaces, either the interface between the two solid phases A and B (internal interface), or the interface between the formed phase B and the environment (external interface). Since the growth process needs the presence of the reaction product between the initial solid phase and the environment, its mechanism involves the surface, the external/internal interface and the formed layer. Figure 27 shows the different reactional zone of the growth process.

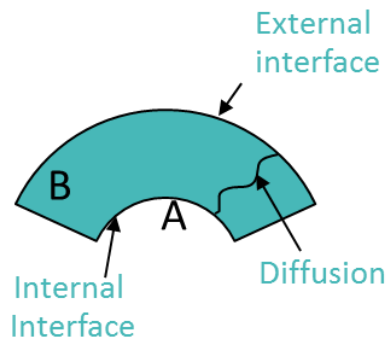


Figure 27: Different reactional zone. A represents the initial solid and B the formed phase after the reaction.

2.2.1 Principles for the growth modelling

The total extent rate of the formed phase is then the result of the contributions of both, nucleation and growth processes, to the reaction extent. However, one can assume that the contribution of the nucleation process is negligible, since the amount of matter produced by the nucleation is very low. Thereby, the total extent rate can be approximated with the growth extent rate as:

$$\frac{d\xi}{dt} \cong \left(\frac{d\xi}{dt}\right)_{growth} \quad (13)$$

Moreover, if we assume that one process is significantly faster than the other one, only one process is enough to describe the kinetics. In this specific case, the model is called *one-process model* and we can refer to two different possibilities: instantaneous nucleation and slow growth or the opposite. In the case of instantaneous nucleation, the whole initial surface of the solid is instantaneously covered by a thin film, having a negligible thickness, of the formed phase, which will grow only normally to the surface.

If nucleation and growth processes have similar rates, one must consider both processes to determine the expression of the reaction rate.

Under the approximation that the reaction is composed of elementary steps and that there is one rate determining step, we can write a general equation for the rate of the growth process. If the rate determining step is a surface or interfacial reaction, its kinetics rate is proportional to an areic rate v_s ($\text{mol m}^2 \text{s}^{-1}$) and can be written as:

$$\left(\frac{d\xi}{dt}\right)_{surf/interface} = v_s S \quad (14)$$

where S is the surface area (m^2) of the reaction zone where the rate determining step takes place. If the rate determining step is a diffusion step, the areic rate is replaced by the diffusion flux J ($\text{mol m}^2 \text{s}^{-1}$) and then:

$$\left(\frac{d\xi}{dt}\right)_{diff} = JS = \frac{D\Delta C}{l_0} G_D S \quad (15)$$

where D is the diffusion coefficient ($\text{m}^2 \text{s}^{-1}$) of the diffusing species, ΔC (mol m^{-3}) is the difference in concentration of the diffusing species at both interfaces, G_D is a geometrical factor and l_0 is a constant length (equal to 1 m). The two previous equations are characterized by the presence of at least one factor (S or G) which depends on the morphological variables and can vary with the time even in isothermal and isobaric conditions. The remaining factors are only dependent on the thermodynamic variables.

In order to have a general expression, the reaction rate can be written as:

$$\frac{d\xi}{dt} = n_0 \phi S_m \quad (16)$$

where ϕ is the areic reactivity of the growth ($\text{mol m}^2 \text{s}^{-1}$) and does not depend on the morphological variables, and S_m is the molar space function of the growth ($\text{m}^2 \text{mol}^{-1}$) equal to $\frac{G_D S}{n_0}$. The geometrical factor G_D depends on the location of the rate determining step. If the step is at the surface/interface the G_D is equal to 1. Instead for the diffusion trough the formed layer, the expressions of G_D represents the solutions of Fick's laws and are given for the different geometry in Table 3, where r_i is the radius of the internal interface, r_e is the radius of the external interface and x the thickness of the diffusion layer.

Table 3: Geometrical factor G_D for rate determining step of diffusion

<i>Particle shape</i>	<i>G_D</i>
Sphere	$\frac{l_0 r_e}{r_i (r_e - r_i)}$
Cylinder	$\frac{l_0}{r_i \ln \left(\frac{r_e}{r_i} \right)}$
Plate	$\frac{l_0}{x}$

In this way, we have a rate expression where the variations with both the partial pressures and temperature are described only by the areic reactivity function, independently from the time. Instead the space function expresses the variation of the overall reaction with time. Finally, using the fractional conversion, the Eq. 26 can be written in the form of:

$$\frac{d\alpha}{dt} = \phi S_m \quad (17)$$

Therefore, as a result of the separable rate, we can model the reaction rate in two parts: space function and reactivity of growth.

2.2.1.1 Modelling of the space function

Under isothermal and isobar conditions, the areic reactivity of growth is considered to vary with partial pressure and temperature, independently with the time. We can thus develop a generic model of the molar space function of growth, which requires the knowledge of the initial shape of the solid, the type of growth, the sense of development of the formed phase and the zone of the rate determining step.

During the growth process, the points of the active interface will move with a certain velocity which has three motion velocity components, i.e. the normal and two tangential components to the surface. If the three motion velocity components are identical, the growth is isotropic. Instead, if the tangential components are considered much larger than the normal one, the growth is anisotropic. Both types of growth are schematized in Figure 28, where the right figure shows isotropic growth of component B into A starting from one point at the bottom of the initial surface of A, while the left figure shows anisotropic growth of B into A, also starting from the same point of the initial surface of A but with a very fast tangential component compared to the growth in normal direction.

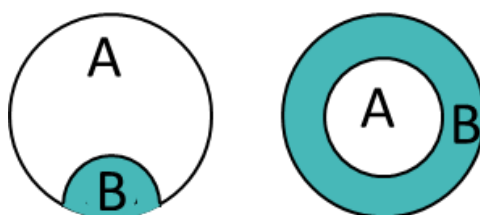


Figure 28: Isotropic and anisotropic growth. A represents the initial solid and B the formed phase after the reaction.

Since the chemical reaction for the formation of B and the consumption of A is the cause of the interfaces motion, the sense of development of the formed phase is essential. As shown in Figure 29, the growth can be inward if the internal interface moves towards the center of the initial solid phase, or outward if the external interface moves towards the environment.

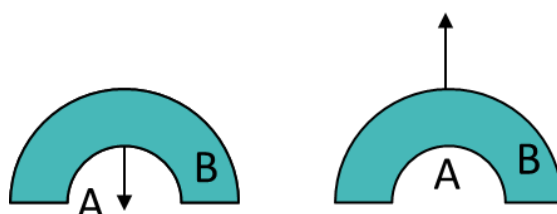


Figure 29: Inward and outward development. A represents the initial solid and B the formed phase after the reaction.

Finally depending on the particle geometry (sphere, cylinder or plate), the type of growth (isotropic or anisotropic), the sense of development (inward or outward) and the localization of the rate-determining step (internal interface, diffusion zone or external interface), it is possible to propose 40 expressions of the molar space function S_m , as presented in Table 4 [41].

Table 4: Expressions of the molar space function S_m [41]

Grain shape		Spherical grains	Cylindrical grains	Platelike grains
Instantaneous growth		(F ₁)	(F ₁)	(F ₁)
Instantaneous nucleation	Inward growth	Internal interface (R ₃) External interface (S ₃) Diffusion (D ₄)	Internal interface (R ₂) External interface (S ₂) Diffusion (D ₂)	Internal interface External interface (S ₁) Diffusion (D ₁)
	Outward growth	Internal interface (R _{3out}) External interface (S _{3out}) Diffusion (D _{3out})	Internal interface (R _{2out}) External interface (S _{2out}) Diffusion (D _{2out})	Internal interface (R _{1out}) External interface (S _{1out}) Diffusion (D _{1out})
Nucleation and anisotropic growth	Inward growth	Internal interface External interface Diffusion	Internal interface External interface Diffusion	Internal interface External interface Diffusion
	Outward growth	Internal interface External interface Diffusion	Internal interface External interface Diffusion	Internal interface External interface Diffusion
Nucleation and isotropic growth	Inward growth	Internal interface	Internal interface	Internal interface

2.2.1.2 Modelling of the reactivity

The modelling of the reactivity needs a defined reaction mechanism, which depends on the nature of the reaction. To build the reaction mechanism we decompose the reaction in a set of elementary steps, i.e. the elementary reaction and diffusion in each zone of the reaction. The mechanism has to obey to the “rule of elimination of the intermediate species” [42] and the combination of the steps has to give the overall reaction, without intermediate species.

The elementary steps are then build up by creation or consumption and diffusion of intermediate species, such as point defects or adsorbed/ desorbed species. We will us the Kröger–Vink notation for the point defects, in which the principal features are [43]:

1. Vacancies: are indicated by the symbol V_X for a vacancy of the site which is normally occupied by X. The subscript designates then the normal occupant of the site.
2. Interstitial atoms: are denoted by a subscript i attached to the normal symbol for the element. They are indicated as X_i .
3. Impurity atoms: are given by their normal chemical symbol and the site occupied is written as a subscript. They are indicated as A_M .
4. Charges on defects: the notation considers only effective charges on defects. The effective charge is the charge that the defect has with respect to that at the same position in a defect-free crystal structure. In order to distinguish effective charges from real charges, the superscript ' is used for each unit of negative charge and the superscript • is used for each unit of positive charge.

If we consider a thermal reaction in the form of:



where Y_i are the reactants and β_i are their arithmetic stoichiometric number. The reaction can be considered as *elementary* if it takes place only in one zone, no experimental detection of intermediates can be possible and its rate can be written as:

$$v = k \prod_i [Y_i]^{\beta_i} \quad (19)$$

where k is the rate constant which is a function of temperature and varies according to Arrhenius law:

$$k = k_0 \exp\left(-\frac{E_a}{RT}\right) \quad (20)$$

where k_0 is the frequency factor, E_a (always >0) is the real activation energy (J mol^{-1}), R is the general gas constant ($8.3144 \text{ J K}^{-1} \text{ mol}^{-1}$) and T is the absolute temperature (K).

If the opposite elementary reaction is possible, the rate of the total reaction is given by the difference of the two opposite elementary reactions, i.e.:

$$v = k \prod_i [Y_i]^{\beta_i} - k' \prod_j [Y_j]^{\beta_j} = k \prod_i [Y_i]^{\beta_i} \left(1 - \frac{k' \prod_j [Y_j]^{\beta_j}}{k \prod_i [Y_i]^{\beta_i}} \right) \quad (21)$$

Thus, in the case of a linear mechanism, i.e. where each intermediate species appears in only two elementary steps and the whole reaction is a linear combination of the elementary steps and under the assumption that the growth process is kinetically controlled by a single elementary step, we can express the areic reactivity of growth as:

$$\phi_{surf/interf} = k \prod_i [X_i]^{\beta_i} - k' \prod_j [X'_j]^{\beta'_j} \quad (22)$$

The reactivity for the diffusion determining step, can be expresses as:

$$\phi_{diff} = \frac{D_{X_i} \Delta [X_i]}{l_0} \quad (23)$$

where $X_{i,j}$ are the intermediate species.

According to the rate-determining step assumptions, all the other elementary steps of the mechanism are at equilibrium. By considering also the electroneutrality in each phase (with or without Brouwer's approximation [44]) and the balance equation of surface sites according to Langmuir's theory of adsorption [45], this leads to a set of equations. It is thus possible to determine the intermediate concentrations by solving this system of equations and so to express the areic reactivity of growth ϕ as a function of partial pressures and temperature.

2.3 Requirements for the modelling

As previously described, the modelling of the reaction using the heterogeneous kinetic formalism requires the knowledge of some basic data. In particular, in order to apply the heterogeneous kinetics formalism to the reaction between oxide fuels and liquid sodium, the main questions this study would need to answer are:

1. Which kind of reaction product(s) is expected to be formed under the internal storage conditions, either for uranium oxide and mixed oxide fuels? And what are their structural proprieties (oxidation states, point defects, etc...)?
2. Is the nucleation process instantaneous? Can be then the reaction described trough the growth process only?
3. What are the involved species and their diffusion path?
4. Which kind of rate determining step governs the reaction?

In order to check if some of the required data are available in literature, a brief overview of the status of the literature is hereafter reported. In particular, the analysis focuses on the thermodynamic aspects from which the stable phase(s) under the internal storage conditions can be extrapolated. Moreover, some kinetic data, such as the rate and diffusion species, are also examined.

2.3.1 Thermodynamic aspects

The Na-U-Pu-O, Na-Pu-O and Na-U-O systems are treated here as far as they are of relevance for the prediction of the phases formed during the fuel-coolant interaction. Indeed, the understanding of the Na-U-Pu-O system is of priority interest because the future fast breeder reactors will be operated with Mixed OXide (MOX) fuel, i.e. (U,Pu)O₂, with a concentration of Pu in the order of 20-40 wt% [3]. Although the Na-U-O system was studied intensively, the thermodynamic assessment of the Na-U-Pu-O system is still in development due to its complexity and the limited data available. Generally, there is a tendency to approximate the Na-U-Pu-O system by the simpler Na-U-O system. Such an approximation is usually accepted, because there is not a large difference between the two systems: actually, the oxygen potential thresholds for the formation of the main product Na₃MO₄, where M=U, Pu or U_{1-x} Pu_x, are similar in both systems (Na-U-O and Na-U-Pu-O) as reported by Mignanelli and Potter [17] and Adamson et al. [14].

There are much less data available in the literature for the Na-Pu-O system compared to those of the Na-U-O system. The investigation of the Na-Pu-O system started with Keller [46, 47, 48] and Pillon [49], as part of more complex systems involving alkali and actinide elements. More recently, the investigation was extended by Smith et al. [50, 51, 52], Bykov et al. [53] and Kovacs [54]. Additional details for the Na-O and Na-Pu-O systems are reported in the annex.

2.3.1.1 Oxygen solubility in liquid sodium

Oxygen dissolved in liquid sodium is the prime cause of the structural material corrosion in SFRs. A solid knowledge of oxygen solubility limit in liquid sodium is then required for the safety analysis of SFR, especially for the modelling of the Fuel-Coolant Interaction (FCI), since it allows to determine the stable phases after the reaction between sodium and fuel and to calculate the oxygen concentration in equilibrium with them, at a given temperature. The oxygen solubility in liquid sodium was intensively investigated [55, 56, 57, 58, 59, 60, 61], but there are many different equations available, which are not in good agreement [62], leading to uncertainty in the calculation. Claxton [55, 56] suggested that the best expression for oxygen solubility is in the form $\log C_0 = A + \frac{B}{T}$, in which C_0 (expressed in weight part per million, wppm) is the solubility limit, i.e. solubility at saturation, T is the absolute temperature (expressed in Kelvin) and A and B are constants. The two constants, A and B are related to thermodynamic quantities of the solution. Between the temperature range of 110 and 550 °C, his equation corresponds to:

$$\log C_0(\text{wppm}) = 5.21 - \frac{1777}{T(K)} \quad (24)$$

Noden [63, 57] critically reviewed all the available data in literature in 1973, in the temperature range of 100 and 600 °C. His equation was confirmed by Maupré a few years later [58]. The oxygen solubility expression of Noden can be written as:

$$\log C_0(\text{wppm}) = 6.2571 - \frac{2444.5}{T(K)} \quad (25)$$

In the temperature range of interest, i.e. 800-1000 K, the discrepancy between the expressions proposed by Noden and Claxton is significant, as illustrated in Figure 30 (black and red curve, respectively). However, the equation of Noden is the most recommended expression. This expression is in good agreement with the equation proposed by Eichelberg [59] (green curve in Figure 30), in the same temperature range, and corresponding to:

$$\log C_0(\text{wppm}) = 6.239 - \frac{2447}{T(K)} \quad (26)$$

From Noden's law it is then possible to determine the oxygen solubility limit (saturation) in sodium as function of temperature. However, in the operational temperature range (500-550 °C) of SFR, the saturation and thereby the formation of sodium oxide (Na_2O) will correspond to an oxygen concentration of about 1000 wppm, a value which is well above the specified oxygen concentration in the coolant during the operation. The purification systems are indeed used to maintain the oxygen content in liquid sodium below 3-5 wppm, to prevent corrosion issues of structural materials [64]. Oxygen dissolved in liquid sodium is then present in small quantities and can be treated in the form of a dilute solution.

At a given temperature, the reaction between liquid sodium and uranium or plutonium oxide and the formation of a new phase (e.g. Na_3MO_4) depends on the available oxygen within both the liquid sodium and the fuel solid solution. Then, the reaction stands still when the oxygen content of the sodium and the fuel reaches the equilibrium threshold value. Such threshold defines the conditions under which the system is in equilibrium. To establish the formation of the Na-U-O and Na-U-Pu-O systems, the equilibrium oxygen potential should be linked to the concentration of oxygen dissolved in liquid sodium and to the O/M ratio of the fuel. The relationship between oxygen potential and oxygen concentration can be derived from the Gibbs energy of sodium oxide formation and the equation of the solubility of oxygen in liquid sodium.

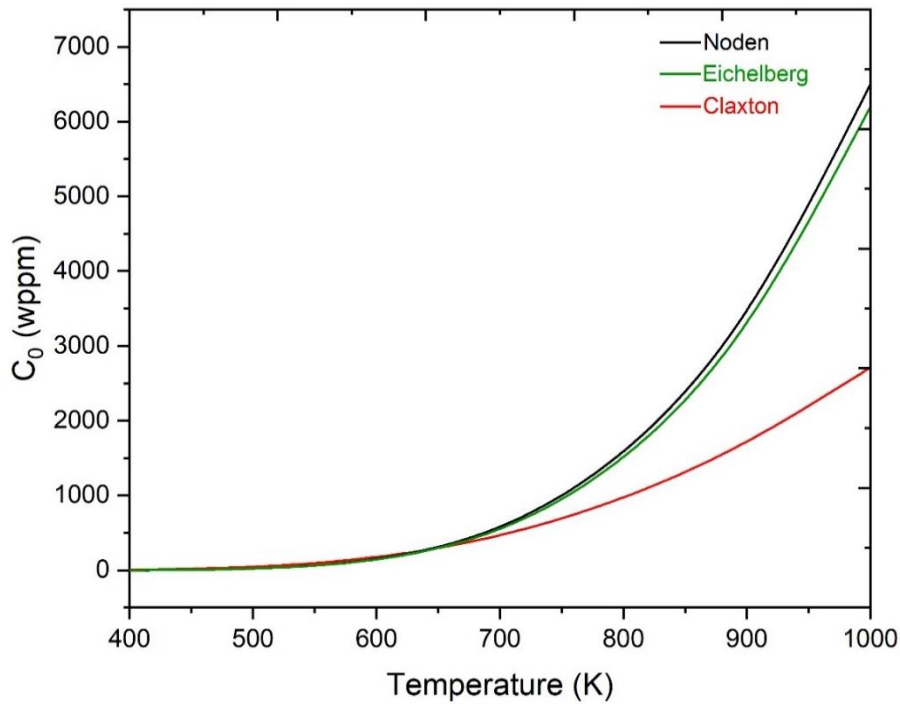


Figure 30: Oxygen solubility in liquid sodium. Comparison between the available equations in literature.

Using the expression of the oxygen solubility in liquid sodium proposed by Noden, the equilibrium oxygen potential, in the Na-O system, is:

$$\Delta G_{\text{O}_2}^{\text{eq}} \left(\frac{\text{J}}{\text{mol}} \right) = -735691.3 + 33.232T + (38.287 \log C_0)T \quad (27)$$

Detailed calculation is given in the Annex. However, we must be careful with the calculation of the oxygen concentration threshold in sodium, because its accuracy is strongly affected by the discrepancy of the various solubility equations, as above mentioned.

2.3.1.2 Na-U-Pu-O system

The Na-U-Pu-O is the system with the highest relevance for the safety assessment of the internal storage in an SFR, since it will be operated with MOX fuel. Unfortunately, this is also the system with the highest complexity and only few data are available in literature. Most of the studies performed on the Na-U-Pu-O system were firstly aimed to improve the knowledge of the properties of the phase $\text{Na}_3(\text{U,Pu})\text{O}_4$, because it is the main reaction product formed during a fuel pin failure in an SFR. Therefore, most of the data concern this phase, rather than all the other phases which can be formed in different conditions.

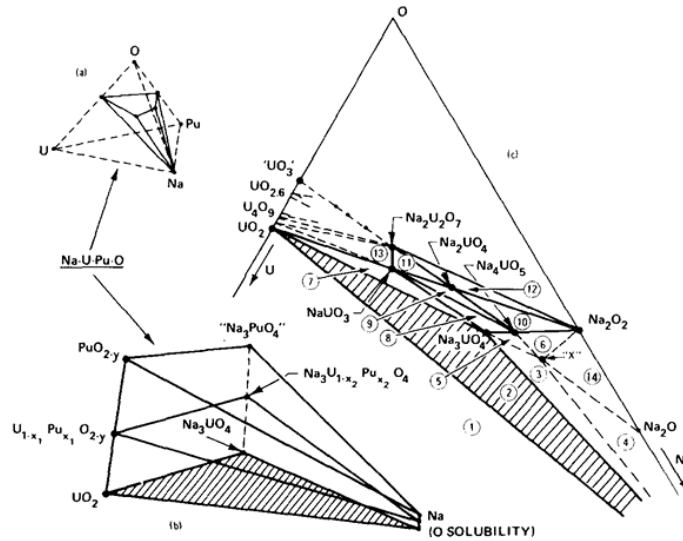


Figure 31: Section of the phase diagram Na-U-Pu-O and Na-U-O systems at 1000 K [18]

The structures of sodium uranoplutonate $\text{Na}_3\text{U}_{1-x}\text{Pu}_x\text{O}_4$ for plutonium concentrations up to 30% was reported to be similar to sodium uranate, i.e. cubic with a cell parameter of 4.79 - 4.81 Å [20, 49, 65]. A tetragonal structure with a cell parameter of 4.79-4.925 Å was reported for a plutonium concentration of 76% [20]. The same tetragonal phase was also observed for a plutonium concentration of 30% at 1123 K [16]. These results indicate that the phase should be cubic at low temperature (<823 K) and the tetragonal one should be stable at temperatures higher than 1123 K. However, more studies would be necessary to confirm these statements.

Table 5 summaries the structural properties of the different $\text{Na}_3(\text{U,Pu})\text{O}_4$ compounds. Pillon [49] reported also a metastable form, isomorphic with Na_3PuO_4 , in a rhombohedral symmetry. The existence of a low temperature phase $\text{Na}_4(\text{U,Pu})\text{O}_4$ was reported as well and should decompose to $\text{Na}_{3+x}(\text{U,Pu})\text{O}_4$ [49] at around 673-773 K, with a cell parameter of 4.8 Å.

Due to the limited data available on the Na-U-Pu-O system, not so many information are reported with regards to the energy of formation of the $\text{Na}_3\text{U}_{1-x}\text{Pu}_x\text{O}_4$ phase. The calculated value of the oxygen potential for the system Na-U-Pu-O should be very close to those for the system Na-U-O [17] and then plutonium does not influence the formation of the quaternary compound $\text{Na}_3\text{U}_{1-x}\text{Pu}_x\text{O}_4$ at least when the Pu content is below 30%.

For a composition with 20% of Pu, Adamson et al. [14], using calorimetry, determined a relation in the range 700-1200 K as follows:

$$\Delta G_{O_2}^{eq} \left(\frac{J}{mol} \right) = -945000 + 261T \quad (28)$$

For a composition with 20-25% of Pu, Mignanelli et al. [18], using EMF cell, determined fairly a similar relation, in the range 800-1000 K, which is:

$$\Delta G_{O_2}^{eq} \left(\frac{J}{mol} \right) = -949789 + 253T \quad (29)$$

Table 5: Structural proprieties of Na-U-Pu-O compounds

<i>Phase</i>	<i>Symmetry</i>	<i>T (K)</i>	<i>Lattice parameters (Å)</i>	<i>Ref.</i>
$Na_3U_{0.7}Pu_{0.3}O_4$	Tetragonal	873-1173	4.77, 4.77, 4.88	[53]
$Na_3U_{0.7}Pu_{0.3}O_4$	Tetragonal	1123	4.78, 4.78, 4.88	[16]
$Na_3U_{0.7}Pu_{0.3}O_4$	Cubic	823	4.80, 4.80, 4.80	[16]
$Na_{3+x}U_{0.72}Pu_{0.28}O_4$	Cubic	<1273	4.79, 4.79, 4.79	[49]

2.3.1.3 Na-U-O system

Due to the chemical similarity between uranium and plutonium, the Na-U-O system can provide useful information, which can be adopted for the Na-U-Pu-O system. Thus, the Na-U-O ternary system was intensively investigated and data are generally complete. A wide range of sodium uranium oxides forms the Na-U-O system. These are Na_3UO_4 , Na_4UO_5 , Na_2UO_4 , $Na_2U_2O_7$, $Na_6U_7O_{24}$, Na_4UO_4 and $NaUO_3$. Their structural properties [66, 67, 68, 69, 70, 71, 72, 73, 50, 49] are fairly well-known and established up to now.

Table 6 summarizes these proprieties. $NaUO_3$ was subject of investigation over many years [74, 75, 76, 77] because of its pentavalent uranium which is usually rare for uranium compounds in the solid state. The compound shows an orthorhombic perovskite structure with the cell parameters 5.774, 5.905, 9.278 Å [76]. Tetragonal Na_4UO_5 shows a tetragonal symmetry, with cell parameters 7.517Å-4.632Å [72, 78]. More recently, Smith et al. [73, 50] confirmed the existence of the low temperature cubic form $m - Na_4UO_5$, with a lattice parameter of 4.764 Å, which was reported in literature [46] but never verified. The phase is metastable at low temperature (800°C), with disordered fluorite cubic type of structure. Na_2UO_4 , hexavalent as well, has two polymorphs: α and β phases with orthorhombic symmetry, in space group Pbam and Pbca, respectively. The phase transition was measured at 920°C. The structure and phase

transitions of $\text{Na}_2\text{U}_2\text{O}_7$ have recently been reviewed by Smith et al. [50]. The authors confirmed the existence of three polymorphs: the monoclinic α -phase is stable at room temperature and transforms to monoclinic β -phase at the temperature of circa 300°C and to rhombohedral γ -phase between 950°C-1050°C. Since the main compound, formed during the reaction between sodium and MOX fuel under SFR core conditions, is $\text{Na}_3(\text{U}, \text{Pu})\text{O}_4$, the trisodium uranate, Na_3UO_4 , is the compound with major relevance and further explored. Na_3UO_4 was synthesized by Scholder and Gläser [67] for the first time in 1964. They indicated trisodium uranate in a disordered fluorite structure with a lattice parameter of 4.77 Å and space group Fm-3m, but it is still subject of controversy. Kleykamp [65] reported that Na_3UO_4 should have a narrow homogeneity range $\text{Na}_{3-x}\text{U}_{1-x}\text{O}_4$ up to $x = 0.1$ at $\sim 700^\circ\text{C}$. Bartram and Fryxell [66] suggested the existence of a phase $\text{Na}_{11}\text{U}_5\text{O}_{16}$ but it was rejected by Lorenzelli et al. [79]. Marcon et al. [68] found a high temperature phase of Na_3UO_4 , called β , which was confirmed by Lorenzelli et al., later on. They also established that the stable Na_3UO_4 exists in two allotropic forms with a transition at $1075 \pm 25^\circ\text{C}$. The high temperature phase β - Na_3UO_4 was identified as face centered cubic (fcc) and the low temperature α - Na_3UO_4 as tetragonal. Pillon [49, 69] reported the formation of a Na_4UO_4 phase stemming from the direct reaction between UO_2 and Na_2O . This form was believed to be metastable and to exist below $\sim 600^\circ\text{C}$. The structure was described as fcc with a cell parameter of 4.78 Å, very similar to the structure of Scholder and Gläser. Its irreversible decomposition to Na_3UO_4 starts above 600°C with progressive loss of sodium toward the $\text{Na}_{3+x}\text{UO}_4$ composition.

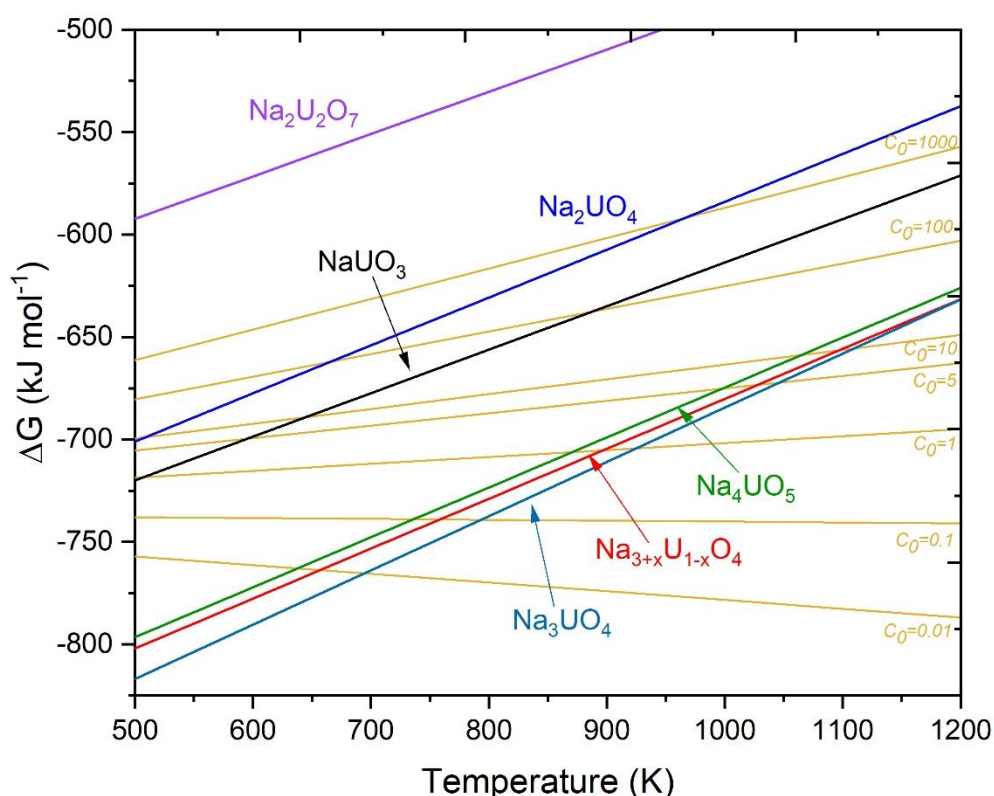


Figure 32: Oxygen potential thresholds for the formation of Na-U-O ternary phases, adapted from [80]. C_0 lines correspond to the potential of sodium containing a concentration of C_0 ppm of oxygen.

Table 6: Summary of structural proprieties of Na-U-O compounds

<i>Phase</i>	<i>Symmetry</i>	<i>Space group</i>	<i>Lattice parameters (Å)</i>	<i>Oxide state</i>	<i>Ref.</i>
$m - Na_3UO_4$	Cubic	Fm-3m	4.77, 4.77, 4.77	V	[65]
$\gamma - Na_3UO_4$	Cubic	Fm-3m	9.56, 9.56, 9.56	V	[68]
$m - Na_4UO_5$	Cubic	Fm-3m	4.764, 4.764, 4.764	VI	[50]
Na_4UO_5	Tetragonal	I4/m	7.517, 7.517, 4.632	VI	[78]
$\alpha - Na_2UO_4$	Orthorhombic	Pbam	9.762, 5.728, 3.495	VI	[70]
$\beta - Na_2UO_4$	Orthorhombic	Pbca	5.808, 5.975, 11.718	VI	[70]
$Na_2U_2O_7$	Rhombohedral	R-3m	3.911, 3.911, 17.857	VI	[81]
$\alpha - Na_2U_2O_7$	Monoclinic	P2/a	12.762, 7.846, 6.889	VI	[71]
$\beta - Na_2U_2O_7$	Monoclinic	C2/m	13.130, 7.939, 6.926	VI	[71]
$Na_6U_7O_{24}$	Rhombohedral	R3m	3.95, 3.95, 17.82	VI	[82]
Na_4UO_4	Cubic	Fm-3m	4.780, 4.780, 4.780	IV	[49]
$NaUO_3$	Orthorhombic	Pbnm	5.774, 5.905, 9.278	V	[76]

More recently, also Matsunaga et al. [23], reported the Na_4UO_4 phase as product of the interaction between UO_2 and sodium containing sodium oxide. Finally, Smith et al. [73] reported that the α form of Na_3UO_4 can accommodate cationic disorder up to 14–18% of sodium on the uranium site, which corresponds to a mixed valence state compound with composition $\text{Na}_3(\text{U}_{1-x},\text{Na}_x)\text{O}_4$ [73]. Instead, up to now, the cubic $m - \text{Na}_3\text{UO}_4$ of Scholder and Gläser is still under discussion. Thermodynamic data of the Na-U-O ternary system are also available in literature and satisfyingly complete. As mentioned before, the crystalline structure of Na_3UO_4 is still subject of controversy and the available data are only coming from the unique batch produced by O'Hare et al. [83, 84, 85]. These data refer to those of the α -phase only, and m - and β -phase are still missing. Recently, Smith et al. [50] reported the data of Na_4UO_5 and confirmed the values of enthalpy of formation of $\alpha\text{-Na}_2\text{U}_2\text{O}_7$ at 298.15 K [86, 87, 88]. Accurate thermodynamic data allow performing a more precise evaluation of the oxygen potential thresholds, which is required for the formation of the sodium uranate phases. A good knowledge of those threshold values is important to better estimate the predominant phases, which can be formed under the core conditions. In our case, it is also important to fix the thermodynamic conditions required to better simulate the real environment of coolant-fuel interaction. Smith et al. [80, 50] reported the calculated oxygen potential thresholds of sodium uranates formation in the temperature range between 300 and 900 °C. Oxygen potential thresholds for the formation of Na-U-O ternary phase are plotted in Figure 32. One should notice that the oxygen concentration needed for the formation of the hexavalent Na_4UO_5 is close to the one of the pentavalent Na_3UO_4 . This aspect needs to be deeper investigated since is of relevance for the safe assessment of the internal storage in a SFR, because fuel disintegration and dissolution into the primary coolant are strongly influenced by the actual reaction product (i.e. the uranium oxidation state).

2.3.1.4 Comparison of Na-U-Pu-O and Na-U-O systems

Finally, to have a comprehensive view of the general thresholds for the formation of the concerned phases in Na-U-O and Na-U-Pu-O systems, we report in Figure 33 the oxygen potential thresholds for the formation of Na_3UO_4 and $\text{Na}_3\text{U}_{1-x}\text{Pu}_x\text{O}_4$ and the correspondent oxygen concentration in liquid sodium. A very high oxygen concentration (higher than 1000 wppm) in liquid sodium is required to allow the formation of Na_2O . This reaction is therefore not possible under the SFR conditions. Nevertheless, in the operation range of temperature (700-900 K in the internal storage) and oxygen concentration (3-5 wppm) in liquid sodium of SFR, the formation of Na_3UO_4 and $\text{Na}_3\text{U}_{1-x}\text{Pu}_x\text{O}_4$ are thermodynamically allowed. The formation of Na_3UO_4 and $\text{Na}_3\text{U}_{1-x}\text{Pu}_x\text{O}_4$ with a Pu content of 20-25% (as measured by Mignanelli et al. [18]) are very close and they can be reasonable approximated.

However, a different Pu content, as well as a different initial O/M ratio, leads to a change of the thresholds, which are not yet well-known and further investigation are needed to establish exactly those thresholds. One should also take into account the state of the fuel, especially if irradiated, may locally change the oxygen availability for the reaction and can induce to several phase formations. Indeed, most of the post irradiation examinations of failed fuel pins indicates $\text{Na}_3\text{U}_{1-x}\text{Pu}_x\text{O}_4$ as the main formed phase, but not the only.

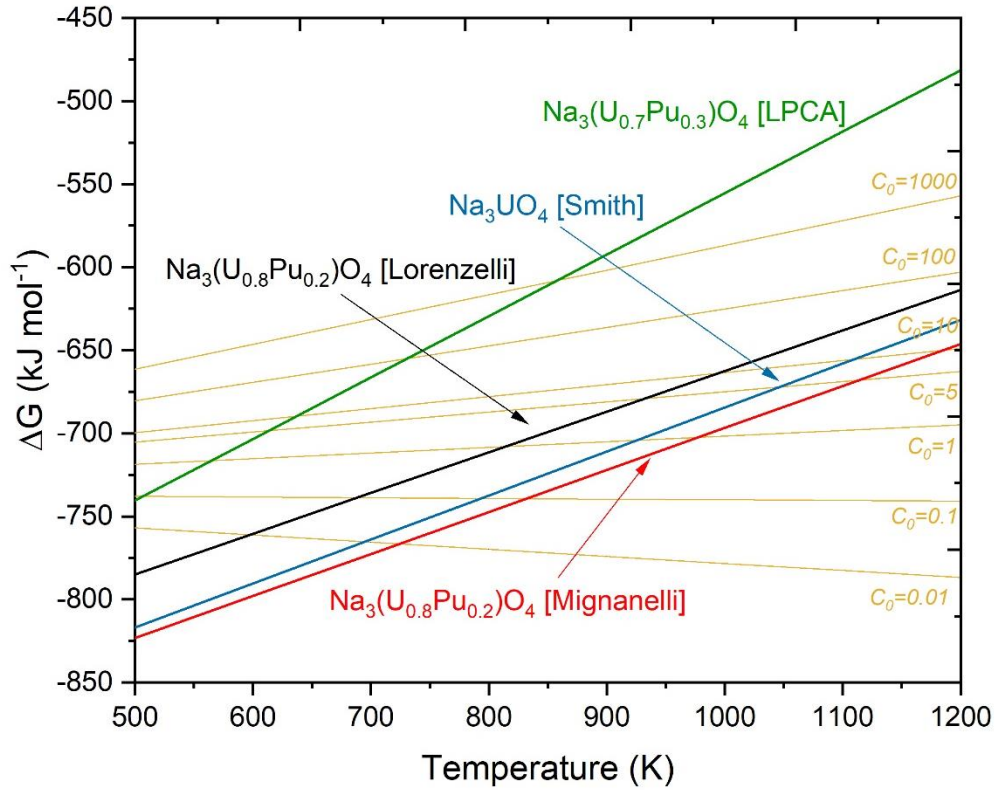


Figure 33: Oxygen potential thresholds for the formation Na_3UO_4 and $\text{Na}_3\text{U}_{1-x}\text{Pu}_x\text{O}_4$ and the correspondent oxygen concentration in liquid sodium in wppm.

2.3.2 Kinetic aspects

There is a lack of knowledge on the reaction kinetic between liquid sodium and nuclear fuel, because only a limited amount of systematic experimental data is available. Up to now, no kinetic data are available for the reaction between sodium and uranium dioxide. On the sodium and mixed oxide reaction kinetics, two main out-of-pile works were performed, between 1970 and 1985, by Housseau [20] and Mignanelli [16] and are hereinafter discussed.

In the kinetic study performed by Housseau et al. [20], the authors focused on the influence of the initial O/M ratio and the Pu content on the formation of the reaction product, as well as on the role of temperature and fission products. The reaction tests were carried out using both pure plutonia PuO_2 and mixed oxide $(\text{U,Pu})\text{O}_2$, with different initial O/M ratios and in the temperature range 600-900 °C. The evaluation of the pellet swelling was made from the results of thickness measurements of the reaction layer after the interaction and is reported as the volume expansion.

The results are illustrated in the right side of the Figure 34. Swelling appears greater when the plutonium content is high and, for the same content, when the O/M ratio is high. For example swellings of pure plutonia PuO_2 , mixed oxide with a high content of Pu (76%) and mixed oxide with 30% of Pu reach 47%, 43% and 9%, respectively for an initial O/M ratio of 2; swelling of

mixed oxide with 30% of Pu with O/M ratio equal to 2.00, 1.95 and 1.91 are about 9%, 5% and 0%, respectively). The temperature does not seem to have an effect on the maximum swelling, even if it has a role in the swelling rate. For example, the swelling rate of mixed oxide with 76% of Pu changes from a strictly decreasing shape at 750°C to a profile exhibiting a maximum (sigmoidal shape of the swelling curve) at 600°C regardless of the O/M ratio). In the composition range of interest for the fuel of SFR, i.e. with a Pu content of circa 30%, in the specific case of an initial O/M ratio of 1.95, the swelling started faster when increasing the temperature even if the final swelling is almost the same. In the same composition, no reaction occurred for an initial O/M ratio of 1.91. The authors concluded that, in the case of fresh fuel, the rate of formation of the reaction product is strongly dependent from Pu content and initial O/M ratio. The reaction is then much faster and greater with higher Pu content or O/M ratio. This correspondence between the Pu and O/M ratio with the reaction production seems to indicate that the driving force for the reaction product formation should be the oxygen availability. Indeed, because of the great capability of Pu reduction, its high content can be accounted as source of oxygen during the reaction. The influence of O/M ratio on the swelling is in good agreement also with the in-pile observations, where it was estimated that per 0.01 change in O/M ratio, the sodium-fuel reaction causes volume increases by circa 1% [12].

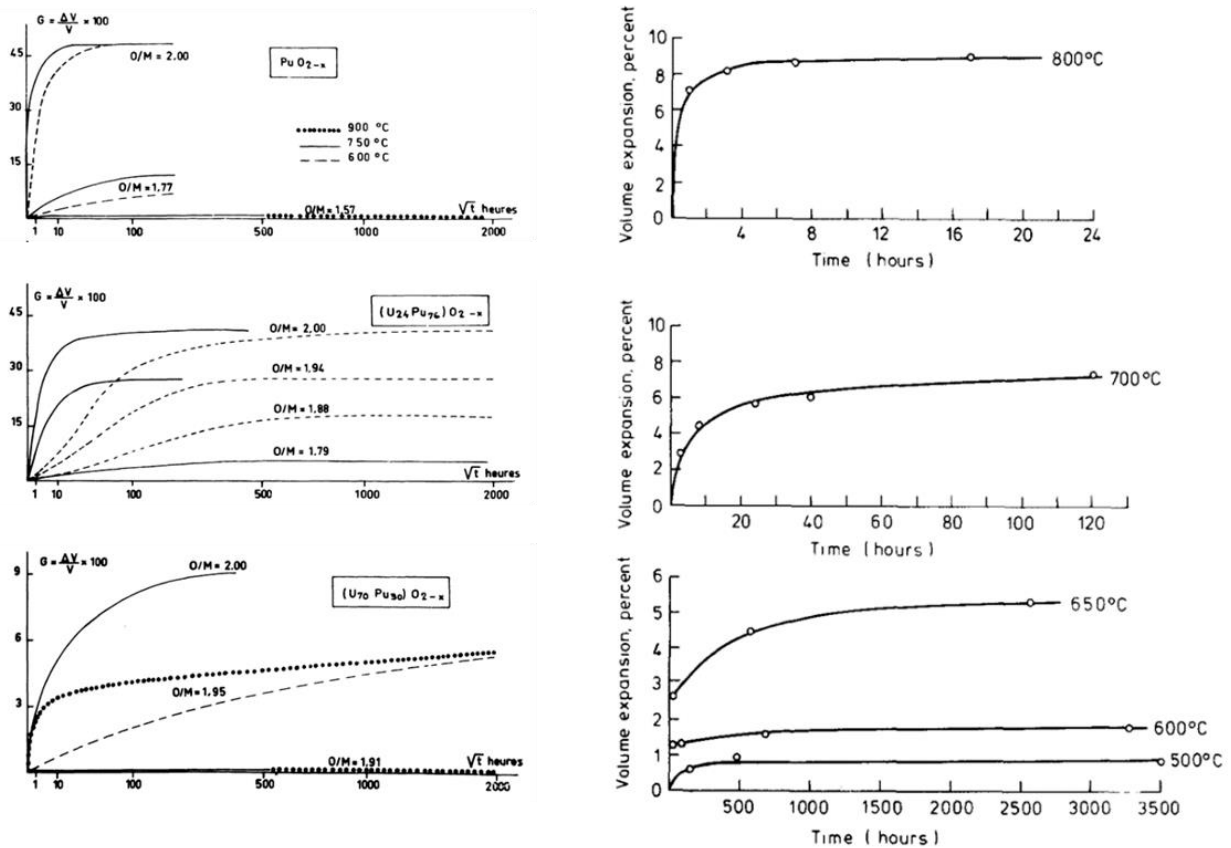


Figure 34: Kinetic curve for out-of-pile experimental tests. Left: Kinetic curves over a broad range of fuel composition and initial O/M ratio [20]. Right: Kinetic curves for the reaction between pure sodium and $(\text{U}_{0.7}\text{Pu}_{0.3})\text{O}_2$ in the temperature range 500-800 °C [16].

The results obtained for mixed oxide (U,Pu)O₂ with 30% Pu and initial O/M ratio of 2, by Mignanelli and Potter [16], in the same temperature range 500-800°C (left side of Figure 34) exhibit an not only on the rate shape but also on the final value of the swelling, the latter increasing when temperature increases. The curves obtained by Mignanelli and Potter seems to demonstrate a parabolic behaviour even if further investigations are needed to confirm this trend. In any case the potential strong influence of the temperature over the reaction rate represents a key point in the building of an accurate model of the sodium-fuel reaction under internal storage conditions and consequently needs to be further investigated.

Since the first interest of the sodium-fuel reaction was the understanding of its evolution under core conditions, several in-pile tests were carried out in the past. In in-pile tests, the swelling rate is usually referred to the diameter variation of the fuel pin, which can be approximatively considered to be caused only by the development of reaction product. The reaction product growth certainly causes the pin volume to increase and one could assume that it also leads to a further opening of the cladding breach, but post irradiation data of failed pins provided circumstantial evidence that the reaction product acted in a plastic manner and did not enlarge the breach [29]. In an attempt to generalize the experimental data, only few empirical relationships on the diameter growth of defected pins as function of time or burnup are reported in literature. A general one is given by [89]:

$$\frac{\Delta d}{d} \% \approx 1.6t^{0.25} \quad (30)$$

where t is the time in minutes. Considering the contribution of the burnup on the diameter growth, the following relationship is given [90]:

$$\frac{\Delta d}{d} \% = 1.66 \cdot 10^{-2} + \exp\left(-\frac{1.17 \cdot 10^5}{a}\right) \quad (31)$$

where a is the burnup in MWd t⁻¹. However, due to the large number of parameters influencing the reaction under irradiation conditions, it is preferable to calculate the final diameter increase for each failed fuel pin individually.

In spite of this, most of the in-pile experimental observations are in agreement with the parabolic growth trend reported in the out-of-pile experiments. Figure 35 shows some of the measured diameter variation of the reaction product formation from out-of-pile and in-pile experiments [12]. Out-of-pile data are usually conservative values when compared with the in-pile ones. The values were obtained for large and small hole-type (CEA values) defects. Obviously, large defects resulted in high-growth values, while small hole-type defects resulted in a more slowly progressing diameter increase. Among all the differences between out-of-pile and in-pile tests, the “freedom” of the pellet in out-of-pile tests against the constrains imposed

by the cladding in the in-pile tests, such as the sodium flow, might be the most significant cause of the discrepancies between the obtained results.

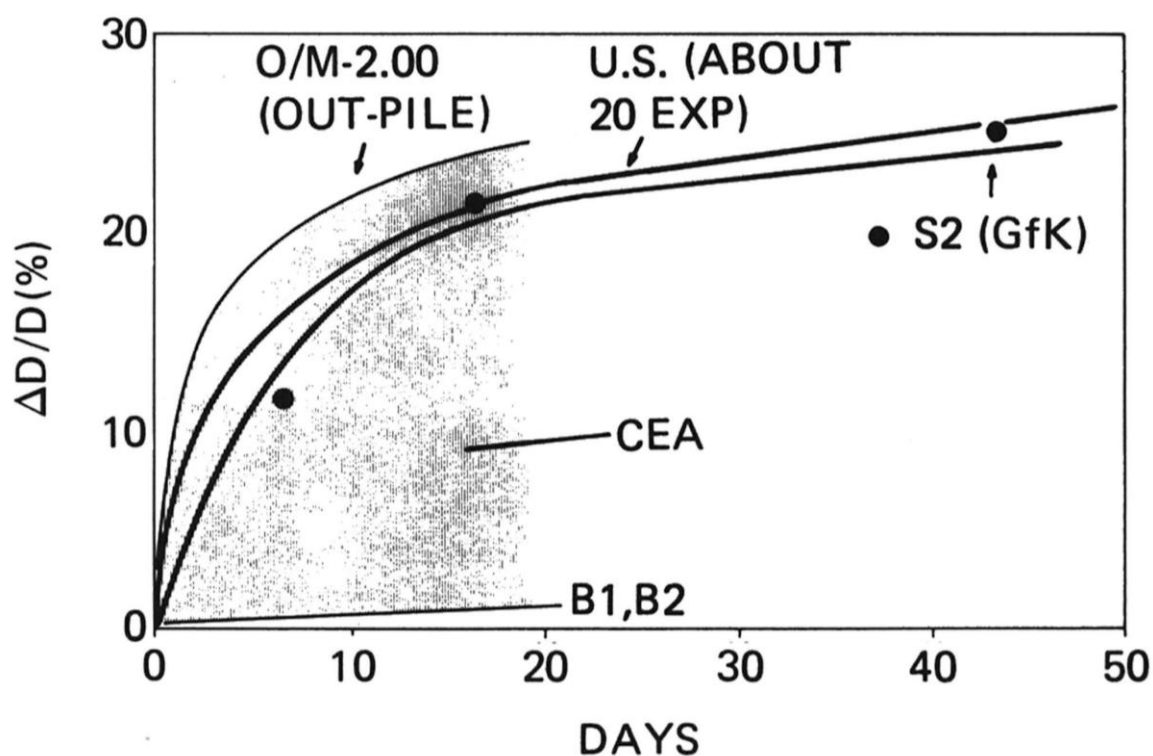


Figure 35: Measured diameter variation of the reaction product formation from out-of-pile and in-pile experiments [12]. The values were obtained for large and small hole-type (CEA values) defects.

The complexity behind the pin failure phenomena does not allow generalizing the evolution of the diameter growth for all the different failed pins. For a realistic kinetic model, indeed, several aspects have to be taken into account, such as O/M ratio distribution, temperature gradients in fuel, reaction surface area and burnup, fuel morphology and cracking, as well as the defect location and size which may impact the extend of the reaction. Moreover, if the oxygen content of the sodium is below the threshold level for the reaction with the fuel, the reaction product could be dissolved and the swollen pin may perhaps shrink. Technically, due to the poor thermal conductivity and low melting temperature of the reaction product, the high heat rating during the reactor operation could also result in a thinner reaction layer compared to the one measured in the post irradiation examination. Consequently, the integral pin swelling will be as well much less. Due to the poor knowledge about the reaction and reaction product properties, we cannot exclude that some changes can be induced in the time between the pin removal from the reactor and the post irradiation examination. The flattening of the temperature gradient in the fuel after operation can perhaps induce the layer to increase because the reaction product may solidify. Nonetheless, if this picture does not properly describe the in-core scenario, it can satisfactorily represent the initial status of the pins in the internal storage.

2.3.3 Sodium diffusion

Although the experiments were performed under different conditions and within a broad range of mixed oxide compositions, the extent of the reaction usually achieves its completion in short time and the reaction rate generally follows a parabolic trend. Consequently, in most of the cases, the reaction is considered as obeying to a diffusion-controlled growth, but no experimental evidences of the species determining the reaction rate are reported in support of the kinetic curves. Under irradiation conditions, the growth rate of the sodium-fuel reaction product should be dependent on the oxygen diffusion from the fuel bulk to the interface between the fuel and the reaction product layer [12] and the oxygen or sodium diffusion through the reaction product layer. Because the diffusion of sodium is usually considered to be relatively slow compared with that of oxygen, except from Blackburn [19], who suggested to consider a complex mechanism behind the sodium-fuel reaction, the diffusion of sodium cations through the layer of reaction product is generally considered as the rate-determining step [12, 21, 28].

Although most of the authors considered sodium diffusion as the rate determining step during the reaction between liquid sodium and mixed oxide based fuel, only few data of its diffusion coefficient are reported in literature. Moreover, these data are only calculated values from the different tests and their accuracies are questionable. Caputi et al. [91] reported a diffusion coefficient of sodium in the order of $10^{-10} \text{ m}^2 \text{ s}^{-1}$. Kleykamp [28] calculated the chemical diffusion coefficient of sodium as $\bar{D}_{Na} = \frac{d^2}{2t}$ by assuming the formed layer $\text{Na}_3(\text{U,Pu})\text{O}_4$ as only single phase.

Here, d indicates the thickness of the product layer and t the time. Table 7 reports the calculated values at different temperatures.

Table 7: Calculated chemical diffusion coefficients of sodium at different temperature

$\bar{D}_{Na} [\text{m}^2/\text{s}]$	$T [\text{K}]$
$3 \cdot 10^{-15}$	873
$2 \cdot 10^{-14}$	1073
10^{-11}	1473

Assuming that the diffusion is activated, then, the chemical diffusion coefficient of sodium will obey the Arrhenius relationship:

$$\bar{D}_{Na} = D_0 \exp\left(\frac{Q}{RT}\right) \quad (32)$$

where Q is the activation energy, which equals to 166 kJ/mol [65] between 800 and 1500K, in good agreement with the one reported by Hosseau [20], R is the general gas constant (8.3144 J K⁻¹ mol⁻¹) and T the absolute temperature (K). However, the evaluation of the apparent activation energy determined by the volume expansions in the temperature range between 650 and 800 °C leads to a value of 335 kJ/mol [16], almost double of the one reported above.

2.4 Conclusion

Trisodium uranate compound is usually assumed to be similar to the one expected for the interaction between mixed oxide and sodium in reactor conditions. Although the thermodynamic of the Na-U-O system was intensively investigate, the formation of the trisodium uranate and its existence as pure pentavalent compound is still under discussion. Moreover, the system Na-U-Pu-O is still uncompleted and is difficult to extrapolate the required data for the modelling. Regarding instead the kinetics aspects of the interaction between oxide fuel and liquid sodium, only few and spread tests were reported in literature. In most of the cases, the reaction rate followed a parabolic regime and the reaction was then assumed to be diffusion-controlled. Diffusion of sodium was considered to be the rate determining step, but no experimental evidence was reported in support of this assumption. Based on the available literature, the current data do not allow answering to the questions previously reported. Indeed, the needed information are not available and the reaction cannot be modelled in a precise and predictive manner. For this reason, additional experimental investigations are needed to further explore the reaction.

3 Research objectives

Ce chapitre présente les objectifs de cette étude, la structure et la méthodologie choisies pour atteindre ces objectifs.

The aim of the present research is to propose a theoretical model, which is capable to predict the evolution of the reaction between liquid sodium and oxide based fuel under the internal storage conditions of the SFRs. As previously described, in order to build the needed model, some basic data are still missed in literature, such as the effective oxidation state of the corrosion layer, nucleation and growth processes. To gain the required information, the present studies was organized in the way to:

1. Obtain the needed information on a system easy to study, i.e. uranium oxide-sodium system rather than on the mixed oxide-sodium system.

The study of this system was developed to:

- a) Establish the uranium oxidation state in the corrosion layer. Indeed, the synthesis route used for the preparation of the trisodium uranate compound did not allow exactly establishing its structural proprieties so far. Its existence, as pure pentavalent uranate compound, is still under discussion [80]. Most of the synthesis reactions were carried out by direct reaction between stoichiometric UO_2 , or hyper-stoichiometric UO_{2+x} , and sodium oxide/sodium peroxide in the required ratio. However, a reductive atmosphere, by using an excess of metallic sodium as done, for instance, by O'Hare [83], is probably needed to get a pure pentavalent compound.
- b) Explore the nucleation process and understand the reaction. In particular, to know if the nucleation process results in an instantaneous process. Additional features such as the verification of whenever the reaction between sodium and oxide based fuel can proceed along the grain boundaries were also investigated. Indeed, the dissemination of fuel into the primary coolant is strictly linked with the grain boundaries attack. In contradiction to what was observed by Mignanelli and Potter [15], Matsunaga et al. [23] reported the grain boundaries penetration by sodium even using stoichiometric UO_2 . The reduction of stoichiometric UO_2 under the experimental conditions of Matsunaga et al. is unlikely. Thereby the absence of oxygen at the grain boundaries should not lead to the formation of the reaction product at the grain boundaries. This aspect needs additional investigations to be clarified.
- c) Study of the growth process, with particular regard to type of growth and the determination of the rate determining step. As previously reported, all the kinetic data in literature refers to mixed oxide fuel and no kinetics data are available so far for the reaction between liquid sodium and uranium dioxide.

2. Check that the uranium oxide behaves at the same manner of mixed oxide. Usually, the proprieties and the behaviour of the trisodium uranate are extended to those of the trisodium uranoplutonate. From a kinetic point of view, further investigations are needed to establish whether the two can be effectively considered as similar. The knowledge on the sodium and mixed oxide reaction kinetics is limited to the out-of-pile works of Housseau [20] and Mignanelli [16]. Nevertheless, although the available experiments were performed under different conditions and within a broad range of mixed oxide compositions, the extent of the reaction usually achieves its completion in short time and the reaction rate generally follows a parabolic trend. Consequently, in most of the cases, the reaction is considered as obeying to a diffusion-controlled growth, but no experimental evidences of the species determining the reaction rate are reported in support of the kinetic curves. Except from Blackburn [19], who suggested to consider a complex mechanism behind the sodium-fuel reaction, most of the authors [12, 21, 28] considered the diffusion of sodium cations through the layer of reaction product as the rate determining step during the reaction between liquid sodium and mixed oxide based fuel. Diffusion of sodium is usually considered to be relatively slow compared with that of oxygen. However, only few data of sodium diffusion coefficient are reported in literature. These data are only calculated values from the different tests and their accuracies are questionable. Besides, these data cannot be compared to any other diffusion coefficient, such as oxygen, uranium or plutonium diffusion through the layer of $\text{Na}_3(\text{U,Pu})\text{O}_4$, since no data are available.
3. Make reasonable hypotheses in order to build the model.

Experimentally, the points above described were explored through:

- i. Surface studies in order to assess of the oxidation state of the corrosion layer (point 1.a)). These studies were carried out through the interaction between thin films of sodium and uranium oxide, under ultra-high vacuum. The characterization was done by X-ray Photoelectron Spectroscopy (XPS), since this technique is known to be one of the most useful technique to get the oxidation state near the surface.
- ii. Compatibility tests, i.e. interaction tests using closed capsule in which the oxygen concentration was fixed at the beginning of the interaction to allow investigating the nucleation process (the point 1.b). Through this study, the early stage of reaction was analyzed and were achieved significant information concerning the reaction features.
- iii. Kinetics studies, i.e. interaction tests using closed capsule under fixed potential oxygen to investigate the growth process (point 1.c).

The compatibility tests and kinetic studies (described in ii. and iii., respectively) were carried out even for mixed oxide fuel (MOX), with a Pu content close to 30%, to understand the similarity and difference with uranium oxide (point 2). Finally, based on the collected experimental data, hypothesis (point 3.) were extrapolated and a theoretical kinetic model was proposed using the heterogeneous kinetics formalism.

4 *Experimental and characterization methods*

Les méthodes expérimentales utilisées pour obtenir les données nécessaires sont décrites dans ce chapitre : X-Ray Photoelectron Spectroscopy (XPS), X-Ray Diffraction (XRD) and Grazing Incidence X-Ray Diffraction (GIXRD), Scanning Electron Microscopy (SEM) and Energy Dispersive X-Ray Spectroscopy (EDX), Focus Ion Beam (FIB) and Transmission Electron Microscopy (TEM). On présente aussi les laboratoires haute activité du JRC, où le travail expérimental a été réalisé, ainsi que la méthode de préparation des échantillons, les appareils de caractérisation utilisés et quelques rappels de physiques.

Accordingly to the objectives of the present study, the experimental investigations of the reaction between oxide fuel and liquid sodium were focused on the improving the understanding of reaction features. Particular regard was given to the determination of the oxidation state of the uranium atoms in the corrosion layer and the establishment of the nucleation and growth process. The experimental approach and the characterization methods used in the present studies are herein described.

4.1 *Surface studies*

As previously reported, the corrosion layer which forms due to the interaction between uranium or mixed oxide fuel is expected at the periphery of the fuel pellets. In order to investigate the oxidation state of such superficial corrosion phase, the most useful experimental method is the surface study.

In the present studies, the preparation of thin films and their characterization were carried out in-situ using the Labstation developed at JRC-Karlsruhe. The Labstation is shown in Figure 36. The main advantage of the Labstation is the modularity. The machine is indeed composed of different chambers, which are kept under Ultra-High Vacuum (UHV), at pressure of 10^{-9} - 10^{-11} mbar.

The Labstation is a unique equipment at JRC Karlsruhe thanks to some extensions, e.g. the sputter source for the film preparation and modifications, which were added to fulfil the experimental requirements. The sample holders are loaded from the ambient to ultra-high vacuum atmosphere via the load lock chamber. The latter was specially designed to perform multiple sample handling and to limit the air contamination of the system.

Samples are mounted on specific sample holders and transferred between different chambers through a linear transfer chamber (of about 7 m long and represented in light yellow in the schematic view) using a transport wagon with five sample loading positions (red).

The transport wagon is driven by an external magnet and controlled by a computer program. Each chamber is connected to the central chamber through a valve. In this way, the chambers can be isolated from the central channel individually. A transfer rod is mounted on each chamber to allow recuperating the sample holder from the linear transfer. The preparation chamber is shown in Figure 37. There, thin films of uranium oxide UO_{2+x} were prepared by a

direct current (DC) reactive sputtering from a uranium metal target in a gas mixture of Ar (6N) and O₂ (6N). The uranium target voltage was fixed at -700 V. Thin films were deposited for 100 up to 300 seconds at room temperature on polycrystalline gold substrates. The thickness of the uranium oxide film was estimated by comparing the intensity of the Au4f (substrate) and U4f (overlayer) photoemission lines. A continuous overlayer was assumed, without interdiffusion or extended island formation and an inelastic mean free path of about 1.79 nm and 2.14 nm for U4f and Au4f lines, in the UO₂ overlayer respectively [92].

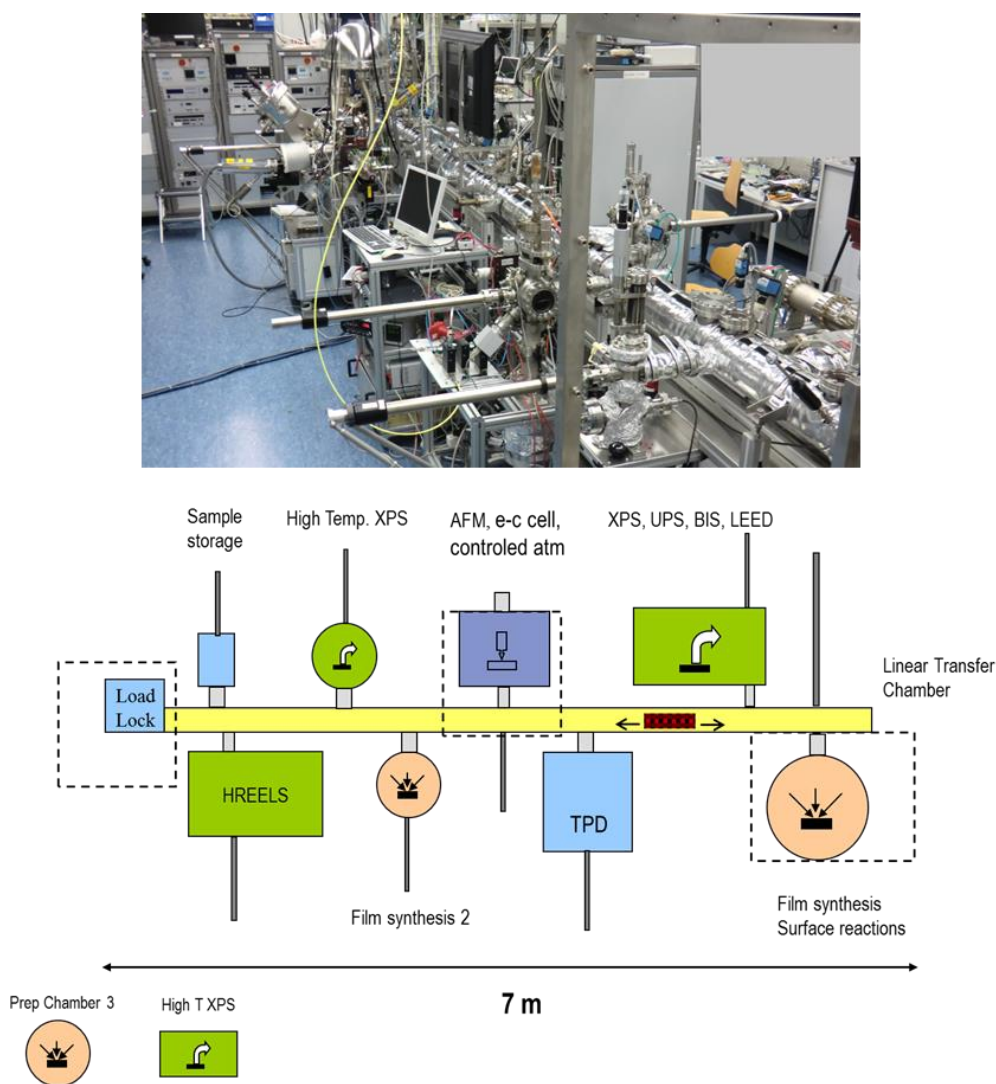


Figure 36: Surface analysis Labstation at JRC-Karlsruhe

Hyper-stoichiometric uranium oxide UO_{2+x} ($0 < x \leq 1$) films were produced by further oxidation of the deposited uranium oxide films with atomic oxygen, produced by an Electron Cyclotron Resonance (ECR) Plasma Source Gen I from Tectra GmbH, Frankfurt/M.

The atom flux was $>10^{16}$ atoms cm⁻² s⁻¹, corresponding to an exposure of roughly 10 Langmuir s⁻¹ (i.e. 10⁻³ Pa O). on the other hand, pure stoichiometric uranium oxide was produced by further reduction of the initial slightly hyper-stoichiometric oxide film, as deposited in the

preparation chamber. The films were then reduced by exposure to atomic hydrogen produced in the same ECR source, previously described, for 600 s at 673 K. In this way, the uranium oxide stabilized as stoichiometric UO_2 since all the surplus oxygen reacts with atomic hydrogen. Figure 38 shows the surface treatment and characterization chambers, left and right, respectively.

In the surface treatment chamber, the substrate was usually cleaned by Argon ion sputtering (3 keV) for 5 min and subsequently annealed at 573 K for 5 min. This step allowed getting a substrate free of contamination (carbon). The plasma in the diode source was maintained by injection of electrons of 25–50 eV energy (triode setup), allowing working at low Argon pressure in absence of stabilizing magnetic fields.

Moreover, for this work, an electron beam evaporator from FOCUS was mounted in order to allow depositing metallic sodium by evaporation. The metallic sodium (Aldrich, 99.9%) product was carefully cleaned with Hexane (Sigma Aldrich, 95%) to remove the mineral oil, in which sodium is stored, and cut in small pieces to be mounted in the electron-beam crucible.

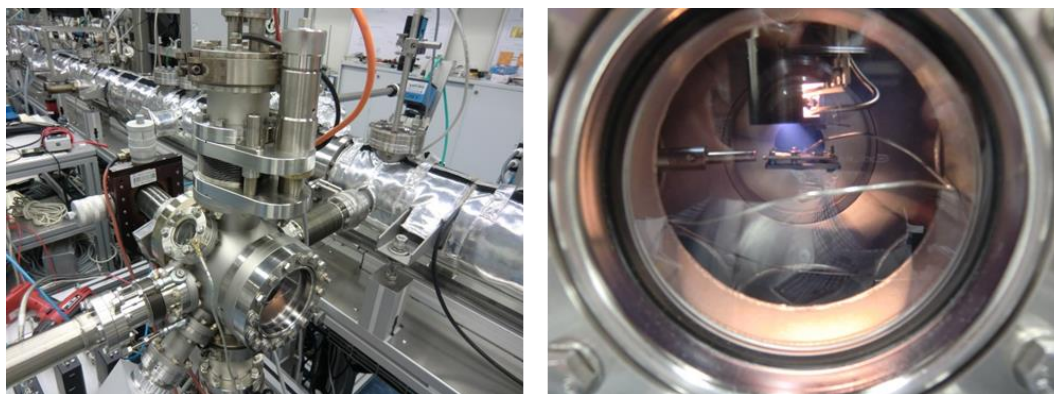


Figure 37: Preparation chamber. Left: view of the thin film preparation chamber. Right: detailed view of the chamber with the uranium oxide source on.

Due to the reactivity of sodium with alumina, a tungsten crucible of 250 mm^3 was used. The applied heating power was 15 W. The chamber was pumped down rapidly to remove the residual moisture bound to sodium. Then, the evaporator was gently heated to 393 K under ultra-high vacuum and kept at constant temperature for several hours. After 24 h of chamber baking, the electron-beam was switched on and the crucible was further heated starting with 1 W heating power.

The acceleration voltage corresponded to 1 kV, with a sample/crucible distance of 200 mm. The beam intensity was measured by the ion current (ionization of sodium atoms by the heating electrons), with a total evaporation amount of 10 mA s (flux time).

The thin film characterization was performed in the characterization chamber by surface spectroscopy technique, i.e. X-ray Photoelectron Spectroscopy (XPS).

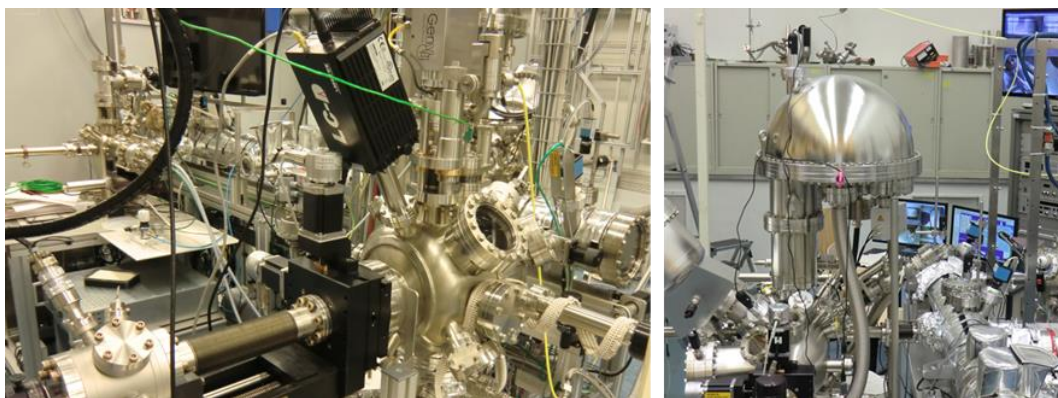


Figure 38: Left: surface treatment chamber. Right: Characterization chamber with the view of XPS device.

4.2 Interaction tests using closed capsule

The handling of both radioactive materials, such as Uranium and Plutonium, and extremely reactive chemicals, such as metallic sodium, required the use of dedicated equipment. To allow dealing with both actinides elements and metallic sodium, the experiments described hereafter were carried out in the Fuels and Materials Research laboratories of JRC-Karlsruhe.

The metallic sodium was handled exclusively in argon-filled glovebox, as shown in Figure 39. The gloves of the box were made of Hypalon material resisting to chemicals and relatively high temperatures. The atmosphere of this glovebox was continuously monitored via an oxygen sensor.

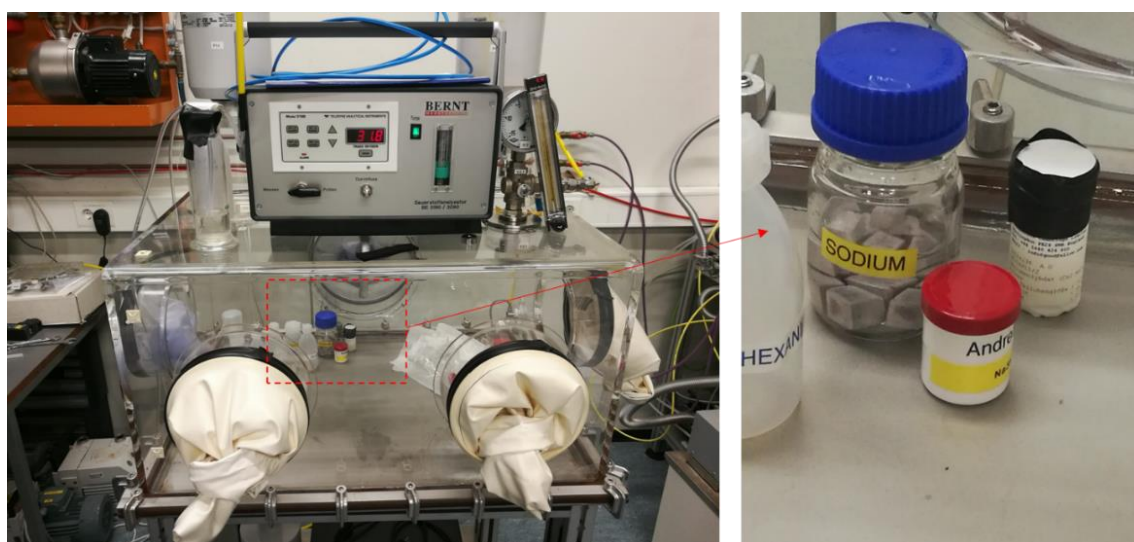


Figure 39: Left: Dry glovebox for the handling of reactive metallic sodium. Right: Detailed view of metallic sodium in mineral oil.

In order to comply to the ALARA radiation safety principle, i.e. to receive As Low As Reasonably Achievable radiation, when handling radioactive material, the minimization of radiation doses was achieved by reducing the time of exposure to the radiation source, increasing the distance to radiation source and using appropriated barriers, i.e. shields such as plexiglas and lead (for β and γ -rays, respectively).

The uranium and plutonium samples were handled exclusively in shielded glove boxes under high purity argon or nitrogen atmosphere. Figure 40 shows a shielded glovebox in the Minor Actinides (MA) laboratory of JRC-Karlsruhe, equipped with tele-manipulators.

The so-called hot laboratories required a period (of about three months) of formation and training before independent working inside the controlled area was possible. This formation period was complemented with a dedicated test on the regulations to ensure the compliance with safety procedures of work in the laboratories.

The transfer of samples between glove boxes required the so-called bag-in and bag-out procedures. These procedures were performed wearing a particulate respirator mask and following specific safety procedures, as previously mentioned. A radioprotection office was present at the JRC-site to ensure a prompt intervention in case of incident. The work in the laboratories was thereby allowed between 8-12 and 13-16 o'clock only, when the radioprotection office was present.



Figure 40: Left: Minor actinides cell equipped with tele-manipulators. Right: view of the calcination furnace for MOX and sodium interaction studies.

4.2.1 Sample preparation

4.2.1.1 UO₂ samples

Sintered pellets of UO₂ were prepared in-situ, using commercial UO₂ powder from the JRC-Karlsruhe stock. The powder was pressed into pellets using a bi-directional press at 550 MPa.

The diameter of each pellet was circa 5.4 mm and the thickness circa 2 mm. Finally, the pellets were sintered at 1650°C under Ar/H₂ atmosphere (4% H₂) for 8 hours.

In addition to the polycrystalline pellets, single crystals of uranium oxide, UO₂, were used in the present study with the aim to investigate the effect of grain orientation on the extent of the reaction product. The uranium oxide single crystals were retrieved from a macroscopic single crystal. The latter were made during out-of-pile experiments simulating a severe accidents with core melt-down, which were performed at the JRC-Ispira Furnace And Release Oven (FARO) [93] in 1987.

Slices were cut off selecting the $\langle 001 \rangle$, $\langle 011 \rangle$ and $\langle 111 \rangle$ crystal lattice directions. Single crystal orientation was established using an X-ray Laue camera. The final orientation of the crystals had a precision within one degree. The crystals were characterized by a block-shape with a thickness of about 2 mm and 5 mm length.

Single crystals and polycrystalline (pellet) samples were characterized by electron scanning microscopy to check their initial status. Figure 41 left and right illustrated the surface morphology of the unpolished and polished single crystals, respectively. The unpolished samples showed a rough surface as result of the cut process, after the orientation. The fine-polished samples exhibited a flat surface on which no significant damages were observed. Polycrystalline uranium oxide surface and cross view are shown in Figure 42 left and right, respectively. The pellets featured grains within a range size of 3 and 20 μm . The characterization was made through the measurements of the grains, since grain boundaries were visible. Moreover, the uranium oxide pellets were free of significant fabrication faults, either on the surface and the cross section.

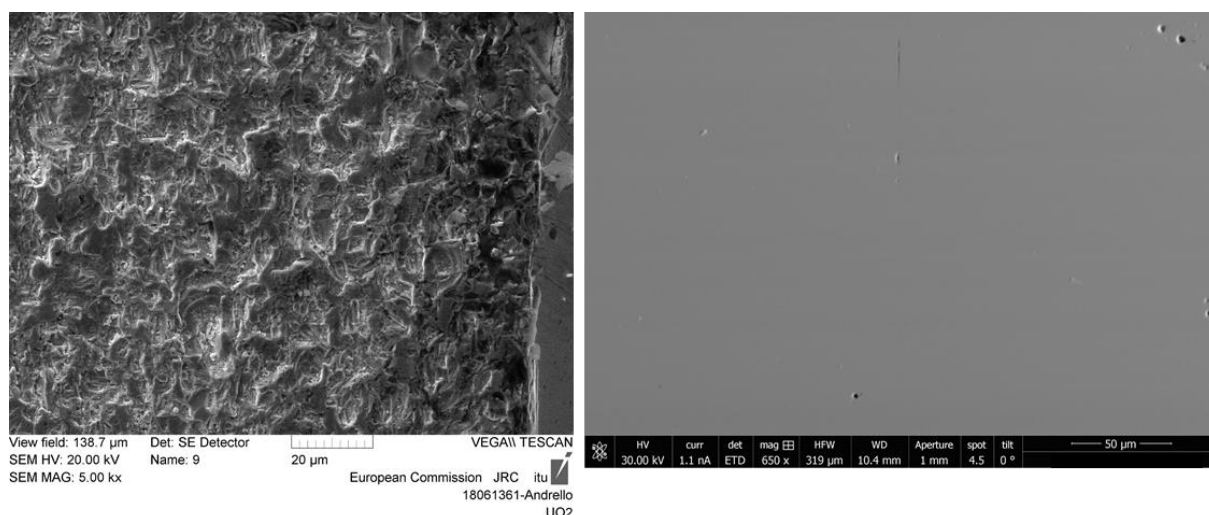


Figure 41: Single crystal surface view. Left: Rough surface after the cut. Right: Fine-polished surface.

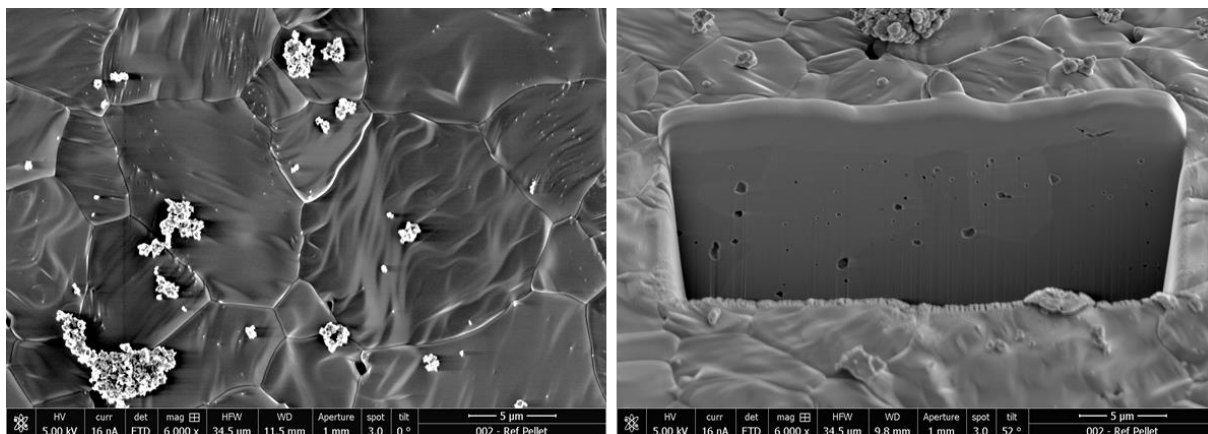


Figure 42: UO_2 pellets after the sintering. Left: surface view. Right: cross section view.

4.2.1.2 $\text{U}_{1-x}\text{Pu}_x\text{O}_2$ pellets

Uranium plutonium mixed oxide fuel with a plutonium content higher than 30% is the target fuel of the future SFRs. Thereby, to comply with such characteristic, MOX powder was prepared in-situ and pressed into pellets. The synthesis of the MOX powder was made by the sol-gel external gelation process. This technique is usually recommended because gives a homogeneous solid solution [94] and produces polydisperse beads, which can directly be pressed into pellets and do not require milling before sintering.

To produce the MOX solution, we dissolved uranyl nitrate in water and PuO_2 in concentrated nitric acid and then we mixed the two solutions in the desired ratio. Droplets were obtained by passing the solution through a high-speed rotating cup, illustrated in Figure 43 (left). The droplets were then collected in an ammonia bath where actinide hydrolysis took place. The formed particles were washed, dried and calcined at 700 °C under air and at 800 °C under Ar-4\%H_2 . The resulting powder was pressed at 550 MPa into pellets using a bi-directional press. The diameter of each pellet was circa 5 mm and the thickness circa 2 mm, with a weight of approximately 0.4 g. The pellets were then sintered at 1600 °C for 8 h under an atmosphere of Ar-4\% H_2 plus 1500 ppm H_2O to get stoichiometric $\text{U}_{1-x}\text{Pu}_x\text{O}_{2.00}$ samples.

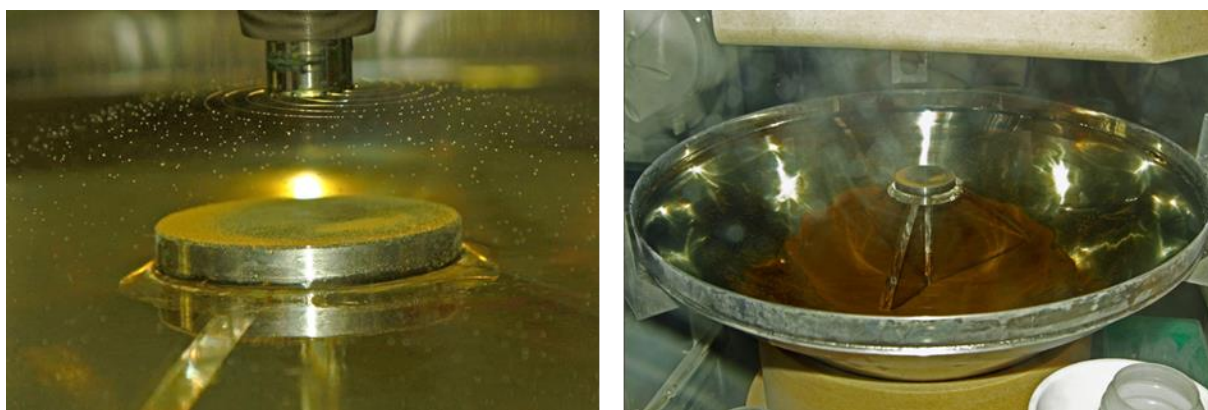


Figure 43: Mixed oxide powder fabrication.

Designations of the sintered mixed oxide pellet are summarized in Table 8. After the sintering, one pellet of the produced batch was crushed into powder and characterized by XRD. Figure 44 shows the XRD pattern of $U_{1-x}Pu_xO_{2.00}$.

The result shows the formation of a single phase. The homogeneity and crystallinity of the material can be clearly seen from the symmetry and the low full width at half maximum (FWHM) of the diffraction peaks, even at high angles. The Rietveld refinement of the diffractogram gives a lattice parameter of 5.446 Å. The Pu content was established by Vegard's law as follows:

$$a_{A_{1-x}B_x} = (1 - x)a_A + xa_B \quad (33)$$

where $a_{A_{1-x}B_x}$, a_A and a_B are the lattice parameters of the solid solution and the pure constituents, respectively, and x is the molar fraction of B.

The obtained value is consistent with the formation of stoichiometric $U_{0.68}Pu_{0.32}O_{2.00}$, in good agreement with the desired Pu content > 30%. Figure 45 reports the plot of the lattice parameter as function of the Pu/(U+Pu) ratio and the corresponding value obtained in our study.

Table 8: MOX sample designations and basic data

<i>Sample n°</i>	<i>Diameter (mm)</i>	<i>Height (mm)</i>	<i>Mass (g)</i>	<i>Geometrical density (g cm⁻³)</i>	<i>Theoretical density (TD%)</i>
NAINT12	5.10	0.77	0.16	-	-
NAINT13	5.05	1.98	0.41	10.28	93.49
NAINT14	5.05	1.95	0.40	10.25	93.18
NAINT15	5.05	1.94	0.40	10.19	92.60
NAINT16	5.04	2.08	0.42	10.22	92.88
NAINT17	5.04	2.11	0.43	10.17	92.49

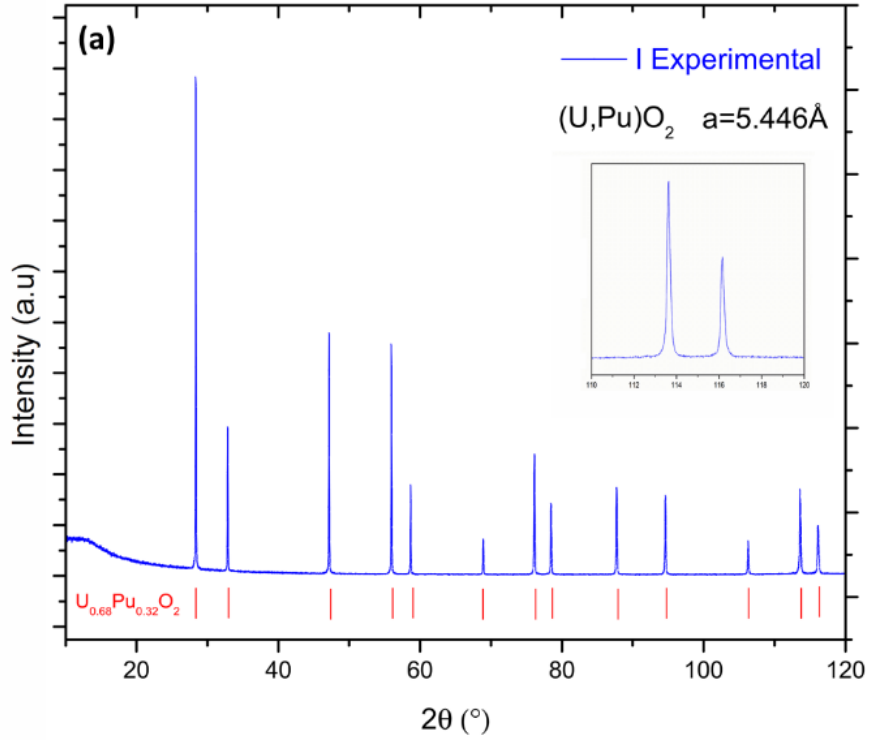


Figure 44: XRD pattern of the sintered MOX showing the formation of a single phase with a lattice parameter of 5.446 Å.

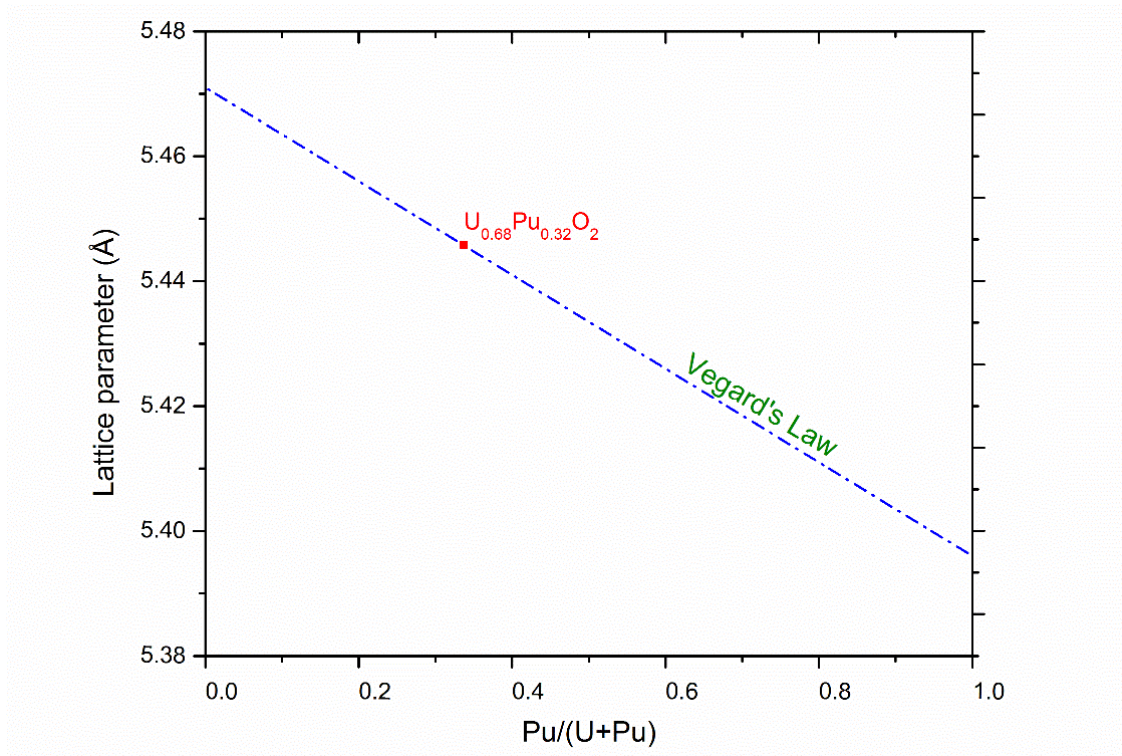


Figure 45: Plot of the lattice parameter as function of the Pu/(U+Pu) ratio according to Vegard's law and the calculated value, corresponding to stoichiometric $U_{0.68}Pu_{0.32}O_{2.00}$.

In order to establish the initial status of the samples, fresh MOX pellets were characterized through ceramography. Two mixed oxide pellets were embedded in resin and polished. The samples were then analyzed through scanning electron microscopy. Micrographs were acquired at different locations and magnifications. The inner zone of the pellet appeared in general free of significant damages. Nevertheless, at the external zone of the pellets, several faults were observed. An example is illustrated in the scanning electron micrographs of the fresh mixed oxide, in Figure 46. The faults were characterized by an elongation from 20 up to 400 μm and were mainly attributed to the fabrication processes. At the external surface, moreover, the appearance of open grain boundaries was also observed, as shown in Figure 47.

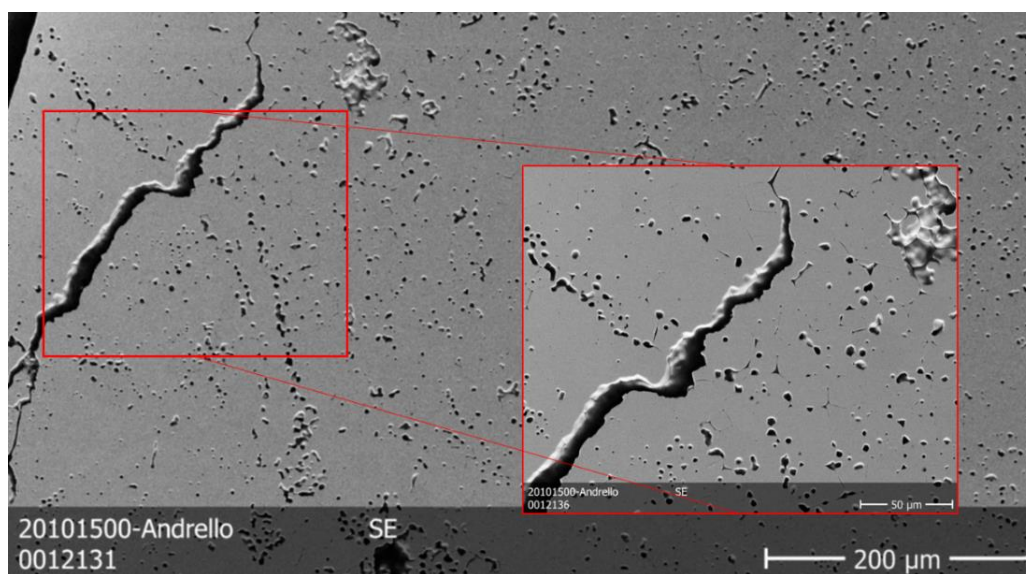


Figure 46: Ceramography of Fresh MOX. The sample showed the presence of fabrication faults.

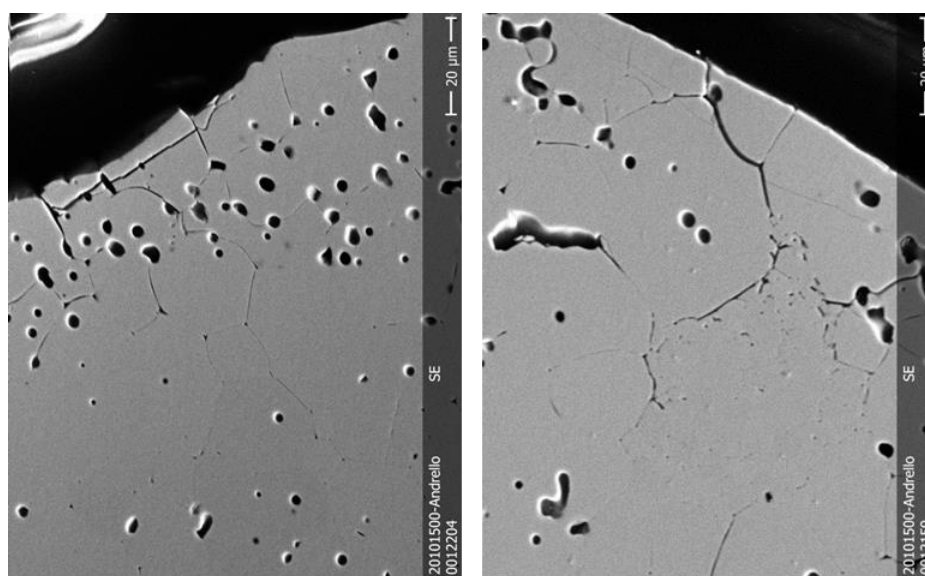


Figure 47: View of the near surface zone of fresh MOX. Presence of open grain boundaries.

4.2.2 Imposed oxygen potential

As mentioned in 2.3.1.1, the reaction between sodium and fuel occurs due to the presence of oxygen impurities rather than by the liquid sodium itself. The key factor for the reaction to proceed is then to keep the concentration of oxygen dissolved in liquid sodium. In order to systematically investigate the growth of the corrosion layer as function of time, a test set-up was created where the oxygen potential was kept constant during the whole duration of the interaction test. The used system was characterized by a closed capsule in which no continuous flow of oxygen could be imposed. Thereby, in the present study, in order to supply oxygen and keep its concentration at a constant value during the whole duration of the tests, a solid oxygen buffer was employed. The buffering effect was achieved through the oxygen depletion of the buffer material, which led to the oxygen potential stabilization at the thermodynamic equilibrium of the dissociation reaction of the buffer at the given temperature. The stabilization of the oxygen potential inside the liquid sodium was preserved under the condition, that the oxygen buffer was sufficiently large compared to the consumed oxygen during the interaction test and did not deplete completely. Moreover, the buffer had also the aim of reproducing a similar environment of the internal storage, where the concentration of oxygen dissolved in liquid sodium is maintained at about 5 ppm. Among the investigated materials, the one which complied best with these needed was sodium niobate in the form of Na_3NbO_4 . The corresponding Gibbs energy of reaction was of about -675 kJ mol^{-1} at 973 K. A thermodynamic assessment showed that sodium niobate should impose thermodynamic conditions close to those in the internal storage facility, i.e. circa 10 ppm at 973 K, and allow forming the expected phase of trisodium uranate in the form of Na_3UO_4 , as illustrated in Figure 48. However, based on the calculated thresholds, at the temperature of interest of 973 K, the formation of additional phases could be allowed as well.

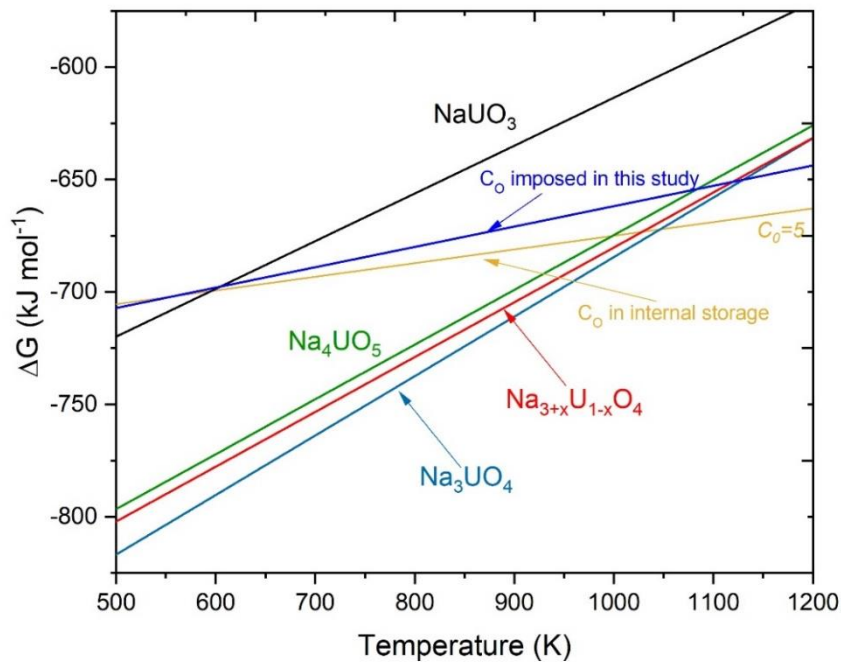


Figure 48: Oxygen potential thresholds for the formation of Na-U-O ternary phases. Oxygen levels in liquid sodium (C_0) and oxygen potential imposed by the Na_3NbO_4 buffer (Blue line).

4.2.3 Sodium niobate buffer preparation

The sodium niobate buffer Na_3NbO_4 was produced by grinding sodium oxide together with niobium powder in a $(\text{Na}_2\text{O}:\text{Nb}) = (1:1)$ ratio. Several small batches of the mixture were then introduced into an alumina container and heated in air at 973 K for 10 hours. A second heat treatment was performed to improve the crystallinity of the compound. Sodium niobate (Na_3NbO_4) was obtained, as confirmed by the XRD diffraction pattern showed in Figure 49. Na_3NbO_4 showed a monoclinic symmetry, in the space group $C2/m$ and with lattice parameters of $a=11.136 \text{ \AA}$, $b=13.012 \text{ \AA}$ and $c=5.763 \text{ \AA}$. The sodium niobate powder was characterized by a white color. The powder was pressed into disks (inset of Figure 49) to simplify the handling and to not scatter the powder during the interaction tests.

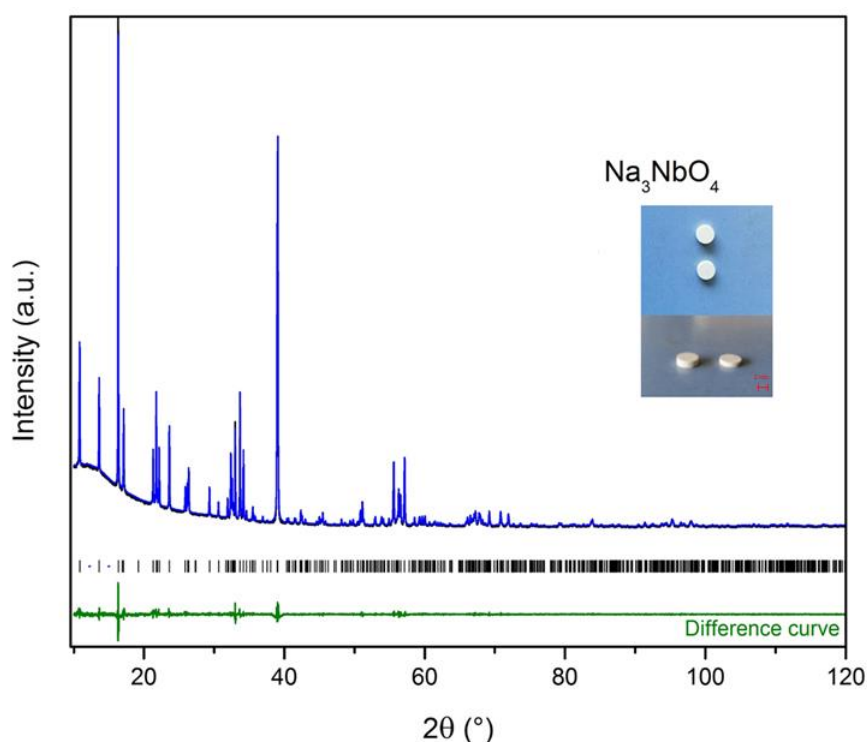


Figure 49: XRD patter of the Na_3NbO_4 buffer for stabilization of the oxygen potential. View of the disks after pressing.

The compound was afterwards stored in an uncontaminated glove box, under high purity argon atmosphere, in order to avoid any contaminations, which may affect the reaction. Since zirconium is known to be an oxygen getter material, the efficiency of the sodium niobate buffer was firstly tested through interaction tests using either zirconium foil and like-disk shape samples. The tests were performed under the same conditions of the fuel interaction tests, i.e. 973 K at the representative time of 48 hours. The tests resulted in the pulverization of the zirconium foil and in the formation of more than 100 μm thick oxide layer on the zirconium bulk sample. As will be later discussed, uranium and mixed oxide reaction with sodium in the same experimental leads to a much smaller quantity of corrosion products (around 5 μm thick

layer). This result indicates that the buffer can efficiently release oxygen. Therefore, the oxygen release from the buffer is not the rate determining of the reaction of uranium or mixed oxide corrosion. About 0.5 g of sodium niobate were added to metallic sodium. This amount was enough to transform completely uranium and mixed oxide into trisodium uranate and uranoplutonate, respectively. However, the complete transformation into sodium uranate was not expected, but this ensured a sufficient supply of oxygen during the test duration. In this way, the oxygen potential was kept constant during the whole interaction test.

4.3 Experimental set-up

The interaction tests were carried out under static conditions, i.e. in stagnant liquid sodium without relative movement of the sodium and the specimen. Metallic sodium was loaded into a capsule in a dry glovebox and under an inert-atmosphere, to keep the impurities, especially oxygen, at the minimum. Each capsule was prepared when the oxygen concentration in the glovebox was below 10 ppm. The heat treatment took place in a tubular furnace, which was constituted by a vertical quartz tube in the case of the interaction tests between mixed oxide and sodium interaction, as illustrated in Figure 40 (right). For the interaction tests between uranium oxide and sodium, the used furnace was constituted by a horizontal quartz tube and it is illustrated in Figure 50(left). The capsule was held isothermally at a given temperature and for a given time. Two capsule designs were used and are herein briefly reported. Figure 51 shows both designs of the capsule. The preliminary tests of interaction between stoichiometric uranium oxide and sodium were performed using stainless-steel capsules, which were divided into two chambers by a stainless steel cross. The cross was fixed inside the capsule by welding. For each test, metallic sodium (Aldrich, 99.9%) was cut in slides, which were placed into the upper chamber. Before the cutting, metallic sodium was carefully cleaned with Hexane (Sigma Aldrich, 95%) to remove the mineral oil, in which sodium is stored. The uranium oxide sample was inserted into the lower chamber and the capsules were placed into a furnace in an upright position.



Figure 50: Left: Calcination furnace for the interaction tests between UO_2 and sodium. Right: detailed view of the capsule before the interaction test.

During heat-up, the sodium melted and flowed into the lower chamber coming in contact with the sample and allowing the reaction. However, by using this type of capsule, we experienced loss of sodium during the interaction tests, which resulted in undesirable effects on the furnace. Therefore, the capsule design was modified by elimination of one end and improving its tightness. Interaction tests between uranium oxide or mixed oxide and sodium for kinetics studies were then performed using a stainless steel capsule, which was constituted by a single chamber. For each test, the fuel sample was placed at the bottom of the capsule and slides of metallic sodium were then placed on top of it.

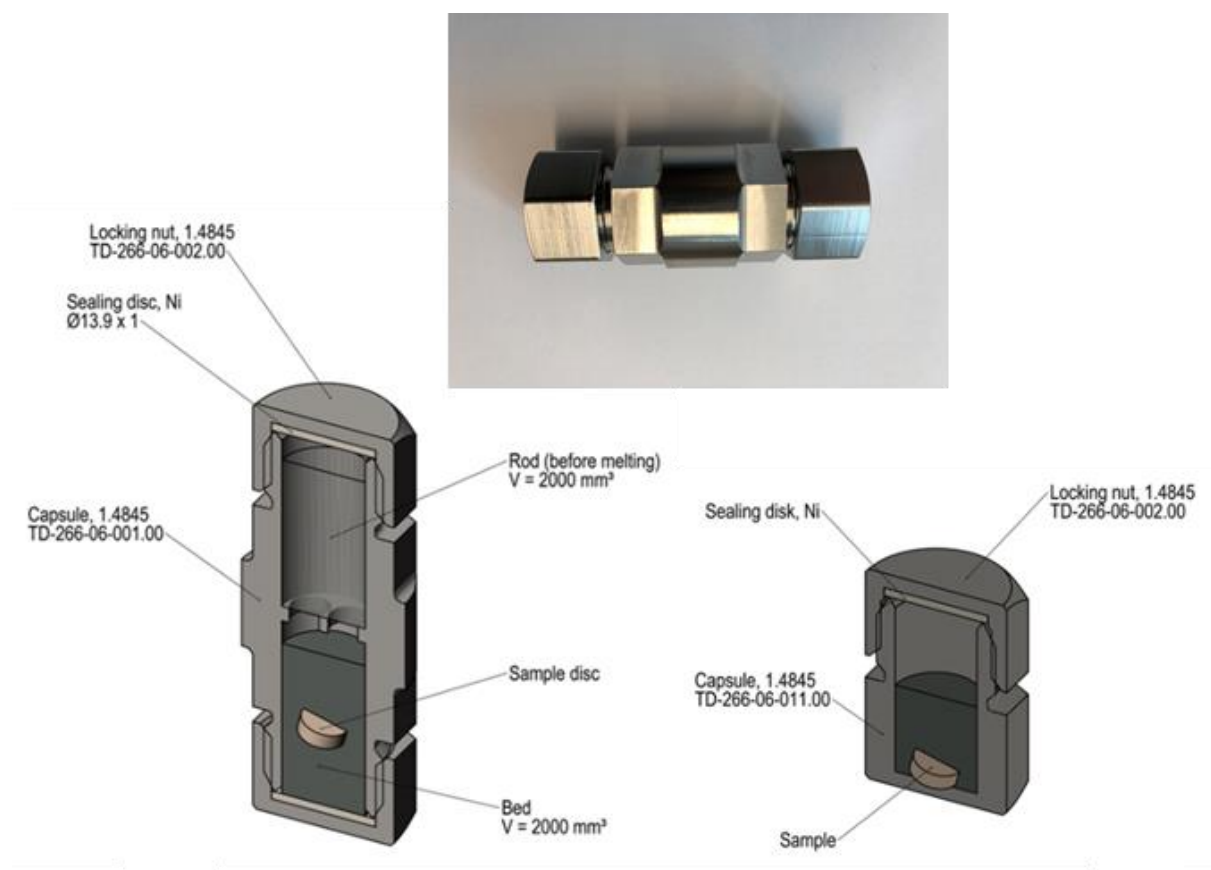


Figure 51: Two design of the capsule for interaction tests. Left: Capsule design with two chambers and sample position; Right: Capsule design with a unique chamber and sample position.

Each capsule was placed into a furnace in an upright position and the heating program was performed in three steps, as follows:

- Heating-up to target temperature at a heating rate of 200 °C/h,
- staying at target temperature for a given time
- cooling down to room temperature at a cool down rate of -200 °C/h.

At the conclusion of the interaction test, when the furnace was at room temperature, each capsule was removed from the furnace.

Then, the capsule was fixed on a support and opened by cutting through its body, as illustrated in Figure 52 (left). The sample, still covered by metallic sodium (Figure 52, middle), was recovered after dissolution of the sodium with ethanol alcohol, as shown in Figure 52 (right). When the sodium was completely dissolved, the sample was taken out and transferred to the characterization.



Figure 52: View of a cut capsule after the interaction. Due to the tightness, the capsule was cut by saw. Left: capsule fixed on the support for the cut. Middle: view of the excess of sodium after the interaction. Right: dissolution of the sodium excess with Ethanol.

4.4 Characterization methods

The nature of the corrosion product was observed and characterized by using several experimental techniques, such as X-ray Photoelectron Spectroscopy (XPS), X-ray Diffraction (XRD), Scanning Electron Microscopy (SEM) and Transmission Electron Microscopy (TEM). A general overview of the physics and the technical aspects of these techniques is hereafter given.

4.4.1 X-ray Photoelectron Spectroscopy

X-ray Photoelectron Spectroscopy (XPS) belongs to the electron spectroscopic techniques. The technique relies basically on the photoelectric effect. Figure 53 (right) shows the photoelectron process. Indeed, when a surface is irradiated with X-ray photons, the electrons can be liberated from their bound atomic states by photoionization. Energy and momentum are transferred from the incoming radiation to the excited electron and by means of an inelastic scattering process. Indeed, an electron, with binding energies E_B , in interaction with a photon, absorbs the entire photon energy $h\nu$, resulting in the ejection of a photoelectron with the kinetic energy E_{kin} :

$$E_{kin} = h\nu + E_B - \phi_S \quad (34)$$

Herein, ϕ_S is a work function term (usually small and constant). In general, the attention is focused on the ejected electrons coming from the core levels, but we can also detect valence band electrons. Each element is characterized by its own set of electronic binding energies, thereby photoelectron kinetic energy measurements allow elemental identifications. Moreover, the relationship between E_B and E_{kin} (Eq. 49), allows getting chemical information. Indeed, any change in the chemical environment of an atom is reflected on the E_B , which implies necessarily a change of the E_{kin} . Following the emission of a photoelectron from core levels or from the valence band, a core hole is created in the atom. The hole can be filled by an electronic transition from higher unresolved shell. The transition energy can be either dissipated as a characteristic X-ray photon or transferred to an electron in the same or in a higher shell. The latter is called Auger electron emission process. The two processes are obviously competitive, but due to the shallow core levels, the Auger process is more likely in XPS. Nevertheless, the Auger electron emission features can be useful, but are not crucial for the XPS technique. Moreover, it has to be considered that XPS is a surface-specific technique. Indeed, an electron with kinetic energy E , which moves through a solid, has a certain probability to travel a given distance before losing all of its energy due to inelastic collision. The average distance which the electron can travel before the collision is known as inelastic mean free path $\lambda_M(E)$ and it is a function only of the solid M and of E . In the range of secondary electron kinetic energies used in XPS, the values of λ are very small, i.e. corresponding to a few monolayers. This simply means that only the electrons originated very near from the surface can be detected.

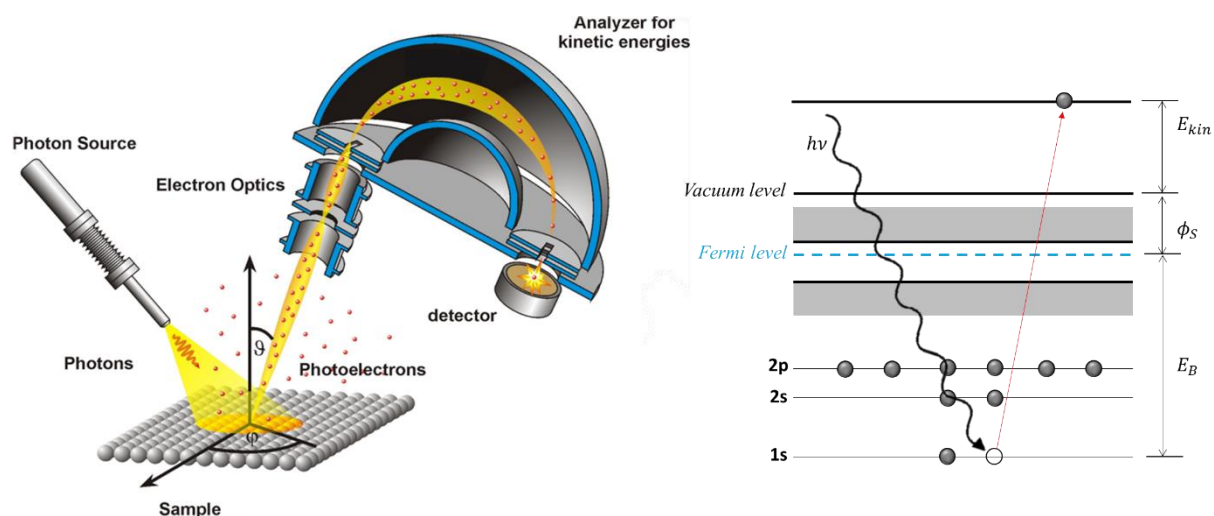


Figure 53: Basic components of a monochromatic XPS system. Right: schematic diagram of photoelectron process.

The XPS surface-specificity technique requires vacuum levels in the order of 10^{-8} Pa or lower (ultrahigh vacuum-UHV). The vacuum allows measuring the surface without gas contamination interference, thereby improving the resolution quality. The X-ray source needs to have an energy photon much higher than the E_B and a line-width smaller than 1.0 eV for a good resolution. The source material, which represents the target for the electron bombardment for the production of the X-ray, is generally made by Al-K α and Mg-K α . These materials comply with the needed requirements having an energy of 1486.6 and 1253.6 eV, respectively, and a

line-width of 0.85 and 0.7 eV, respectively. Moreover, a monochromator is usually used to remove satellite lines and Bremsstrahlung background, and to separate the $K\alpha$ doublets, which are usually coming from the principal lines of the $K\alpha$ lines of Al and Mg. In this way, the XPS spectrum is much cleaner but the photon flux to the sample is much lower when compared to the flux without monochromator. Finally, the E_{kin} of the ejected electrons is measured using an electron energy analyzer. Universally, the employed analyzer is a Concentric Hemispherical Analyzer (CHA). The electron energy analyzer generates a spectrum with a series of photoelectron peaks. The peak analysis allows determining the composition of the materials surface by the peak areas (with appropriate sensitivity factors). In addition, the chemical bonding information can be extrapolated from the peak shape and E_b , since they indicate the chemical state of the emitting atom. The nomenclature used in XPS is here briefly reported because it is different from the one used for the X-ray notation. The XPS is also based on the so-called $j-j$ coupling scheme, which describes the orbital motion of an electron around the atomic nucleus. The total angular momentum is the vectorial sum of the individual electron spin and angular momenta. If l is the electronic angular momentum quantum number and s is the electronic spin momentum quantum number, the total angular momentum is given by $j = l + s$. In spectroscopic notation, the $l = 0, 1, 2, 3, \dots$ are designed as s, p, d, f, \dots respectively. The letter is preceded by the principal quantum number $n = 1, 2, 3, 4, \dots$ and the j values are appended as suffixes.

In this study, the background pressure in the analysis chamber was of 2×10^{-10} mbar. The $\text{Al-}K\alpha$ radiation was produced by an XRC-1000 micro-focus source, equipped with a monochromator and operating at 120 W. The high resolution of the XPS measurements were performed using a Phoibos 150 hemispherical analyzer. The spectrometer was calibrated by using an $\text{Au-}4f_{7/2}$ line of metal to give a value at 83.9 eV E_B and a $\text{Cu-}2p_{3/2}$ line of metal at 932.7 eV E_B . Photoemission spectra were taken at room temperature.

4.4.2 X-ray Diffraction

X-ray Diffraction (XRD) is a classical method for identification of crystallographic phases. The technique relies on the elastic scattering process of X-rays, herein briefly discussed. As already mentioned in the XPS section, when matter interacts with X-ray photons, different processes can take place in terms of adsorption or scattering effects. In particular, when the photons interact with the electrons surrounding the nucleus, an elastic scattering (also referred to Rayleigh scattering) may occur. In this case, the scattered wave energy does not change and it remains in relation with the incident wave. Moreover, the periodicity of a crystalline structure leads to characteristic constructive or destructive interference of the scattered radiation, which results in the diffraction phenomena. Indeed, for a particular wavelength, diffraction occurs if the Bragg's law:

$$n\lambda = 2d_{hkl} \sin(\theta) \quad (35)$$

is obeyed. In this case, the reflected beam is in phase and leads to constructive scattering. Figure 54 (left) shows the way to derive Bragg's law. In the Bragg's law, d_{hkl} is the distance between two adjacent lattice planes, θ is the angle of incidence, also called Bragg angle, n is the order

configuration. The device is implanted in a radioactive glovebox. This diffractometer is equipped with a curved Ge monochromator (111) and a Lynxeye linear position-sensitive. The patterns were recorded using a step size of 0.01° across the angular range $10^\circ \leq 2\theta \leq 120^\circ$. Moreover, since the formed phase coming from the interaction of the fuel with sodium was expected as a surface layer, XRD patterns were obtained from the sample surface. The sample was accommodated in a dedicated silicon holder. The sample holder was prepared for each sample in order to fit its shape and height. Figure 55 shows an example of the sample and sample holder. The circular holes in the holder which appear at the sample corner have the aim of helping the extraction of the sample after the XRD measurements. In such a way, the sample surface and edge morphologies were not strongly affected by the sample handling.

The XRD diffraction patterns obtained in Bragg-Brettano configuration were simulated using JANA software. Most of the time, it was not possible to perform real Rietveld refinement because. When single crystals were used, orientation effects were too large for usual Rietveld. When polycrystals were used, very often the crystalline structure of one amongst the observed phase was not known. Therefore, in most of cases, only simulations using the full pattern matching option were performed: this means that the unit cell and the profile function were refined, but the intensities of the diffraction peaks were set arbitrarily by the software.

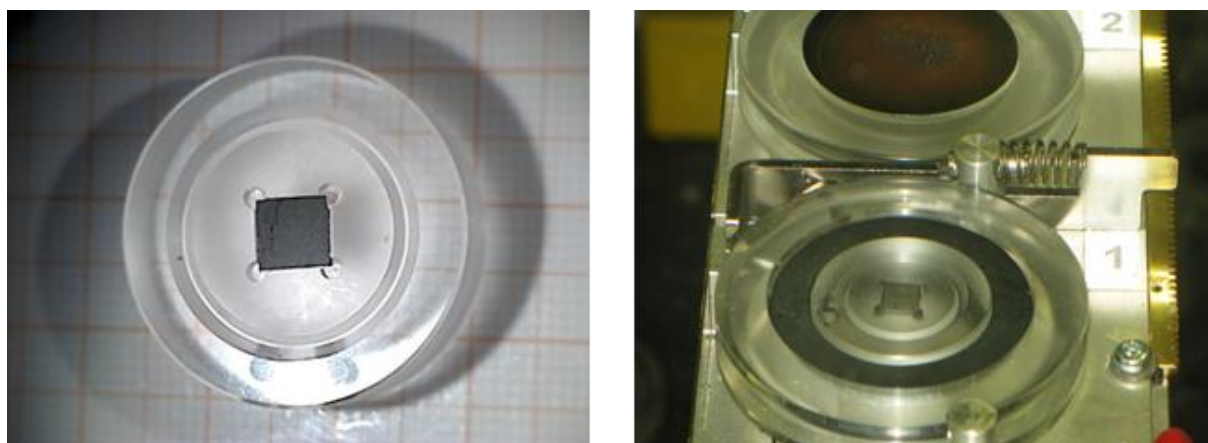


Figure 55: View of the sample and sample holder for XRD measurement. Left: UO_2 single crystal as mounted on a silicon sample holder. Right: view of the sample ready for the XRD measurement.

4.4.2.1 Grazing Incidence X-ray Diffraction

Grazing Incidence X-ray Diffraction (GIXRD) is an X-ray diffraction method which is more surface-sensitive. The physics behind the GIXRD relies on the same principles as XRD, above mentioned. The main difference between a standard XRD and the GIXRD consists in the geometry. Since information have to come from the surface, the penetration depth of the X-ray is reduced by simply reducing the angle of incidence θ of the beam. In the present study, GIXRD measurements were performed at the Institute of Mathematics and Physics, ASCR, Prague

(Czech Republic). The used device was a Rigaku SmartLab diffractometer equipped with 9 kW copper rotating anode X-ray source (CuK α radiation $\lambda = 0.15418$ nm). Moreover, a parabolic multilayer mirror in the primary beam, a set of axial divergence eliminating soller slits in both the incident and diffracted beam (acceptance 5°), a parallel beam soller slit collimator (acceptance 0.5°) and a HighPix-3000 2D hybrid pixel single photon counting detector in the diffracted beam. The constant incidence angle of the primary beam $\omega = 3.0^\circ$ was used for the measurement.

With grazing incidence, Rietveld procedure for peak fitting has to be adapted in order to incorporate the changes induced by this specific geometry. The analysis in this study did not go in such complexity and only simulations were performed with the full pattern matching option using JANA.

4.4.3 *Scanning Electron Microscopy*

On a microscopic scale, the surface structure was observed by Scanning Electron Microscopy (SEM). The general concept of the SEM technology is herein briefly mentioned. To produce an image of the sample surface, SEM relies on the electron beam collision with the surface of the specimen. A finely collimated beam of electrons is focused into a small probe. The latter scans across the surface of a specimen and, as result of the interactions between the beam and the material, electron and photon emissions are produced because of the surface penetration by electrons. The emitted particles are thereby collected by the appropriate detector to yield information about the surface. Also in this case, a good vacuum is required because electrons cannot travel long distance through air. SEM is constituted of two major parts [95], i.e. the electron column and the cabinet. Electrons are generated from a heated filament (usually tungsten) and accelerated down the column. The emitted electrons traverse the column before reaching the sample. Then, they hit the specimen surface and the scattered fraction is captured by the detector. The electron source is constituted by the electron gun at the top of the column. The electron column holds the condenser, objective and scanning lenses. The condenser lenses are placed near to the electron gun. The aim of these latter lenses, together with the magnetic ones, is to focus the electron beam on the target. Instead, the objective lenses are close to the sample and are used to catch the sample surface, which corresponds to focusing the image. Finally, the signals are sent by the detector to the control cabinet which is equipped with specific electronic systems able to quantify such signals and turn them into analyzable information (images and graphs).

In this study, we used a FEI (Philips) XL 40 Scanning Electron Microscopy (200 V-30 keV, tungsten filament, emission-current till 200 μ A), equipped with SAMx EDX-System (multi-channel Pulse, 110 eV - 80 keV X-ray energy range, <138 eV Resolution) and implanted in a radioactive glovebox for the studies of radioactive samples.

4.4.3.1 Energy Dispersive X-ray Spectroscopy

Energy Dispersive X-ray Spectroscopy (EDS or EDX) was used to detect the elemental composition of the phases. EDS belongs to the X-ray spectroscopic methods and it is usually integrated into a SEM. The method uses the measurement of the characteristic energy of the emitted X-rays to identify and quantify the elemental composition of a sample. Indeed, when the atoms on the surface are excited by the electron beam, they emit X-rays with wavelengths, which are characteristic of the atomic structure of each chemical element. An energy dispersive detector can detect and analyze these X-ray emissions. The results are strongly affected by the spatial extension of the volume from which the signal is gained and thereby from the material itself. However, the diameter of the electron beam, the primary electron energy and the specimen thickness are also relevant for such measurement.

4.4.4 Focus Ion Beam

The Focused Ion Beam (FIB) uses a precisely controlled stream of charged particles to generate the image, together with a stream of gallium ions, which can also be used to ballistically etch material away from the surface. The inherent precision of the FIB also allowed performing “micro-surgery”. Indeed, the main advantage of this beam is that it can be targeted accurately and the exposed surface can be treated without inducing any damage of the surrounding. In this study, a Thermo-Fisher Scientific Versa 3D dual beam FIB was used either for sample characterization and lamella preparations. The device was equipped with a 30 kV FEG electron gun and 30 kV Ga liquid metal ion source. Figure 56 shows the FIB device which was installed into a glove box, still under construction, for further high-radioactive materials characterization.

Quick cross-sections were performed on the sample surface to investigate small areas of interest. In addition, it was particular useful in the preparation of thin lamella having a thickness of about 50 nm for the transmission electron microscopy (TEM) analysis, since the latter required extremely thin samples to produce meaningful data. Thick lamella, having a thickness of about 3 μm , were also prepared with the aim of performing target EDX mapping measurement. The first step for the lamella preparation was the deposition of a Platinum protective layer on the sample surface to reduce curtaining and minimize damage to the specimen surface during milling operations. This was followed by the extraction of the lamella from the sample. The latter was then mounted on the sample holder, where cleaning and thinning steps were performed. The sample holder with attached the ultimate lamella were then transferred to the TEM and SEM for the analyses.

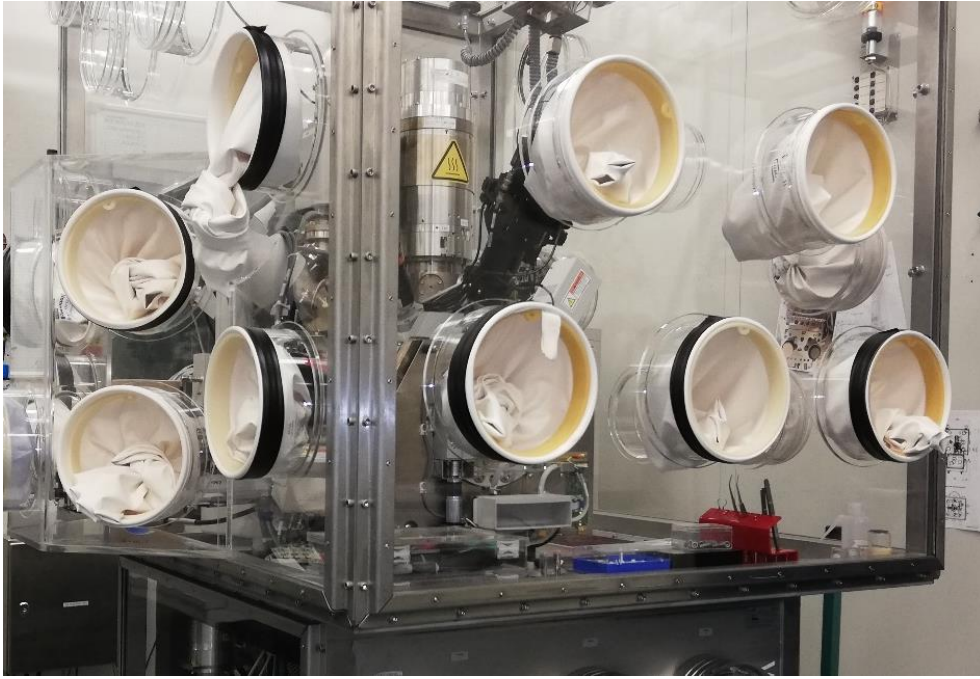


Figure 56: Focus Ion Beam installed in the glove box for the analysis of high-radioactive materials. The glovebox is still under preparation.

4.4.5 Transmission Electron Microscopy (TEM)

Transmission Electron Microscopy (TEM) was used, in conjunction with the other mentioned techniques, because it is an exceptionally powerful technique for revealing the crystal structure, as well as the chemical composition of materials. In the TEM, a beam of high-energy electrons, typically 100–1000 keV, is focused on a thin sample of the material under investigation. Electrons transmitted through the sample are detected. These electrons can be used to form an image of the sample showing internal microstructural features. TEM is constituted by three essential systems which are the electron gun, for the production of the electron beam, and the condenser system, which focuses the beam onto the object. The image-producing system consists of the objective lens, a movable specimen stage and intermediate and projector lenses. The latter focus the electrons passing through the specimen to form a highly magnified image. Finally, an image-recording system converts the electron image into a visible image.

At last, the system of image-recording, which converts the electron image into a visible image. In this study, we used a TEM model FEI Tecnai G2 TEM, equipped with a GATAN Tridiem camera and a Gatan Imaging Filter. The field emission gun was operated at 200 kV. The TEM can be used for the examination of highly active or irradiated nuclear materials thanks to a flange which is inserted in the octagon which hold the objective lenses, and a glove box mounted on this flange around the compustage. Thus, the sample can be moved from the glove box where it was prepared to the microscope making use of a La Calhène DPTE® system. The sample preparation process makes use of FIB-lamella.

5 *Surface studies*

Dans ce chapitre, on s'attache à déterminer l'état d'oxydation de l'uranium dans la couche de corrosion formée par l'interaction combustible-sodium. Pour ce faire, des couches minces ont été préparées sous ultravide sur des substrats divers et leur surface a été caractérisée par XPS. Ces études ont permis d'établir que le degré d'oxydation de l'uranium est U(V). A température ambiante, le sodium pur ne réagit pas avec le dioxyde d'uranium stœchiométrique et l'inter-diffusion entre sodium et oxygène conduit à la réduction du trioxyde d'uranium, UO_3 , pour donner le dioxyde d'uranium stœchiométrique, UO_2 . L'inter-diffusion entre sodium et oxygène est thermiquement activée et permet la formation de composés ternaires. La présence du degré d'oxydation U(VI) n'est possible que si on a présence de d'oxyde de sodium sous la forme Na_2O_2 .

The herein presented surface studies were aimed to establish the oxidation state of the corrosion layer (point 1. a) reported in Chapter 3). One method frequently used to determine the oxidation state of elements near the surface of materials is X-ray Photoelectron Spectroscopy (XPS). However, it is known that when dealing with bulk materials containing uranium, the surface may undergo to some changes if it is exposed to air or to an atmosphere containing impurities in appreciable amount. Etching process of the surface is then usually suggested before XPS measurements. By this way, the surface can be cleaned and the residual impurities, such as carbon and oxygen, can be eliminated. However, the etching process can locally alter the properties of the material. To prevent all these issues and then to obtain accurate results, the interaction between thin films of sodium and uranium oxide were carried out directly under ultra-high vacuum.

5.1 *Reference studies*

The present studies were the first of a kind dealing with the interaction between metallic sodium and stoichiometric and hyper-stoichiometric uranium oxide UO_{2+x} ($0 \leq x \leq 1$) using thin films as a surface model. A very few XPS results on metallic and oxide sodium are reported in literature [96, 97]. Hence, some of the properties of metallic sodium were firstly established on a gold substrate as a reference of the system, before investigating the interaction of metallic sodium and uranium oxide films. Moreover, reference spectra for the different oxidation state of uranium are also reported, with the aim to follow the changes when sodium was deposited on the uranium oxide substrate. Finally, the thermal stability of the metallic sodium and UO_{2+x} film under ultra-high vacuum was also checked.

5.1.1 *Reference of metallic sodium and sodium oxide*

Deposition of metallic sodium on gold substrate was performed to establish some of its main features such as the binding energy (BE) at core-level and the stability. In addition, oxidation of sodium was afterward performed to allow distinguishing the presence between metallic sodium and sodium oxide. Heat treatment of metallic sodium deposited on gold substrate

showed that sodium evaporation took place at temperature less than 483 K under UHV. Figure 57 reports the Na-1s core-level spectra of clean gold (gray), deposition of metallic sodium (blue) and after the oxidation (red) by molecular (left) and atomic (right) oxygen, respectively. Clean gold resulted obviously in the absence of a sodium peak. After the deposition of metallic sodium on gold substrate, the Na-1s peak appeared at 1071 eV. The latter asymmetric peak is usually reported as characteristic of metallic sodium, with a binding energy of 1071.2 eV [96, 97]. The thickness of the sodium film was calculated by the Na-1s/Au-4f intensity ratio (detailed calculation are reported in the Annex) and corresponded to about 4 nm for a deposition time of 30 s. The oxidation of metallic sodium was found to depend on the reactive species used to perform the oxidation. Oxidation through the use of molecular oxygen led to a broadening and higher symmetry of the Na-1s peak, but its binding energy remaining invariable at about 1071.1 eV ($\Delta BE = -0.2$ eV). On the other hand, oxidation with atomic oxygen led to a symmetric peak shifted to 1073.2 eV ($\Delta BE = +2.2$ eV). This shift in binding energy arose from a real chemical shift and indicated the transformation from metallic sodium to sodium oxide. Table 9 summarized the corresponding binding energies of metallic sodium and sodium oxide found in these studies.

Table 9: Binding energy of metallic sodium and sodium oxide in this study

<i>Level</i>	<i>Binding Energy</i>		<i>Chemical shift</i>	<i>Binding Energy</i>	<i>Chemical shift</i>
Na1s	Na metal	Na+O ₂ *	+ 0.1	Na ₂ O**	+ 2.2
	1071	1071.1		1073.2	

*Molecular oxygen

** Atomic oxygen

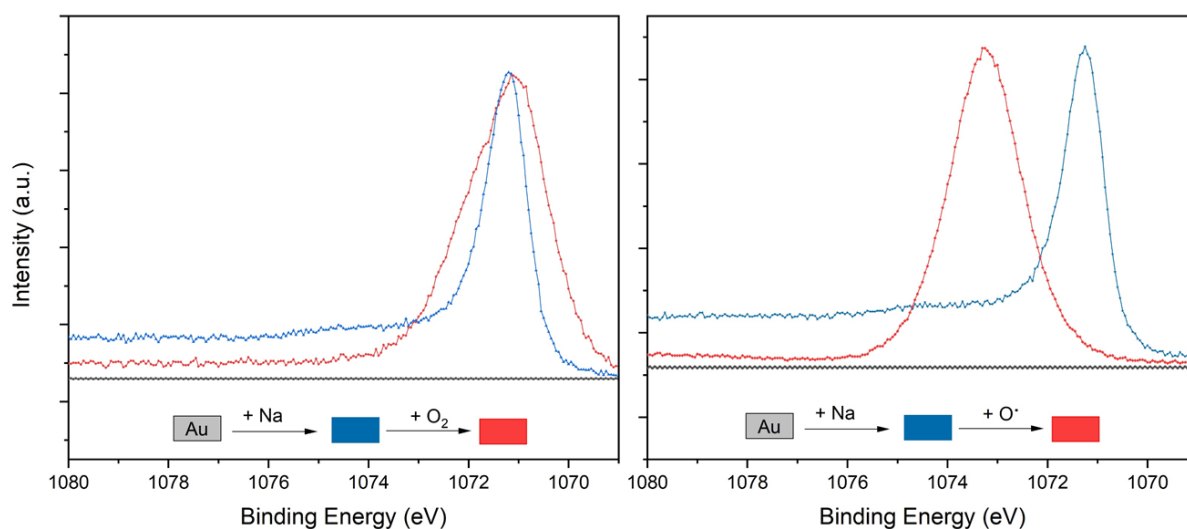


Figure 57: Na-1s core-level spectra with equalized peak intensities. Left: after deposition of metallic sodium followed by oxidation with molecular oxygen. Right: after deposition of metallic sodium followed by oxidation using atomic oxygen.

A study on sodium adsorbed on MgO [98] assigned the Na-1s line at about 1072.2 eV to the sodium oxide Na₂O formation. Others [96, 99] found its core level peak Na-1s at 1073.01 eV, in good agreement with the present study. The higher reactivity of atomic oxygen compared to the molecular oxygen clearly led to a more significant and faster oxidation. Instead, as concerns the oxidation through molecular oxygen, no catalytic effect was observed and the dissociation of molecular O₂ should be the limiting step for sodium oxidation.

5.1.2 Reference of uranium oxidation state

Stoichiometric and hyper-stoichiometric uranium oxide films were prepared as described in section 4.1. The U4f spectrum of stoichiometric uranium oxide showed narrow and symmetrical peaks, with maxima at 380.2 and 390.9 eV for the 4f_{5/2} and 4f_{7/2} emission lines, respectively. The relative energy between the satellite peak and the 4f_{5/2} emission line can be generally used as the marker of the oxidation state of the uranium atoms, which range from (IV) to (VI).

In the case of stoichiometric UO₂, which is characterized by an oxidation state of the uranium atoms (IV), the satellite peak was placed at 6.9 eV higher binding energy than the 4f_{5/2} emission line, as illustrated in Figure 58 (left). Symmetrical sharp peaks characterized uranium trioxide UO₃ spectrum.

The oxidation state of uranium (VI), can be observed through the presence of two satellite peaks at 4.4 and 9.7 eV higher binding energy than the 4f_{5/2} emission line, as illustrated in Figure 58 (right). Due to the strong peak of the 4f_{5/2} emission line, the satellite at ~10 eV of the 4f_{7/2} peak was hidden, and only the 4.4 eV satellite was visible. A summary of the corresponding binding energy of the emission lines and the distance from satellites is reported in Table 10.

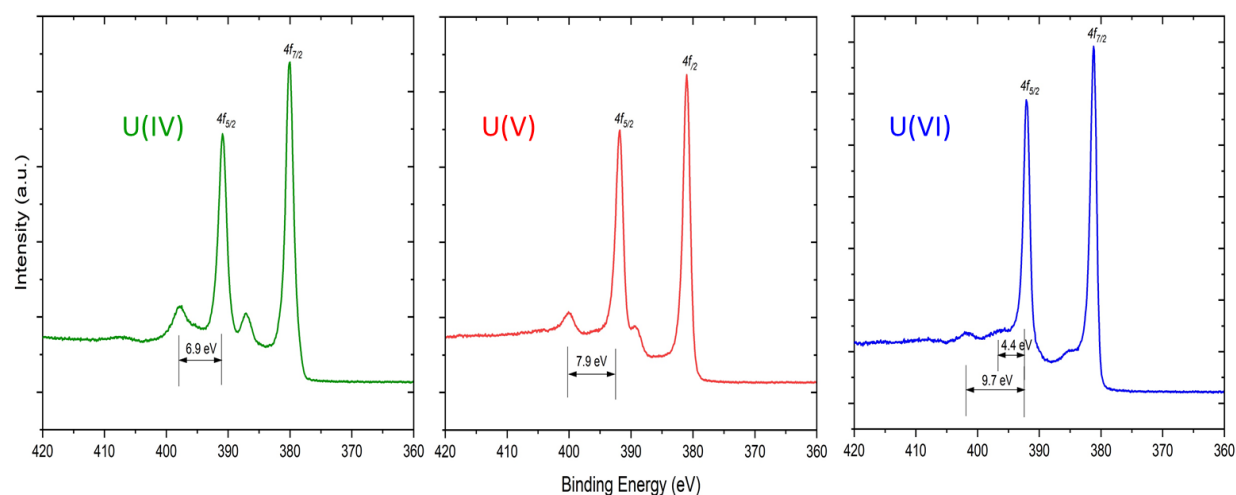


Figure 58: Uranium 4f core level X-ray Photoemission Spectra recorded for U(IV) (left, green), U(V) in U₂O₅ (middle, red), and U(VI) (right, blue).

As concern the reference of uranium (V) oxidation state, the spectrum was obtained by the study of a U_2O_5 film. The latter was prepared as reported elsewhere [100]. The U4f spectrum of U_2O_5 showed slightly broader peaks compared to those of stoichiometric uranium oxide and uranium trioxide. The satellite peak lay at intermediate value between those of stoichiometric uranium oxide and uranium trioxide and corresponded to 7.9 eV higher binding energy than the $4f_{5/2}$ emission line, as illustrated in Figure 37 (middle).

Table 10: Binding energy of U(IV), U(V) and U(VI)

<i>Level</i>	<i>Binding Energy (eV)</i>		
	<i>U(IV)</i>	<i>U(V)</i>	<i>U(VI)</i>
U4f _{5/2}	390.9 ± 0.2	391.7 ± 0.2	392.1 ± 0.2
U4f _{7/2}	380.2 ± 0.2	380.9 ± 0.2	380.9 ± 0.2
$\Delta\text{BE}_{\text{satellite}}$ (eV)	6.9	7.9	4.4 and 9.7

5.1.3 Stability of UO_{2+x} films

The thermal stability of the hyper-stoichiometric uranium films was investigated in order to establish whenever the presence of sodium could influence the behavior of the film. A heat treatment was carried out on uranium trioxide film under ultra-high vacuum conditions in the temperature range between 373 K and 773 K. Figure 59 shows the spectra of the uranium trioxide heat treatment. The progressive increase of the temperature led to the reduction of the film. The reduction started between 573 and 673 K, without passing through a compound purely uranium U(V). Nevertheless, uranium trioxide film with an oxidation state U(VI) was reduced to uranium oxide having an oxidation state U(IV) when the temperature reached 773 K.

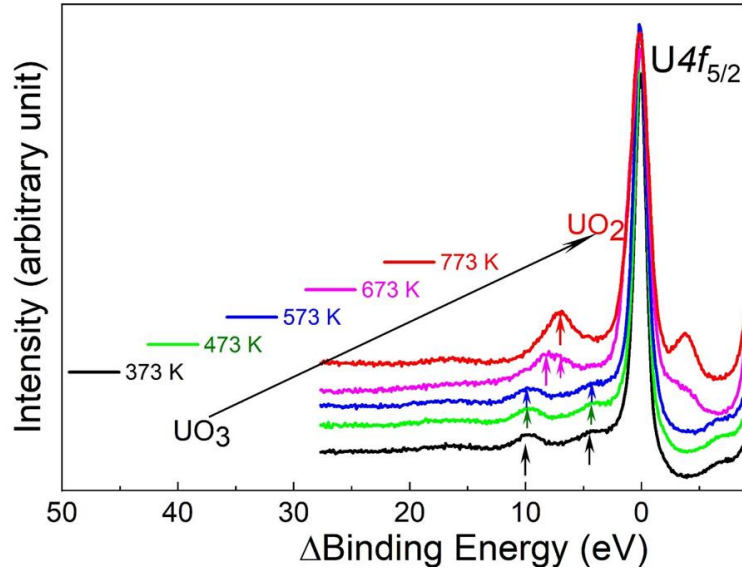


Figure 59: Heat treatment of UO_3 thin film under UHV showing the progressive reduction to UO_2

5.2 Interaction studies

5.2.1 Deposition of metallic sodium on stoichiometric UO_2 at room temperature

At room temperature, when metallic sodium was deposited on stoichiometric uranium oxide substrate, Na-1s peak appeared at 1071 eV, indicating the presence of pure metallic sodium. Na-1s spectrum reported also the appearance of the plasmon loss peaks at $\Delta E = 5.8$ eV. The corresponding spectra are reported in Figure 60. This figure reported the comparison between the normalized U-4f, O-1s, Na-1s and valence-band spectra before (black spectra) and after sodium deposition (blue spectra). The increase of the background after sodium deposition was due to the inelastic scattering of U-4f photoelectrons, showing uranium underneath the sodium overlayer. The satellite peak position, fingerprint of U(IV) oxidation state, remained constant at 6.8 eV higher BE than the main line. The O-1s spectra obtained after deposition of sodium underwent a slight shift to higher binding energy. A second peak appeared at about 537 eV and could be attributed to the Na-KLL emission.

Table 11: Summary of the results of the interaction between pure sodium and stoichiometric uranium oxide

T (K)	$\Delta BE_{\text{satellite}}$ (eV)	U oxidation state	BE_{Na1s} (eV)
298	6.9	IV	0
298	6.9	IV	1071

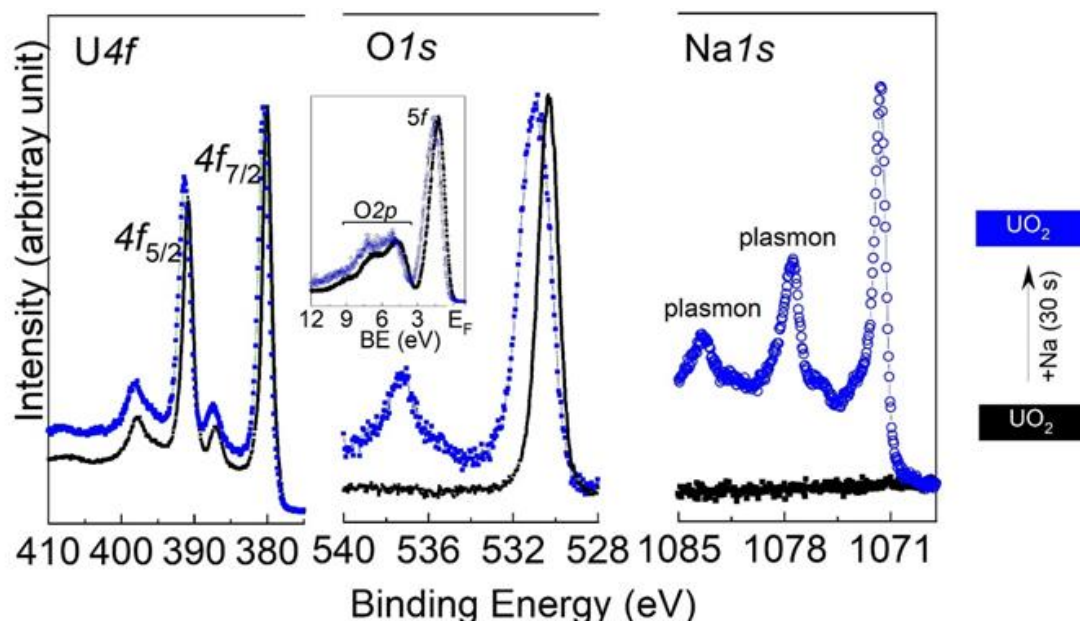


Figure 60: Comparison between the normalized U-4f, O-1s, Na-1s and valence-band spectra before and after deposition of about two nm of sodium on UO_2 at room temperature

5.2.2 Deposition of metallic sodium on UO_{2+x} ($0 \leq x \leq 1$) at room temperature

At room temperature, when metallic sodium was deposited on hyper-stoichiometric uranium oxide, the corresponding Na-1s line appeared at 1073 eV and was characterized by a single and symmetric peak. The corresponding binding energy and peak shape were characteristic of sodium oxide.

The interstitial oxygen present in UO_{2+x} seemed to play the same role observed for the sodium oxidation by atomic oxygen, leading to a higher BE of Na-1s line. Figure 61 reported successive depositions of metallic sodium on uranium trioxide, UO_3 . The corresponding O-1s and U-4f core-level spectra were also reported for each step of the experiment.

The oxidation state of uranium at each step was determined following the position of the satellite peaks. The deposition of metallic sodium leads to two peaks in the O-1s spectra, the main peak located at about 530.4 eV and the second one at 5.1 eV higher BE. They shifted towards the higher BE with ongoing reduction of uranium oxide by sodium and the second peak disappeared.

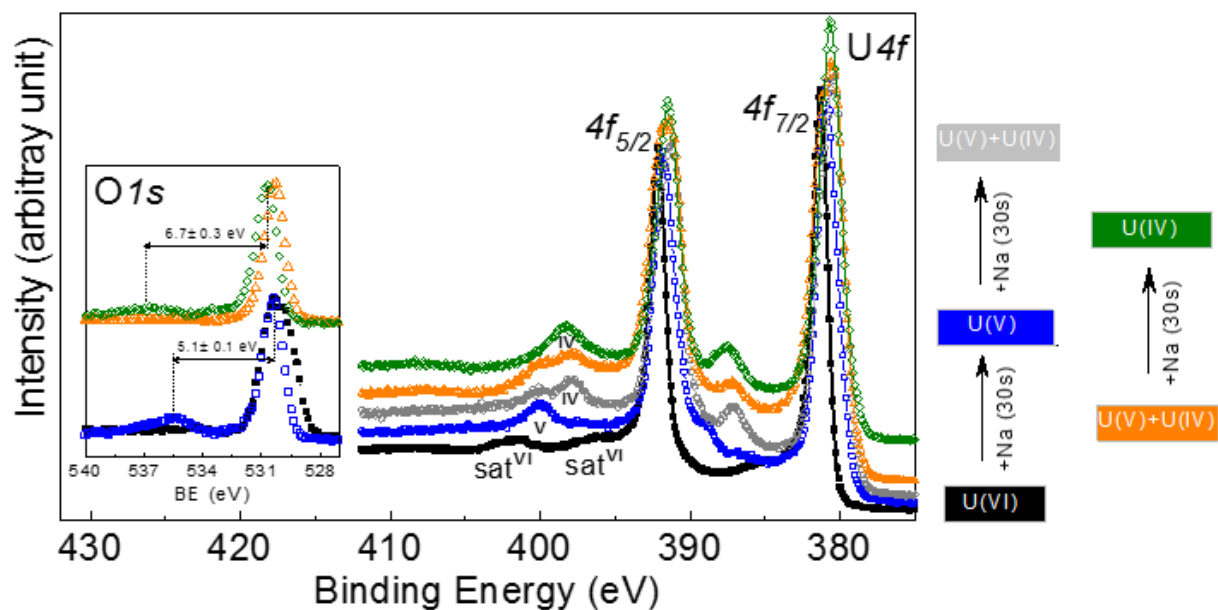


Figure 61: Successive depositions of metallic sodium on UO₃ at room temperature, which resulted in a complete reduction of UO₃ into UO₂.

Table 12: Summary of the results of the progressive deposition of metallic sodium on hyperstoichiometric uranium oxide

T (K)	$\Delta BE_{\text{Satellite}}$ (eV)	U oxidation state	BE_{Na1s} (eV)
298	4.4-9.7	VI	0
298	7.9	V	1073
298	7.9-6.9	IV-V	1073
298	7.9-6.9	IV-V	1073
298	6.9	IV	1073

5.2.3 Formation of a ternary compound and its phase identification

As above showed, at room temperature, the deposition of metallic sodium on hyperstoichiometric uranium oxide led to the formation of a heterogeneous system, in which hyperstoichiometric uranium oxide was progressively reduce and sodium was oxidized through the interdiffusion between oxygen and sodium atoms. Based on the Na1s line, no ternary compounds were probably formed. The heat treatment of the metallic sodium deposited on the UO_3 film was then carried out, with the aim to potentially form a ternary compound. The film was heated from room temperature to 973 K. Several spectra were acquired at different temperature to follow the reaction. Figure 62 displays the U-4f, O-1s, Na-1s spectra at various temperatures. It is insightful to compare the satellites in the 4f spectra plotted as a function of relative energy difference to the main peak. At room temperature, sodium reduced UO_3 into UO_{2+x} with mixed U(V) and U(IV). At 523 K, U(V) becomes the major oxidation state in the sample. Then, from 673 K up to 873 K, U(V) was the single oxidation state. Relating the spectra to ΔBE we can easily compare the broadening of the peaks as a function of temperature. Without considering the UO_3 spectrum, the smallest broadening is observed at 673 K and 773 K, which points to a single phase (or oxidation state) formed at these temperatures. The largest broadening is obtained at room temperature for sodium deposited on UO_3 , corresponding to a heterogeneous system. The O-1s spectrum showed a shift of the main peak in two steps (black arrow), first to higher BE and then, for temperature greater than 523K, it went to lower BE. A second peak appears at 5 eV higher BE from the main peak. Na-1s showed one single and symmetric peak, being representative of oxidized sodium, all along the experiment. It shifts monotonously to lower BE from 1073 to 1071.6 eV. The potential formation of a ternary compound can be also supported by the Na-1s peak at 1071.6 eV, which can be considered as a fingerprint of ternary compounds containing sodium [101].

Table 13: Summary of the results at various temperatures for the studies of the ternary compound formation

<i>T (K)</i>	<i>$\Delta BE_{\text{Satellite}}$ (eV)</i>	<i>U oxidation state</i>	<i>BE_{Na1s} (eV)</i>
298	4.4-9.7	VI	0
298	6.9-7.9	IV-V	1073
523	7.9	V	1072.7
673	7.9	V	1072.3
773	7.9	V	1072
873	7.9	V	1071.6
973	7.9	V	1071.6

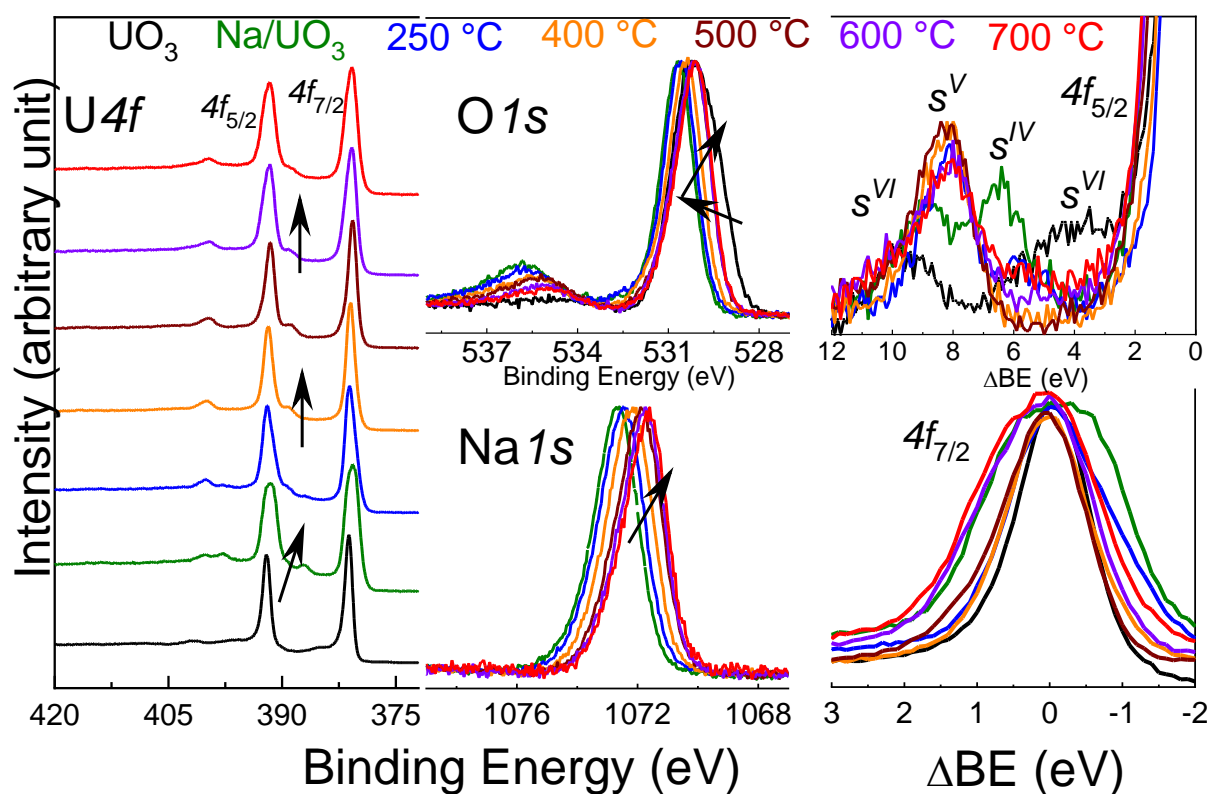


Figure 62: U-4f, O-1s and Na-1s spectra at various temperatures for the studies of the ternary compound formation.

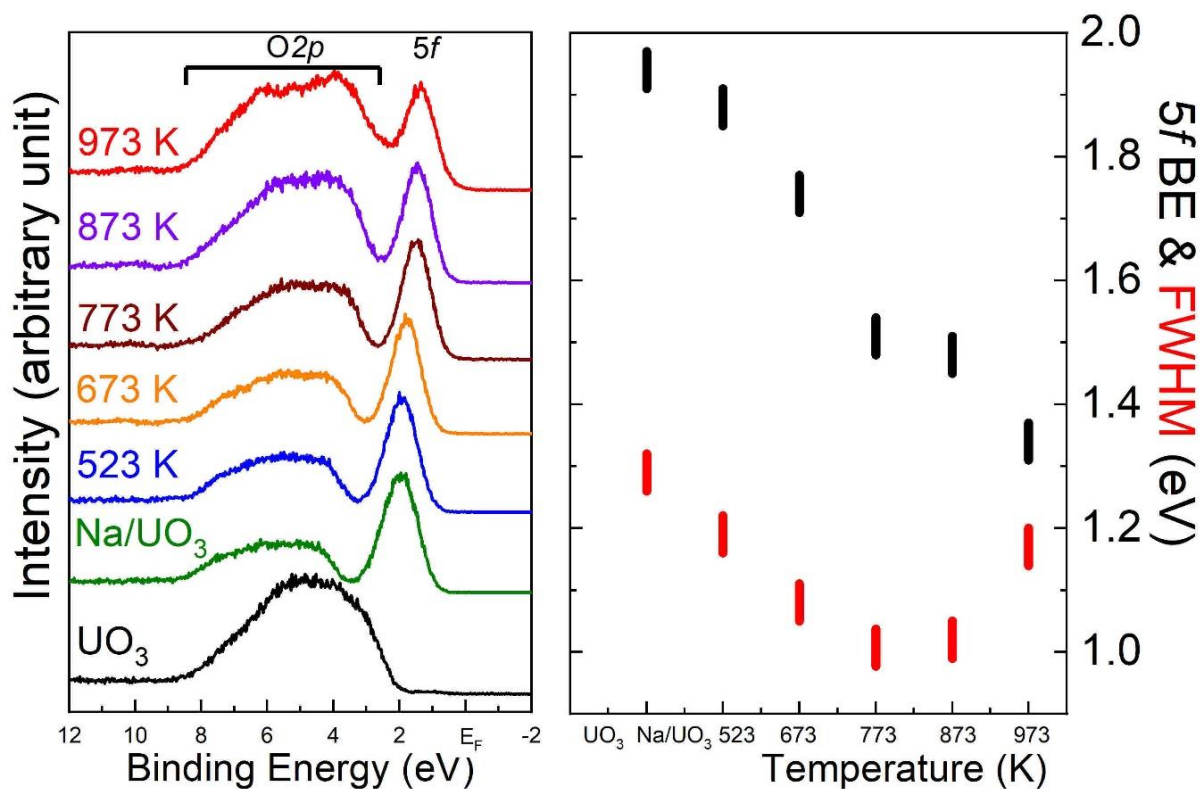


Figure 63: Effect of temperature on Na/UO_3 followed by valence band spectra (left) and energy of the 5f peak and its FWHM (right).

To obtain the confirmation of the formation of a compound, the produced films was analyzed by grazing-incidence x-ray diffraction and wide reciprocal space maps. The GIXRD diffraction pattern is shown in Figure 64 left. The pattern was compared to the known peak positions of NaUO_3 and to the gold substrate. Indeed, the identified peaks can be assigned mainly to the gold substrate and to NaUO_3 . A broad peak at about 28° in 2θ can be attributed to amorphous UO_3 or UO_{2+x} .

Figure 64 right illustrated the Reciprocal Space Mapping (RSM) map which resulted from a combination of θ - 2θ scans for various axial tilt angles ϕ of the sample. The red indexes (hkl) and red circles are peaks of gold. The reflections with pink (hkl) indexes are instead sticking out several wide peaks of UO_2 . The simulation of the pattern was made by using a single crystal UO_2 pattern, since it has a very strong preferential growth on gold. Finally, the blue lines are the powder pattern of NaUO_3 , with the most intensive lines. The simulation fitted with the NaUO_3 phase, lattice parameters $a = 5.773(9) \text{ \AA}$, $b = 5.905(1) \text{ \AA}$, $c = 8.278(4) \text{ \AA}$, in the space group Pbnm.

Both results confirmed the formation of NaUO_3 by the reaction of UO_3 with sodium at 773 K under UHV conditions.

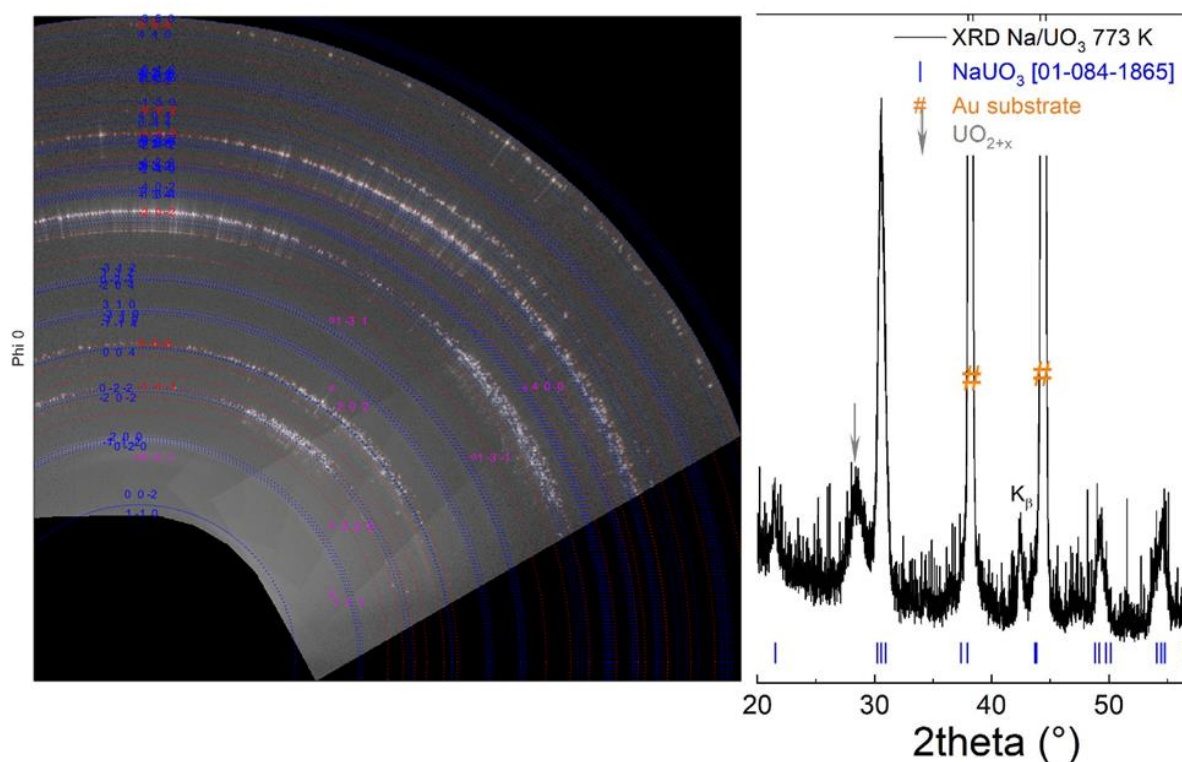


Figure 64: Left: Reciprocal Space Mapping (RSM) of the NaUO_3 phase produced in this study. Right: Corresponding GIXRD pattern of the NaUO_3 phase.

5.2.4 Oxidation by molecular oxygen

After deposition of metallic sodium on stoichiometric uranium oxide substrate, Figure 60, the sample was introduced to $\text{PO}_2 \sim 10^{-5}$ mbar and heated at 673 K. Figure 65 reports the U4f, Na1s and O1s core level spectra of the obtained film. When compared with the starting spectra (Figure 60), under oxygen and a heat treatment of 673 K, the U4f core level spectrum changed by displaying an apparent single peak at 380.2 eV for $\text{U}4f_{7/2}$, while the satellite peak displayed two component located at 6.8 eV and at about 8.7 eV. The former satellite peak was linked to U(IV), instead the latter was close to the one expected for U(V) satellite BE. The plasmons of Na1s and the double peak of O1s were replaced by a single peak at 1072 eV characteristic of oxidized sodium and at 530.5 eV for oxygen respectively.

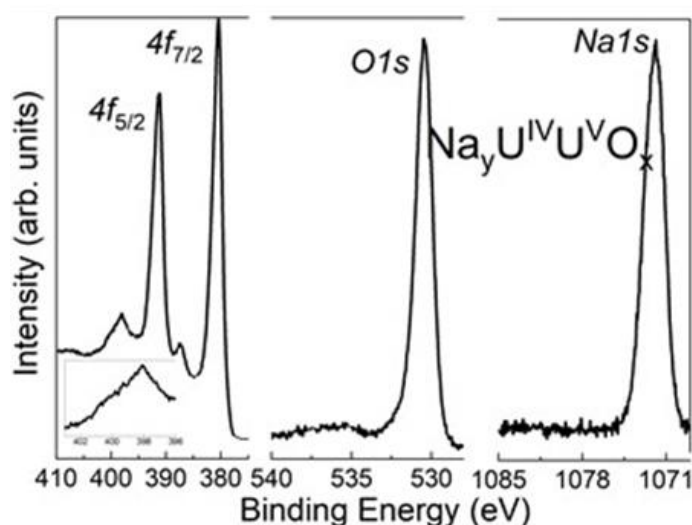


Figure 65: U4f, Na1s and O1s core level spectra after oxidation by molecular oxygen at 673 K of the film of sodium on stoichiometric uranium oxide

The same exposure and heat treatment were performed after deposition of metallic sodium on hyper-stoichiometric uranium oxide. When sodium was first in contact with UO_{2+x} , a reduction at room temperature of uranium into U(IV) took place together with a strong oxidation of sodium (Na1s shift of ~ 1.1 eV to higher BE). At this stage, the binding energy of U4f core level at 380.5 eV and 381.1 eV showed a mixed valence state, supported by satellite peaks made of two components at 6.6 eV and 7.6 eV from the main characteristic of U(IV) and U(V) respectively.

The corresponding O1s single peak was at 530.2 eV. The deposition of sodium at ambient temperature on reported UO_{2+x} showed the reduction into UO_2 with $\text{U}4f_{7/2}$ BE at 380.6 eV with its satellite peak at 6.8 eV higher than BE. The O1s core level peak was herein located at 530.7 eV, with a shift of 0.5 eV. Between 535 and 540 eV, a broad and flat peak was present. At the binding energy of 1072.8 eV was located a single peak of Na1s. After oxidation of this latter film with molecular oxygen at 673 K, the appearance of a single and well-defined peak of U4f was observed and expected for a homogeneous compound.

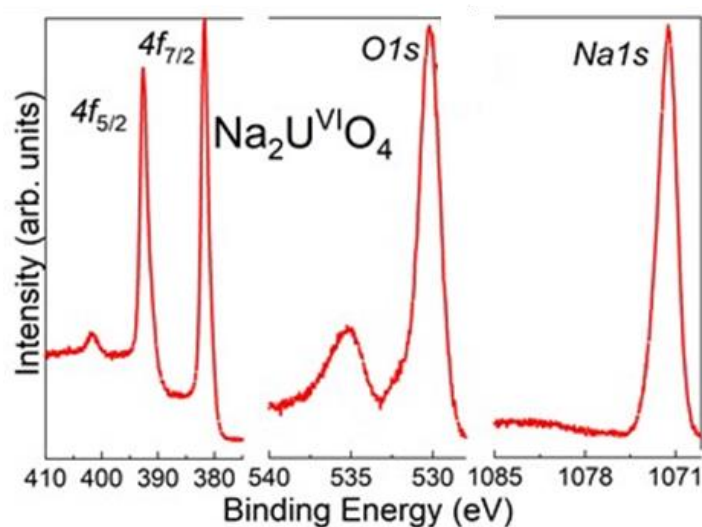


Figure 66: *U4f, Na1s and O1s core level spectra after oxidation by molecular oxygen at 673 K of the film of sodium on hyper-stoichiometric uranium oxide*

As illustrated in Figure 66 the effect of a temperature at 673 K induced Na1s shift of 1.1 eV to lower BE and U4f shift of 1.1 eV to higher BE. For O1s, two peaks appeared at 530 eV and 535.1 eV. This latter, if not linked to Auger NaKLL peak, associated to U4f and Na1s correlated BE shift, supporting the formation of a ternary compound Na-U-O with single oxidation state. Considering a higher oxidation of sodium when sodium is deposited on hyper-stoichiometric UO_{2+x} (in comparison to the sodium deposition on stoichiometric UO_2), the presence of sodium oxide in the form of Na_2O_2 (versus Na_2O) could be present. This former would increase the oxidation and reactivity with uranium.

5.3 Conclusion

To answer the question about the oxidation state of the corrosion layer, the synthesis of ternary compound and interaction studies were carried out under ultra-high vacuum. Metallic sodium tends to reduce hyper-stoichiometric uranium oxide and under thermal treatment, the stabilization to pure pentavalent uranium was observed. This clearly indicates that in storage conditions, ternary compound with U(V) oxidation state are potentially formed rather than compound with higher oxidation state. Considering that at room temperature sodium reduces uranium trioxide, UO_3 , to uranium oxide, UO_2 , through the formation of heterogeneous layers ($\text{Na}_2\text{O} + \text{UO}_{2+x}$), it was evident that the compound developed through thermally activated interdiffusion of sodium and hyper-stoichiometric uranium oxide. The results showed also that once U(V) was formed, it remained stable up to at least 973 K (in this study).

There is little evidence in literature about XPS on a bulk sample of NaUO_3 . The U-4f spectra by Liu et al [74] are displayed in Figure 67 together with $\text{Ba}_2\text{U}_2\text{O}_7$ bulk samples and compared

to the NaUO_3 film obtained in our present study. The binding energies and presence of the satellite peaks are similar. The better resolved the “8 eV” satellite peak for the NaUO_3 film can be due to the disorder or changes of stoichiometry induced by Ar ion sputtering, used by Liu et al. [74] to clean the surface. On the other hand, in-situ synthesized samples do not require any cleaning. The bulk sample of $\text{Ba}_2\text{U}_2\text{O}_7$ exhibits very similar spectrum, shifted by 0.6 eV towards higher binding energies due to a different chemical environment.

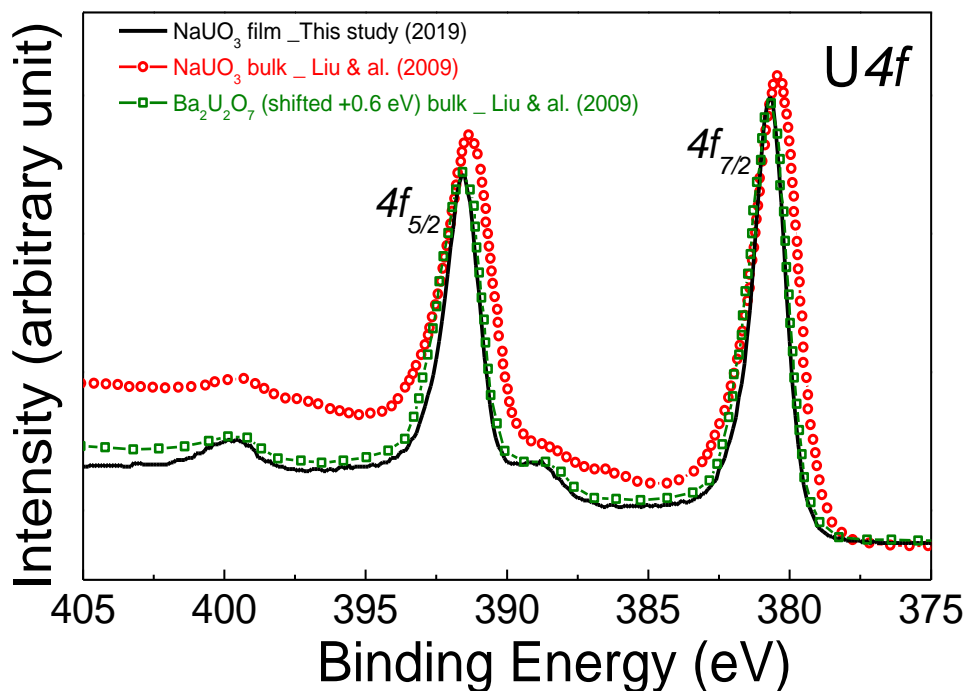


Figure 67: NaUO_3 film obtained in the present study compared to $\text{Ba}_2\text{U}_2\text{O}_7$ and NaUO_3 bulk

In agreement with the calculated phase diagram at room temperature illustrated in Figure 68, thermodynamic, this study corroborated that sodium does not reduce stoichiometric UO_2 at room temperature. Following the dash lines, which indicate the experimental conditions of this study, when pure metallic sodium is deposited on stoichiometric uranium oxide, there is a formation of heterogeneous system in which the two layers, uranium oxide covered by sodium, do not react. At room temperature, deposition of metallic sodium on UO_3 leads to a complete reduction from U(VI) to U(IV). On the calculated phase diagram (at room temperature), illustrated in Figure 68 (right), this can be interpreted as the progressive reduction of hyperstoichiometric uranium oxide due to the continuous addition of metallic sodium. The system is still heterogeneous and constituted by two layers, uranium oxide covered by sodium oxide. Formation of ternary compound was not observed at this stage.

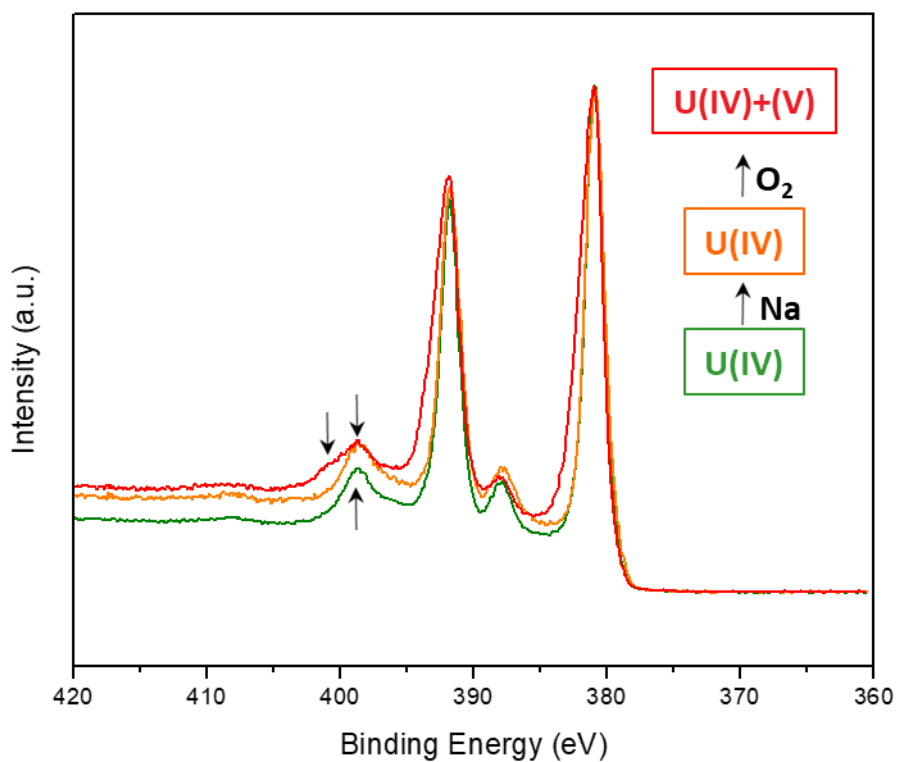


Figure 69: U4f core spectra for the oxidation by molecular at 673 K after deposition of sodium on stoichiometric uranium oxide UO_2 .

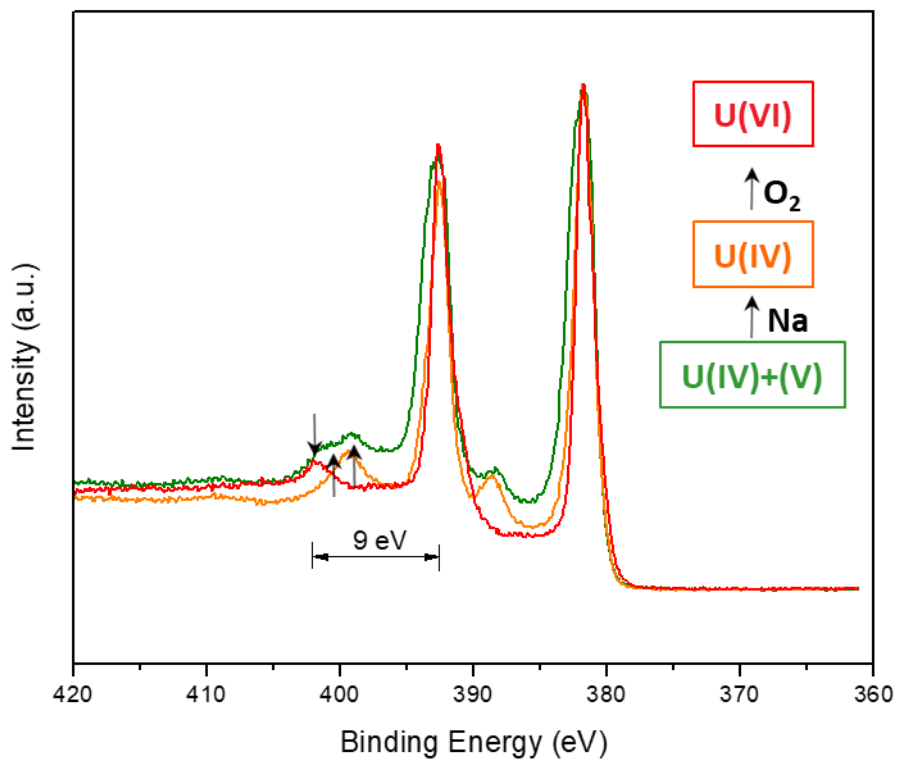


Figure 70: U4f core spectra for the oxidation by molecular at 673 K after deposition of sodium on hyper-stoichiometric uranium oxide UO_{2+x} .

6 *Compatibility tests*

Ce chapitre vise à étudier le processus de germination et à identifier les principales caractéristiques de la réaction oxyde –sodium, comme l’impact potentiel de l’orientation cristalline ou la pénétration du sodium le long des joints de grains. Pour ce faire des tests d’interaction en capsules étanches ont été réalisées dans différents conditions en utilisant des mono ou des polycristaux de dioxyde d’uranium. Les échantillons ont été caractérisés après les tests d’interaction par diffraction des rayons X, MEB-EDX et MET. Ces examens ont confirmé le mécanisme de germination instantanée. L’uranate de trisodium se forme dans les conditions expérimentales des tests de compatibilité. La caractérisation des phases formées a mis en évidence que la phase de corrosion avait une orientation préférentielle, mais qui ne dépendait pas de l’orientation des grains d’oxyde sous-jacents. Toutefois, l’épaisseur de la couche de corrosion est indépendante de l’orientation des grains. Le sodium ne pénètre pas dans les joints de grains lorsqu’il interagit avec le dioxyde d’uranium, même en présence d’oxygène dissous dans le sodium en relativement grandes quantités.

6.1 *Introduction*

The main aim of this experimental section is to provide information about the nucleation process of the reaction between sodium and uranium oxide. In addition to the nucleation process, the purpose is to achieve a better understanding of the reaction through several compatibility tests. The reaction between liquid sodium and uranium oxide was investigated via so-called compatibility tests, i.e. heat treatment of uranium oxide samples with liquid sodium in closed stainless steel capsules. The corrosion tests hereafter presented covered an initial oxygen concentration in the range between 10 and up to 1000 ppm. Table 14 summarizes the performed interaction tests and the corresponding conditions.

Each test was performed at 1073 K for 50 h. The initial concentration of oxygen due to “glovebox impurities” was evaluated to be about 10 ppm. Instead, the addition of sodium oxide (NaO_2 Aldrich 80% ($\text{NaO}_2 + \text{Na}_2\text{O}_2$)) increased the initial oxygen concentration up to 1000 ppm. A unique test with a pre-oxidized UO_2 was carried out to check whatever an excess of oxygen of the UO_2 may have an influence on the reaction. The oxidation of the latter took place in air, at 350°C per 1h. The recorded XRD pattern after the oxidation, as reported in Figure 71, showed the appearance of a slight surface oxidation corresponding to the U_3O_7 phase. Scanning Electron Microscopy (SEM) characterization did not exhibit the appearance of surface damage due to the oxidation process.

Table 14: Test matrix for corrosion resistance tests

<i>Sample number</i>	<i>Orientation</i>	<i>Oxygen</i>	<i>Temperature (K)</i>	<i>Time (hours)</i>
NAINT1	111	Glovebox impurities	1073	50
NAINT2	001	Glovebox impurities	1073	50
NAINT3	Polycrystalline	Glovebox impurities	1073	50
NAINT 4	001	Pre-oxidation + Glovebox impurities	1073	50
NAINT5	111	Sodium Oxide	1073	50
NAINT6	Polycrystalline	Sodium Oxide	1073	50

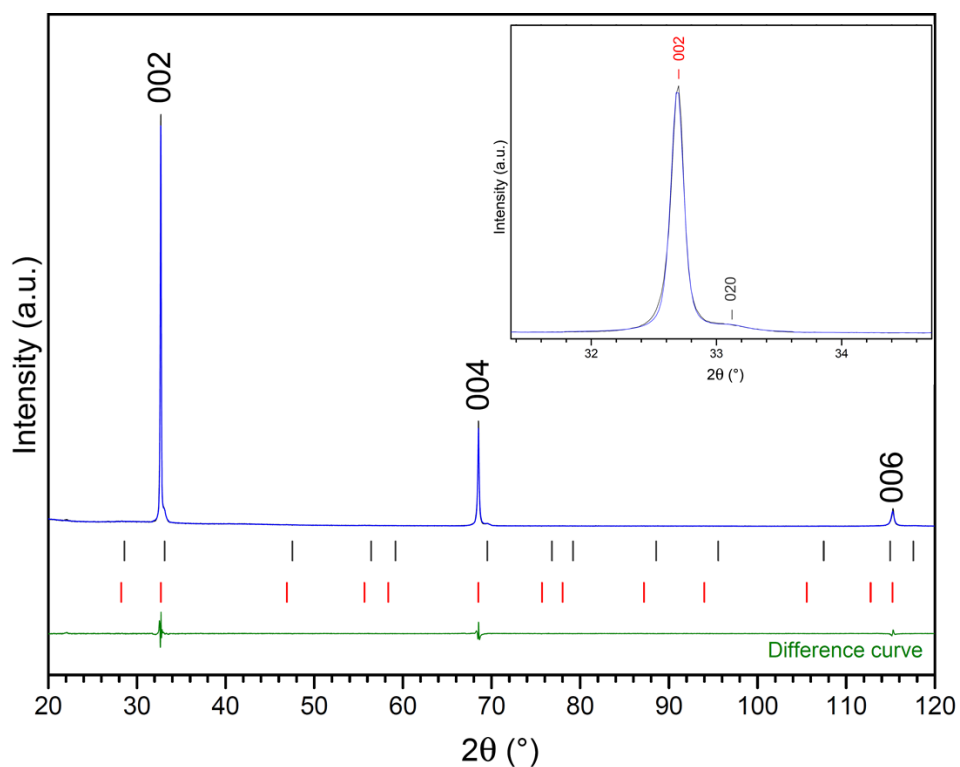


Figure 71: XRD of the single crystal 001 after oxidation in air at 350 °C for 1 h. Red: UO_2 and Black: U_3O_7 . The sample was slightly oxidation to U_3O_7

6.2 *Reaction products characterization*

The structural characterization of the reaction product was established by X-Ray Diffraction (XRD) and Transmission Electron Microscopy (TEM). Structural analyses were performed using Jana2006 software. Energy Dispersive X-ray Spectroscopy (EDX) was used as support of the elemental composition determination, in order to corroborate the potential chemical form of the formed phase. The characterization of the nature and the extent of the reaction product was determined by using Scanning Electron Microscopy (SEM). Image analyses were carried using ImageJ software.

6.2.1 *Phase identification*

As result of the interaction between uranium oxide and liquid sodium, a reaction product was obtained together with unreacted uranium dioxide. Table 15 summarized the XRD results obtained from the tests NAIN1, NAIN3 and NAIN4. XRD was not carried out on NAIN2 due to the fact that it was unintentionally cut in several pieces during the capsule opening. On the latter, the presence of the reaction product was observed through SEM and will be presented in dedicated paragraph in the following.

A representative XRD pattern, measured on a corroded single crystal, is shown in Figure 72. The Bragg reflection at 2θ value of 22° is a characteristic peak of the silicon sample holder and then not taken into account for the phase identifications. The unreacted uranium dioxide was found unchanged and exhibited a lattice parameter of $5.47(1) \text{ \AA}$, in agreement with stoichiometric uranium dioxide phase. Considering a uniform appearance of the corrosion layer and taken into account the penetration depth of X-ray, the detection of uranium oxide, even at low angles, indicated that the reaction product should be confined at the sample periphery and having approximately a thickness less than $5\mu\text{m}$. The measured reaction product corresponded to the cubic phase of trisodium uranate Na_3UO_4 . The unit cell parameter of this phase was determined as $4.78(7)\text{--}4.79(1) \text{ \AA}$ using Jana2006 pattern matching. The resulted patterns were collected from the sample surface of single crystal and polycrystalline samples, and then Rietveld refinement was not performed for the phase identification.

XRD analysis of single crystals and polycrystalline samples indicated that the trisodium uranate phase showed a preferential growth, along certain orientations, independently from the substrate orientation. This point will be presented in dedicated paragraphs in the following.

Table 15: Summary of the XRD results

Sample number	Unreacted surface orientation	Phases after reaction	Space group	Reacted surface orientation	Lattice parameter Å
NAINT1	UO ₂ 111	UO ₂	Fm-3m	111	5.47(1)
		Na ₃ UO ₄	Fm-3m	111	4.78(7)
NAINT4	UO ₂ 001	UO ₂	Fm-3m	001	5.47(1)
		Na ₃ UO ₄	Fm-3m	111-001	4.79(1)
NAINT3	UO ₂ Polycrystalline	UO ₂	Fm-3m	All	5.47(1)
		Na ₃ UO ₄	Fm-3m	All	4.78(7)

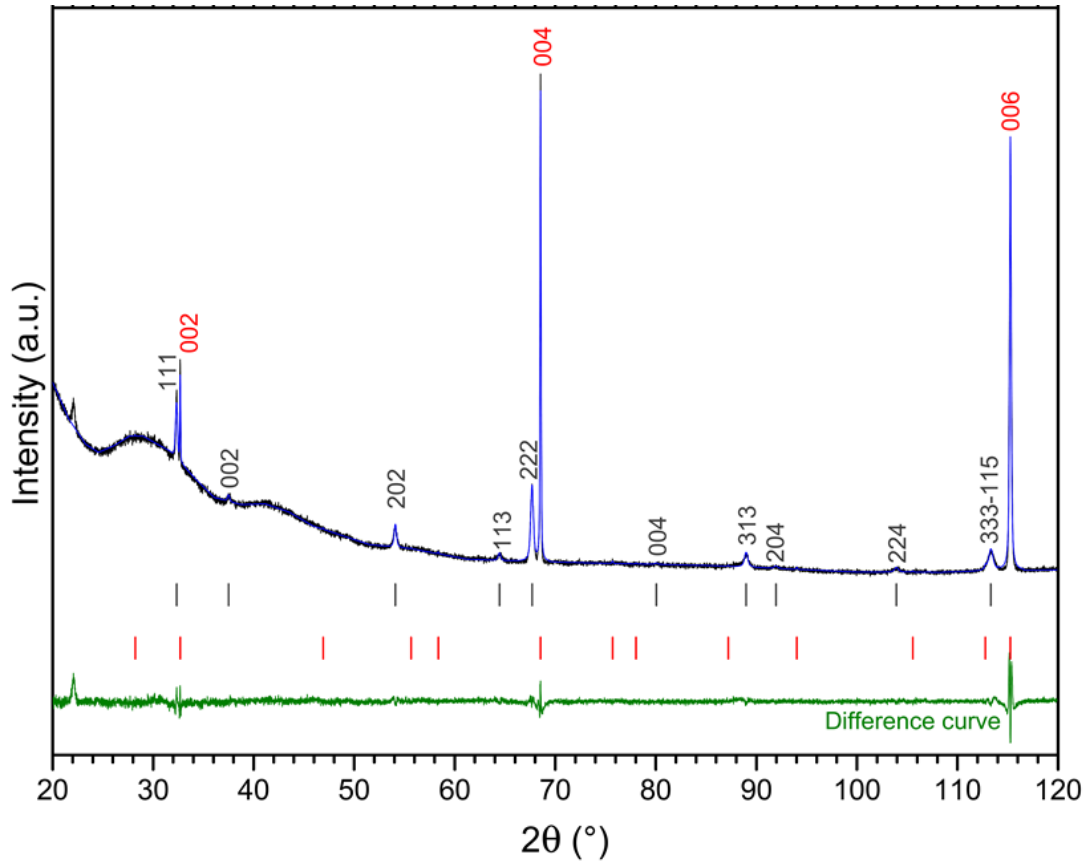


Figure 72: Characteristic XRD pattern of the single crystal having the surface well oriented on the {001} direction (NAINT4). Red index: UO₂ phase. Black index: Na₃UO₄ phase.

The identification of Na_3UO_4 in the corrosion layer was confirmed by TEM analysis of lamella prepared by FIB on the surface of NAIN4 sample. Figure 73 shows the ring diffraction pattern of a selected area of the trisodium uranate.

The ring pattern with the Miller indices according to the interplanar spacing of the crystal structure is given. Interplanar spacing and lattice parameter were determined by analyzing the ring diffraction pattern. Ring indexing was made applying the following relationship [102]:

$$Rd_{hkl} = L\lambda \quad (37)$$

where R is the distance between collision points of transmitted and diffracted beams with the screen, d_{hkl} is the interplanar spacing, L is the distance between the specimen and the screen and λ is the wavelength. The used transmission electron microscope operated at an accelerating voltage of 200 kV with a wavelength λ of 2.5 pm and camera length L of 180 mm. The scale on the picture of patterns was defined and then used to measure the radius diffraction pattern of specimen. However, the accuracy and focus of TEM were very important to obtain accurate results. In the present study, the error was evaluated to be approximately $\pm 10\%$.

The calculated lattice parameter corresponded to 4.78(6) Å, in agreement with XRD analysis. Moreover, the results indicated that the product layer was characterized by a cubic crystal structure.

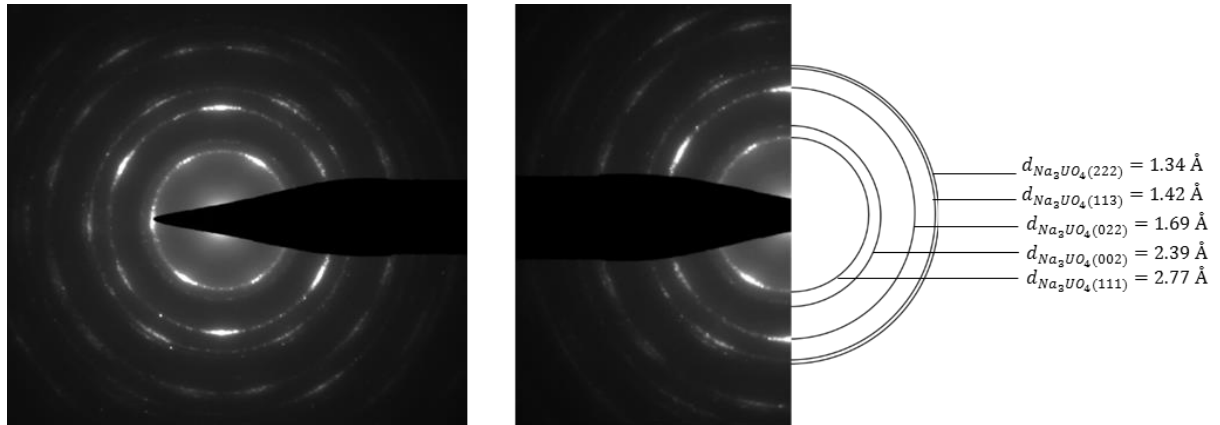


Figure 73: Left: Ring diffraction pattern from the corrosion phase with a cubic crystal structure. Right: Crystal planes and interplanar spacing by Miller indices.

6.2.2 Elemental composition

Analysis by Energy Dispersive X-ray Spectroscopy (EDX or EDS) was a useful complementary approach to identify qualitatively the chemical elements present in the sample. The concentration of each specific element was measured by the intensities of peaks, leading to a

quantitative estimation of the relative compositions. An example of the characteristic EDX spectra obtained from the sample surface characterization is shown in Figure 74. The spectra were recorded in selected area of interest on the sample surface. Peaks at 0.525, 1.041 and 3.164 keV corresponded to the energy level of oxygen, sodium and uranium (with an additional peak at 13.612 keV), respectively. The spectrum displayed then that the sample contained the three chemical elements, which are expected for the reaction product Na_3UO_4 at the surface. Although the oxygen quantification was fairly inaccurate, probably due to some external contamination, the combination between the measured phase by XRD and the qualitative uranium and sodium ratio detected by EDX was in good agreement with the composition of trisodium uranate Na_3UO_4 as reaction product. However, additional analysis such as EPMA are suggested for a better quantification.

EDX analysis of several zones showed that the surface was somewhere covered by sodium oxide. The latter exhibited the characteristic sheet-shape. The appearance of sodium oxide was most likely caused by residual sodium, which oxidized under the glove box atmosphere after sample removal from the experimental capsule. Thereby, the samples were cleaned several times with ethanol, to prevent, as far as possible, the formation of sodium oxide before each analysis.

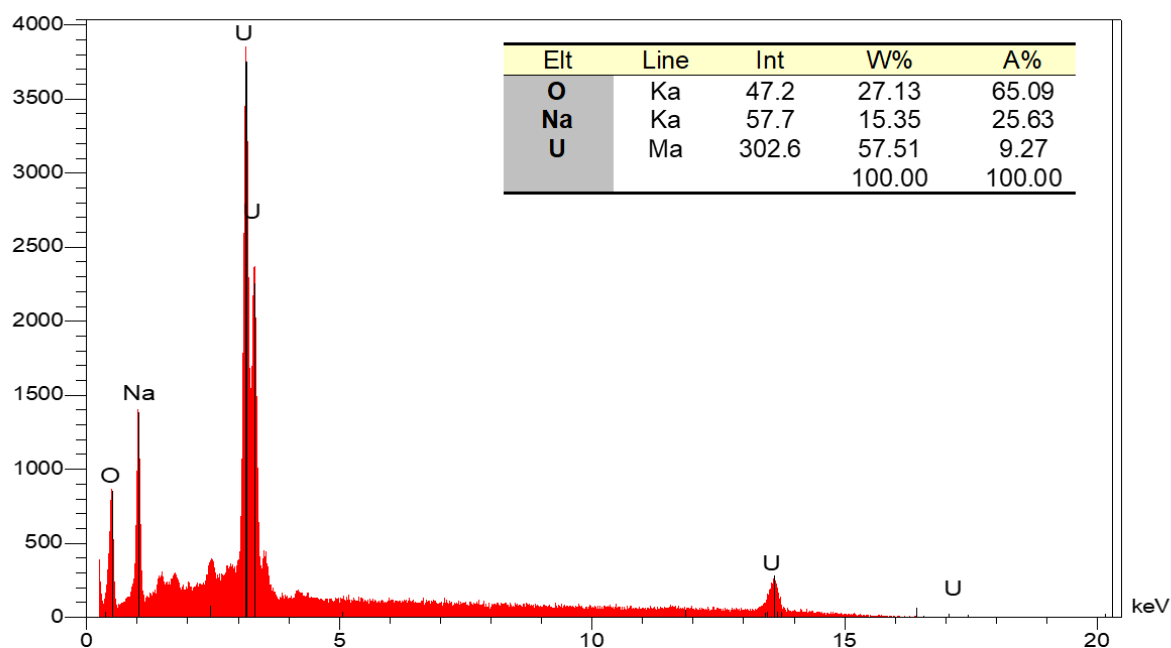


Figure 74: Example of a characteristic EDX spectrum reordered on the sample surface and the table with the corresponding element composition in weight % (w%) and atomic % (A%).

6.2.3 Influence of the crystallographic orientation

6.2.3.1 Surface with the $\langle 111 \rangle$ crystal lattice direction

The evaluation of morphological changes due to the interaction with liquid sodium was observed by SEM analysis [15]. The morphology of the grain surface is usually reported as having characteristic cracking. However, no indications of the influence of the grain orientation on the surface transformation are reported. Figure 75 shows the secondary-electron image of the surface of a single crystal having the orientation along the $\langle 111 \rangle$ crystal lattice direction before and after liquid sodium exposure. The morphology of the un-reacted single crystal was characterized by a rough surface as a result of the cutting process following the crystallographic orientation. The sample was not polished before the interaction test. The morphology of the reacted sample was still characterized by the characteristic roughness of the surface of the initial sample. The corroded surface seemed indeed not altered, even though the specimen had a relatively long exposure (50 hours) to molten sodium. When compared to the initial surface, the corroded surface did not exhibit visible cracks or significant damages.

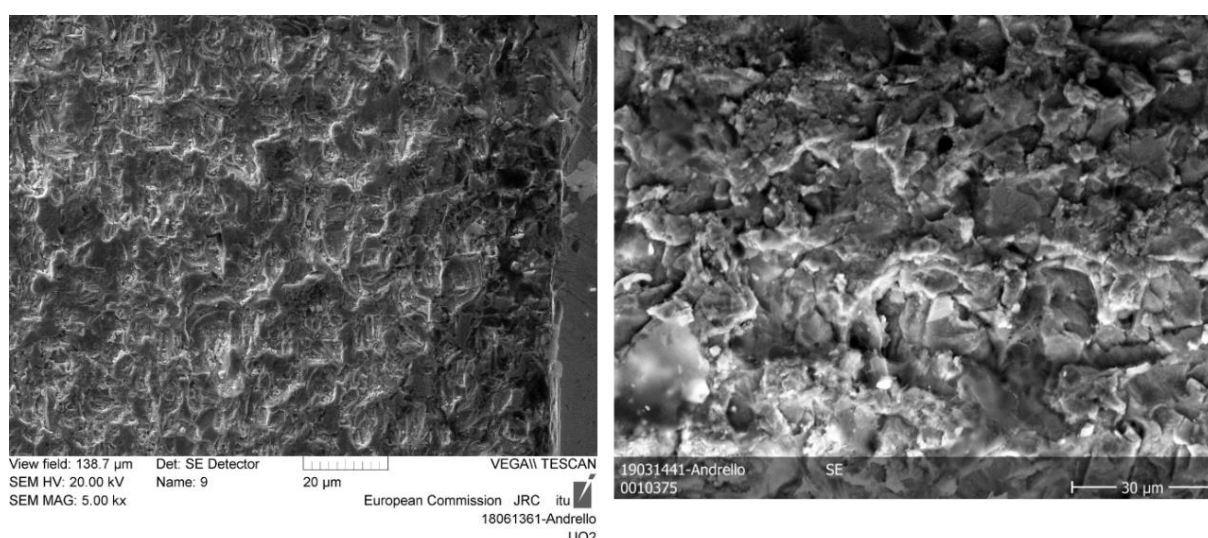


Figure 75: Comparison between the initial (a) and the corroded (b) surface of the single crystal $\langle 111 \rangle$ (NAINT1).

The morphology of the single crystal having the orientation along the $\langle 111 \rangle$ crystal lattice direction could be related to the preferential orientation of the trisodium uranate. The measured interaction product, as shown in Figure 76, do not exhibited the formation of a polycrystalline reaction product, but rather a well-oriented trisodium uranate phase. The reaction product showed indeed the orientation along the $\langle 111 \rangle$ crystal lattice direction as its substrate. The surface transformation of uranium oxide due to the reaction with liquid sodium seemed then to be influenced from the substrate orientation, at least in terms of morphology.

The preferred orientation of the Na_3UO_4 planes was confirmed by a TEM examination of a FIB lamella extracted at the sample surface after the interaction test. The diffraction pattern shown in Figure 73 in evidences diffraction rings with non-uniform intensity. Indeed, if the crystal structure in the specimen is oriented in a preferred direction, the pattern will be composed from

many partial rings. The position with the highest intensity on the diffraction rings correspond to the preferred orientation of Na_3UO_4 crystallites.

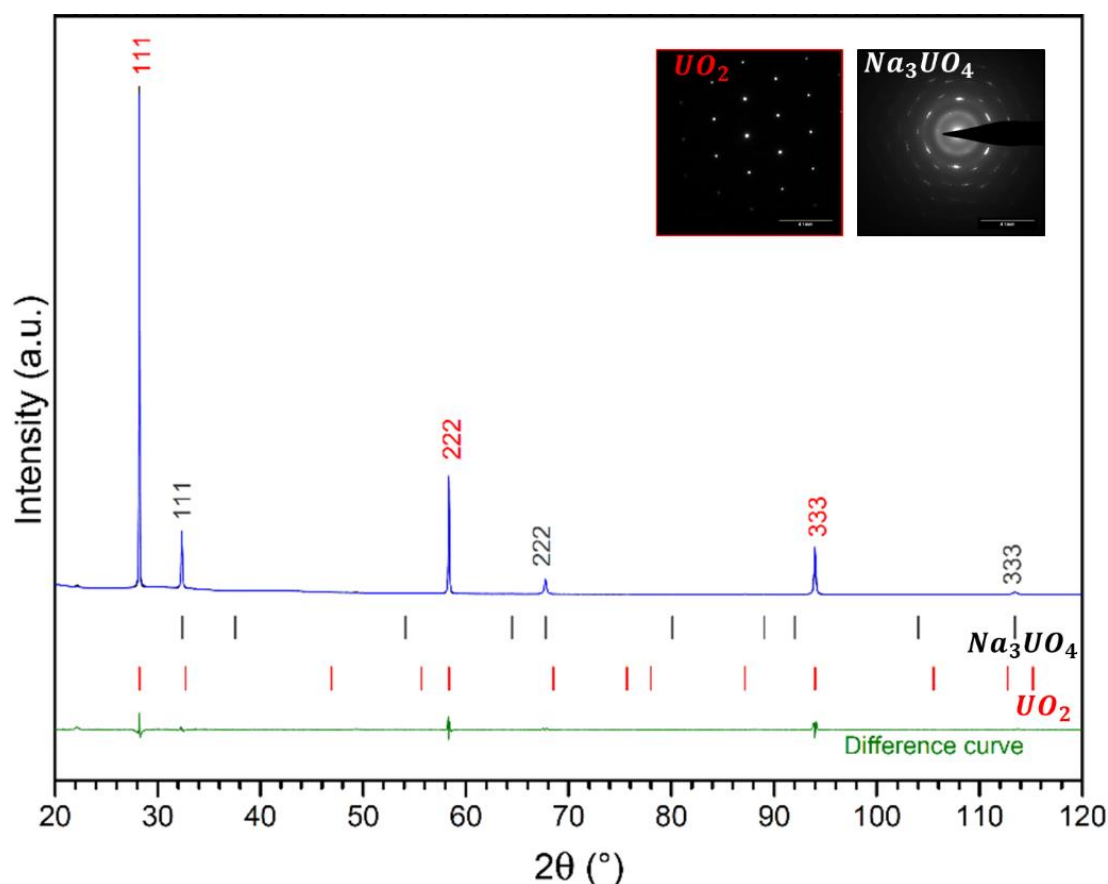


Figure 76: XRD of the single crystal with the $\langle 111 \rangle$ crystal lattice direction (NAINT1) and details of the ring diffraction of the UO_2 bulk and the Na_3UO_4 phase

6.2.3.2 Surface with the $\langle 001 \rangle$ crystal lattice direction

The attack of sodium on the single crystal oriented in the $\langle 001 \rangle$ crystal lattice direction was instead much more evident through the appearance of characteristic cracking as shown in Figure 77. The secondary-electron images display the UO_2 single crystal having the $\langle 001 \rangle$ crystal lattice orientation before and after liquid sodium exposure (NAINT4).

It was excluded that the cracking was induced by the relatively fast cooling rate of -200°C/h , because even at a lower cooling rate of -50°C/h , the cracking appeared (NAINT2), as illustrated in Figure 78.

In agreement with the XRD result (Figure 72), the new phase formed indeed as a polycrystalline phase and the formation of the cracks should thereby be linked to the reaction itself.

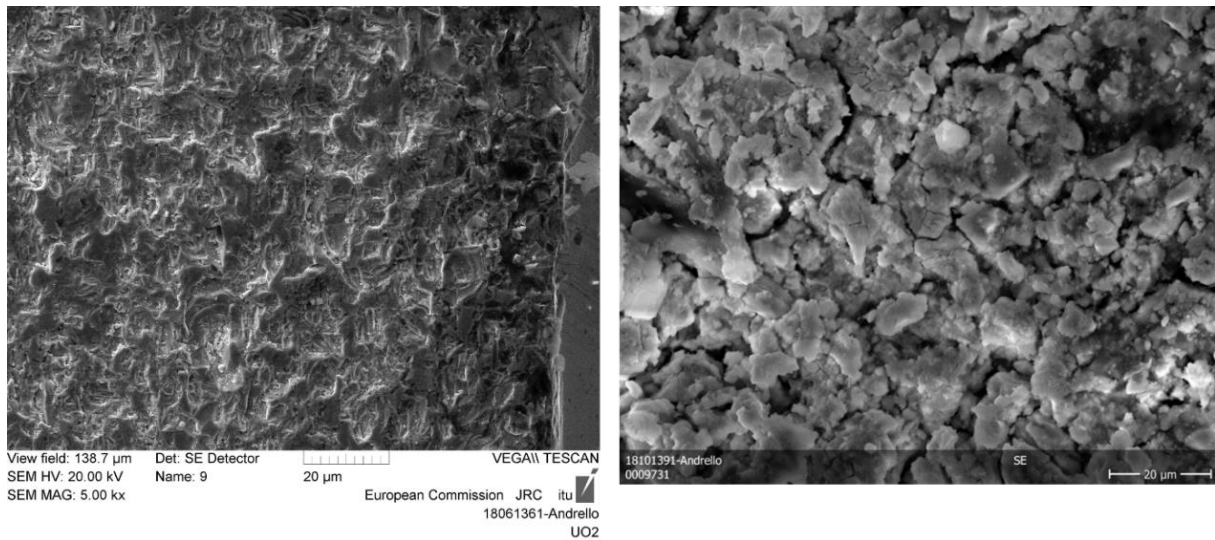


Figure 77: Comparison between the initial (a) and the corroded (b) surface of the single crystal $\langle 001 \rangle$ (NAINT4).

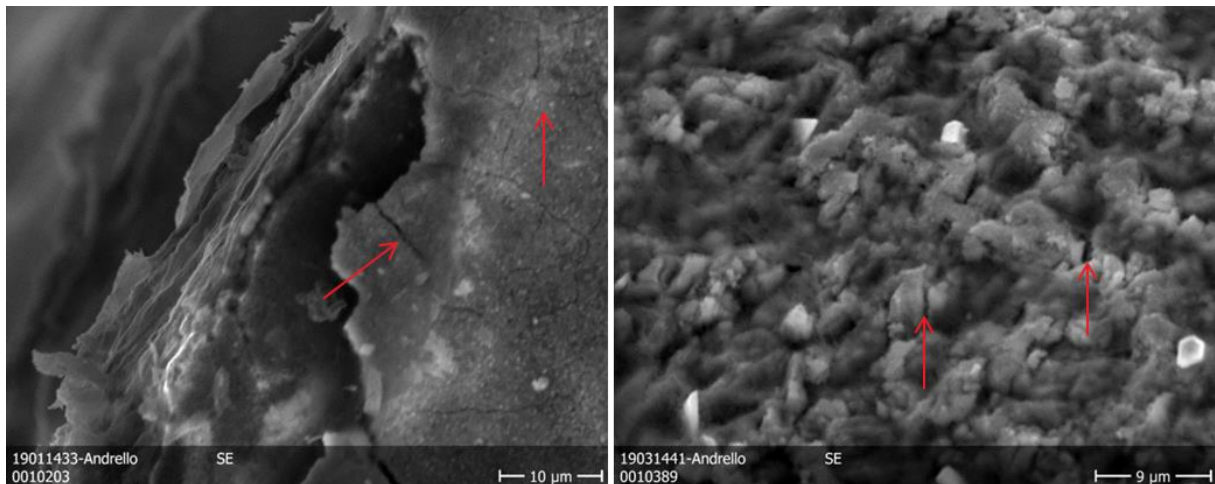


Figure 78: Corroded surface of the single crystal $\langle 001 \rangle$ (NAINT2).

6.2.3.3 Polycrystalline sample

The morphology of the grains of the polycrystalline sample, after 50 h of interaction at 1073 °C, reflected the results obtained from the single crystals. Grain boundaries were still clearly visible, and each grain showed different morphologies, in agreement with the previous observations of the surface transformation of the single crystals. In Figure 79 are shown the secondary-electron images of the polycrystalline sample before and after liquid sodium exposure. When the grain was oriented in the $\langle 111 \rangle$ direction, the surface of the corrosion layer, Na_3UO_4 , was relatively smooth, without cracks and also oriented in the $\langle 111 \rangle$ direction

(marked in red). However, when the grain was oriented in the $\langle 001 \rangle$ direction, the corrosion layer showed a similar cracking as was observed for the $\langle 001 \rangle$ oriented single crystal, and no clear orientation.

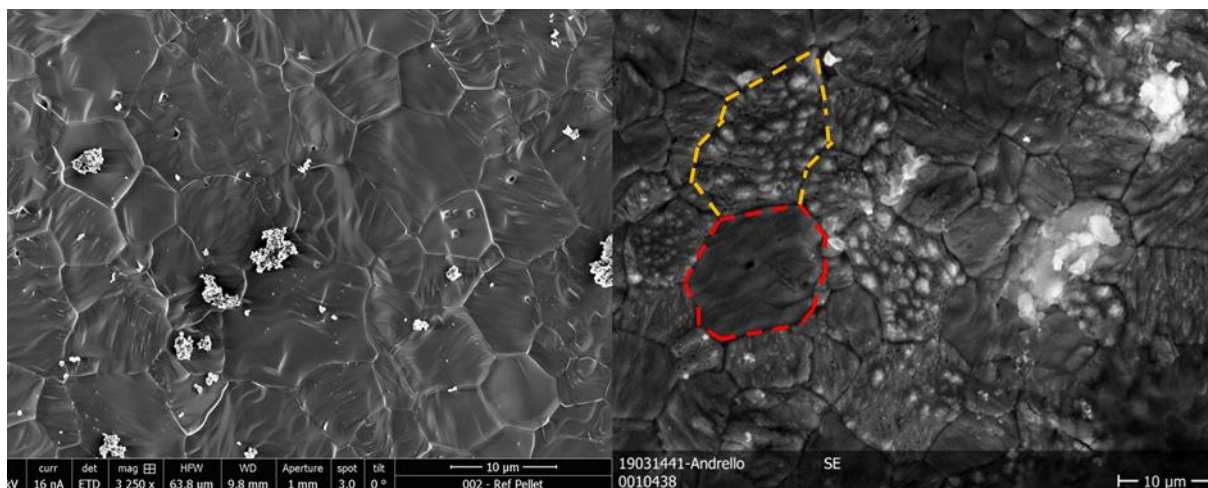


Figure 79: Comparison between the initial (left) and the corroded (right) surface of the polycrystalline sample.

6.2.3.4 Cross section

Due to the brittle nature of the corrosion layer and its potentially hygroscopic behavior, the resin embedding and polishing processes were avoided. Each sample was thereby mechanically broken in pieces in order to check the cross-section. Figure 80 illustrates the cross section view of the broken surface of single crystals and polycrystalline uranium oxide samples after the reaction with liquid sodium.

The sodium corrosion of uranium oxide after 50 hours at 1073 K resulted in the formation of a uniform corrosion layer. The corrosion layer was clearly visible through the appearance of a net boundary between the corrosion layer and bulk. The layer was fully developed, but appeared somewhere no completely adherent to the uranium oxide bulk. The un-adherence could be attributed to either the sample breaking procedure or the reaction product development. The formation of an un-adherent corrosion layer was already reported by Mignanelli et al. [15] for the reaction between stoichiometric uranium oxide UO_2 and liquid sodium. Then, the un-adherence could be likely considered as characteristic of the reaction product.

On the single crystal specimens, the formation of the product layer was observed at the periphery of the sample only, without intragranular penetration. The confinement of the corrosion layer to the sample periphery was also observed in the polycrystalline specimen. No penetration and grain boundaries attack by sodium was evident, even at high magnification. Consequently, for stoichiometric uranium oxide it may be assumed that the sodium penetration

along the grain boundaries does not occur without presence of additional oxygen and thereby does not lead to grain boundary attack.

The thickness of the corrosion layer was measured afterwards and resulted in a thickness of about 5 μm . The thickness of the layer was roughly the same for all the samples. The theoretical volume variation due to the presence of the corrosion layer should be close to $\sim 1\%$ of the initial volume. Nevertheless, no appreciable weight gain was measured, but neither a weight loss.

Although the surface transformation was characterized by different morphologies depending on the grain orientation, the extent of the reaction product did not show any dependence on the grain orientation or grain size (in the range of 5 to 20 μm). This means that the rate of the reaction was not influenced by the grain orientations, grain size or by the use of single crystal or polycrystalline specimens.

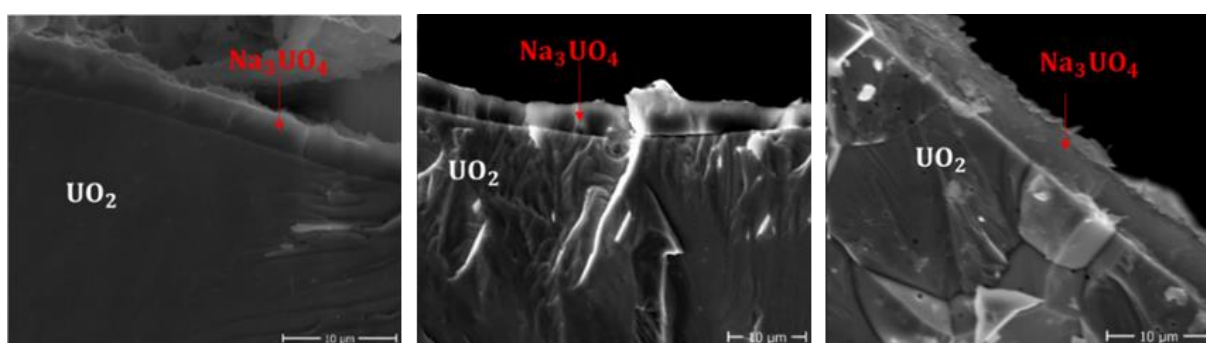


Figure 80: Cross-section view of the samples after the interaction with liquid sodium for 50h at 800°C. Left: single crystal $\langle 001 \rangle$ Middle: single crystal $\langle 111 \rangle$ Right: polycrystalline

6.2.4 Diffusion species

Particular interest was placed on the examination of the near-surface zone of the specimen, with particular focus on the interface between the product layer and the bulk. Indeed, the surface was the zone exposed to liquid sodium and the interface is the one of major interest for the understanding of species diffusion. With the main purpose of investigating the potential sodium diffusion into stoichiometric uranium oxide, Energy Dispersive X-ray Spectroscopy (EDX) was performed. Figure 81 reports an example of a characteristic EDX-line scan pattern recorded across the boundary between the bulk and the corrosion layer. The line-scan was the results of the measurements done on 40 points located at a distance of about 0.1 μm each other. Oxygen measurement was not reported because not relevant in view of the potential sodium diffusion into uranium oxide. The resulted pattern showed the appearance of sodium only at the proximity of the corrosion layer and thereby no sodium diffusion into stoichiometric uranium oxide could be observed, within the accuracy of the geometrical beam size (of about 1.5 μm). As for the EDX results of the surface, the U/Na ratio in the corrosion layer was in good agreement with the one expected for the chemical composition of the trisodium uranate Na_3UO_4 compound.

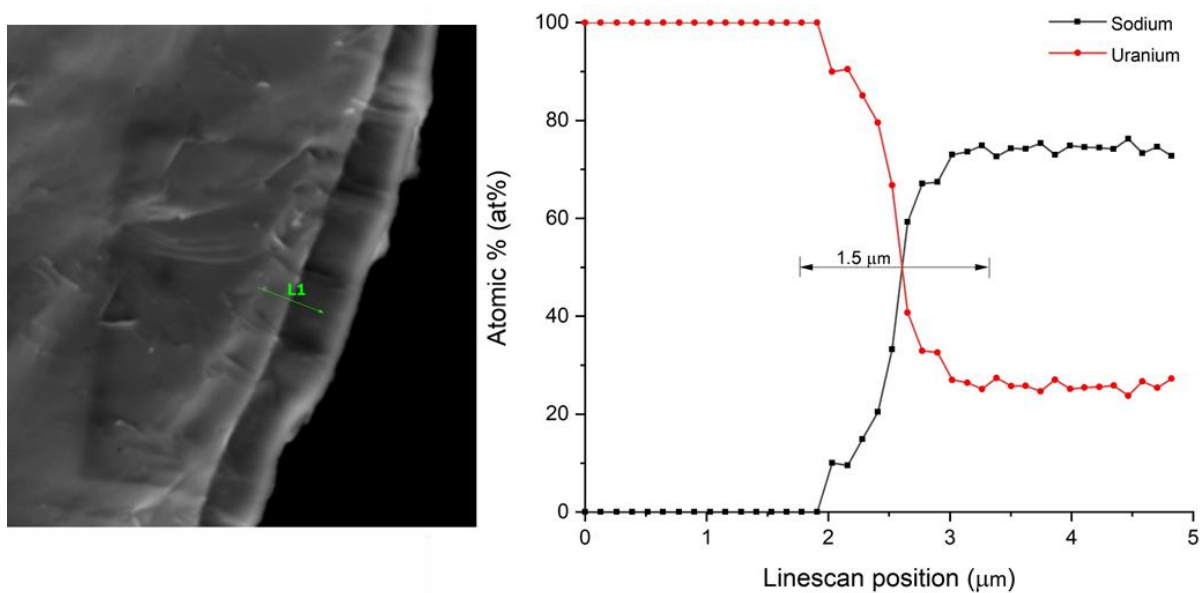


Figure 81: EDX line-scan across the boundary bulk-new phase. No diffusion of sodium into the UO_2 bulk was measured. The geometrical size of the beam is close to $1.5\text{-}2\mu\text{m}$ and leads to a not well defined border with the new phase.

6.3 Excess of oxygen

Hereafter are presented the observations made on the UO_2 samples after the reaction with sodium and in which sodium oxide was added. Despite the addition of sodium oxide, each sample was recovered still intact after the interaction. Surface transformation was checked through SEM characterization. Figure 82 and Figure 83 show the secondary-electron images of the corroded surface of the single crystal having the orientation along the $\langle 111 \rangle$ crystal lattice direction and the polycrystalline specimens, respectively. The first significant observation came from the comparison between the single crystal tested in liquid sodium containing few ppm of oxygen (Figure 75) and the one with addition of sodium oxide (Figure 82). In the latter case, the attack of the sodium was much more pronounced and the corroded surface appeared visibly damaged through the presence of cracks. Nevertheless, even in this case, the corrosion layer was uniform and confined to the sample periphery. After a repeated cleaning by ultra-sound, the corrosion layer was partly removed, probably due to the partly missing adherence between the uranium oxide bulk and the corrosion layer, which was also observed previously.

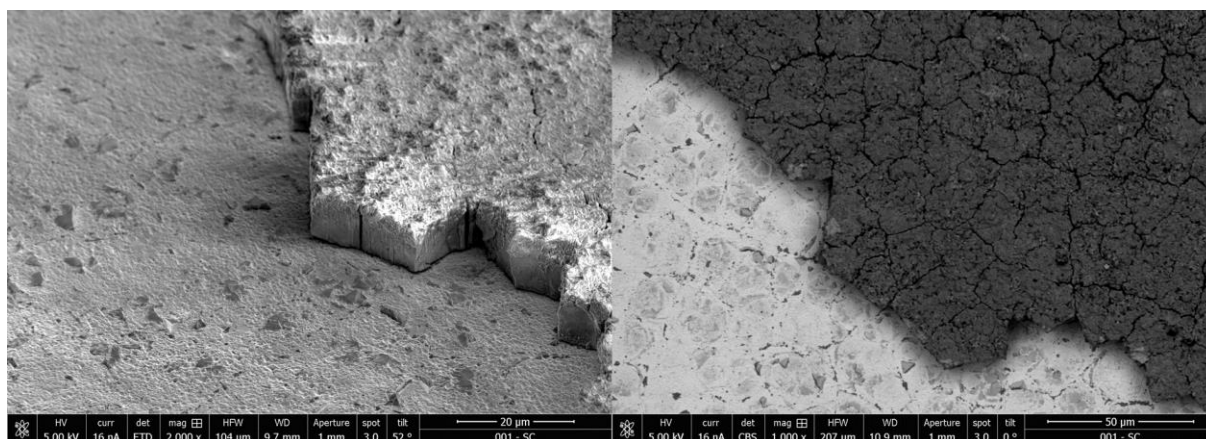


Figure 82: Single crystal after 50h interaction at 1073 K with liquid sodium containing sodium oxide. Left: tilted view of the sample surface showing the presence of a uniform corroded layer. Right: top view of the corroded surface.

The inspection of the interface between uranium oxide bulk and corrosion layer revealed the appearance of well-defined cracks. These exhibit a characteristic hexagonal shaped structure typical of the UO_2 oxidation products at 350°C. This can perhaps be attributed to a fast oxidation, which may have taken place before the corrosion layer formation. Moreover, taken into account that the extent of the reaction product was greater than the one observed previously, it is reasonable to assume that the oxygen diffusion was faster than the diffusion of sodium, especially since no diffusion of sodium is allowed into stoichiometric UO_2 .

The polycrystalline specimen did not show the initial grain boundaries after the interaction test, which is contrary to the observations of the polycrystalline specimen tested without sodium oxide. The surface appeared completely covered by the corrosion layer, which was once again visibly damaged through the presence of characteristic cracks. However, even in the presence of sodium oxide, the corrosion layer was confined to the pellet periphery and no grain boundaries penetration occurred.

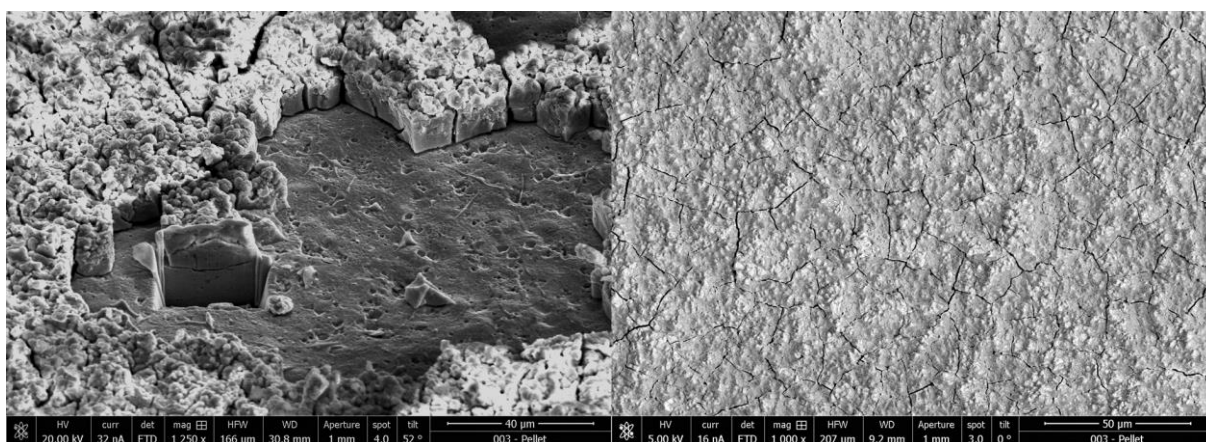


Figure 83: Polycrystalline sample after 50h interaction at 800°C with liquid sodium containing sodium oxide. Left: tilted view of the sample surface showing the presence of a uniform corroded layer. Right: top view of the corroded surface.

In agreement with what was observed previously, no influence of the grain orientation and grain size was observed on the reaction layer morphology and reaction extent. Indeed, the thickness of the corroded layer was measured and resulted to be about 8 μm in both, single crystal and polycrystalline specimens, with a theoretical variation of the initial volume of $\sim 2\%$.

TEM measurements were performed on a 50 nm-thick lamella extracted from the sample NAIN5. Diffraction measurements were carried out through the whole lamella length, from the uranium oxide bulk to the corrosion layer. The preferred orientation of the planes was observed also through the ring diffraction pattern as shown in Figure 84 Right. The results indicated that the product layer was characterized by a cubic crystal structure.

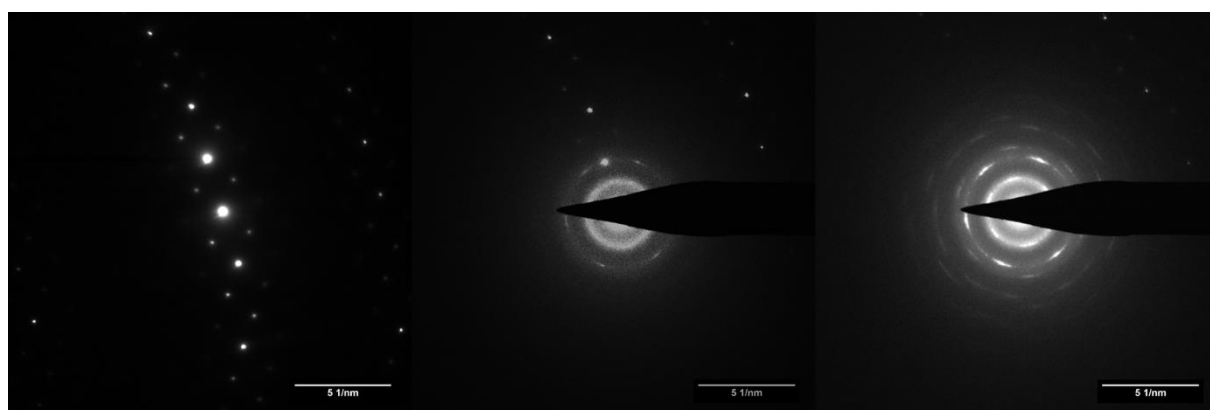


Figure 84: Left: Uranium bulk. Middle: interface between the bulk and the corrosion layer. Right: Corrosion layer

6.4 Conclusions

The present study confirmed that nucleation is an instantaneous process during the reaction between liquid sodium and uranium oxide. The reaction product developed uniformly and covered the whole sample surface either for low or high initial oxygen concentration.

Although the surface transformation was characterized by different morphologies depending on the grain orientation, the extent of the reaction product did not show any dependence upon the grain orientation neither from their dimensions (in the range 5 to 20 μm). This means that the rate of the reaction was not influenced by the grain orientations and size. The results are not affected by the use of single crystal or polycrystalline specimens. The corrosion layer resulted not fully adherent to the uranium oxide bulk. The un-adherence could be attributed to either the sample breaking procedure or the reaction product development. The formation of an un-adherent corrosion layer was already reported by Mignanelli et al. [15] for the reaction between stoichiometric uranium oxide UO_2 and liquid sodium. Then, the un-adherence could be likely considered as characteristic of the reaction product.

The inability of the sodium to diffuse into stoichiometric UO_2 was corroborated, within the accuracy of the EDX. Although the extent of the reaction was affected by the oxygen

concentration, the physical form of the corrosion layer did not show any depends from the oxygen availability. The corrosion layer appears indeed as a uniform layer and confined at the periphery of the sample in both cases. If oxygen impurities are present as dissolved in liquid sodium, the reaction with stoichiometric uranium oxide did not result in a disintegration of the samples, even in presence of excess of oxygen (up to 1000 ppm). This result is not consistent with the loose corrosion layer [23], or the complete disintegration of the uranium oxide samples that were reported in literature [15] as consequence of the addition of few mg up to about 1 g of sodium oxide, respectively, to metallic sodium.

The same was valid in the case of a slightly oxidized uranium oxide (U_3O_7). Grain boundaries attack did not take place in the polycrystalline samples, neither at low and high oxygen availability. Indeed, it seems reasonable that grain boundaries attack by liquid sodium can be allowed in presence of hyper-stoichiometric uranium oxide only. The presence of oxygen at the boundaries should be thereby necessary to allow reacting with sodium.

Finally, the formation of the trisodium uranate Na_3UO_4 phase was obtained at 1073 K after 50 hours of interaction in presence of excess of liquid sodium. The lattice parameter of this phase was in good agreement with these reported in literature by Scholder and Gläser [67] with a cell parameter 4.77(3) Å and Pepper [103] with a cell parameter 4.79-4.80 Å. However, Smith et al. [80] did not observed this phase at 1073 K after 12 hours of reaction, but rather a low temperature phase *m*- Na_4UO_5 , with a cell parameter 4.764(3) Å.

The cubic crystal symmetry and the lattice parameter of 4.78(6) Å were also confirmed through ring diffraction analysis, obtained by TEM. The formation of the trisodium uranate in presence of excess of metallic sodium, as suggested in literature [83], can be thereby supported by the present study. Trisodium uranate showed a preferential growth, along $\langle 111 \rangle$ orientation, independently from the substrate orientation. The preferential growth was confirmed by TEM diffraction. The initial orientation of the grains could affect the morphological aspect of the corroded surface, but it did not influence the reaction extent. The formation of the trisodium uranate Na_3UO_4 as pentavalent compound could be also supported by the previous observations obtained by the XPS studies, in which the stabilization of a ternary compound with U(V) is expected for interaction of UO_2 with an excess of metallic sodium. Since the amount of oxygen dissolved in liquid sodium was closed to 10 ppm, the formation of the Na_3UO_4 was also expected under the thermodynamic conditions of the experiments.

7 *Kinetic studies: imposed oxygen potential*

Dans ce chapitre, on vise à décrire le processus de croissance, et plus particulièrement le sens du développement de la couche de corrosion ainsi que la nature de l'étape limitante. Pour ce faire, des tests d'interaction, avec un potentiel oxygène fixé, ont été réalisés en utilisant un tampon REDOX. Les échantillons ont été caractérisés après les tests d'interaction par diffraction des rayons X en incidence rasante, MEB-EDX et MET. Ces examens ont permis de mesurer la cinétique de croissance de la couche de corrosion. Deux faits originaux ont été mis en évidence qui n'avaient jamais été ni observés ni discutés précédemment : la croissance externe de la couche de corrosion impliquant que l'uranium est l'espèce qui contrôle le processus de croissance, la formation d'une couche de corrosion biphasée sous potentiel d'oxygène imposé. En outre, on a trouvé que la cinétique de réaction était de type parabolique, on a montré qu'elle était contrôlée par un mécanisme de diffusion de l'uranium au travers de la couche de corrosion.

7.1 *Introduction*

In accordance with the objectives (point 1.c) in chapter 3) of this study, the goal is here to investigate the growth process of the reaction between liquid sodium and uranium oxide. The study focuses mainly on the identification of potential point defects, which characterize the reaction product. Furthermore, the data are analyzed to achieve an understanding of the growth rate and the rate-determining step.

7.1.1 *Compatibility tests with imposed oxygen potential*

In the tests with imposed quantities, reported in Chapter 6, no influence of the grain orientation on the extent of the reaction product was observed. Therefore, in the kinetic studies at constant oxygen potential hereafter described, single crystals were used. The sample surface of the single crystals was fine-polished using mono-dispersed diamond suspensions with decreasing grain diameters down to 1 μm . The polishing was done to create a flat surface, which helped to better interpret the corrosion layer thickness, even after long time sodium exposure. Five interaction tests between uranium oxide and liquid sodium, containing a sodium niobate buffer (described in section 4.2.3), were performed and each interaction took place at 973 K for 12 h, 24 h, 48 h, 96 h and 192 h. Table 16 summarizes the characteristics of the tested samples and the corresponding interaction conditions. Each uranium oxide single crystal was introduced into the capsule, together with the buffer and metallic sodium. Also in these tests, the preparation of the capsules took place in a highly purified glovebox, to avoid any additional oxygen contamination.

Table 16: Test matrix for kinetic studies

<i>Sample n°</i>	<i>Length x Width (mm)</i>	<i>Height (mm)</i>	<i>Mass (g)</i>	<i>Temperature (K)</i>	<i>Time (hours)</i>
NAINT7	3.2x3.2	2.1	0.22	973	12
NAINT8	4.5x4.5	1.7	0.33	973	24
NAINT9	4.5x4.5	2	0.40	973	48
NAINT10	3.2-4.5	2	0.14	973	96
NAINT11	3.15x3.17	1.5	0.13	973	192

7.2 Characterization

7.2.1 Sodium niobate buffer

After each interaction test, the buffer was retrieved in order to check its status. From the visual point of view, the buffer did not keep the initial white color, but turned black as shown in the inset of Figure 85. The change in color could be attributed to a potential oxygen depletion of the buffer. Indeed, the release of oxygen was expected and is consistent with the aim of the buffer. Figure 85 reports the XRD pattern after each interaction. No changes were observed when compared to the unreacted buffer. Indeed, the phase was still sodium niobate, Na_3NbO_4 , and no other phases were detected at this stage. However, the expected reduction of the buffer corresponds to a few mg of the initial powder, even after 192 hours of reaction, and was thereby probably not detectable by XRD. Nevertheless, the detection of the sodium niobate confirmed the presence of sufficient buffer for the entire duration of the test and no deficiency of oxygen should have occurred.

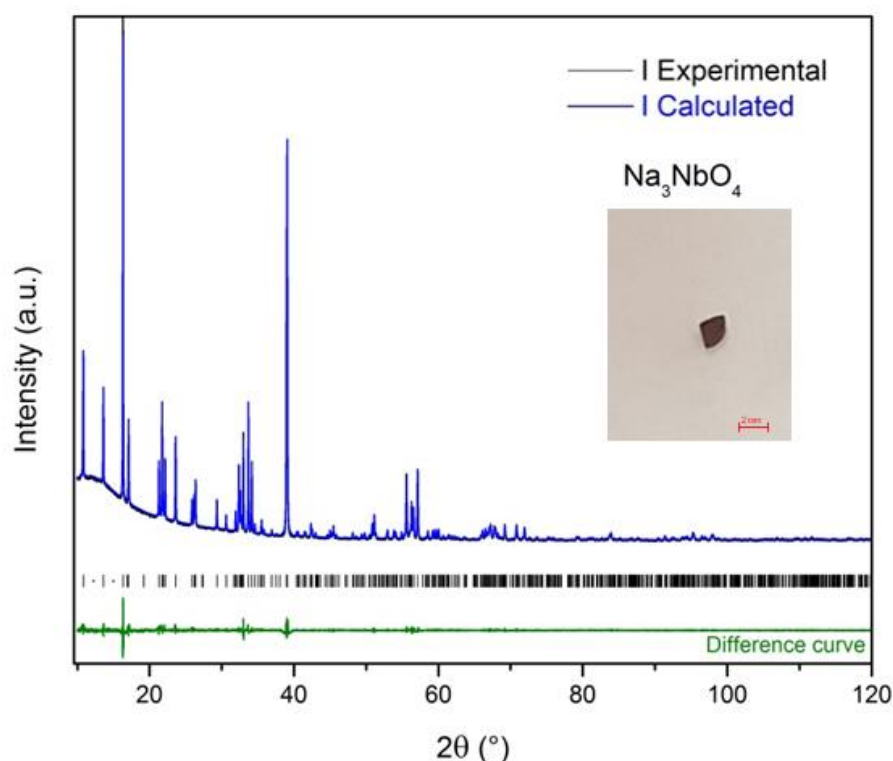


Figure 85: XRD of the sodium niobate buffer after the interaction tests. The insert shows how the buffer looked like after the interaction.

7.2.2 Reaction product: characterization and phase identification

7.2.2.1 X-Ray Diffraction

A comprehensive study on microstructure was performed, to understand if the formation of more than one phase was possible under the experimental conditions of the sodium interaction at fixed oxygen potential. The phase characterization of the reaction product was done through Grazing Incidence X-Ray Diffraction (GIXRD) at the Institute of Mathematics and Physics of Prague. GIXRD is a more surface sensitive measurement technique and then appropriate to better identify the surface corrosion of the uranium oxide sample. Figure 86 reports a section ($10^\circ < 2\theta < 50^\circ$) of the recorded pattern. The pattern resulted in several diffraction peaks among which broad peaks at 2θ values of 17.42° - 17.75° , 25.82° - 26.50° and 32.22° - 32.85° can be recognized. The phases characterization was made through Jana2006 software and was firstly focused on the identification of the sharp peaks.

The Bragg reflection at a 2θ value of 46.9° corresponded to the phase of stoichiometric uranium oxide, with a lattice parameter of $5.47(1) \text{ \AA}$. The initial bulk was orientated along the $\langle 011 \rangle$ crystal lattice direction. The bulk exhibited its initial orientation, without any considerable change. Through Rietveld refinement, a second phase was identified as reaction product

corresponding to an orthorhombic structure of NaUO_3 . The refinement was fitted with the NaUO_3 phase having lattice parameters $a=7.83(1)$ Å, $b=7.45(1)$ Å and $c=6.78(1)$ Å, but the space group was not determined.

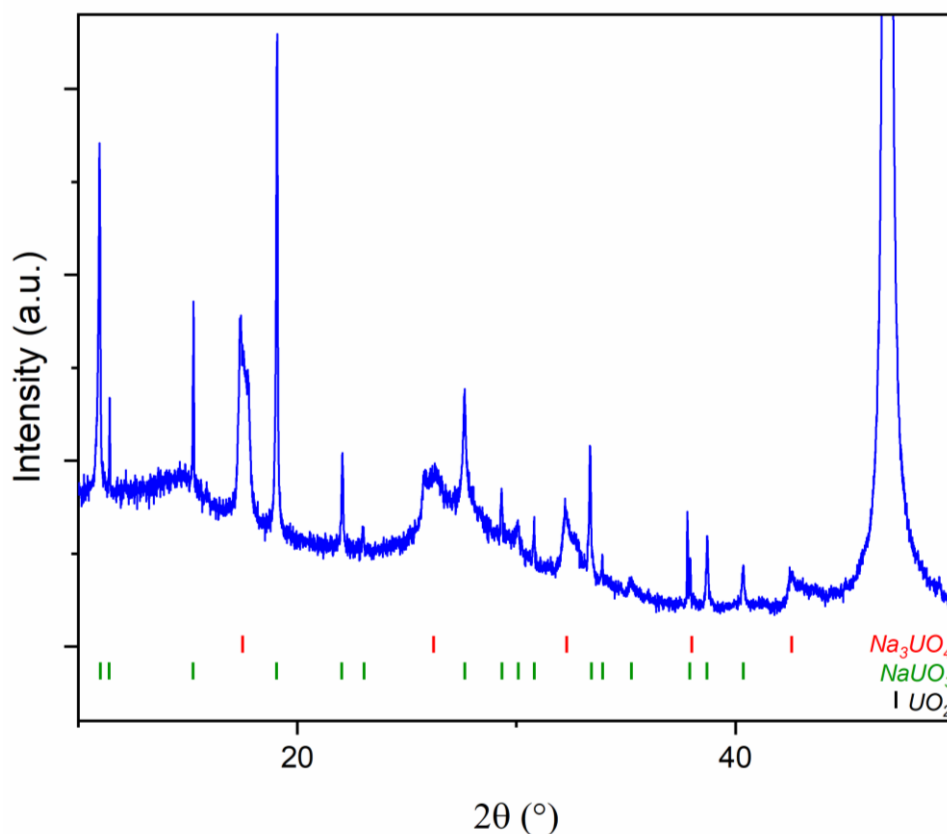


Figure 86: GIXRD on single crystal after 24 hours of interaction. Presence of uranium oxide bulk and two additional phases, NaUO_3 and Na_3UO_4 , were detected.

The characterization of the broader peaks was more complex. The approach of the indexing of the peaks was based on the theoretical calculation of the potential Bragg reflection at 2θ values which may correspond to the trisodium uranate phase. The calculation was made assuming the same lattice parameter of the trisodium uranate phase measured previously, i.e. $4.78(6)$ Å, and applying the Bragg law. The corresponding values are reported in Table 17. With the exception of the 2θ value calculated for the $\langle 001 \rangle$ orientation, where the difference between the calculated value and the measured one was of about 1° , all the other values matched the measured values of the diffraction pattern. Based on these results, it was assumed that the second phase belonged to the trisodium uranate in which a distortion of the crystalline structure and some out of center position was expected.

Table 17: Measured and calculated values of the trisodium uranate phase

<i>Lattice parameter</i>	<i>Orientation</i>	$2\theta_{\text{calculated}}$	$2\theta_{\text{measured}}$	<i>Difference</i>
4.78(6)	<001>	18.517	17.42-17.75	±0.9
4.78(6)	<011>	26.303	25.82-26.50	±0.1
4.78(6)	<111>	32.361	32.22-32.85	±0.2
4.78(6)	<200>	37.540	37.81	±0.3
4.78(6)	<210>	42.170	42.48	±0.3

Based on the diffraction theory, in a face centered cubic (fcc) structure (100) peak is a so-called forbidden reflections meaning that no constructive diffraction exists for that orientation. The appearance of the peak corresponding to the <100> orientation of the trisodium uranate phases, as indexed herein, indicated thereby that the concerned crystal structure cannot be considered a fcc structure, but rather a simple cubic structure.

Both the symmetry and the low full width at half maximum (FWHM) of the diffraction peaks of the sodium uranate phase, in the form of NaUO_3 , even at high angles, revealed good homogeneity and crystallinity of the material. Due to the high intensity of the peaks, this phase was probably present at the external zone, indicated in light blue in Figure 87. This observation is in agreement with the EDX mapping (see next paragraph), where a phase with a lower concentration of sodium was identified in the upper region of the corrosion layer compared to a higher concentration of sodium in the region close to the interface between the bulk UO_2 and the corrosion layer. The broad peaks could be instead linked to a polycrystalline phase not fully crystallized. Based on the high FWHM of the diffraction peaks, the phase was characterized most probably by nano particles, with a distorted structure. This phase, based on both EDX and peak intensity of XRD should be located between the uranium oxide bulk and the NaUO_3 phase, and was identified as Na_3UO_4 , illustrated in yellow in Figure 87. Finally, illustrated in red, the large reflection peak at 46.9° corresponded to the uranium oxide bulk which appeared well-defined and oriented on its initial orientation.

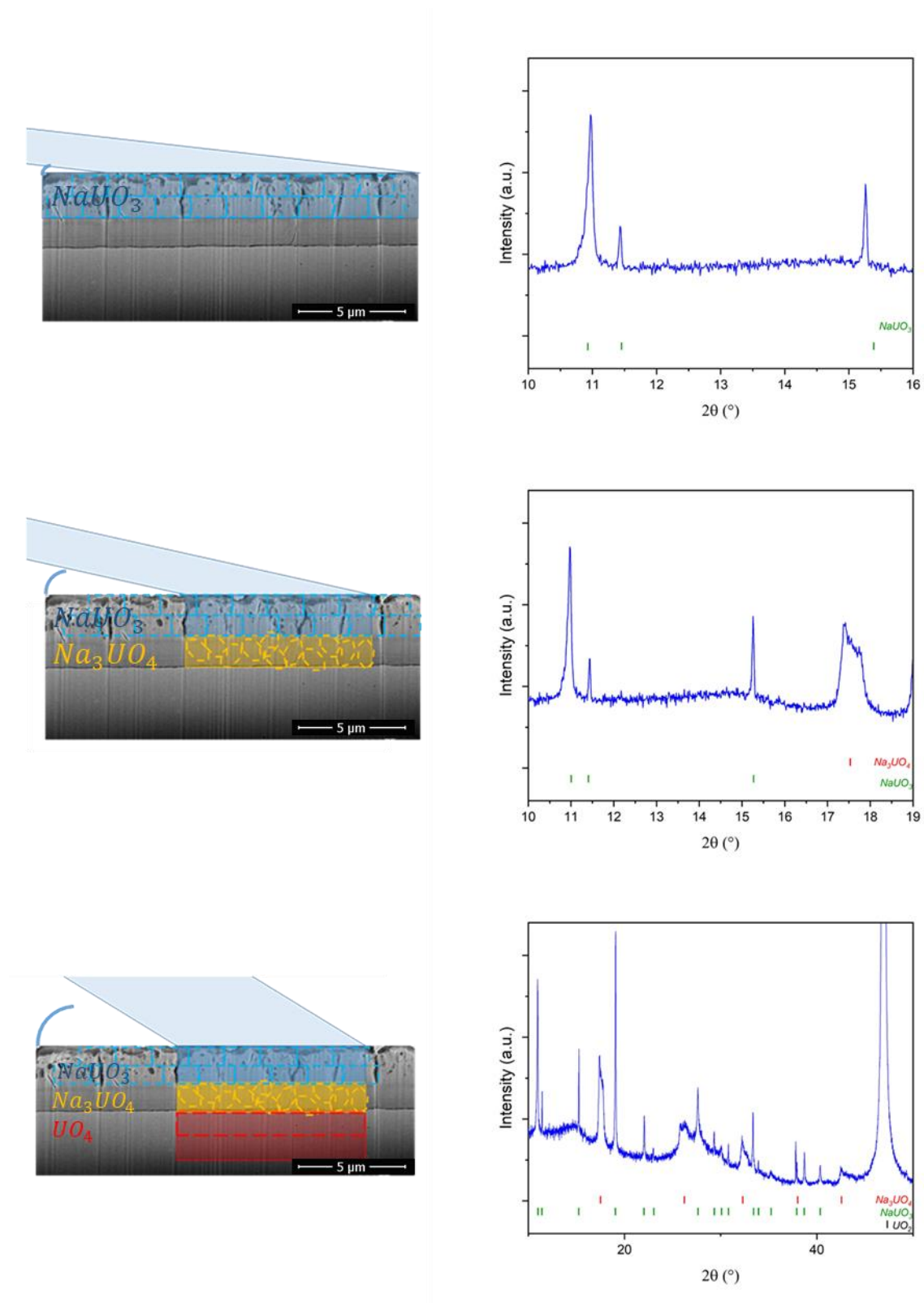


Figure 87: Interpretation of the different peak, which appeared in the GIXRD pattern.

7.2.2.2 EDX

Chemical and elemental mapping was conducted on cross section lamellae prepared by focused ion beam (FIB). This allowed directly characterizing the elemental content of the surface exposed to sodium, the near-surface and the bulk of the sample.

Platinum was used to protect the cross-section area during the gallium ion beam section. Picture number 5 of Figure 88 shows a platinum mapping (light blue), which was measured by EDX to discriminate the zone where it was deposited. As reported in Figure 88 (5), platinum was still confined at the top of the lamellae, indicating that the cut and cleaning processes did not lead to its spreading. The analysis evidenced several material changes induced by sodium exposure in presence of a fixed oxygen potential.

Among the different element maps of Figure 88, uranium (red) and sodium (green) were of major interest. The presence of uranium was clearly observed in both, the uranium oxide bulk and the corrosion layer. The appearance of the corrosion layer at the periphery of the uranium oxide was marked by the difference of the color intensities. The position of the corrosion layer is much more evident in the sodium map, which shows that no sodium diffused into the bulk UO_2 . The picture also shows a thin layer of highly concentrated sodium between the corrosion layer and the Pt cover, which stems from the formation of sodium oxide after the test (see before) and can be neglected in the further discussion. However, inside the corrosion layer, even though the uranium concentration appeared sufficiently uniform, the sodium mapping revealed two different sodium concentrations, which divided the layer into an upper and a bottom zone. Surprisingly, the external zone (upper zone), which was directly in contact with sodium, was less rich in sodium compared to the zone close to the uranium bulk.

The elemental content in atomic % (a%) in each zone is given in Table 18. The composition could only be obtained within the limited accuracy of the EDX, therefore the displayed elemental contents are not perfectly in agreement with the assumed chemical composition. However, the bottom zone of the corrosion layer was richer in sodium, compared to the upper zone, indicating that more than one phase was probably formed.

Table 18: Elemental composition measured by EDX

<i>Spectrum from bottom to top</i>	<i>Uranium [a%]</i>	<i>Sodium [a%]</i>	<i>Oxygen [a%]</i>	<i>Platinum[a%]</i>	<i>Chemical composition</i>
UO ₂ bulk	37.35	-	62.65	-	UO ₂
Corrosion layer bottom	16.37	31.46	52.17	-	NaUO ₃
Corrosion layer upper	15.84	23.8	60.36	-	Na ₃ UO ₄
Sodium oxide	-	51.04	48.96	-	Na ₂ O
Platinum	-	-	-	100	Pt

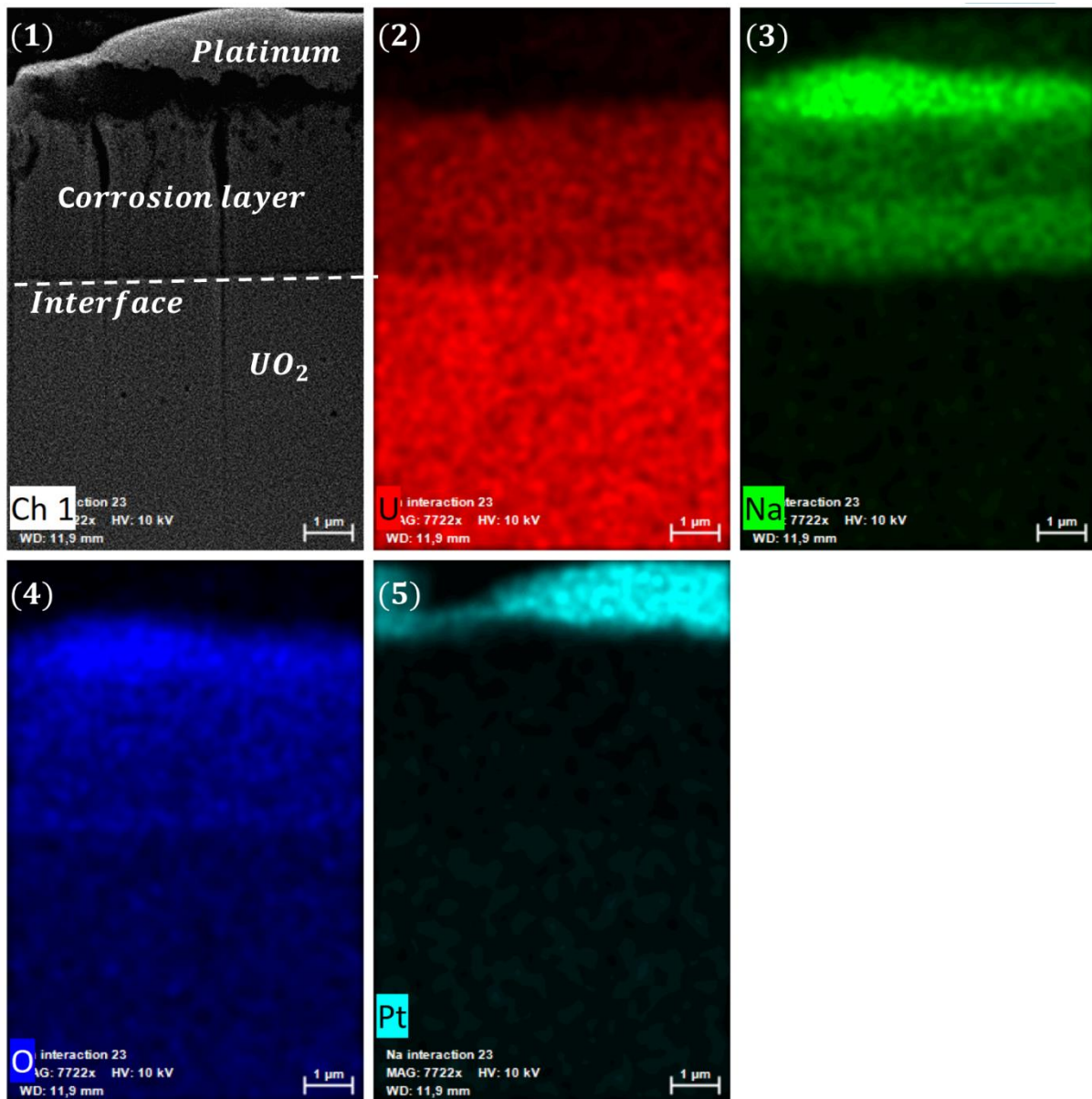


Figure 88: EDX mapping on cross section lamellae. (1) View of the lamellae and the corresponding phases. (2) Uranium mapping. (3) Sodium mapping. (4) Oxygen mapping. (5) Platinum mapping.

An EDX line scan along the lamellae was recorded in order to establish if also in conditions of fixed oxygen potential the diffusion of sodium into the uranium oxide could not occur. The results, reported in Figure 89, confirmed the absence of sodium inside the bulk UO_2 . Indeed, sodium is detected only between the interface of UO_2 with the corrosion layer and the outer surface. Quantitative assessment of the corrosion layer showed that it was indeed composed of two different phases, in which the phase close to the bulk was richer in sodium than the one close to the external surface. In agreement with XRD analysis, the two phases should correspond to trisodium uranate, Na_3UO_4 , for the bottom phase, which was richer in sodium, and to sodium uranate NaUO_3 for the upper phase, which was less rich in sodium.

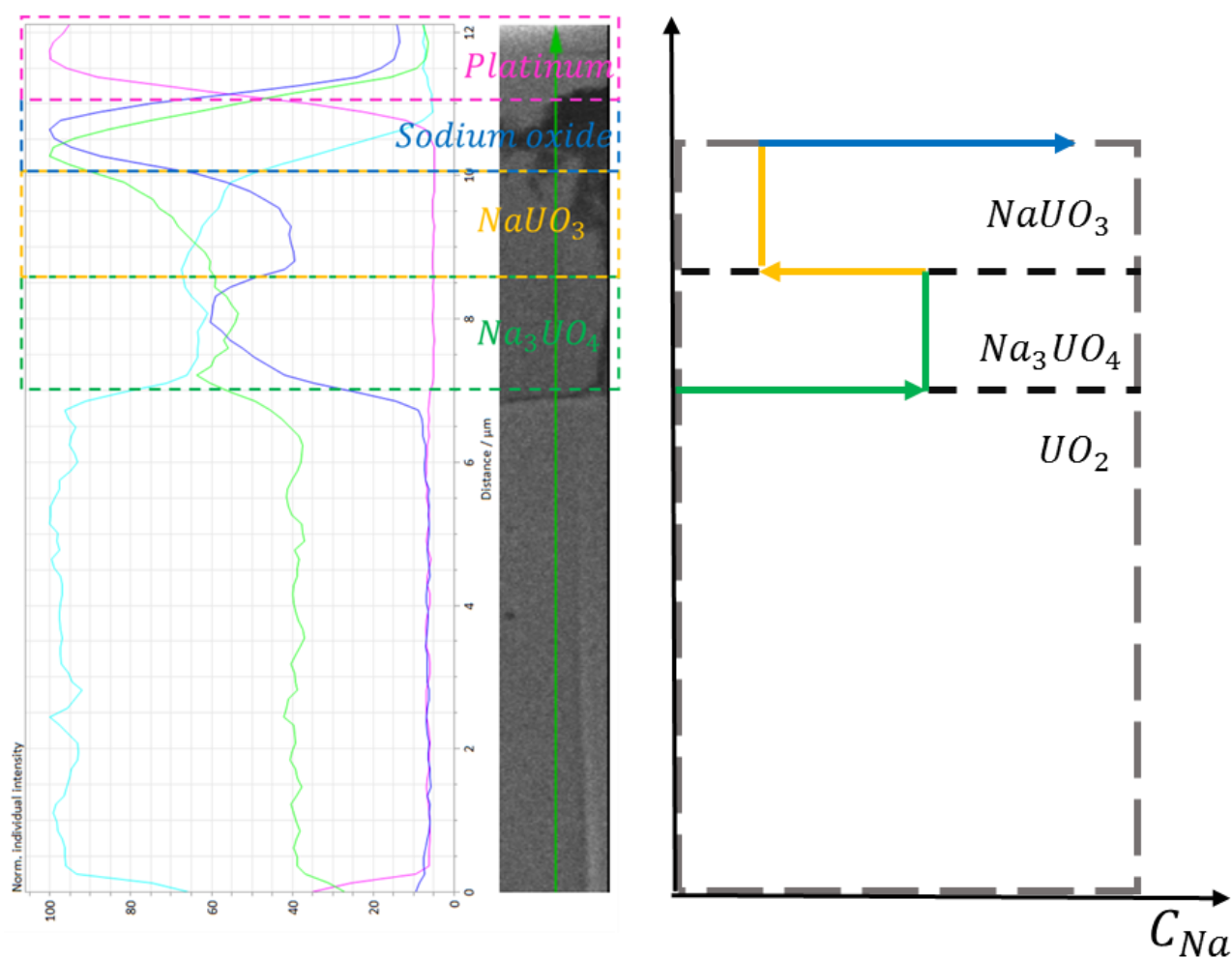


Figure 89: EDX line scan performed on the FIB-lamellae. Normalized individual intensity results from the uranium oxide bulk to the platinum protection layer.

7.2.2.3 Transmission Electron Microscopy

TEM and High Resolution TEM analyses were performed on a 50 nm-thick lamella extracted from the sample NAIN8. The lamella is illustrated at the left of Figure 90. Diffraction measurements were carried out through the whole lamella length, from the uranium oxide bulk to the corrosion layer. A characteristic high-resolution TEM picture is illustrated at the right of Figure 90. The picture was taken at the interface between the bulk UO_2 and the corrosion layer.

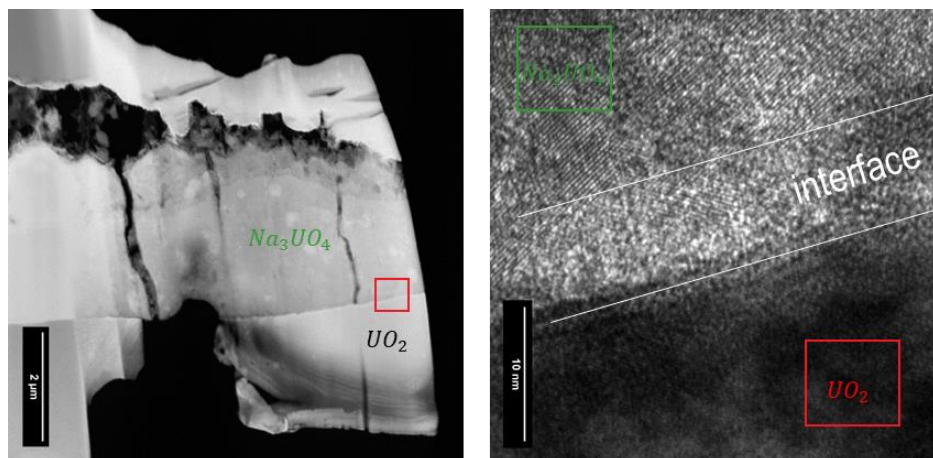


Figure 90: Left: View of the lamella for TEM analysis. Right: High resolution TEM at the interface between the bulk, UO_2 , and the corrosion layer.

Detailed diffraction pattern and high-resolution images are illustrated in Figure 91 and refer to different locations. The diffraction pattern of the uranium oxide bulk is reported in Figure 91 on the right. The pattern revealed a regular array of sharp spots typical of a single crystal. The high-resolution image showed the corresponding lattice planes of the oriented bulk, having a good crystallinity. Moving through the interface between the bulk and the corrosion phase, the diffraction pattern, as reported in Figure 91 in the middle, exhibited a ring-like diffraction pattern attributable to a kind of nano-size polycrystalline phase, since the diffraction pattern is the sum of individual crystals of random orientations. In this case, the high-resolution image showed the lattice planes in which a change in orientation appeared and which was perhaps less crystallized. Finally, the diffraction pattern of the corrosion phase, reported in Figure 91 on the left, appeared in many partial rings, which indicated a favored and preferred orientation. The phase exhibited a cubic symmetry. Even in this case, the high-resolution image showed the corresponding lattice planes of a preferred oriented phase, which appears well-crystallized.

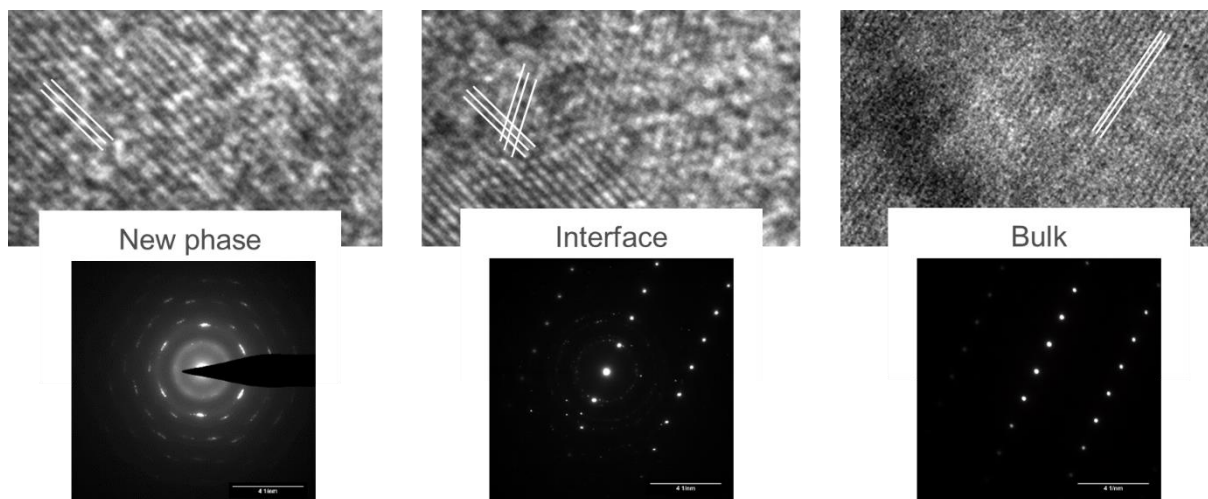


Figure 91: Comparison of high resolution (upper) and diffraction pattern (bottom) images obtained by TEM . Left: corrosion layer. Middle: interface between the bulk and the corrosion layer. Right: uranium oxide bulk.

7.2.2.4 Morphology and cross section view

The morphological changes of the uranium oxide single after the exposure to liquid sodium were characterized by SEM analysis. Figure 92 shows a secondary electron image of the characteristic surface morphology of uranium oxide after the exposure to liquid sodium. The appearance of cracks was in agreement with the previous observations made after the interaction tests where the oxygen was imposed in a fixed amount at the beginning of the interaction. The corroded surface in this case exhibited a sort of tile-shape. Morphological changes appeared unaffected by the initial conditions, i.e. a fixed amount of oxygen at the beginning of the test or an imposed oxygen potential. Also in this case, the surface is somewhere covered by sodium oxide particles, as result of the oxidation of the left-over sodium in contact with the glovebox atmosphere.

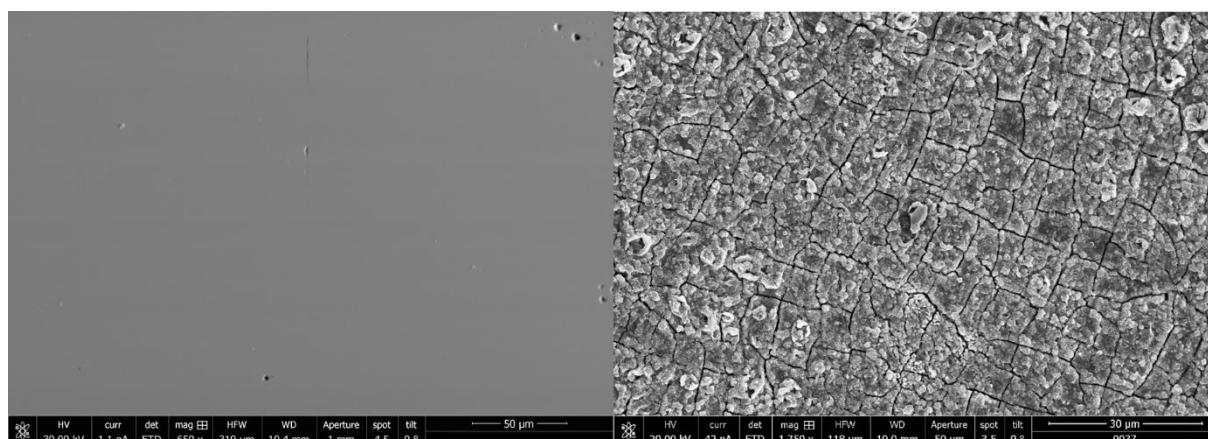


Figure 92: Morphology changes after sodium exposure. Left: Initial uranium oxide single crystal fine-polished. Right: Characteristic morphology of the uranium oxide after exposure to liquid sodium.

As previously observed in the test where the oxygen was imposed in a fixed amount at the beginning of the interaction, the corrosion layer was confined to the periphery of the sample. Figure 93 shows the cross section of each sample. The cross sections were made by the use of the gallium ion beam, which supports the evaluation of the presence of structural changes underneath the sample surface. Each micrograph refers to each interaction test, from 12 to 192 hours, from left to right, respectively. The thickness of the corrosion layer appeared uniform and the layers were not everywhere fully adherent to the uranium oxide bulk. The un-adherence seemed to be enhanced by the time of exposure to liquid sodium. Indeed, this behavior is expected as a consequence of the outward growth migration of uranium from the uranium oxide. This could result in the creation of holes close to the surface and then into a net separation between the bulk and the reaction product.

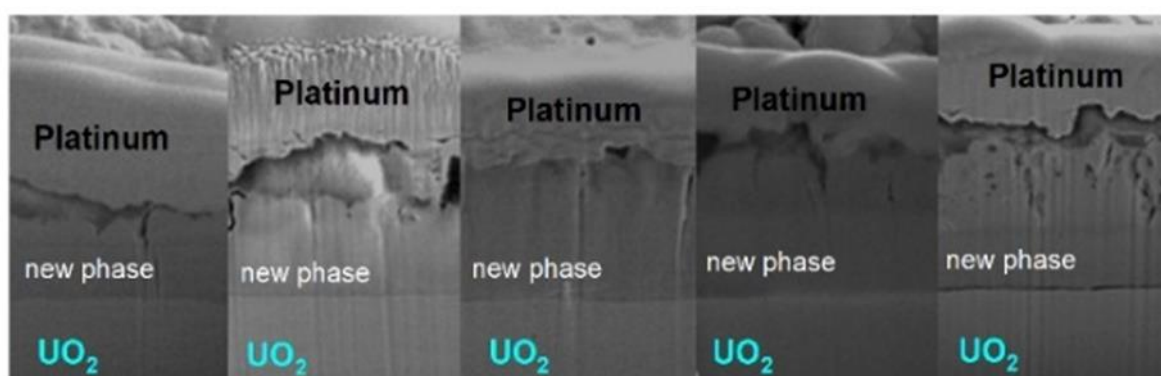


Figure 93: Cross section view of the corrosion layer. Evolution with time from 12 to 192 hours of interaction, from left to right.

7.2.3 Geometrical model and instantaneous nucleation

The contact between liquid sodium and uranium oxide occurs at the uranium oxide surface and the corrosion should be confined to the surface as previously shown. Then the surface is expected to exhibit a visual change through the sodium exposure. When a fixed amount of oxygen was imposed at the beginning of the interaction test, as described in Chapter 6, no destructive effects were observed on the uranium oxide samples, even at high oxygen amounts in presence of sodium oxide. Also after each of the interaction tests with fixed oxygen potential using sodium niobate buffer, the samples were recovered still intact, even after 8 days of sodium exposure. After the interaction tests, the samples were characterized by visual inspection, in order to establish whether the initial features of the samples were affected by the sodium interaction. The direct comparison between un-reacted and reacted samples was obtained through the inspection of each sample by optical microscope before and after the sodium interaction. Figure 94 shows the characteristic images of the unreacted and reacted samples after 12, 24 and 48 hours. The effect of the sodium corrosion was clearly visible by the change of color, from light gray of the un-reacted surface, as result of the fine-polishing, to dark gray-black of the reacted sample as result of the corrosion. From a macroscopic point of view, the

samples kept the initial shape and, as expected, no destructive effects were observed. The initial defects due to the sample preparation were also still visible.

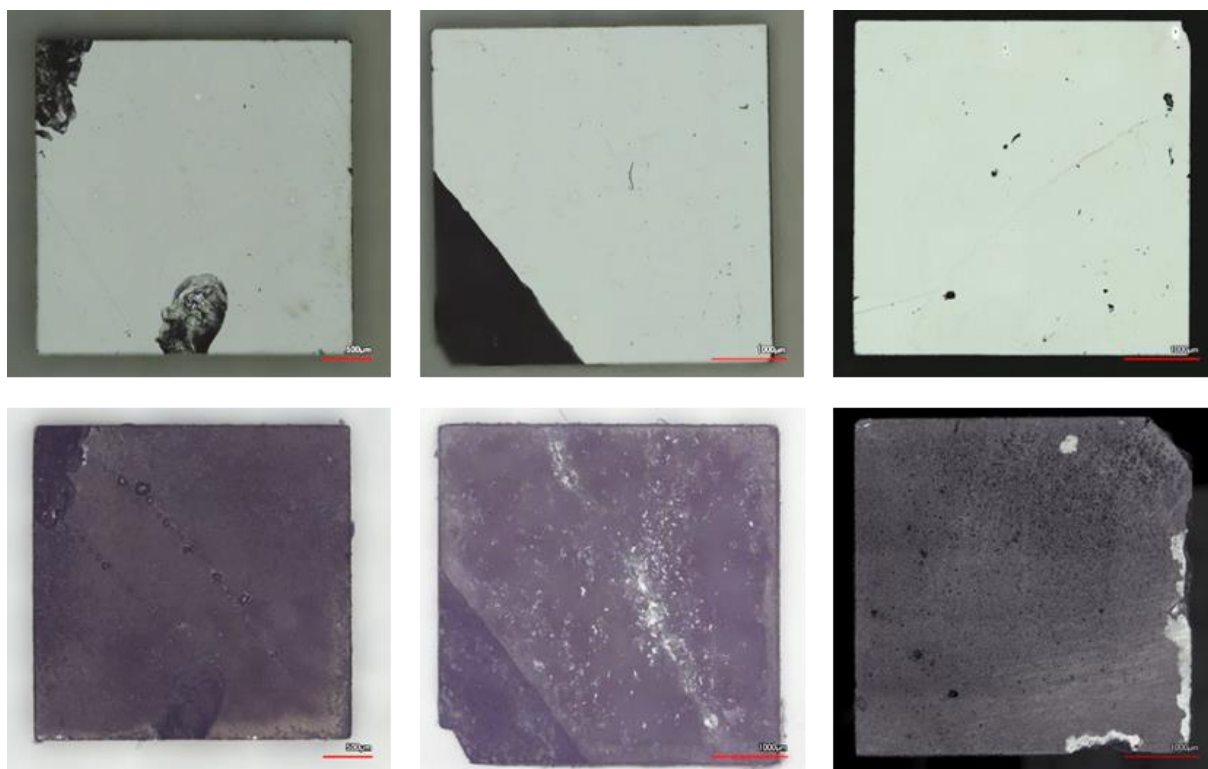


Figure 94: Visual inspection of the samples before and after the reaction with liquid sodium. Upper: Unreacted sample. Bottom: From left to right: reacted samples after 12, 24 and 48 hours.

Nevertheless, the appearance of some shallow cracks was observed. These could be related to the corrosion phase and were perhaps enhanced by the sample handling during the retrieval. The surface roughness of the initial sample surface as well as of the reacted surface was determined by a confocal laser scanning profilometer with a high-resolution height measurement capability. An example is illustrated in Figure 95 and refers to sample NAIN7.

The initial surface showed a good flatness, due to the fine-polishing. As expected, the samples after the sodium exposure showed a rough surface supporting the morphological change of the exposed surface.

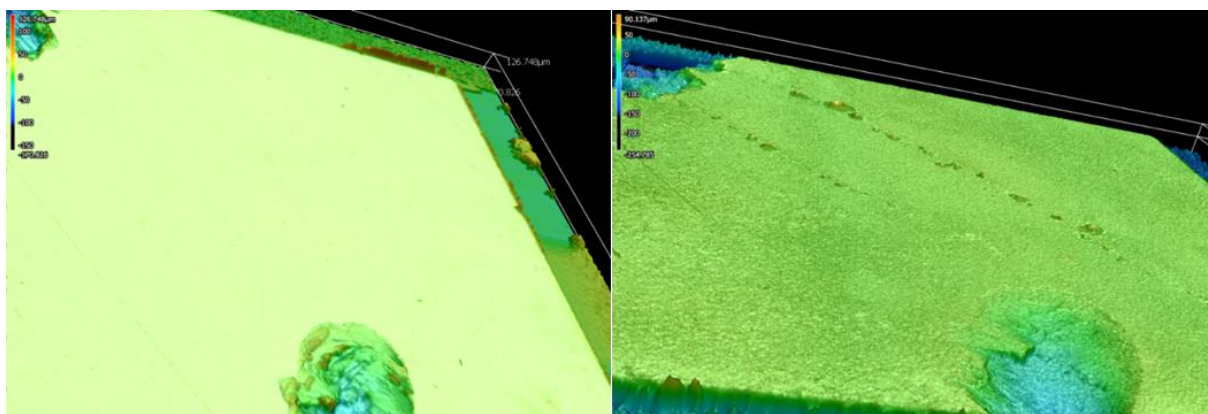


Figure 95: Surface roughness evaluation by confocal laser scanning profilometer of the initial sample surface (left) and of the reacted surface (right) of NAlNT7.

7.2.4 Sense of development of the reaction product

The sense of development of a growing solid phase is of particular interest, because to properly model the reaction using a heterogeneous formalism a good knowledge of the involved point defects is required.

Data on the point defects of trisodium uranate, i.e. the reaction product of the sodium-uranium oxide reaction, are missing in literature. However, some assumption on the expected point defects can be made in coherency with the direction of growth. Indeed, the point defects involved in an outward development may be cation vacancies or cation interstitials. In the case of an inward development, instead, the point defects may be anion vacancies or anion interstitials.

There exist several ways to check the sense of development, such as interdiffusion test and marker method. An interdiffusion test is usually based on the principle of the process of diffusional exchange of atoms across two materials that are in contact. However, in the present study, an interdiffusion test was attempted, but unfortunately without success due to the low decomposition temperature of sodium oxide. Commercial sodium oxide, in the form of $\text{Na}_2\text{O} + \text{Na}_2\text{O}_2$ could not be purified by removal of sodium peroxide, and the compound was completely melted in the attempts to prepare sodium oxide disks for the interdiffusion tests.

A second approach can be the marker method in which the surface in contact with the interacting medium is marked by deposition of a foreign and inert material in order to recognize the sense of development after the reaction. Figure 96 shows the outward and inward sense of development of the new phase. If the initial surface is marked, the position of the marker after the interaction indicates the original position of the initial surface and thereby the sense of development of the reaction product. However, dealing with metallic sodium implies complexity in selecting the inert material to mark the surface. Indeed, most of the materials, even precious metals such as gold, form alloys with liquid sodium. Then, simple deposition of metals on the sample surface could not be applied.

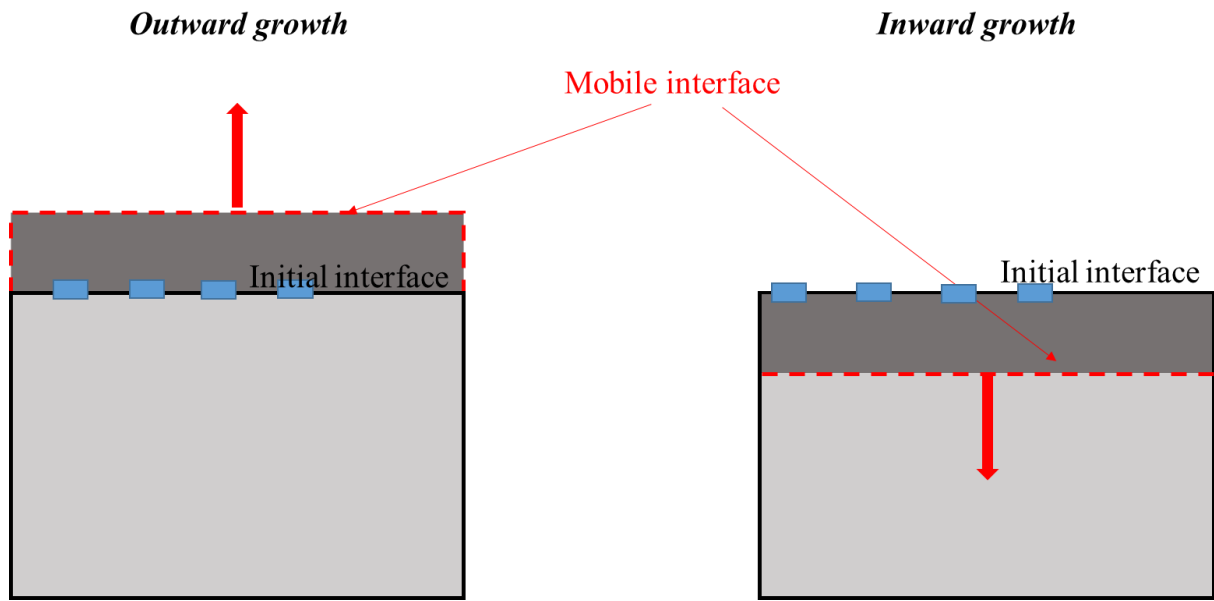


Figure 96: Sense of development of a solid phase. Illustration of both outward and inward growth and the correspondent mobile interface. Blue squares represent the markers.

To allow marking the initial surface in a precise and observable manner after the sodium reaction, each sample was marked with deep trenches on the reference surface made by the FIB. Afterwards, the trenches were filled with platinum metal. Figure 97 (left) illustrates the top view of the platinum marker, with the corresponding dimensions of the marker having a length of about $16\text{ }\mu\text{m}$ and a width of about $3\text{ }\mu\text{m}$. The cross view of one platinum marker is illustrated in Figure 97 (right). The markers were characterized by a depth of about $2.5\text{ }\mu\text{m}$, i.e. the distance between the surface and the bottom of the trench. The marker showed also a characteristic cone-shape, with a visible free-space at its center as result of the platinum deposition process. To protect the marker, an additional platinum layer of about $1\text{ }\mu\text{m}$, was deposited at the top of it.

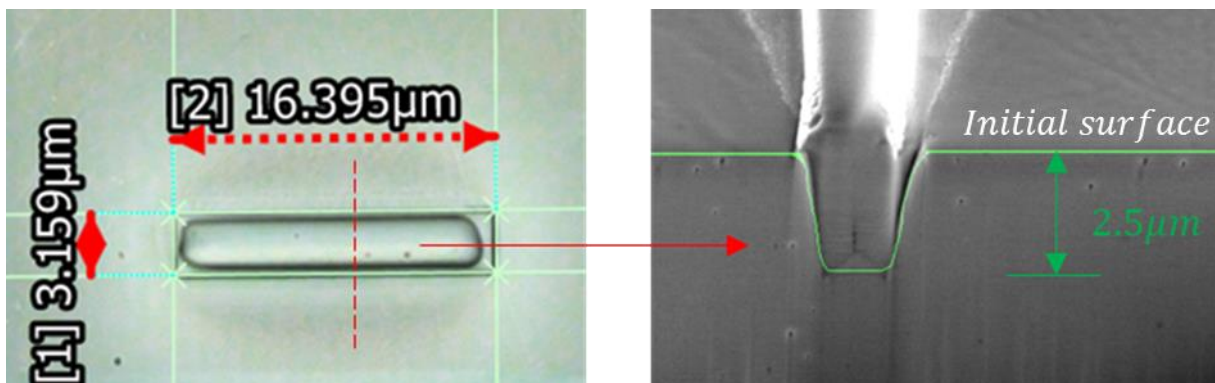


Figure 97: Platinum marker for the study of the sense of development. Left: top view of the platinum marker with the corresponding dimensions. Right: cross section view of the platinum mark for the determination of the sense of development.

After each interaction test, the cross section of the markers was characterized and compared with the reference. Figure 98 reports the cross section view of the platinum marker of the reference sample and after 12 and 24 hours of sodium exposure. The platinum markers were still recognizable through the appearance of their characteristic cone-shape and the enhanced free-space at the center. The latter was probably caused by the thermal treatment and the interaction with liquid sodium. The appearance of enhanced smoothed edges, when compared with the initial ones, could be also attributed to the thermal treatment.

The direct comparison between the unreacted and the reacted marker was made by overlapping the depth profiles (green line). In all the cases, the new phase showed a preferential outward growth. A slight inward growth of about 0.2 and 0.5 μm was observed on the samples NAIN7 and NAIN9, respectively. However, such an observation could be influenced by the cross section cut position and/or the marker preparation.

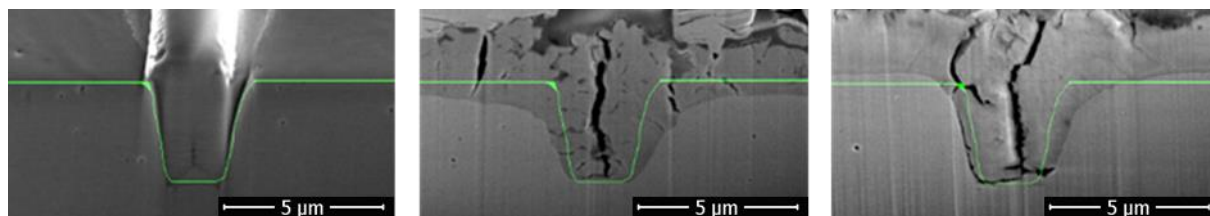


Figure 98: Platinum markers. Left: Reference marker on unreacted sample. Middle: After 12 hours of interaction with liquid sodium. Right: After 24 hours of interaction with liquid sodium.

The observation of a preferential outward growth is an indication for diffusion via cationic point defects, such as uranium vacancies or interstitials, in the specific case of the uranium oxide. The diffusion of uranium from the bulk to the external surface is expected in outward growth. Various morphologies may thus be encountered according to such migration, as for example, the appearance of voids close to the internal interface. In the interaction tests between uranium oxide and sodium, the corrosion layer appeared no fully adherent to the bulk, which may indicate the potential coalescences of these voids, as illustrated in Figure 99.

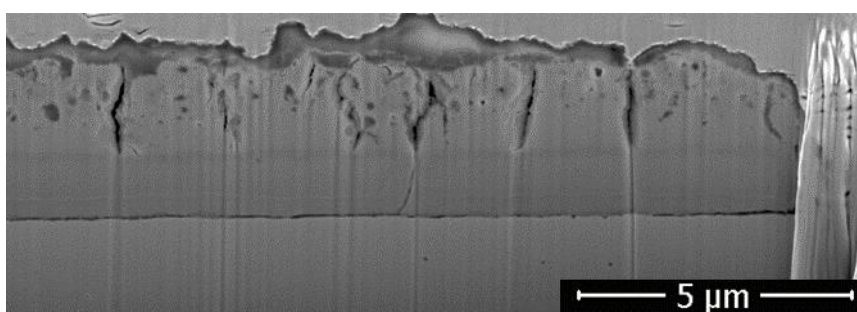


Figure 99: Detailed view of the corrosion layer after 192 hours of interaction. Potential void formation at the internal interface in support to the outward growth assumption.

7.2.5 Rate determining step

If the reaction mechanism can be described through elementary steps, and one step is significantly slower compared to the others, the growth process is kinetically controlled by this single elementary step, i.e. the so-called rate determining step. Several types of processes can be accounted as rate determining steps. Experimentally, the rate determining step can be identified looking at the thickening evolution with time of the reaction product. In the case of a plate-like sample, if the rate-determining step is an interface reaction, the rate of production is constant which means that the thickness is proportional to time and follows then a linear regime. On the other hand, if the reaction is diffusion-controlled, the growth rate is equal to the rate of transport of the reactants through the reaction layer. In this case the thickness is proportional a square root function of the reaction time and follows then a so-called parabolic regime. The layer thickening as function of the time was then evaluated by measuring the thickness of the corrosion layer after each interaction test. Cross sections were usually made with the FIB stage tilted of 52° . The real thickness resulted then from the measured value corrected by a tilt factor corresponding to $1/\cos(38^\circ)$. The thickness was measured in several zones and the mean value was used. Through these measurements, the corrosion layer thickness was found to approximately grow parabolically in the initial timeframe, as illustrated in Figure 100.

The corresponding law can be approximated to:

$$y = 0.55t^{0.5} \quad (38)$$

where t is the time and y the thickness of the corrosion layer.

However, for a longer timeframe as illustrated in Figure 101, the rate slows down, following rather the law:

$$y = 1.3t^{0.25} \quad (39)$$

From a general point of view, this deviation from parabolic law ($n=0.5$) coming from Wagner's theory [104] has been the subject of numerous hypotheses in the literature for different reaction systems. Among other things, it has been suggested that the slowdown in the rate of corrosion is related to the increasing size of the grains and therefore to a lower density of grain joints. Other explanations are related to the presence of increasing mechanical stresses within the oxide film.

Although the result concerns uranium oxide, the rate of growth is in good agreement with those reported in literature [16, 20, 89] for the reaction between sodium and mixed oxide, with less than 30% of Pu content.

The comparison between literature data and the UO_2 results obtained in this study is illustrated in Figure 102.

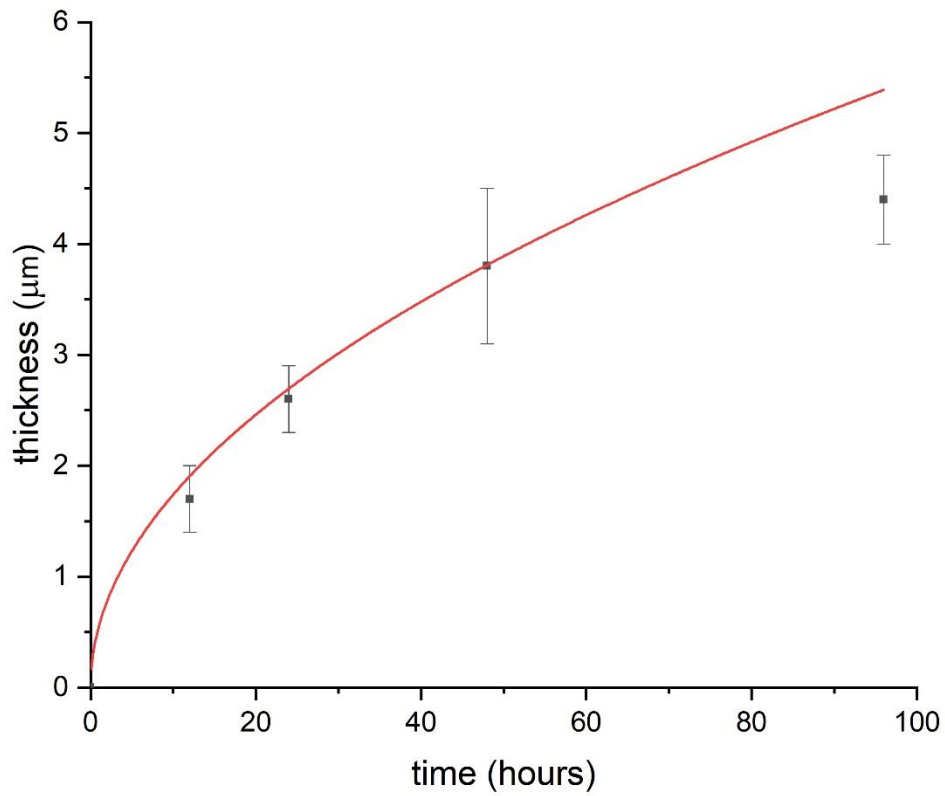


Figure 100: Fit of the experimental point at 12, 24, 48 and 96 hours of interaction.

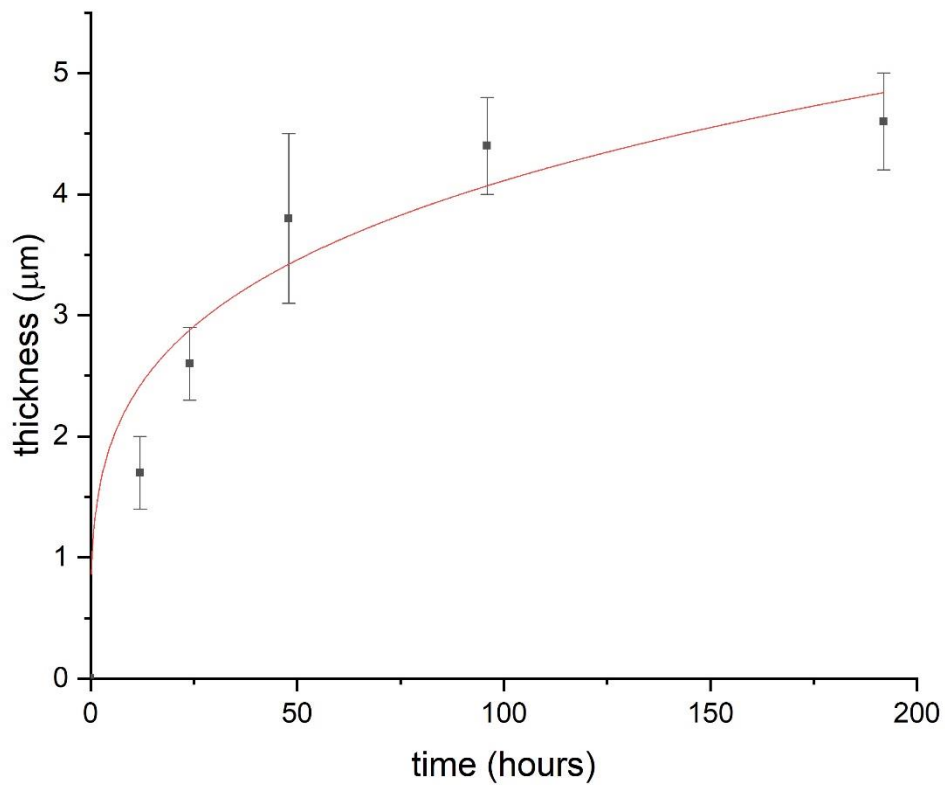


Figure 101: Fit of the experimental point at 12, 24, 48, 96 and 192 hours of interaction and corresponding law as function of time.

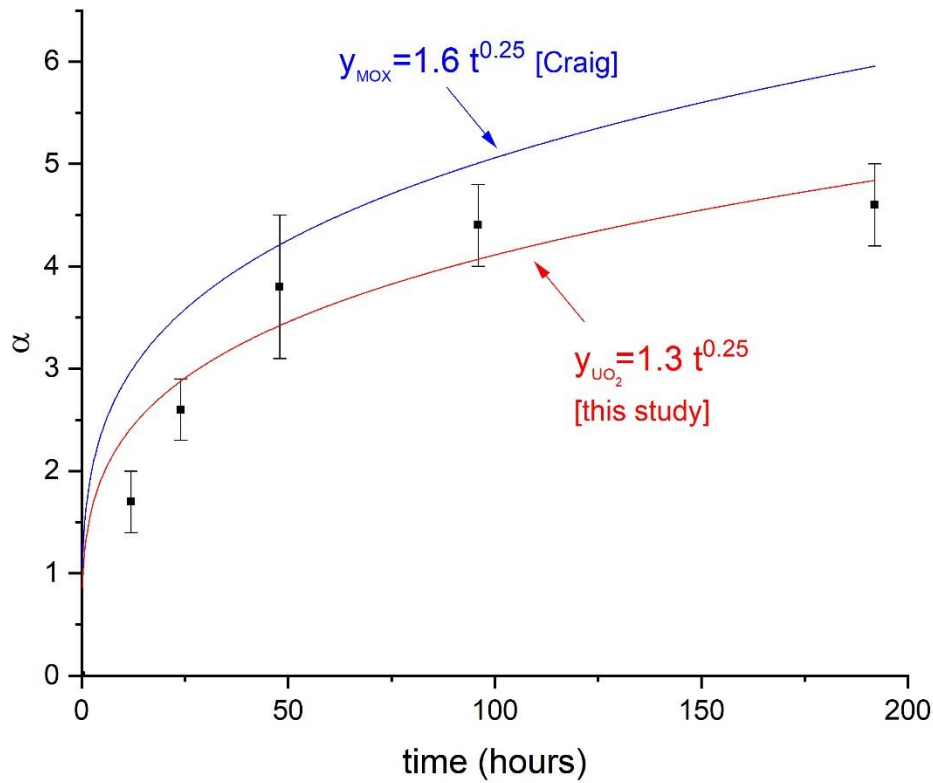


Figure 102: Comparison between the general law given in literature [89] and UO_2 results.

7.3 Conclusions

The study of the growth process of the reaction between liquid sodium and uranium oxide led to observe for the first time:

3. The outward growth of the corrosion layer, implying uranium cations as main species controlling the growth process, which was never considered before;
4. The formation of a double phase under imposed oxygen potential within a value close to the one expected in the internal storage, which was never assessed before and opened the question of the possibility to get more than one phase also for the mixed oxide.

Considering the parabolic regime of the growth rate, it can be concluded that the reaction should be diffusion-controlled. The latter observation is generally consistent with those reported in the literature for mixed oxide pellets, under fresh [16] and irradiated conditions [89]. However, the diffusion-controlled evolution of the reaction was attributed to the sodium diffusion so far. Herein, this aspect cannot be supported since no diffusion of sodium into the uranium oxide was observed and most important, the outward growth direction of the product phase was

detected. This clearly indicated that uranium diffusion via vacancies or interstitials have to be taken into account when a reaction mechanism would be proposed.

The formation of two different phases is supported by the thermodynamic conditions at which the tests were performed. As illustrated in Figure 103 the oxygen potential imposed during the interaction tests was between the oxygen threshold values for the formation of NaUO_3 and Na_3UO_4 ternary phases.

The formation of both phases was thereby allowed. However, these results induced two main questions which are relevant for the safety assessment of the internal storage of an SFR. The first question is, if it is reasonable to consider the formation of one phase only under reactor conditions, given that the existence of more than one phase was observed under similar oxygen potential conditions as expected in the SFR coolant. Indeed, as reported in Figure 103, the oxygen potential in the internal storage will be in the region where, thermodynamically, both NaUO_3 and Na_3UO_4 ternary phases could be formed, as observed in the present study.

The second question concerns the general approximation of the Na-U-O system with the Na-U-Pu-O system. Under this approximation, also for the Na-U-Pu-O system the formation of two phases could be expected. The higher oxygen threshold for the formation of trisodium uranoplutonate reported in literature (illustrated in Figure 33, in 2.3.1.4) should indicate that, in the presence of mixed oxide with an plutonium content close to or higher than 30%, a single phase of trisodium uranoplutonate could be formed under reactor conditions. Unfortunately, no exact oxygen thresholds are yet available for the formation of the quaternary phase in the Na-U-Pu-O system, and this leads to the conclusions that the approximation of the two systems should be used with great care.

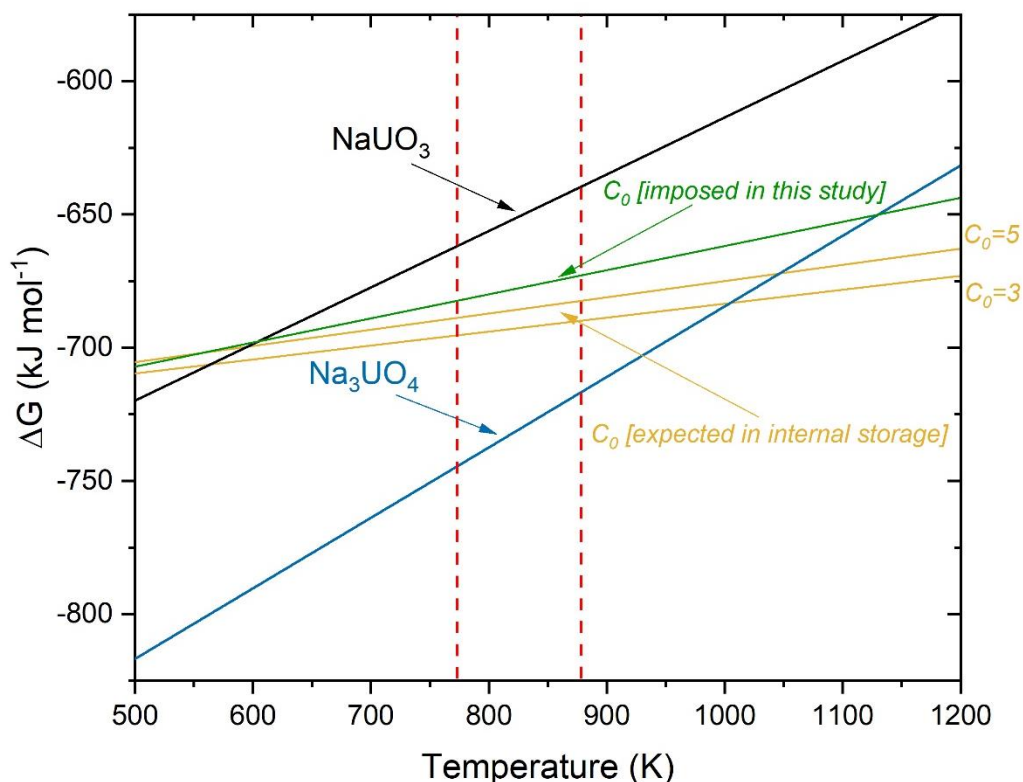


Figure 103: Section of the oxygen potential thresholds for the formation of the NaUO_3 and Na_3UO_4 ternary phases. Green line: oxygen potential imposed in the sodium interaction tests.

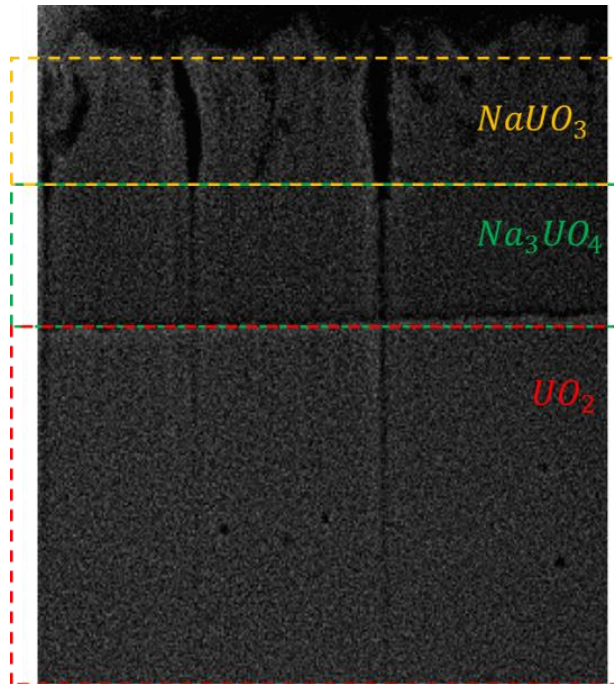


Figure 104: Identified phases trough XRD and EDX analyses.

8 *MOX kinetic studies*

Dans ce chapitre, on s'intéresse à la réaction entre le MOX et le sodium liquide, pour savoir si ce dernier se comporte de la même manière que le dioxyde d'uranium. Dans cette perspective, les mêmes expériences que celles réalisées avec le dioxyde d'uranium seront répétées avec le MOX. Les échantillons ont été caractérisés après les tests d'interaction par tomographie, diffraction des rayons X, MEB-EDX et MET. Le dioxyde d'uranium et le MOX se comporte de manière similaire, à l'exception de la corrosion aux joints de grains observée pour le MOX.

8.1 *Introduction*

In order to check if the behavior of stoichiometric mixed oxide matches with stoichiometric uranium oxide under the same initial conditions, compatibility and kinetic tests were performed on mixed oxide samples in the same manner as these presented in Chapter 6 and 7, respectively, for uranium oxide. A summary of the test conditions is reported in Table 19. A unique stoichiometric mixed oxide sample was treated in liquid sodium containing oxygen impurities. The test was performed at 1073 K for 50 hours (NAINT12). In addition, kinetic studies were carried out on mixed oxide samples using sodium niobate buffer, to impose the oxygen potential simulating the internal storage conditions. Interaction tests for kinetic studies were performed for 12, 24, 48, 96 and 192 hours at 973K (NAINT13 to NAIN17).

Table 19: Test matrix for MOX-sodium interaction tests (compatibility and kinetic studies).

<i>Sample n°</i>	<i>O:M</i>	<i>Temperature (K)</i>	<i>Time (hours)</i>
NAINT12	2	1073	50
NAINT13	2	973	12
NAINT14	2	973	24
NAINT15	2	973	48
NAINT16	2	973	96
NAINT17	2	973	192

8.2 Compatibility tests

8.2.1 Characterizations

The pellet remained intact during the heat treatment (NAINT12) and the reaction product was expected to be mainly confined to the sample surface. The sample was fixed into a silicon holder, as described in the uranium oxide section, and X-ray diffraction was carried out on the sample surface. Although the mixed oxide interacted for 50 hours, no reaction product was detected as shown in the diffraction pattern in Figure 105. Excluding the reflection at 22° due to the silicon holder, all the Bragg reflections corresponded to stoichiometric mixed oxide only, having the initial lattice parameter of 5.446 \AA . However, the difference of relative intensities of the diffraction peaks from the initial mixed oxide (see Figure 44) could indicate the presence of an amorphous layer which altered the bulk diffraction. Bykov et al. [53] reported that “*Samples of the sodium plutonium oxides were found to be moisture sensitive... exposed to the glovebox atmosphere for longer times showed either formation of other phases or amorphization*”. Most probably, the dissolution of metallic sodium with ethanol after the interaction test and storage in the glove box atmosphere resulted in the amorphization of the corrosion layer.

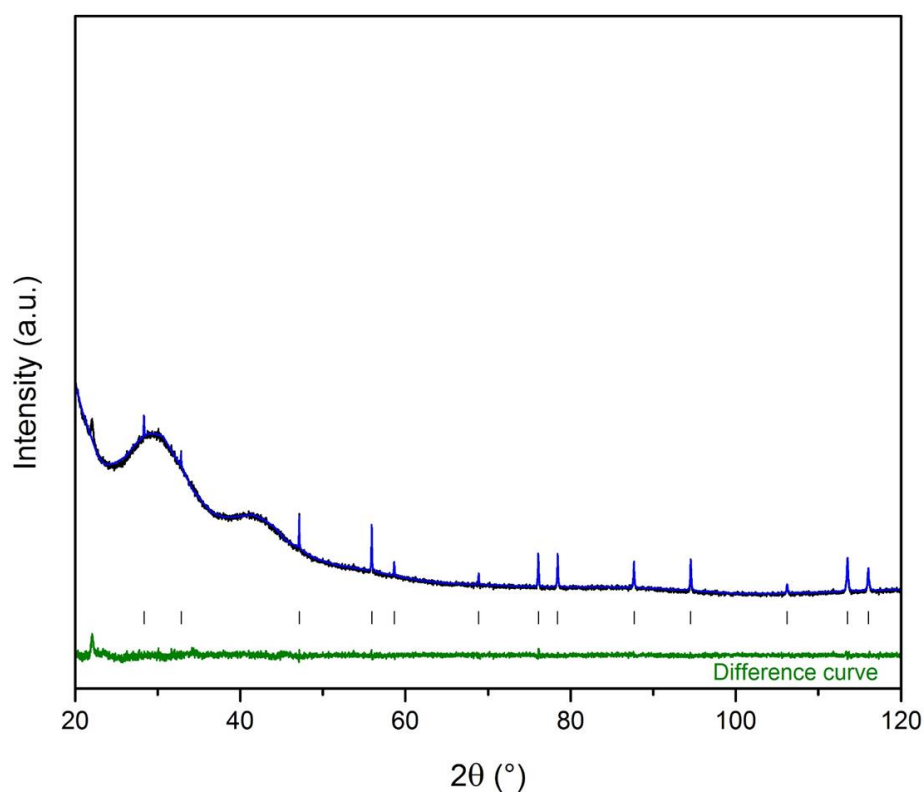


Figure 105: XRD pattern on MOX after 50 hour interaction

The morphological aspects of the sample surface were analyzed by SEM. Micrographs were taken at different locations and magnifications. A characteristic surface view of the mixed oxide sample after sodium exposure is reported in Figure 106.

Grain boundaries were still visible and the sodium attack was evident through the formation of some cracks. In agreement with the presence of initial faults due to the fabrication process, as detailed in Chapter 4, an evident fracture was also observed after the sodium interaction, indicated by a red arrow in Figure 106. Sodium penetration into the pellet is thereby also expected but the integrity of the recovered pellet, indicates that the potential sodium penetration did not allow considerable damaging or breaking of the pellet.

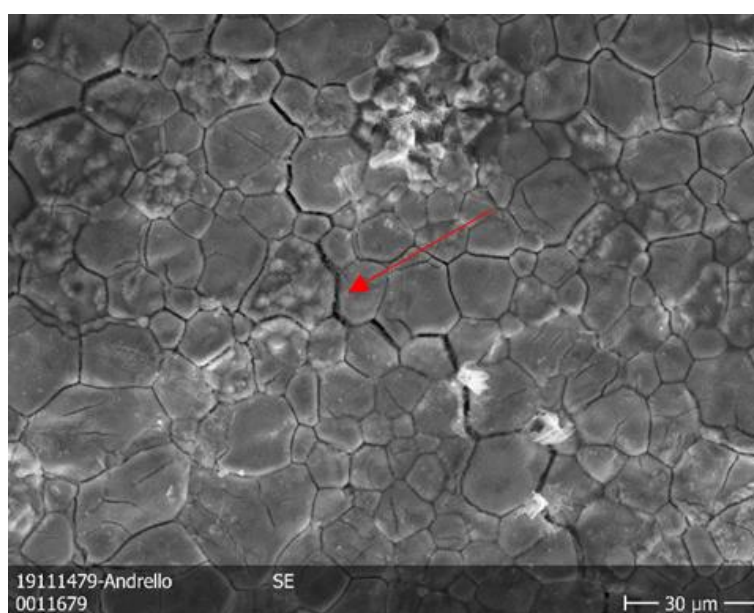


Figure 106: Surface view of the MOX after sodium interaction

The cross section check was crucial to understand the presence of the corrosion. Based on the literature, Mignanelli et al. [16] and Blackburn et al. [19] indicated the presence of a corrosion layer confined to the pellet periphery and accompanied by grain boundaries penetration in the case of stoichiometric mixed oxide or even with an oxygen to metal ratio exceeding 1.96.

In agreement with those observations, the present study confirmed the presence of a corrosion layer, as illustrated in Figure 107. Even though the corrosion phase was not detected by XRD, the corrosion layer appeared fully developed and covered the entire surface. The extent of the corrosion layer did not seem to be influenced by the grain orientation as suggested by the formation of a layer of uniform thickness. The corrosion layer was perfectly defined through the presence of a net separation from the bulk. However, the corrosion layer appeared thicker than the one of uranium oxide, having a thickness close to about 7 μm (compared to 5 μm (NAINT6) in the case of uranium oxide, in the same conditions). The SEM investigations

supported the assumption from the XRD analysis that a corrosion layer was formed during the interaction test, and that an amorphization of the produced phase took place afterwards.

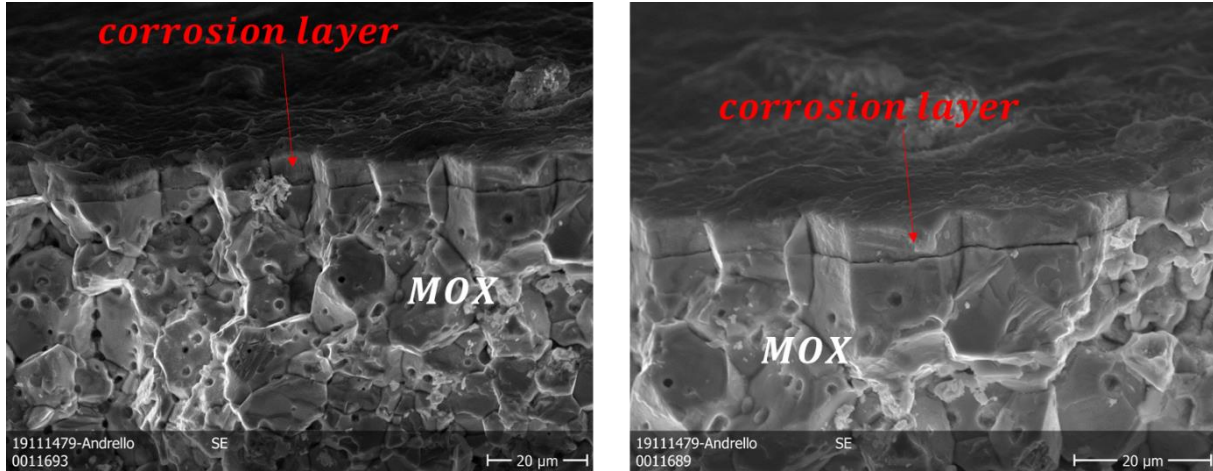


Figure 107: Cross section view of the MOX sample after sodium exposure

The sodium penetration at the grain boundaries was observed through the appearance of a dark grey phase as shown in the scanning electron micrograph in Figure 108. However, it can be seen that the sodium penetration remained confined to the grain boundaries without intragranular penetration. A little sodium penetration into the pellet was observed. The internal section of the pellet did not show the presence of this dark gray phase, which appeared over a distance of about 50 µm from the pellet surface only. The formed phase was also observed within the pores.

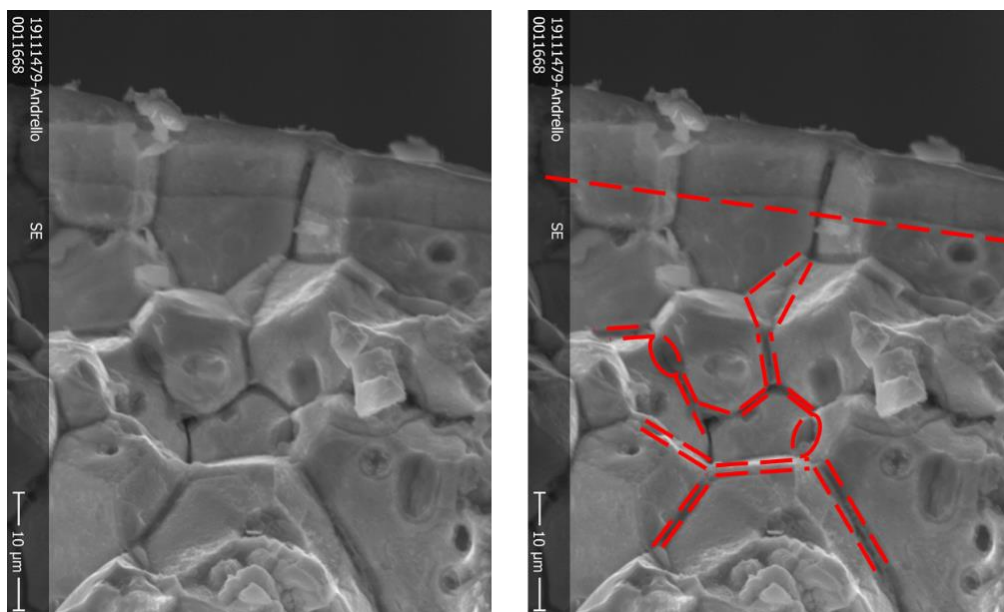


Figure 108: Fractured surface of mixed oxide pellet after 50 hours of sodium interaction

8.3 Kinetics tests: Imposed oxygen potential

8.3.1 Characterization

8.3.1.1 X-ray radiography

In the present study, X-ray radiography was used as complementary technique to determine the integrity of the pellets after each interaction test. The measurements were performed using a XT H 225 X-ray system. The radiography was carried out on the closed capsule, before and after the interaction with liquid sodium.

Before the interaction test, an intact mixed oxide sample was visible inside the capsule, as illustrated in Figure 109 (left). Due to the handling and the transport of the capsule to different gloveboxes, the sample was sometimes placed in vertical position.

The low density of sodium did not allow seeing it in the X-ray pictures. Nevertheless, the low sodium density allowed clearly distinguishing the shape of the mixed oxide discs after the interaction of 12 and 192 hours in liquid sodium, as reported in Figure 109 middle and right, respectively. The presence of sodium probably allowed also keeping the vertical position of the sample after 192 hours of interaction and did not resulted in dispersed pieces.

The radiography confirmed that the disintegration of the stoichiometric mixed oxide pellets was achieved in less than 12 hours, when the interaction took place under imposed oxygen potential. Extensive penetration of sodium into mixed oxide pellets would be expected since the pellets broke into several separated pieces. The pellet could be distinguished from the niobium buffer because of its original disk shape (having a height of about 2 mm), which was still visible in the X-ray pictures and is illustrated in the red frame. The small disks/pieces next to the mixed oxide pellets are the sodium niobate buffer.

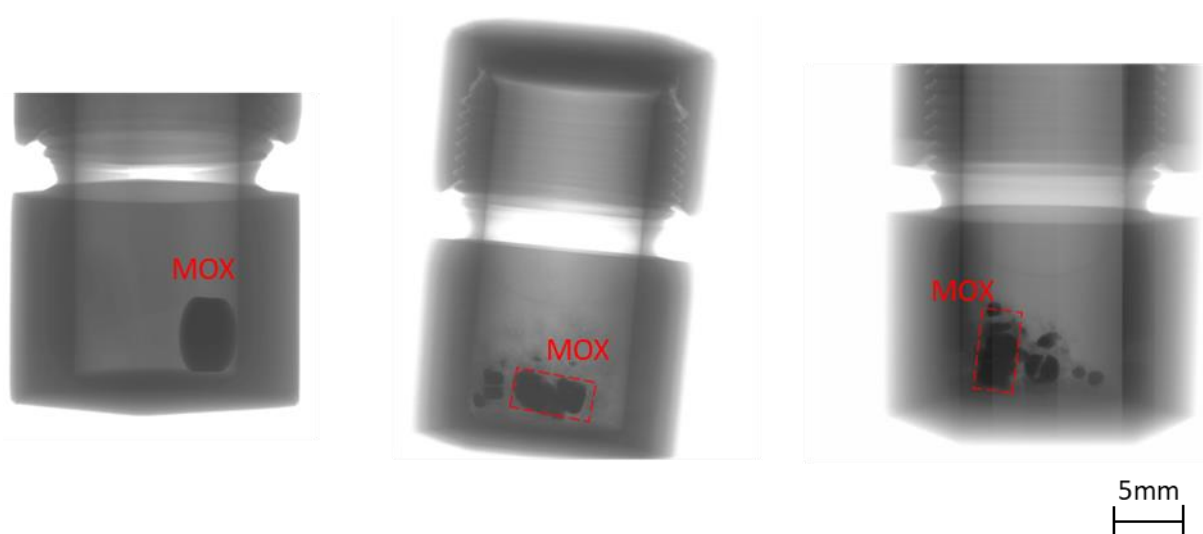


Figure 109: X-ray radiography of the capsule after sodium interaction at 973K. Left: before interaction Middle: after 12 hours of sodium interaction. Right: after 192 hours of interaction.

The considerable sodium attack, which caused the mixed oxide pellets to break into pieces, made the recovery of the pellets difficult. As illustrated in the scanning electron micrograph of Figure 110, only the sample after 48 hours of interaction was recovered still intact. All the other samples were recovered in pieces or even as powder, as for the sample after 12 hours of interaction. Table 20 summarizes the conditions of each sample after the retrieval from sodium.

The presence of a pellet still intact after 48 hours of interaction with liquid sodium at fixed oxygen potential compared to the damaged pellets after 12 and 24 hours can probably be explained by the influence of the initial status (fractures/damages due to the pressing process) of the pellet on the reaction. Indeed, it seems reasonable to consider that the completely pulverization of the pellet after 12 hours of interaction could be due to the presence of preexisting damages, which enhanced the sodium penetration through the pellet and led to its destruction. The observed initial faults within the pellet, originating perhaps from the pressing, could lead to a rapid penetration of sodium during the heat treatment. The fabrication process has thereby to be considered as parameter influencing the extent and evolution of the sodium-fuel reaction. Moreover, even the sodium dissolution by ethanol should have affected the final integrity of the pellet. The X-ray radiography (Figure 109 middle) of the pellet after 12 hours interaction illustrated a damaged pellet, but still in pieces. However, after the sodium dissolution the pellet was completely pulverized.

Table 20: Summary of the sample recovery after each interaction

<i>Interaction time (hours)</i>	<i>Initial shape</i>	<i>After reaction</i>
12	Disk	Powder
24	Disk	Damaged disk
48	Disk	Disk
96	Disk	Damaged disk
192	Disk	1 small piece

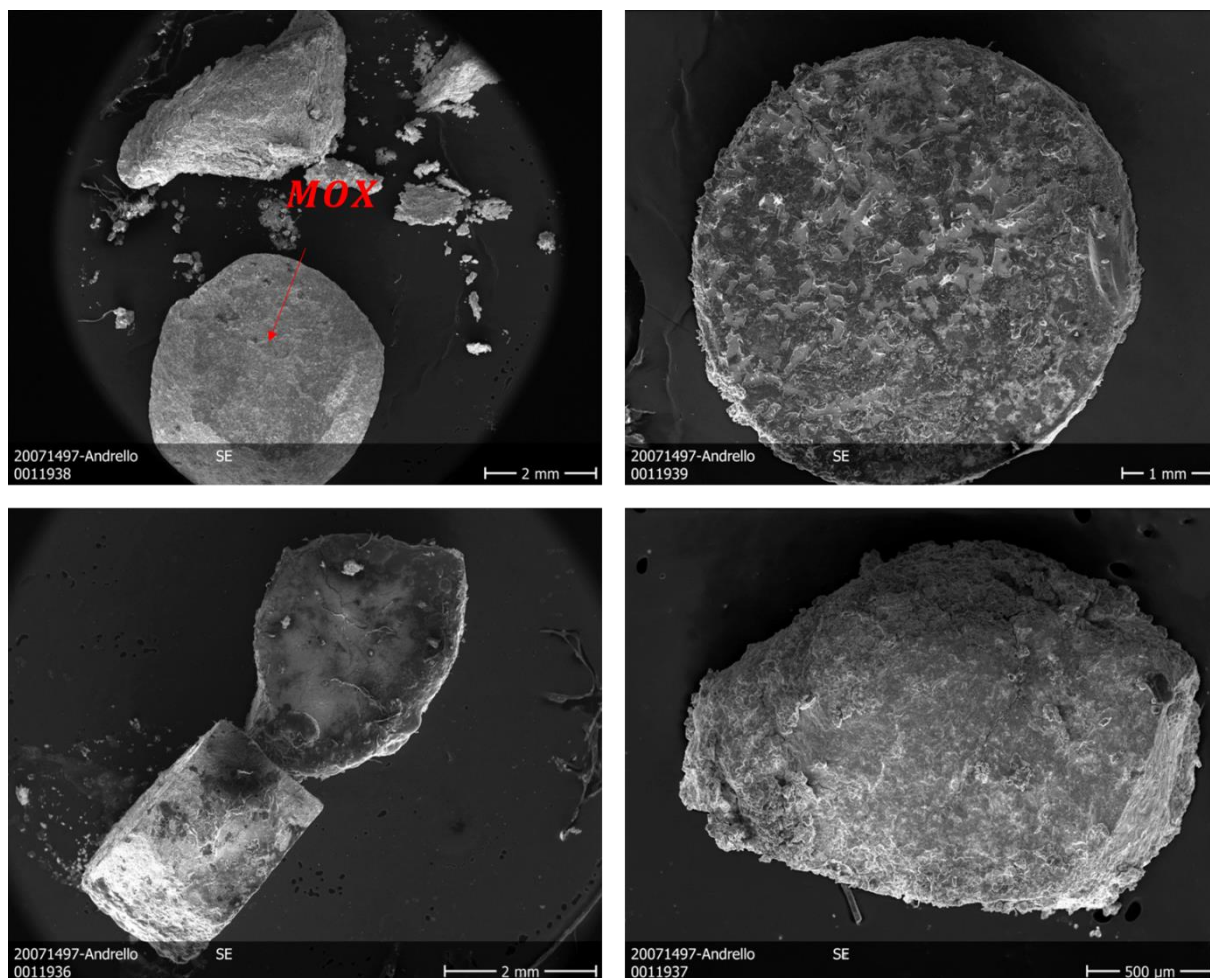


Figure 110: View of the samples after the recovery. Top left: NAIN14. Top right: NAIN15. Bottom left: NAIN16. Bottom right: NAIN17.

8.3.1.2 XRD

The recovered powder after the sodium dissolution was characterized by XRD in order to confirm the presence of the sodium niobate buffer, proving that it was not fully depleted during the interaction tests. However, the XRD analyses showed, with exception of the sample tested for 48 hours, the presence of an additional phase which did not belong to the sodium niobate.

An example of the recorded pattern is reported in Figure 111. However, as resulted from XRD analysis, for the interactions of 12, 24, 96 and 192 hours the presence of an additional phase was observed, which did not belong to the sodium niobate. Additional Bragg reflections were observed at the 2θ values of $28.373(6)^\circ$, $32.874(9)^\circ$, $47.174(9)^\circ$, $55.947(1)^\circ$, $58.658(4)^\circ$, $76.110(7)^\circ$, $78.453(5)^\circ$, $87.666(6)^\circ$, $94.563(3)^\circ$, $106.198(1)^\circ$, $113.502(8)^\circ$ and $116.016(7)^\circ$ and corresponded to the mixed oxide phase.

The sodium niobate powder included indeed a significant amount of mixed oxide, but no traces of trisodium uranoplutonate were observed. However, as previously observed, the expected

corrosion layer which should form during the reaction between sodium and mixed oxide, was probably converted into an amorphous phase during glovebox handling, which is not detectable by XRD. Moreover, it has to be accounted that, even in presence of a crystalline phase, the amount of the formed phase should be no appreciable compared to the mixed oxide phase (considered in the form of powder) and thereby not visible through XRD.

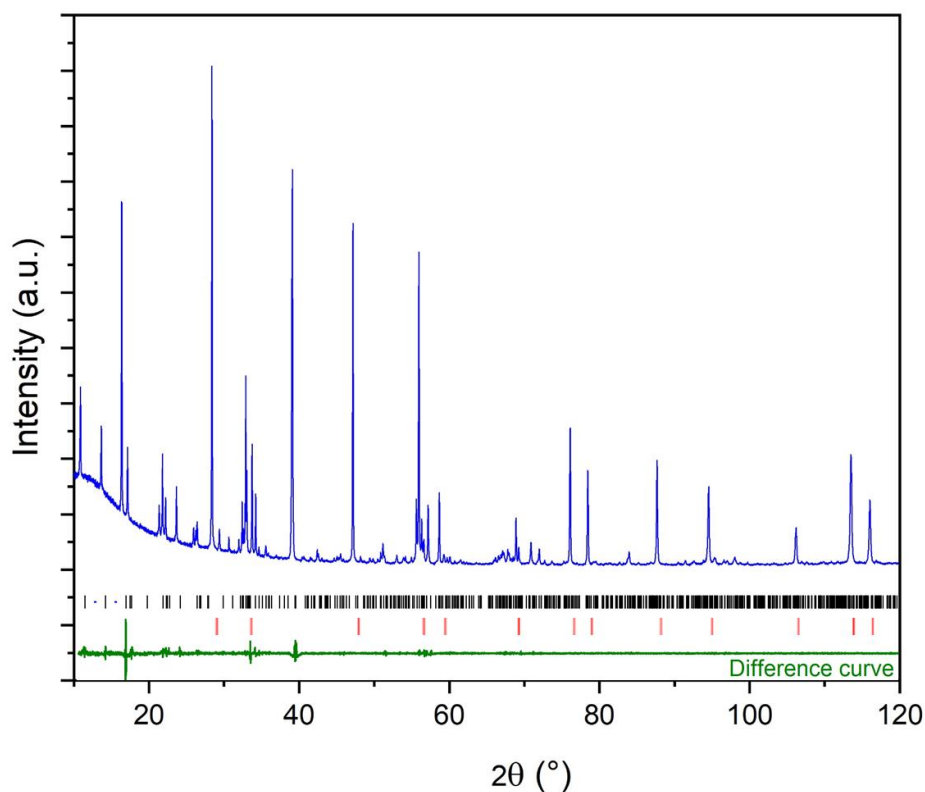


Figure 111: XRD pattern of the moisture Na_3NbO_4 and reduced mixed oxide. Black: Na_3NbO_4 . Red: $(\text{U,Pu})\text{O}_{1.99}$

Rietveld refinement of the diffractograms showed that the lattice parameter of the mixed oxide phase corresponded to about 5.451 Å. Detailed data of the lattice parameter of the mixed oxide phase after each sodium interaction are given in Table 21.

When compared with the initial lattice parameter of the mixed oxide, i.e. 5.446 Å, the lattice parameter after the sodium reaction seemed a bit higher. The higher lattice parameter can be due to a reduction of the stoichiometric mixed oxide due to sodium interaction.

The deviation from stoichiometry was calculated from the lattice parameter using the following formula [105]:

$$a(\text{pm}) = 547.0 - 7.4y + 32x \quad (40)$$

where x and y correspond to the general formula $(U_{1-y}Pu_y)O_{2-x}$.

The corresponding sub-stoichiometric mixed oxide correspond to an oxygen to metal ratio close to 1.99 for interaction tests of less than 24 hours and 1.98 for longer interactions, indicating the influence of the interaction time.

Table 21: MOX lattice parameter after sodium interaction at 973 K

Interaction time (hours)	Initial composition ($M = U_{0.68}Pu_{0.32}$)	Lattice parameter (Å) after interaction	O:M after sodium interaction
12	MO_2	5.451(5)	1.985(3)
24	MO_2	5.450(3)	1.988(5)
48	MO_2	-	-
96	MO_2	5.452(8)	1.978(7)
192	MO_2	5.451(8)	1.982(8)

8.3.2 SEM

The presence of initial faults originating from the pressing step during the pellet fabrication was also supported by the observation of cracks on the pellet surface after the sodium reaction. As illustrated in Figure 112, the cracks became well visible and their extent was probably increased during the interaction with liquid sodium. The pellet breaking and its separation into pieces could not be attributed to the extent of the reaction product only, but it was probably enhanced by the presence of preexisting faults. This led to a rapid sodium penetration into the pellet which made more surface available for the sodium reaction.

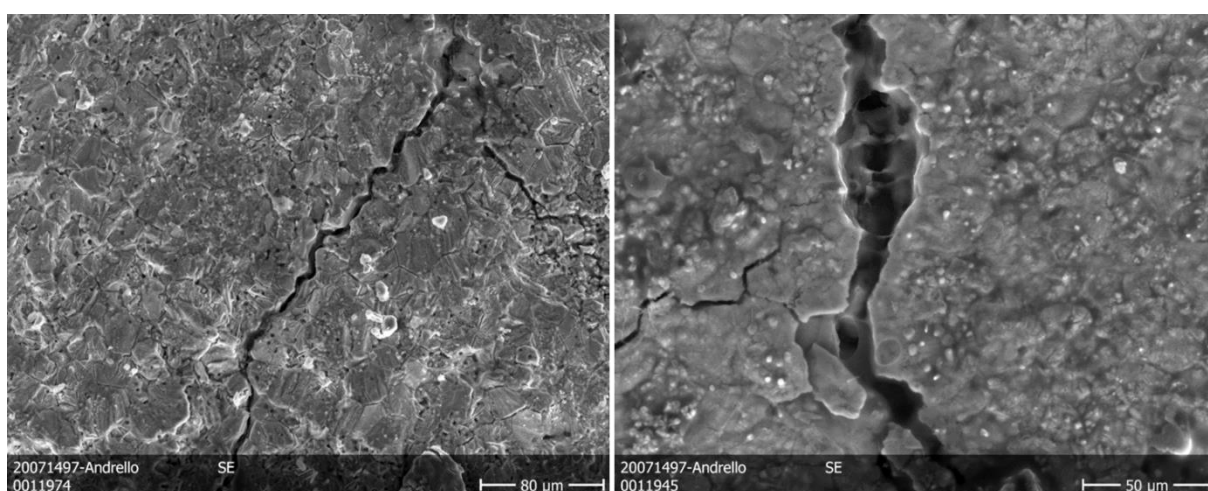


Figure 112: View of faults on the pellet surface after sodium interaction at 973 K. Right: NAIN17. Right: NAIN16.

Cross section analyses were made on fracture surfaces. Pellets or pieces were mechanically broken. Polishing was avoided in order to limit as much as possible the damage and loss of reaction product. Characteristic scanning electron micrographs of fractured surface of mixed oxide pellets after interaction with liquid sodium at 973 K are reported in Figure 113. The appearance of a corrosion layer confined to the pellet periphery was observed on all pellets, together with a little sodium penetration at the grain boundaries, where the pellet was probably dense. Sections of the internal surface, which were exposed to sodium during the heat treatment, resulted in an evident sodium attack. For comparison two micrographs are reported in Figure 114. Grain boundaries were clearly visible in the fracture surface. Instead, damaged grains were present on the section exposed to sodium during the interaction. The latter exhibited a so-called *popcorn* morphology.

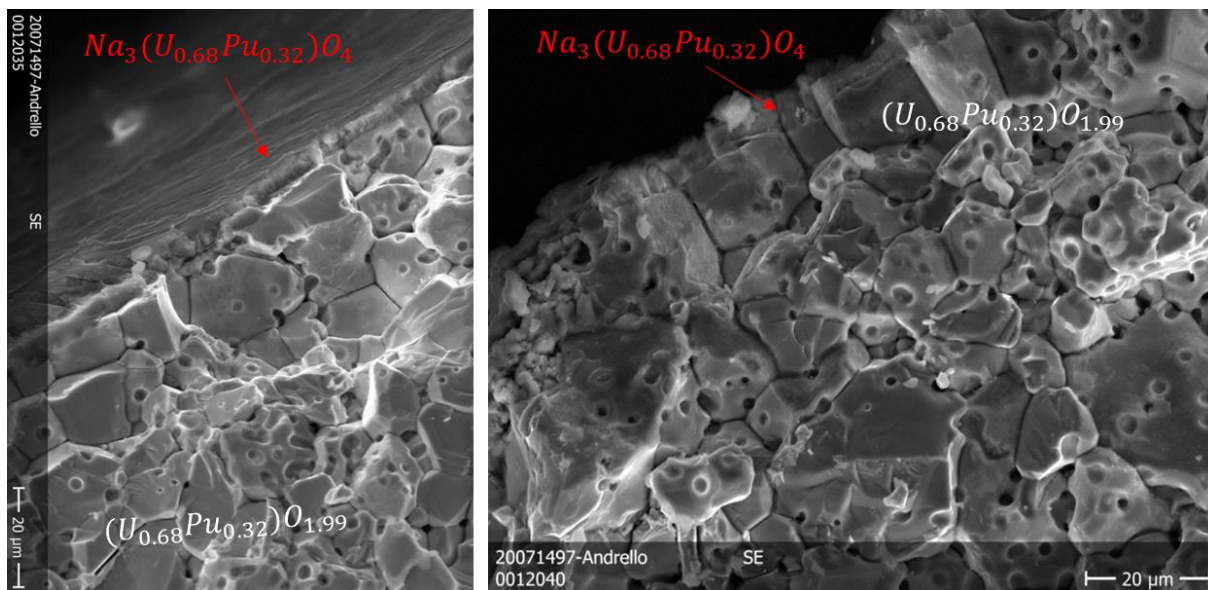


Figure 113: Scanning electron micrograph of a fracture surface of mixed oxide pellet. Appearance of a corrosion layer confined at the pellet periphery.

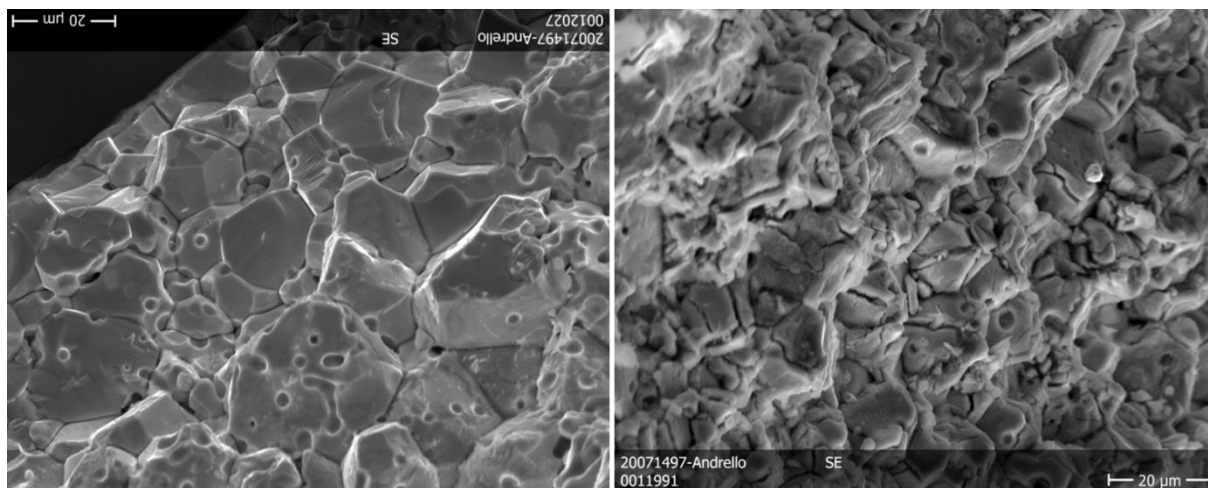


Figure 114: Comparison between an internal fracture surface which did not come into direct contact with sodium (left) and an internal surface exposed to sodium (right) during the interaction test.

8.3.3 EDX

Energy Dispersive X-ray Spectroscopy (EDX) was used as complementary technique to identify the chemical elements present in the sample. In particular, EDX was used to corroborate the presence of the corrosion phase, since due to its amorphization, the reaction product could not be revealed by XRD analysis.

An example of the characteristic EDX spectra obtained from a selected area of the sample surface is shown in Figure 115. Peaks at 0.525, 1.041, 3.164 and 3.348 keV corresponded to the energy level of oxygen, sodium, uranium (with an additional peak at 13.612 keV) and plutonium (with an additional peak at 14.276 keV), respectively. Impurities of aluminum were also detected, but they were not related to the sodium interaction.

These impurities were most likely due to the long storage of the samples inside the aluminum containers, which were used to store the samples. The EDX analysis supported the presence of an additional phase, which was chemically different from the mixed oxide bulk. The corresponding phase should contain the expected chemical elements of a reaction product in the form of $\text{Na}_3(\text{U,Pu})\text{O}_4$.

The EDX analysis of the samples revealed also the presence of sodium oxide in some zones of the surface, stemming from residual sodium which oxidized under the glove box atmosphere.

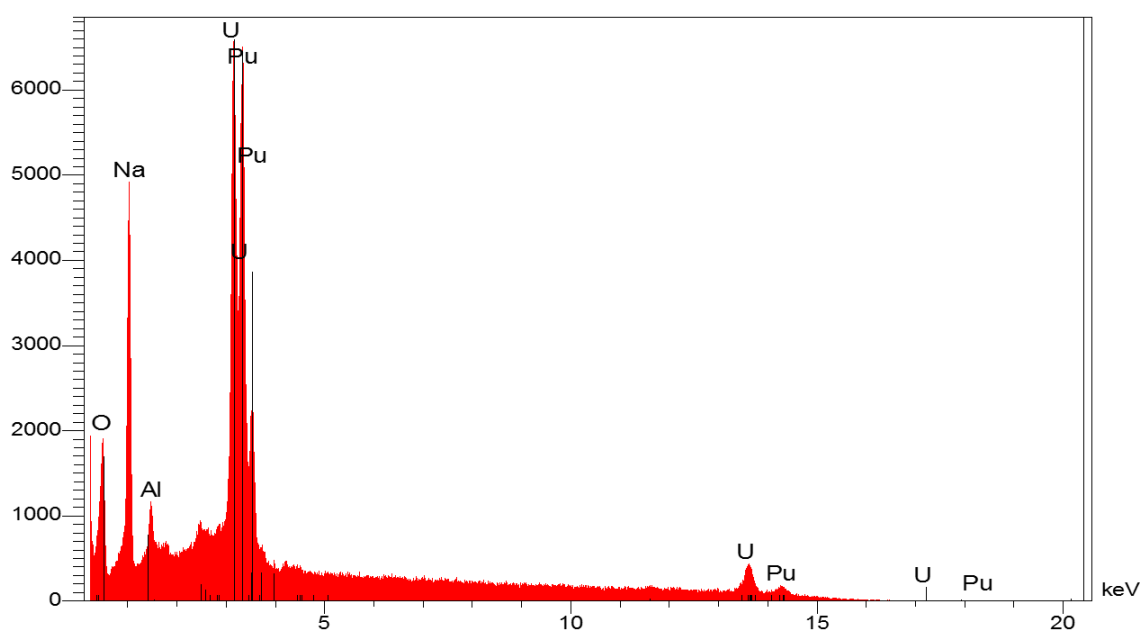


Figure 115: EDX spectrum of mixed oxide after sodium interaction

8.3.4 Rate determining step

The determination of the extent of the reaction was difficult due to the intensive damage induced by the sodium attack on the mixed oxide pellets. The extent of the reaction was determined through the analysis of micrographs taken from the sections of the recovered pieces of the pellets. The reaction rate was evaluated considering the corrosion layer at the periphery of the pellet only. The growth rate of the corrosion layer as function of time was evaluated by measuring the thickness of the corrosion layer present at each sample, representing different reaction times.

The measurements were performed on fracture surfaces at different positions. Due to the nature of the fracture surface, the measurements on mixed oxide were less accurate when compared to those on uranium oxide, where cross sections were flat and clean thanks to preparation by FIB. Due to all these issues, the uncertainties of these measurements were higher than for uranium oxide.

As observed for uranium oxide (in 7.2.5), the corrosion layer thickness was found to grow parabolically in the initial timeframe of interaction, as reported in Figure 116. In this case, the reaction rate obeys to the following law:

$$y = 0.65 t^{0.5} \quad (41)$$

where t is the time.

Still in agreement with uranium oxide, a change occurred in the long timeframe of interaction, as illustrated in Figure 117 and the corresponding law is:

$$y = 1.55 t^{0.25} \quad (42)$$

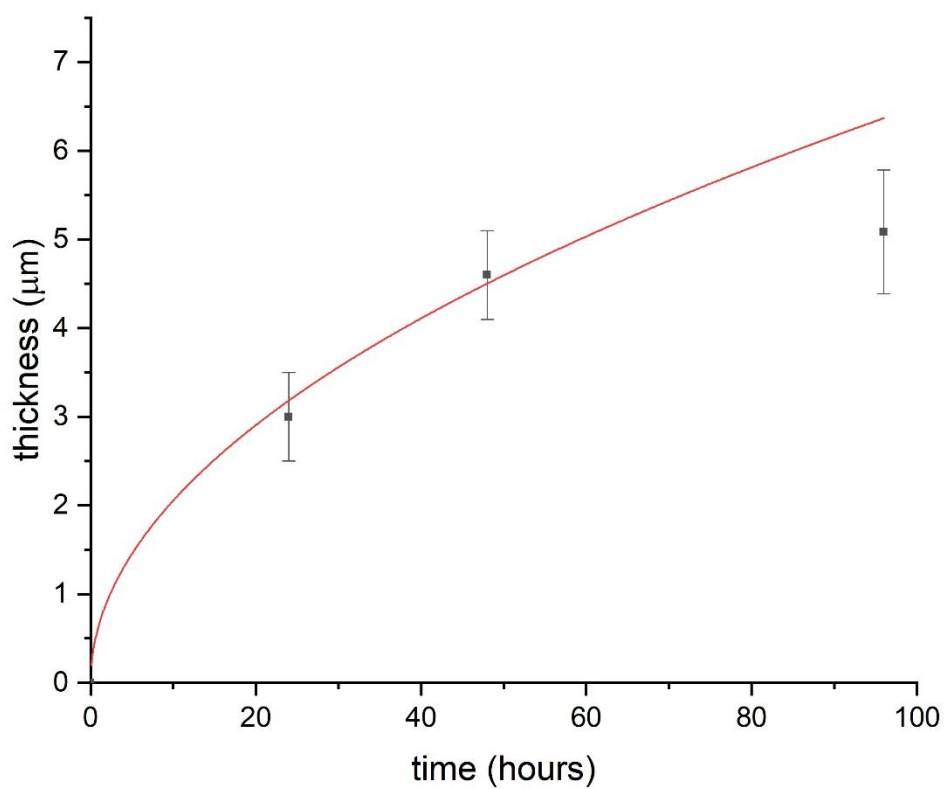


Figure 116: Fit of the experimental point at 24, 48 and 96 hours of interaction at 973 K.

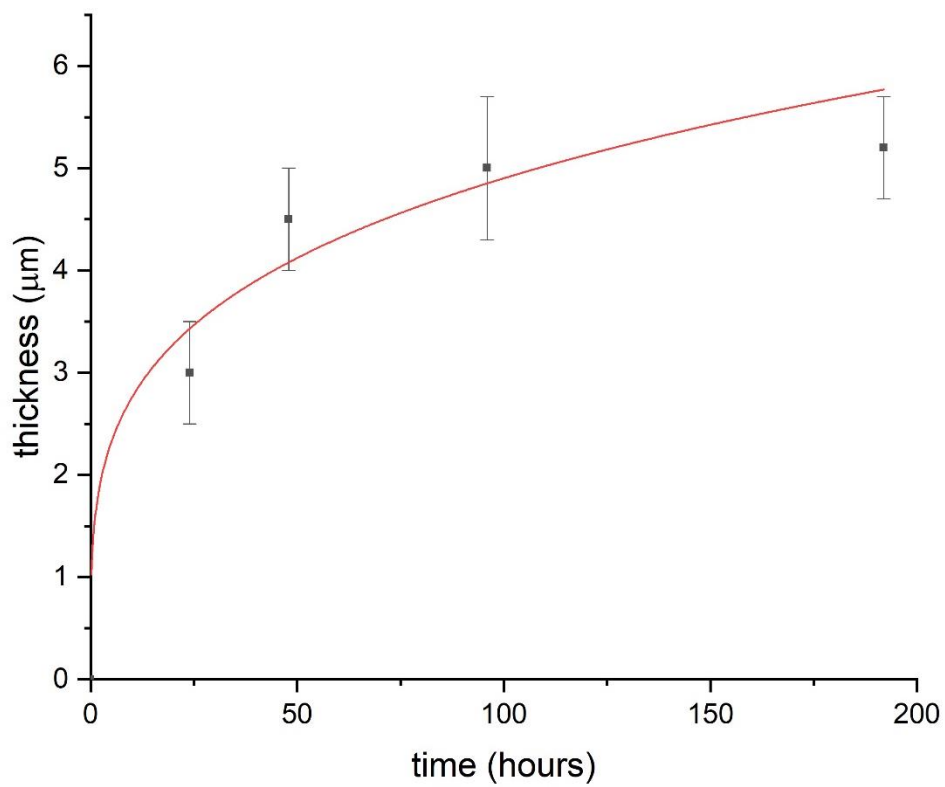


Figure 117: Fit of the experimental point at 24, 48, 96 and 192 hours at 973 K.

8.4 Conclusion

With exception of the observed grain boundaries attack in mixed oxide, uranium oxide and mixed oxide reacted in a similar manner with liquid sodium under the same conditions of temperature and oxygen partial pressure. As observed for the uranium oxide interaction, mixed oxide exhibited the formation of a uniform corrosion layer confined to the pellet periphery. In this study, the law of rate growth was obtained from the fit of the experimental points, which were gained through the measurement of the thickness of the superficial corrosion layer only. The influence of grain boundaries attack was not accounted for at this stage, due to evident difficulties in the measurement. Also for the mixed oxide, as illustrated in Figure 118, the rate of the reaction followed a parabolic law in the initial timeframe, indicating that the reaction was likely diffusion-controlled. However, still in agreement with the behavior of the uranium oxide as illustrated in Figure 119, a change of the rate growth was observed for longer interaction timeframe.

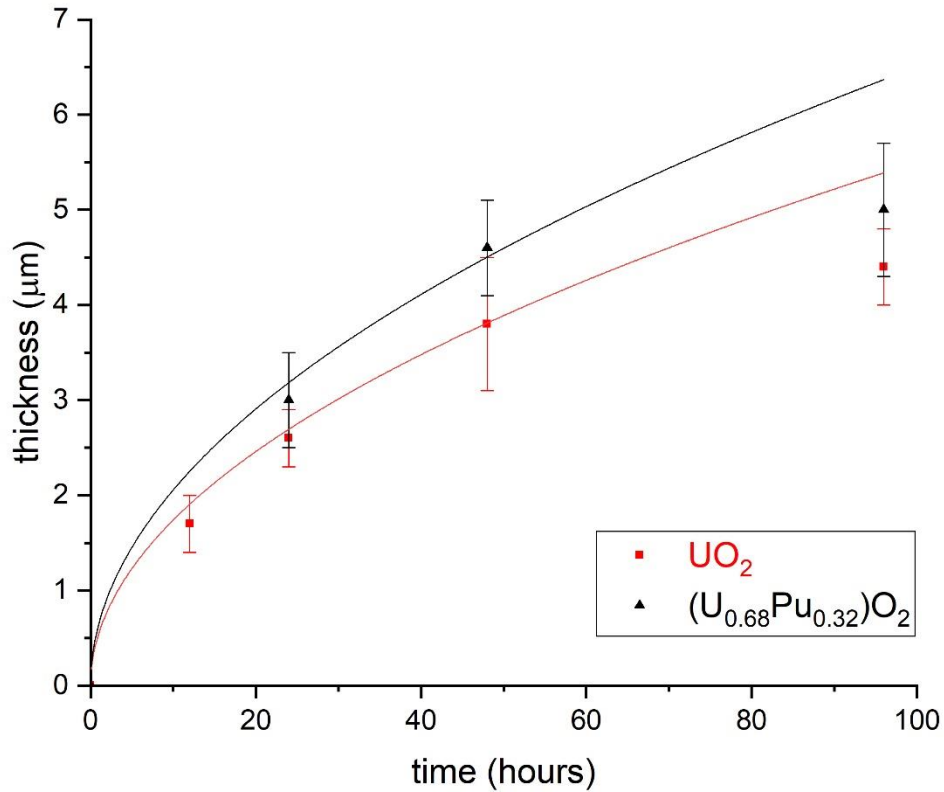


Figure 118: Comparison between the experimental data obtained for interaction tests between UO_2 (black line) and MOX (red line) with liquid sodium at the beginning of the reaction.

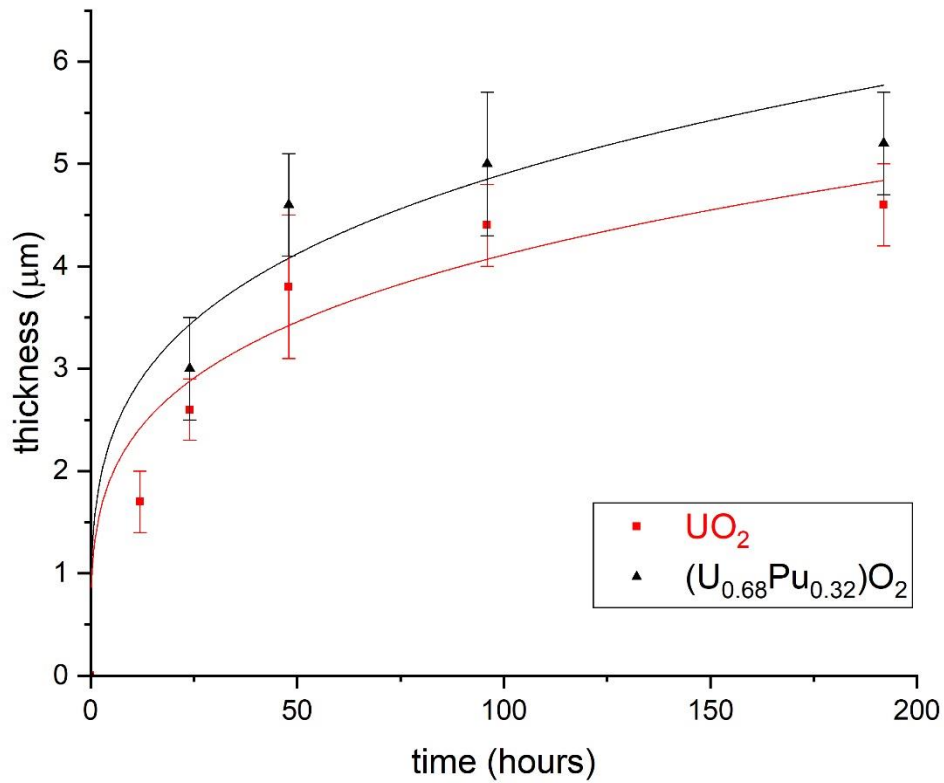


Figure 119: Comparison between the experimental data obtained for interaction tests between UO_2 (black line) and MOX (red line) with liquid sodium for long-period reaction.

The comparison between the experimental data of this study with the curve given in literature is illustrated in Figure 120. The blue curve refers to the general law given by Craig et al. [89]. As can be noted, the gained experimental trend at 973 K of this study is in good agreement with the general law reported by Craig et al. [89].

Figure 121 reports the comparison between the experimental data of this study with the curve (green) extrapolated from the data reported by Mignanelli et al. [16]. The authors did not report the accuracy of their data, but indicated that a significant uncertainty exists, due to the way in which they measured the experimental data. For this comparison, there is less agreement compared with the previous one, but still the similar regime of variation as function of time.

The good match between the experimental results of this study with those reported in literature gave confidence on the validity of the used experimental approach.

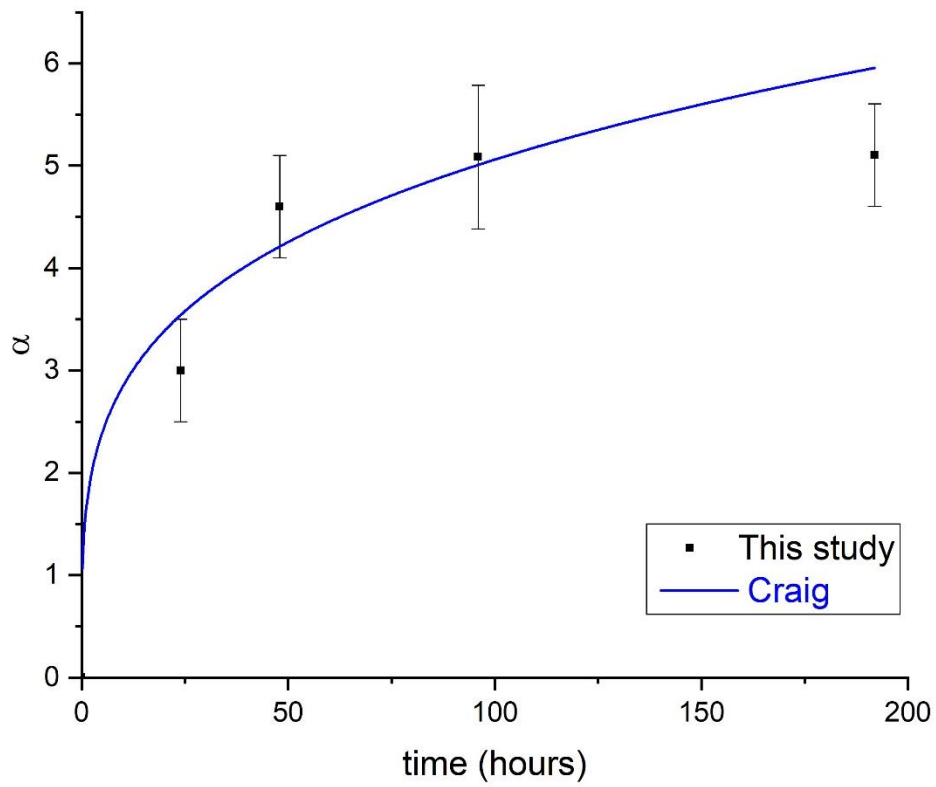


Figure 120: Comparison between the experimental result of the present study and data in literature.

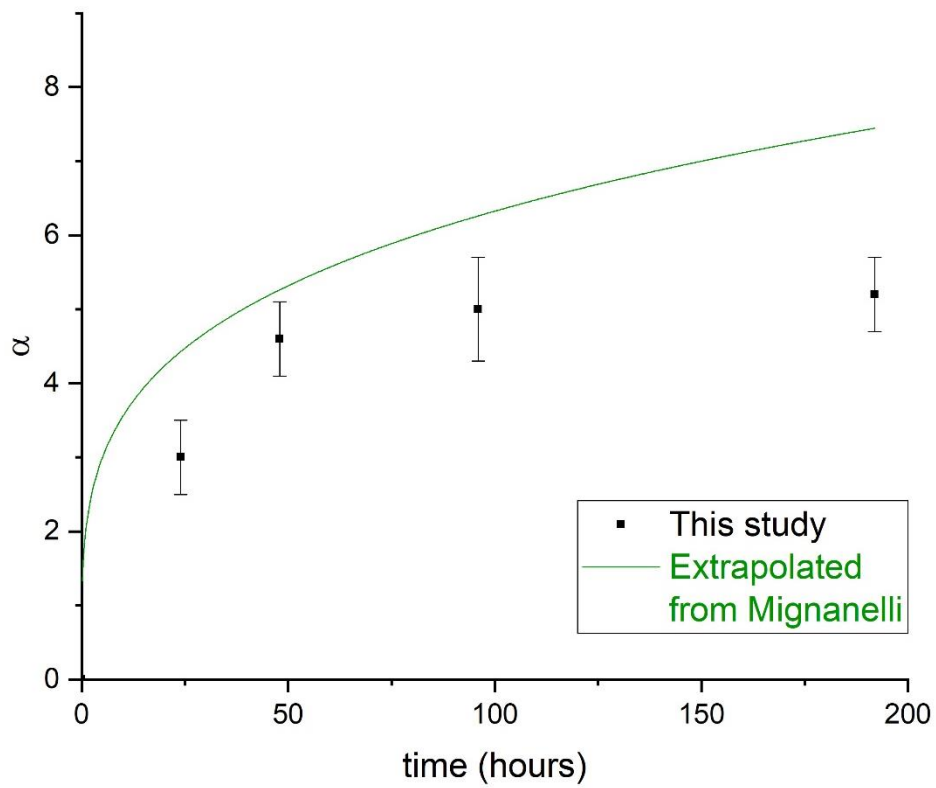


Figure 121: Comparison between the experimental result of the present study and data in literature.

In addition to the similarity between uranium and mixed oxide, additional information was gained through the experimental observations made out of the reaction between mixed oxide and liquid sodium. This study, indeed, highlighted the importance of the fabrication process of the mixed oxide on their integrity during the sodium interaction. The presence of “open” grain boundaries and significant cracks in the starting sample represented pathways easily reachable by liquid sodium. In this way, sodium was likely to penetrate into the pellets, leading to their breaking. This hypothesis is supported by the retrieval of an intact pellet after 48 hours of interaction, which could indicate that the disruption of the mixed oxide pellets can be likely linked to the presence of significant initial faults rather than to the sodium reaction. The enhancement of the sample breaking due to initial faults was reported in literature [16] and confirmed by this study. The amorphization of the corrosion phase did not allow structural characterization and phase identification. However, the presence of a corrosion phase was observed by electron scanning analysis and detected by EDX measurements. Additional investigations are needed to understand if the corrosion layer corresponds exactly to trisodium uranoplutonate.

The reduction of stoichiometric mixed oxide due to the reaction with sodium is well-known in literature [106]. In the present study, the reduction of stoichiometric mixed oxide was also achieved. The deviation from stoichiometry was found to be dependent on the interaction time. The final O/M ratio corresponded to about 1.99 for interaction tests shorter than 24 hours and to circa 1.98 for longer interaction tests. However, it has to be taken into account that the O/M ratio of the powder immediately after the sodium reaction could be even less. Indeed, the mixture of sodium niobate and mixed oxide was stored inside the glove box for a long period (more than 3 months) before the XRD examination. The long storage time may have resulted in a slight oxidation of the mixed oxide powder, under the glovebox atmosphere. The oxidation of mixed oxide powder under glovebox atmosphere was indeed observed by Vigier et al. [107] and cannot be excluded even in the present study.

The reduction of mixed oxide due to the reaction with sodium can be compared with the reduction of hyper-stoichiometric uranium oxide observed in the thin film studies detailed in Chapter 5. Indeed, the exact O/M ratio threshold value at which the reaction between uranium oxide and sodium does not take place corresponds to 2.00. As concern mixed oxide, even if the exact O:M ratio value at which the reaction with sodium does not occur is not established yet, a value close to 1.96-1.97 [], depending on the plutonium content, is expected. This means that at higher O/M values extra oxygen is given to the reaction resulting in a potential destructive (sample breaking) effect for mixed oxide close to stoichiometry. This conclusion is in agreement with the results of the present study and with these reported in literature either for hyper-stoichiometric uranium [15] and for mixed oxide [16].

9 *Modelling of the reaction mechanism*

The last chapter deals with the modelling of the mechanism of the reaction between uranium oxide and sodium. The main experimental results obtained in order to build this modelling are first briefly recalled. Then the transposition from uranium oxide, UO_2 , corrosion kinetics to mixed oxide corrosion kinetics will be discussed. All these elements will be the building block that will be used for the proposed modeling, which is described in the last part.

Ce chapitre décrit une proposition pour le mécanisme de réaction de croissance cohérent avec les observations expérimentales. À partir de ce mécanisme et en cohérence avec les résultats expérimentaux, une loi cinétique est proposée et comparée aux données cinétiques expérimentales. La modélisation inclut l'influence de la pression partielle en oxygène ainsi que celle de la température et peut être utilisée pour des études de conception.

9.1 *Experimental data for the modelling*

The experimental results gained by this study allowed to answer the questions reported in Chapter 2 as follows:

1. The corrosion product has uranium atoms with (V) oxidation state;
2. The nucleation is an instantaneous process and the reaction rate can be considered through the growth process only;
3. The sense of development is outward and the involved point defects are cationic interstitial or vacancies;
4. The rate determining step is attributable to a diffusion step.

Moreover, additional information was also gained, that are listed below:

Using XPS in UHV conditions:

- interaction studies confirmed that the formation of a ternary compound only appeared when the temperature is increased: this could be interpreted considering the mobility of uranium atoms which would be enhanced under temperature effect allowing the formation of a ternary compound. The fact that at room temperature deposition of metallic sodium on either stoichiometric or hyper-stoichiometric uranium oxide did not lead to the formation of a reaction compound, but rather to heterogeneous systems, can be likely interpreted as the result of the lack uranium diffusion at room temperature.
- Even in presence of a more oxidative environment of the one expected in the internal storage of future SFR, the ternary compound stabilized pure pentavalent uranium atoms.
- At room temperature, pure metallic sodium should not diffuse into the stoichiometric uranium oxide, since the appearance of plasmon loss peaks could be attributed to the formation of 3D islands of metallic sodium on the uranium substrate. Schematic illustration is given in Figure 122 (left). This behavior can be likely due to the low wettability of uranium oxide by metallic sodium. Nevertheless, in presence of interstitial oxygen, i.e.

hyper-stoichiometric uranium oxide, the reduction together with the sodium oxidation indicated an interdiffusion between oxygen and sodium atoms. When excess of metallic sodium was deposited on uranium trioxide, the latter was completely reduced to uranium oxide.

- The potential diffusion of sodium into hyper-stoichiometric uranium oxide is in good agreement with the grain boundaries attack reported in literature [15]. Indeed, the reduction of hyper-stoichiometric uranium oxide could be interpreted as potential release of oxygen at the grain boundaries, which allow attacking by sodium. At the same manner, the latter behavior can be likely extended to this observed for stoichiometric mixed oxide. Indeed, mixed oxide can much more easily be sub-stoichiometric by reducing Pu (IV) to Pu (III), compared to the reduction of stoichiometric uranium oxide to sub-stoichiometric UO_{2-x} , which required high temperatures [108].

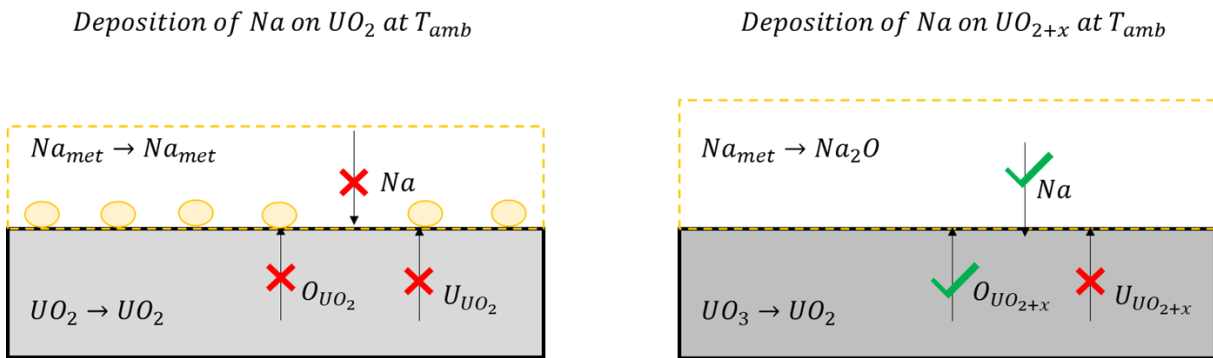


Figure 122: Schematic illustration of the interaction studies at 298 K. Left: deposition of metallic sodium on stoichiometric uranium oxide. Right: deposition of metallic sodium on hyper-stoichiometric uranium oxide

With interaction tests in closed capsules, either with or without imposed oxygen potential:

- EDX measurements did not detected sodium into uranium bulk and corroborated the hypothesis of lack of sodium diffusion into stoichiometric uranium oxide.
- The extent of the reaction product was not influenced by the grain orientations and the corrosion layer grew uniformly on the whole surface, without grain boundaries attack.
- The corrosion layer exhibited a preferential orientation as resulted from both XRD and TEM analysis. These features were not influenced by the presence of excess of oxygen, i.e. when sodium oxide was added to metallic sodium.
- The study of the growth process confirmed that the reaction is controlled by diffusion step, obeying to a parabolic law, at least at the beginning of the reaction. However, the reaction rate slowed down with the time.
- An original result was moreover obtained through the observation of the outward sense of development of the corrosion layer. This aspect was never investigated before although significant for the prediction of the involved point defects.

9.1.1 UO_2 vs MOX for modelling

Fast neutron spectrum of Sodium cooled fast reactors foreseen the use of mixed oxide fuel. The kinetics reaction between liquid sodium and MOX is then the one more interesting. In the present study, in order to check if the features and the evolution of the reaction between sodium the uranium oxide can be extended to the reaction between sodium and mixed oxide, complementary interaction tests were carried out. The imposed oxygen potential well approximated the expected oxygen potential in storage conditions, as illustrated in Figure 123. However, it can be noted that an exact threshold value for the formation of the trisodium uranoplutonate is still unavailable in literature. This led to some uncertainties in the evaluation of a potential formation of more than one phase, as observed for the uranium oxide.

Due to this uncertainty, in first approximation, the model is built considering the formation of single phase only. Moreover, it takes into account the growth of the corrosion layer only, without the grain boundaries attack so far.

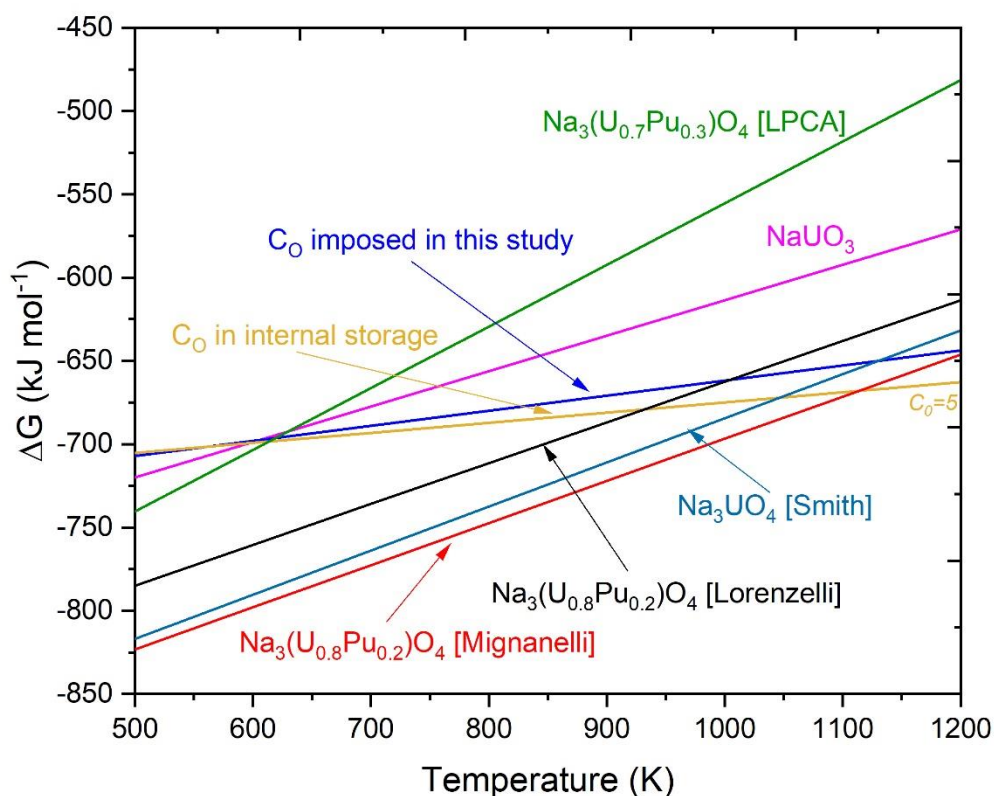


Figure 123: Oxygen threshold for the formation of trisodium uranoplutonate. Blue line: oxygen potential imposed in this study. Yellow line: oxygen potential expected in internal storage.

To justify the potential extension of the reaction mechanism of the superficial corrosion observed in the reaction between stoichiometric uranium oxide with the one of mixed oxide, some arguments are herein given.

The formation of a corrosion layer at the pellet periphery was similar in both stoichiometric uranium oxide and mixed oxide. Thereby, the reaction rate of the layer growth should obey at the same reaction mechanism, as observed by the parabolic regime in both reactions.

Moreover, it has to be considered that mixed oxide for nuclear reactor is expected to be substoichiometric MO_{2-x} , with an oxygen to metal (O:M) ratio of about 1.98. Under these conditions, grain boundaries attack could be avoided or at least confined to the periphery of the fuel, without inducing appreciable effects on the reaction rate. Under these considerations, the evolution of the reaction product in mixed oxide can be supposed to be close to the one observed for stoichiometric uranium oxide.

9.2 Modelling of the reaction mechanism

A growth mechanism with outward development of the trisodium uranate phase foresees a growth from the internal UO_2 - Na_3UO_4 interface to the surface of the Na_3UO_4 in contact with liquid sodium. The mechanism involves the uranium and oxygen diffusion through the Na_3UO_4 .

The mechanism, herein proposed, includes the following steps:

1. The dissociative adsorption of the oxygen O_2 at the external interface, i.e. at Na_3UO_4 surface;
2. The adsorption of sodium, Na, at the same interface;
3. External interface reaction with creation of building units of Na_3UO_4 at the outer Na_3UO_4 surface and creation of uranium vacancies;
4. Diffusion of uranium atoms via uranium vacancies from the internal interface UO_2 - Na_3UO_4 to the external surface of the Na_3UO_4 layer; and oxygen diffusion through the Na_3UO_4 layer to the external surface via interstitial sites;
5. Internal interface reaction with creation of oxygen vacancies in the UO_2 phase and formation of oxygen atoms in interstitial sites of the Na_3UO_4 phase,
6. Internal interface reaction with creation of uranium vacancies in the UO_2 phase and formation of uranium atoms in the sites of the Na_3UO_4 phase;
7. Annihilation reaction between uranium and oxygen vacancies, which should lead progressively to the formation of voids inside the bulk of the UO_2 phase.

The described steps are then written by the following equations using the Kroger-Vink notation for point defects:



$$\begin{aligned}
3Na - s_2 + 2O - s_1 + 2O''_{i,ext} \\
\leftrightarrow 3Na_{Na,ext} + V''''_{U,ext} + 4O_{O,ext} + 3s_2 + 2s_1 + h_{ext}
\end{aligned} \tag{45}$$

$$\begin{aligned}
V''''_{U,ext} &\leftrightarrow V''''_{U,int} \\
U_{U,int} &\leftrightarrow U_{U,ext} \\
O''_{i,int} &\leftrightarrow O''_{i,ext} \\
h_{ext} &\leftrightarrow h_{int}
\end{aligned} \tag{46}$$

$$O_{O,(UO_2)} \leftrightarrow V^{\circ\circ}_{O,(UO_2)} + O''_{i,int} \tag{47}$$

$$U_{U,(UO_2)} + V''''_{U,int} + h_{int} \leftrightarrow U_{U,int} + V''''_{U,(UO_2)} \tag{48}$$

$$V''''_{U,(UO_2)} + 2V^{\circ\circ}_{O,(UO_2)} \leftrightarrow \emptyset \tag{49}$$

The linear combination of these steps gives the balance equation of the reaction. The observation of a reaction rate with a parabolic law implies that the limiting step of the growth is a diffusion step.

The law of mass action applied to each step (except the diffusions) leads to the following equations:

$$K_1 = \frac{[O - s_1]^2}{P_{O_2}[s_1]^2} \tag{50}$$

$$K_2 = \frac{[Na - s_2]}{P_{Na}[s_2]} \tag{51}$$

$$K_3 = \frac{[V''''_{U,ext}][h_{ext}][s_2]^3[s_1]^2}{[O''_{i,ext}]^2[Na - s_2]^3[O - s_1]^2} \tag{52}$$

$$K_5 = [V_{O,(UO_2)}^{\circ\circ}][O_{i,int}''] \quad (53)$$

$$K_6 = \frac{[V_{U,(UO_2)}''''']}{[V_{U,int}'''''] [h_{int}]} \quad (54)$$

$$K_7 = \frac{1}{[V_{U,(UO_2)}'''''] [V_{O,(UO_2)}^{\circ\circ}]^2} \quad (55)$$

A schematic view of the reaction mechanism is illustrated in Figure 124.

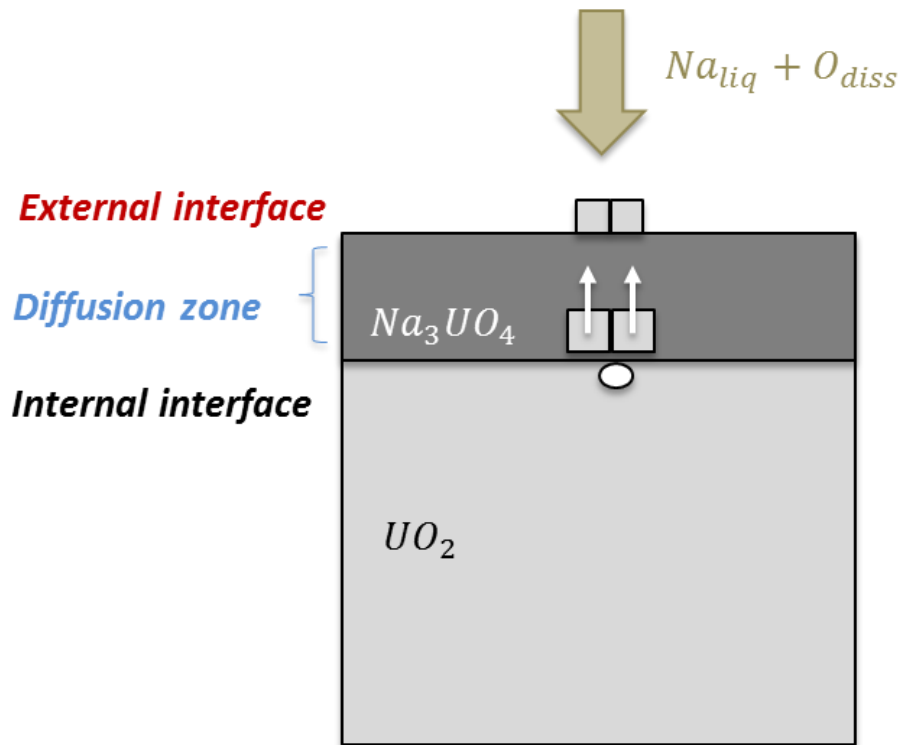


Figure 124: Schematic view of the proposed reaction mechanism. Diffusion zone, external and internal interface are indicated to localize where the steps take place.

The mechanism was used to obtain the expression of the ϕ function. Considering the diffusion of uranium vacancies as rate determining step, the growth reactivity is expressed according to the following expression:

$$\phi = \frac{D}{l_0} \Delta C = \frac{D}{l_0} ([V_{U,ext}'''''] - [V_{U,int}''''']) \quad (56)$$

where ΔC represents the difference in concentration of the diffusing species between the external and internal interface, D is the diffusion coefficient of uranium trough the layer of Na_3UO_4 and l_0 is an arbitrary length equal to 1 m.

By applying the conditions of electroneutrality in each phase:

$$\begin{aligned} [h_{int}] &= [2O_{i,int}''] + [5V_{U,int}'''''] \\ [h_{ext}] &= [2O_{i,ext}''] + [5V_{U,ext}'''''] \end{aligned} \quad (57)$$

Brouwer's approximation [44] implies that the following conditions have to be respected:

$$\begin{aligned} [h] &= [2O_i''] & \text{if } [2O_i''] &\gg [5V_U'''''] \\ [h] &= [5V_U'''''] & \text{if } [2O_i''] &\ll [5V_U'''''] \end{aligned} \quad (58)$$

By solving the previous system of equations for the two Brouwer's approximations, it is possible to express these concentrations in dependence on the partial pressures and the equilibrium constants of each step. The concentration of oxygen interstitials $[O_i'']$ is expected to be much higher than the concentration of uranium vacancies $[V_U''''']$, and consequently the ϕ function will be given by:

$$\begin{aligned} \phi &= \frac{D_{V_U'''''}}{l_0} ([V_{U,ext}'''''] - [V_{U,int}''''']) = \\ &= \frac{D_{V_U'''''}}{l_0} \left(5^{-\frac{1}{2}} 2^{-\frac{1}{3}} \right) K_1^{\frac{1}{2}} K_2^{\frac{3}{2}} K_3^{\frac{1}{2}} K_5 K_7^{\frac{1}{3}} P_{O_2}^{\frac{1}{2}} P_{Na}^{\frac{3}{2}} \left(1 - \frac{P_{O_2,eq}^{\frac{1}{2}} P_{Na,eq}^{\frac{3}{2}}}{P_{O_2}^{\frac{1}{2}} P_{Na}^{\frac{3}{2}}} \right) \end{aligned} \quad (59)$$

Taken into account that sodium partial pressure can be approximated to the sodium activity and results equal to 1, the ϕ function, through which the reaction rate can be described, results strictly depended from the square root of oxygen partial pressure.

Moreover, diffusion coefficient and equilibrium constant can be expressed as:

$$D = D_0 \exp\left(-\frac{E_a}{RT}\right) \quad (60)$$

$$K = K_i^0 \exp\left(-\frac{\Delta H_i^0}{RT}\right) \quad (61)$$

Then the ϕ function becomes:

$$\begin{aligned} \phi(P_i, T) = & \frac{D_{V_U}^0}{l_0} \left(5^{-\frac{1}{2}} 2^{-\frac{1}{3}}\right) (K_1^0)^{1/2} (K_2^0)^{3/2} (K_3^0)^{1/2} K_5^0 (K_7^0)^{1/3} \\ & \exp\left(-\frac{E_{a,V_U} + \frac{\Delta H_1^0}{2} + \frac{3\Delta H_2^0}{2} + \frac{\Delta H_3^0}{2} + \Delta H_5^0 + \frac{\Delta H_7^0}{3}}{RT}\right) \\ & P_{O_2}^{\frac{1}{2}} \left(1 - \frac{P_{O_2,eq}^{\frac{1}{2}}}{P_{O_2}^{\frac{1}{2}}}\right) \end{aligned} \quad (62)$$

This expression is characterized then by a pre-exponential factor k_0 , the temperature dependence through an apparent activation energy E_{app} of the reaction, the dependence from the square root of the oxygen partial pressure and the deviation from the equilibrium, i.e.:

$$\phi(P_i, T) = k_0 \exp\left(-\frac{E_{app}}{RT}\right) P_{O_2}^{1/2} \left(1 - \frac{P_{O_2,eq}^{1/2}}{P_{O_2}^{1/2}}\right) \quad (63)$$

Where

$$k_0 = \frac{D_{VU}^0}{l_0} \left(5^{-\frac{1}{2}} 2^{-\frac{1}{3}} \right) (K_1^0)^{1/2} (K_2^0)^{3/2} (K_3^0)^{1/2} K_5^0 (K_7^0)^{1/3} \quad (64)$$

And

$$E_{app} = E_{a,VU} + \frac{\Delta H_1^0}{2} + \frac{3\Delta H_2^0}{2} + \frac{\Delta H_3^0}{2} + \Delta H_5^0 + \frac{\Delta H_7^0}{3} \quad (65)$$

Considering the geometry of the system, which correspond to plate –like shape, the space function S_m , for instantaneous nucleation, anisotropic and outward growth, can be expressed [41] as:

$$S_m = \frac{V_{mA} l_0}{ze_0^2 \alpha} \quad (66)$$

Finally, coupling the geometrical and the physical model, the reaction rate can be expressed as:

$$\frac{d\alpha}{dt} = \phi S_m = \frac{V_{mA} l_0 k_0}{ze_0^2} \frac{1}{\alpha} \exp\left(-\frac{E_{app}}{RT}\right) P_{O_2}^{1/2} \left(1 - \frac{P_{O_2,eq}^{1/2}}{P_{O_2}^{1/2}}\right) \quad (67)$$

Since the model describes the square root dependence, it can be noted that is in good agreement with the experimental observations. Indeed, the parabolic growth well describes the beginning of the reaction, as illustrated in Figure 125, and is then conservative for higher corrosion times.

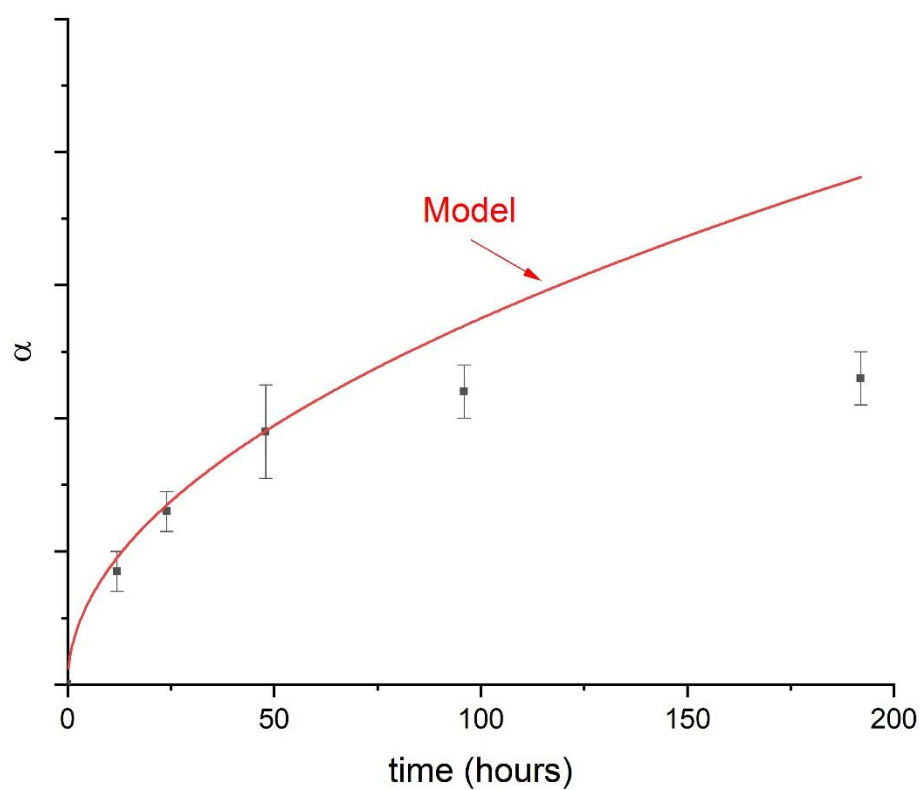


Figure 125: Experimental data and modelling fit. The modelling describes in a precise manner the beginning of the reaction and it is conservative over the long-term.

9.3 Conclusion

The reaction mechanism was proposed considering the experimental observation obtained in this study. The proposed mechanism includes the influence of the temperature and the oxygen partial pressure and can be used for sensitivity studies for the internal storage design. The modelling is well suited for the beginning of the reaction, since it was built to describe a parabolic growth, as observed in the experimental studies. It is then conservative for higher corrosion times, since a slowdown of the rate was observed with time.

The oxygen partial pressure in real conditions is in general maintained at low values and usually can vary from 1 ppm up to 10 ppm. This means that the value of the reaction rate, calculated using the proposed expression, can increase by a factor of about 3 times if it is considered that the reaction rate is a function of the square root of the oxygen potential.

However, additional improvements are needed to describe the grain boundaries attack, as observed for the reaction between mixed oxide and sodium. The potential formation of an additional phase should be also accounted and used to improve the presented model.

10 Conclusions

Dans ce chapitre, on donne les conclusions générales de ce travail et de nouvelles pistes de recherche sont proposées.

10.1 General conclusions

In the introduction, the need for a predictive model of the sodium-oxide reaction in order to assess a safe storage of failed fuel pin in an SFR core was underlined. This work contributed to the building of this model first by a comprehensive experimental study that brought some original results and second by a first step modelling using heterogeneous kinetics that will be further improved.

Surface studies of thin films prepared under ultra-high vacuum demonstrated that the oxidation state of uranium in the corrosion layer is uranium (V). At room temperature, pure sodium does not react with stoichiometric uranium oxide and the interdiffusion between sodium and oxygen atoms leads to the reduction of uranium trioxide, UO_3 , into stoichiometric uranium oxide, UO_2 . Interdiffusion between sodium and uranium oxide atoms is thermally activated and allows forming ternary compounds. The oxidation state of uranium (VI) in ternary compounds is strictly dependent on the initial presence of sodium oxide in the form of Na_2O_2 .

Interaction tests confirmed that nucleation is an instantaneous process. Trisodium uranate was formed under the experimental conditions of the compatibility tests. The characterization of the created phase highlighted that the corrosion phase has a preferred orientation, and does not depend on the orientation of uranium oxide grain. Also the thickness of the corrosion layer is independent of the grain orientations. Sodium does not penetrate through grain boundaries, even under relatively large excess of dissolved oxygen in liquid sodium, when it interacts with stoichiometric uranium oxide.

For the first time, indeed, two main experimental observations were obtained, i.e.:

3. Outward growth of the corrosion layer implying uranium cations as main species controlling the growth process, which was never considered before;
4. Double phase formation under imposed oxygen potential within a value close to the one expected in the internal storage, which was never assessed before and opened the question on the possibility to get more than one phase even for the mixed oxide.

Both these aspects were never observed before and opened the interest in further investigations.

Moreover, the reaction was found to be diffusion-controlled. Although sodium diffusion was usually considered as rate determining for the reaction in the past, the present study could not support this hypothesis, but considers the diffusion of uranium atoms through the corrosion layer as rate determining. Mixed oxide and uranium oxide behave in a similar manner, with exception of the observed grain boundaries attack in mixed oxide. The nucleation process is instantaneous and the reaction is diffusion-controlled.

In the present study, a first attempt of a reaction mechanism was proposed using the heterogeneous kinetics formalism. The model was proposed on the base of the experimental

observations, previously described. The reaction mechanism takes into account the following features:

5. The corrosion product contains uranium atoms in the oxidation state (V);
6. The nucleation is an instantaneous process and the reaction rate can be considered through the growth process only;
7. The sense of development is outward and the involved point defects are cationic interstitials or vacancies;
8. The rate determining step is a diffusion step.

However, the model was proposed assuming the growth of a corrosion layer confined to the sample surface and characterized by only one single phase.

The proposed mechanism includes the influence of the temperature and the oxygen partial pressure and is well suited for the beginning of the reaction, since it was built to describe a parabolic growth, as observed in the experimental studies. It is then conservative for higher corrosion times, since a slowdown of the rate was observed with progressing time. In real reactor conditions the value of the reaction rate, calculated using the proposed expression, can vary between 1 to maximum 3 times the predicted rate of this study.

However, additional improvements are needed to describe the grain boundaries attack, as observed for the reaction between mixed oxide and sodium. The potential formation of an additional phase should be also accounted for and used to improve the presented model.

10.2 Future perspectives

This PhD study provided promising results, together with a number of new experimental data, and encouraged for further developments in order to continue the support of the design of the internal storage.

In particular, the observation of a double phase formation during the interaction of uranium oxide and liquid sodium at an imposed oxygen potential with a value close to the one expected for the internal storage, opened a new question if the same behavior would occur also for mixed oxide.

The missing of exact thermodynamic data did not allow stating the formation of a double phase so far, since the threshold for formation of trisodium uranoplutonate for a mixed oxide with a Pu content higher than 30% is still unclear. This aspect needs to be further investigated in order to get a comprehensive model.

As resulted from the present study, stoichiometric mixed oxide was broken when in interaction with liquid sodium at fixed oxygen potential. Nevertheless, the destructive behavior can be likely linked to initial faults in the mixed oxide pellets due to the fabrication process. For this reason, additional tests with less damaged samples would be useful.

In addition, since the expected mixed oxide for fast reactors should have an initial O/M ratio close to 1.98, additional investigations using sub-stoichiometric mixed oxide are needed to better understand the evolution of the reaction.

Since the proposed mechanism includes the influence of the temperature and the oxygen partial pressure, additional tests at different temperature would be needed to validate this model. Finally, the proposed mechanism should be further improved by including the grain boundaries attack.

Conclusions

Conclusions Générales

Dans l'introduction, nous avons insisté sur le besoin d'une modélisation prédictive de la réaction oxyde-sodium de manière à garantir la sûreté du stockage interne d'aiguilles défectueuses dans un réacteur à neutrons rapides. Ce travail a contribué à construire cette modélisation tout d'abord par un travail expérimental qui a permis d'apporter des résultats originaux, et ensuite une première tentative de modélisation s'appuyant sur la cinétique hétérogène et qui devra être améliorée.

Les études de surface sur des couches minces préparées sous ultravide ont démontré que l'état d'oxydation de l'uranium dans la couche de corrosion est U(V). A température ambiante, le sodium pur ne réagit pas avec le dioxyde d'uranium stœchiométrique et l'inter-diffusion entre sodium et oxygène conduit à la réduction du trioxyde d'uranium, UO_3 , pour donner le dioxyde d'uranium stœchiométrique, UO_2 . L'inter-diffusion entre sodium et oxygène est thermiquement activée et permet la formation de composés ternaires. La présence du degré d'oxydation U(VI) n'est possible que si on a présence de d'oxyde de sodium sous la forme Na_2O_2 .

Les tests d'interaction ont confirmé le mécanisme de germination instantanée. L'uranate de trisodium se forme dans les conditions expérimentales des tests de compatibilité. La caractérisation des phases formées a mis en évidence que la phase de corrosion avait une orientation préférentielle, mais qui ne dépendait pas de l'orientation des grains d'oxyde sous-jacents. Toutefois, l'épaisseur de la couche de corrosion est indépendante de l'orientation des grains. Le sodium ne pénètre pas dans les joints de grains lorsqu'il interagit avec le dioxyde d'uranium, même en présence d'oxygène dissous dans le sodium en relativement grandes quantités.

Deux faits originaux ont été mis en évidence qui n'avaient jamais été ni observés ni discutés précédemment, c'est à dire :

5. La croissance externe de la couche de corrosion impliquant que l'uranium est l'espèce qui contrôle le processus de croissance
6. La formation d'une couche de corrosion biphasée sous potentiel d'oxygène imposé, ce qui ouvre la question de l'existence potentielle de plusieurs phases dans la couche de corrosion, et ce même pour le MOX.

Ces deux faits originaux ouvrent la voie à nouvelles recherches.

En outre, on a trouvé que la cinétique de réaction était contrôlée par un mécanisme de diffusion. Bien que la diffusion du sodium soit généralement considérée comme l'étape limitante dans la littérature, cette hypothèse est incompatible avec nos observations qui mettent en évidence que c'est la diffusion de l'uranium qui doit être considérée comme l'étape limitante. Le dioxyde d'uranium et le MOX se comporte de manière similaire, à l'exception de la corrosion aux joints de grains observée pour le MOX. La germination est instantanée et la réaction contrôlée par la diffusion.

Dans cette étude, une première tentative de modèle cinétique a été proposée en utilisant le formalisme de la cinétique hétérogène. Le modèle a été construit en s'appuyant sur les

observations expérimentales apportées par ce travail. Le mécanisme de réaction prend en compte les éléments suivants :

9. Le produit de corrosion contient des atomes d'uranium à l'état d'oxydation (V);
10. La germination est instantanée et la cinétique peut être décrite par le mécanisme de croissance uniquement;
11. L'étape limitante est une étape de diffusion
12. La croissance suit un mécanisme de croissance externe, ce qui implique une étape limitante de diffusion de l'uranium.

Toutefois, le modèle a été construit en considérant la formation d'une couche de corrosion monophasée à la surface de l'oxyde.

Le modèle proposé inclut l'influence de la pression partielle en oxygène et de la température ; il est adapté pour décrire le début de la réaction : par construction ce modèle décrit une cinétique strictement parabolique. Il fournit une valeur conservative de la couche de corrosion pour les temps plus élevés car on observe expérimentalement un ralentissement de la réaction avec les temps longs. En utilisant la modélisation proposée, on peut évaluer que la cinétique de réaction varie d'un facteur 1 à 3 en fonction de la concentration en oxygène dans le sodium qui existe effectivement dans des conditions réacteurs.

Néanmoins, il est nécessaire d'améliorer ce modèle pour pouvoir rendre compte de la corrosion aux joints de grains observée dans le cas de la réaction MOX-sodium, et, le cas échéant, de l'existence d'une couche de corrosion biphasée.

Perspectives

Ce travail de thèse a produit des résultats prometteurs, et des données expérimentales originales, il plaide pour une poursuite des études en soutien à la conception d'un stockage interne sûr.

Plus spécifiquement, l'observation d'une couche de corrosion biphasée, observée lors de l'interaction du dioxyde d'uranium avec du sodium liquide sous un potentiel oxygène imposé avec une valeur proche de celle attendue en réacteur, ouvre la question d'un comportement équivalent avec le MOX.

L'absence de données thermodynamiques fiables ne permet pas de statuer sur la formation d'une couche de corrosion biphasée, car le potentiel oxygène pour la formation de l'uranate de trisodium à partir d'un MOX contenant 30% de Plutonium n'est pas clair. Cet aspect requiert des investigations complémentaires.

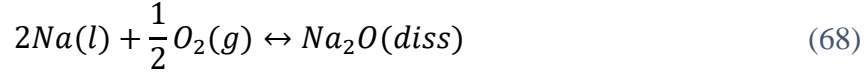
Il ressort de notre étude que les pastilles de MOX stœchiométrique ont été cassées lors de leurs interactions avec du sodium liquide sous un potentiel oxygène fixé. Ce comportement est très vraisemblablement due aux défauts de fabrication des pastilles MOX. Des essais avec des pastilles présentant moins de défauts à la fabrication seraient souhaitables pour éclaircir ce point.

En outre, le MOX qui sera utilisé dans les réacteurs rapides devrait avoir un rapport O/M initial de l'ordre de 1,98. Des études supplémentaires avec des combustibles sous-stœchiométriques seront nécessaires pour comprendre l'effet de la stœchiométrie sur la réaction.

Puisque le modèle proposé inclut l'influence de la température et de la pression partielle en oxygène, des tests complémentaires à différentes températures permettraient de valider le modèle. Enfin le mécanisme proposé doit être amélioré pour prendre en compte la corrosion aux joints de grains.

Annex: Concentration of oxygen dissolved in liquid sodium

In liquid sodium, the formation of Na_2O corresponds to the following chemical equation:



At thermodynamic equilibrium:

$$2\mu_{\text{Na}} + \frac{1}{2}\mu_{\text{O}_2} = \mu_{\text{Na}_2\text{O}} \quad (69)$$

where μ_{Na} , μ_{O_2} and $\mu_{\text{Na}_2\text{O}}$ are the chemical potentials of liquid sodium, oxygen and sodium oxide, respectively. Assuming pure sodium, $\Delta\mu_{\text{Na}} = \Delta G_{\text{Na}} \approx 0$.

The chemical potential of sodium oxide is:

$$\mu_{\text{Na}_2\text{O}} = G_{f,\text{Na}_2\text{O}}^0 + RT \ln a_{\text{Na}_2\text{O}} \quad (70)$$

where $a_{\text{Na}_2\text{O}}$ is the activity of sodium oxide in liquid sodium and $G_{f,\text{Na}_2\text{O}}^0$ is the standard Gibbs energy of sodium oxide formation.

Using Henry's law, the activity of sodium oxide in liquid sodium can be expressed by:

$$a_{\text{Na}_2\text{O}} = \frac{C_{\text{Na}_2\text{O}}(\text{dissolved})}{C_{\text{Na}_2\text{O}}(\text{saturated})} = \frac{C_{\text{O}_2,d}}{C_{\text{O}_2,s}} \quad (71)$$

where $C_{\text{O}_2,d}(\text{wppm})$ is the concentration of oxygen dissolved in liquid sodium and $C_{\text{O}_2,s}(\text{wppm})$ is the concentration of oxygen at saturation. By substitution of the Eq. 7 in the Eq. 6, we obtain a general expression of $\Delta\mu_{\text{O}_2}$ as:

$$\Delta\mu_{\text{O}_2} = \Delta G_{\text{O}_2}^{eq} = 2\Delta G_{f,\text{Na}_2\text{O}}^0 + 2RT \ln \frac{C_{\text{O}_2,d}}{C_{\text{O}_2,s}} \quad (72)$$

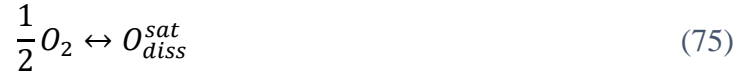
Expressions of the Gibbs energy of formation of Na_2O are reported in literature. Knacke reported [109]:

$$G_{f,\text{Na}_2\text{O}}^0 \left(\frac{\text{J}}{\text{mol}} \right) = -414657.9 + 136.8 T \quad (73)$$

Fredrickson and Chasanov gave a slightly different expression [110]:

$$G_{f,\text{Na}_2\text{O}}^0 \left(\frac{\text{J}}{\text{mol}} \right) = -421700 + 146.4 T \quad (74)$$

The Gibbs energy formation of Na₂O approximates well [111] the Gibbs energy of dissolution or Gibbs free energy change for the reaction:



Herein, O_{diss}^{sat} represents the oxygen dissolved in liquid sodium at saturation. Finally, using the solubility equation of Noden (Eq.2) and the Eq. 9, the equilibrium oxygen potential, in the Na-O system, is:

$$\Delta G_{O_2}^{eq}(\frac{J}{mol}) = -735691.3 + 33.232T + (38.287\log C_o)T \quad (76)$$

Instead, using the Eq. 10:

$$\Delta G_{O_2}^{eq}(\frac{J}{mol}) = -749800 + 53.2T + (38.3\log C_o)T \quad (77)$$

Annex: Na-O system

The review made by Wriedt [62] in 1987 highlights the complexity of the Na-O system, which is not well-known, especially in the region Na_2O_2 - NaO_2 - NaO_3 - O_2 (above 50 at% O). Figure 126 shows the phase diagram published in his work [62]. As consequence of the discrepancies on the oxygen solubility in liquid sodium, it was hard to get the exact location of the boundaries. Sodium forms four oxides, depending on the temperature, namely $\text{Na}_2\text{O}(\text{s})$, $\text{Na}_2\text{O}_2(\text{s})$, $\text{NaO}_2(\text{s})$ and $\text{NaO}_3(\text{s})$. Among them, $\text{Na}_2\text{O}(\text{s})$ is the only which could coexist with liquid sodium, instead the other oxides would decompose to Na_2O [112]. Table 22 summaries the crystal structures of the sodium oxides.

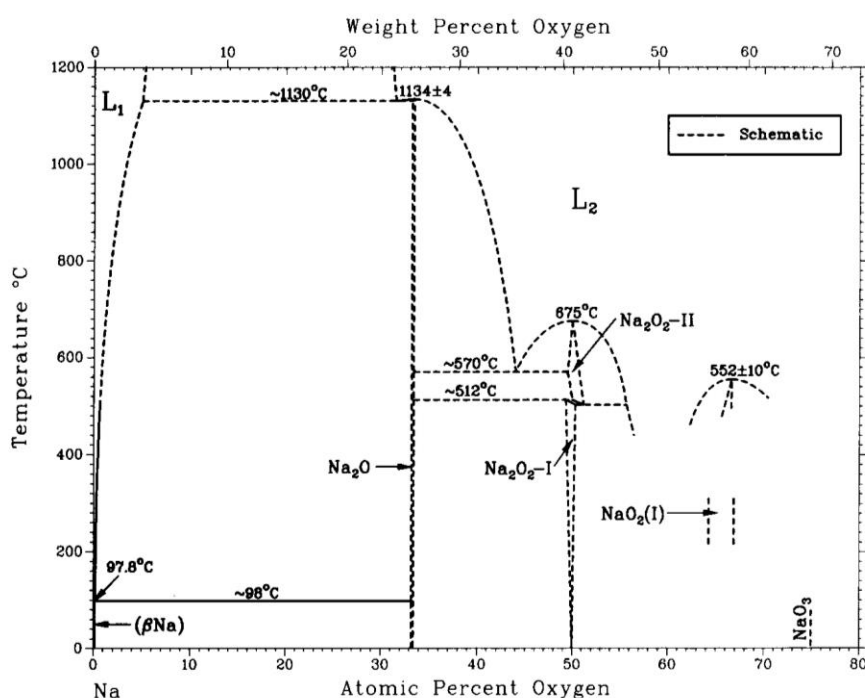


Figure 126: Na-O phase diagram [62]

At room temperature, the stable form of pure sodium is the solid phase $\beta\text{-Na}(\text{s})$ with a body-centered cubic symmetry in the space group Im-3m . All the available data on the melting temperature of metallic sodium are in good agreement and the value corresponds to 97.8°C [62, 113]. In its crystalline form, sodium oxide (Na_2O) has a cubic symmetry in the space group Fm-3m [62] and a melting temperature of 1130°C . In general, sodium oxide is weakly non-stoichiometric, but it is usually treated as stoichiometric compound [80].

The phase transition of the two stable crystalline forms, $\text{Na}_2\text{O}_2\text{-I}$ and $\text{Na}_2\text{O}_2\text{-II}$, of sodium peroxide Na_2O_2 is at 512°C and the melting point of $\text{Na}_2\text{O}_2\text{-II}$ corresponds to 675°C . Only the crystal structure of $\text{Na}_2\text{O}_2\text{-I}$ is reported in the literature [62] and correspond to a hexagonal symmetry in the space group of P-62m . Sodium dioxide NaO_2 exhibits three crystalline forms, $\text{NaO}_2\text{-I}$, $\text{NaO}_2\text{-II}$ and $\text{NaO}_2\text{-III}$ as well as a magnetic transition to $\text{NaO}_2\text{-IV}$ at low temperatures [62]. $\text{NaO}_2\text{-I}$ exhibits a cubic symmetry in the space group Fm-3m . Only the value of its melting point is reported and corresponds to $552 \pm 10^\circ\text{C}$. $\text{NaO}_2\text{-II}$ is reported as cubic in the space group Pa-3 , instead $\text{NaO}_2\text{-III}$ and $\text{NaO}_2\text{-IV}$ are reported to show an orthorhombic symmetry in the

space group Pnnm. Finally, sodium ozonide NaO_3 is reported as tetragonal with the space group Im2m.

Table 22: Summery of the phases in the Na-O system

<i>Phase</i>	<i>Symmetry</i>	<i>Space group</i>	<i>Lattice parameter (Å)</i>	<i>Ref.</i>
$\beta - \text{Na}$	Cubic (bcc)	Im-3m	4.288	[62]
Na_2O	Cubic	Fm-3m	5.55	[62]
$\text{Na}_2\text{O}_2\text{-I}$	Hexagonal	P-62m	6.207, 4.471	[62]
$\text{Na}_2\text{O}_2\text{-II}$	-	-	-	[62]
$\text{NaO}_2\text{-I}$	Cubic	Fm-3m	5.51	[62]
$\text{NaO}_2\text{-II}$	Cubic	Pa-3	5.46	[62]
$\text{NaO}_2\text{-III}$	Orthorhombic	Pnnm	4.26, 5.54, 3.44	[62]
$\text{NaO}_2\text{-IV}$	Orthorhombic	Pnnm	4.335, 5.537, 3.363	[62]
NaO_3	Tetragonal	Im2m	3.507, 5.77, 5.27	[62, 114]

Annex: Na-Pu-O system

There are much less data available in the literature for the Na-Pu-O system compared to those of the Na-U-O system. The investigation of the Na-Pu-O system started with Keller [46, 47, 48] and Pillon [49], as part of more complex systems involving alkali and actinide elements. More recently, the investigation was extended by Smith et al. [50, 51, 52], Bykov et al. [53] and Kovacs [54]. Figure 127 shows the Na-Pu-O diagram taken from the work of Bykov et al. [53], in which several sodium plutonates are reported, such as Na_3PuO_4 , $\text{Na}_4\text{Pu}_2\text{O}_5$, Na_2PuO_3 , Na_4PuO_4 , Na_6PuO_5 , Na_4PuO_5 and Na_6PuO_6 . The plutonium oxidation state in sodium plutonates compounds ranges from IV to VII. Some crystal structures [49, 65, 53] and thermodynamic [86, 87, 115] properties of the solids are available in literature. A summary of the structural properties of various sodium plutonates is reported in Table 23.

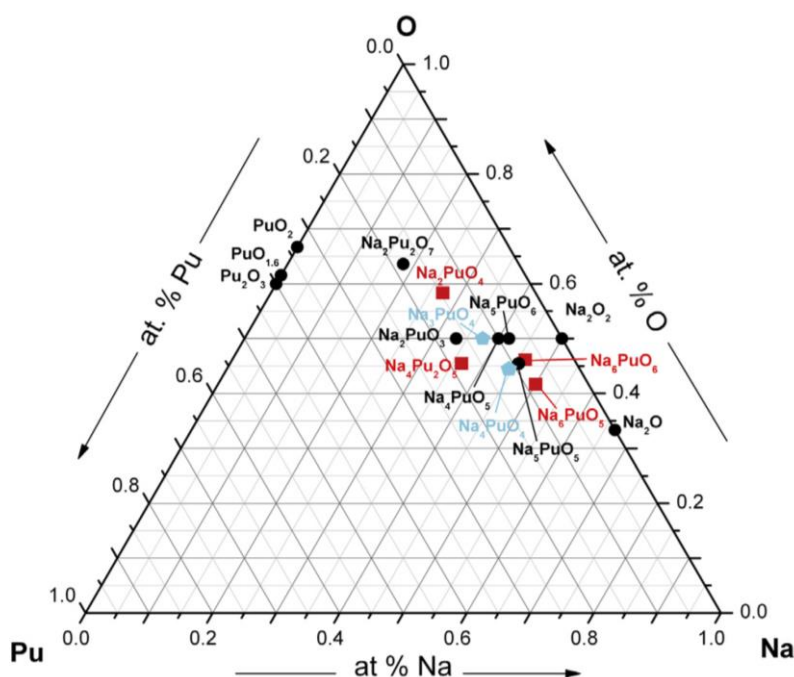


Figure 127: Na-Pu-O phase diagram from [53]

The tetravalent Na_2PuO_3 was reported by Pillon [49] with a rhombohedral symmetry. Instead Bykov [53] suggested two possible symmetries: rhombohedral in space group $R\bar{3}m$, and monoclinic in space group $C2/c$. The authors assigned the coexistence of the two structure to the synthesis conditions. Smith et al. [50] re-investigated the compound and, using the model of Na_2CeO_3 , reported the Na_2PuO_3 with the ordered monoclinic symmetry in space group $C2/c$. The question on the relationships between the ordered and the disordered structures of Na_2PuO_3 obtained by using different synthesis routes is still open. The pentavalent Na_3PuO_4 is reported with a NaCl-type superlattice structure [116], in contrast to the NaCl-type structure of Na_3UO_4 . Na_3PuO_4 shows a modification [53] after a slow heating. Similar to Na_4UO_5 , also for Na_4PuO_5 , a low temperature cubic phase was reported. In addition, Na_4PuO_5 is isostructural with Na_4UO_5 , with a tetragonal symmetry in space group $I4/m$. Although the phase Na_6UO_6 is not existing, the existence of the Na_6PuO_6 was reported.

Table 23: Structural proprieties of Na-Pu-O compounds

Phase	Symmetry	Space group	Lattice parameters (a,b,c)	Pu oxide state	Ref
Na_3PuO_4	Orthorhombic	Fmmm	13.302, 9.634, 6.651	V	[53]
$m - Na_4PuO_5$	Cubic	-	4.718, 4.718, 4.718	VI	[46]
Na_4PuO_5	Tetragonal	I4/m	7.519, 7.519, 4.619	VI	[53]
Na_2PuO_3	Monoclinic	C2/m	5.965, 10.313, 11.772	IV	[50]
Na_5PuO_6	Monoclinic	C2/m	5.823, 9.985, 5.752	VII	[53]
Na_5PuO_5	Monoclinic	C2/m	10.952, 4.616, 6.565	V	[53]
Na_6PuO_6	Hexagonal	-	5.76, 5.76, 15.9	VI	[46]

Annex: Additional information on the Na-U-O system

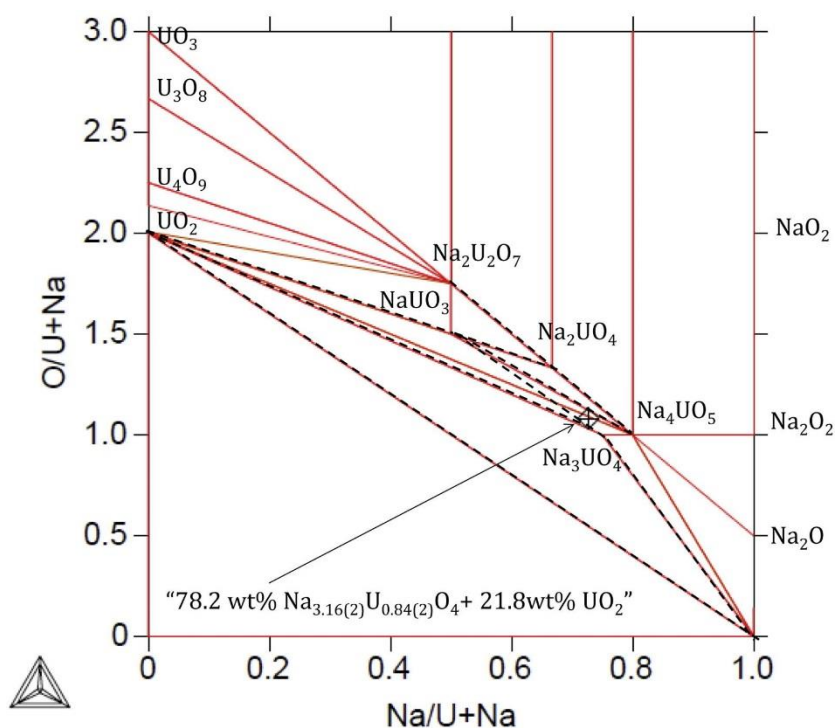


Figure 128: Calculated Na-U-O phase diagram at ~600°C from [80]

Table 24: Calculated oxygen potential thresholds of sodium uranate formation [73]

Compound	$\Delta G_{O_2}^{eq} (J \cdot mol^{-1})$
$\alpha - Na_3UO_4$	$-949072 + 264.55T$
$\alpha - Na_{3.16}U_{0.84}O_4$	$-923910 + 243.72T$
Na_4UO_5	$-918396 + 243.73T$
$NaUO_3$	$-826140 + 212.48T$
Na_2UO_4	$-817778 + 233.75T$
$Na_2U_2O_7$	$-695783 + 206.85T$

Table 25: Thermodynamic data of the Na-U-O system

<i>Compound</i>	$\Delta_f H_m^0$	S_m^0	$C_{p,m}^0$	$\Delta_f G_m^0$	<i>Ref.</i>
<i>Na₃UO₄</i>	-(2024 ± 8)	198.2±0.4	173.0 ± 0.4	-(1899.9 ± 8)	[83, 84, 85]
<i>NaUO₃</i>	-(1494.9 ± 10)	132.84 ± 0.40	108.87± 0.40	-(1412.5 ± 10)	[86, 87]
<i>Na₄UO₅</i>	-(2457.0 ± 2.2)	-(520.9 ± 6.3)	219±6.7	-(2301.7 ± 2.9)	[50]
<i>α</i> <i>– Na₂UO₄</i>	-(3208.4 ± 5.5)	166.0 ± 0.5	146.7 ± 0.5	-(1779.3 ± 3.5)	[50]
<i>Na₂U₂O₇</i>	-(3203.8 ± 4)	275.9 ± 1	227.3 ± 1	-(3011.5 ± 4.0)	[86, 87]

Annex: Detailed calculations of geometrical

In the case of inward growth, we can express the velocity of the reduction of the initial volume of the phase A due to its consumption as:

$$-\frac{dV_A}{dt} = \Re_A n_0 V_{mA} = -s_i \frac{dr_i}{dt} \quad (78)$$

Where s_i and r_i are the area and radius of the internal interface, respectively. In the same way, the variation of the volume of B due to its formations as:

$$\frac{dV_B}{dt} = \Re_B n_0 v_B V_{mB} = s_e \frac{dr_e}{dt} - s_i \frac{dr_i}{dt} \quad (79)$$

Where s_e and r_e are the area and radius of the external interface, respectively. Under steady state modes and by writing the rate of growth in separable rates:

$$\begin{aligned} \Re_A = \Re_B = \Re &= \phi S_m = \frac{\phi G s_p}{n_0} \\ V_{mB} &= \frac{z V_{mA}}{v_B} \end{aligned} \quad (80)$$

Where s_p is the area of the active surface (m^2) and z is the expansion coefficient. Finally, by substitution in Eqs 32 and 33, we obtain:

$$\frac{dr_i}{dt} = -\frac{\Re n_0 V_{mA}}{s_i} = -\frac{\phi G s_p V_{mA}}{s_i} \quad (81)$$

$$\frac{dr_e}{dt} = \frac{\Re n_0 V_{mA}}{s_e} (z - 1) = \frac{\phi G s_p V_{mA}}{s_i} (z - 1) \quad (82)$$

The motion of the external interface is then due to the volume expansion, meaning that if there is no volume change during the transformation of A into B, the expansion coefficient $z=1$, and the external interface is fixed.

In the case of an outward growth, the internal interface does not move and therefore does not contribute to the expansion of B. The production of B involves then only the displacement of the external interface and thereby:

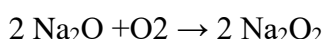
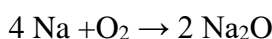
$$\frac{dr_i}{dt} = 0 \quad (83)$$

$$\frac{dr_e}{dt} = \frac{\phi G s_p V_{mA}}{s_i} z \quad (84)$$

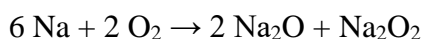
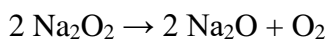
Annex: XPS studies of sodium and sodium oxide

As mentioned in the thermodynamic section, among the sodium oxide compounds reported in literature, there are sodium monoxide (Na_2O , white solid), sodium peroxide (Na_2O_2 , white to yellow solid), sodium superoxide (NaO_2 , yellow-orange, metastable at standard condition) and sodium trioxide (NaO_3). From the standpoint of thermodynamics, sodium peroxide is formed when the oxygen fraction is sufficiently large, and sodium monoxide is formed under a relatively low oxygen fraction.

When sodium is heated in air at 403-673 K, it produces Na_2O_2 , a process that goes through the generation of Na_2O :



Upon heating above 927 K, Na_2O_2 decompose to Na_2O and O_2 .



The melting temperatures of Na_2O and Na_2O_2 are 1405 K and 825 K, respectively. With a higher BE, oxidation of sodium is more efficient in the presence of atomic oxygen compared to sodium in the presence of molecular oxygen. Differences in the Au-4f_{7/2} intensities for different oxidation reactions (molecular versus atomic oxygen) can be linked to the level of coverage of the gold foil. It is becoming more important after oxidation of sodium with atomic oxygen. This can be explained by stronger interaction of the gold surface with sodium oxide than with sodium metal [1]. Once sodium is oxidized, it spreads and covers more the surface of gold. We see that with molecular oxygen, the coverage of gold foil is less effective after the heat treatment and improves slightly after oxidation. It looks that sodium is slightly oxidized, the molecular oxygen is dissolved in sodium, and volume increases at the extent of the surface coverage. After reaction with molecular oxygen, the sodium Na-1s PE line has BE similar to metallic sodium, and the broadening of Na-1s core level peak may support a partial oxidation.

Figure 129 compares the Na-1s spectra obtained on Au after oxidation with atomic and molecular oxygen, on stoichiometric UO_2 , on stoichiometric UO_2 with molecular oxygen and on UO_{2+x} . Sodium stays metallic on Au and UO_2 . Moreover, on UO_2 we observed plasmon peaks, on Au we observe only single and asymmetric peak. The difference could be explained by the shape of sodium deposit at the surface of samples. As sodium has a higher wettability on gold [1], deposition leads to a growth along the layer while on UO_2 it rather forms 3D particles.

Oxidation of sodium requires either a deposition on UO_{2+x} (black spectrum) or oxidation with atomic oxygen on gold foil (grey spectrum). In both cases, the Na-1s peak is at about 1073 eV BE versus 1071.5 eV for metallic Na. An intermediate case between oxide and metallic sodium appears when oxidation is performed with molecular oxygen on gold (blue spectrum) and on the UO_2 film (red spectrum). The corresponding BE between 1071 and 1071.8 eV, respectively, is close to the one of metallic sodium and ternary compounds, such as NaUO_3 . Based on the experiment, we can deduce that the oxidation of sodium is taking place directly with interstitial

oxygen present in UO_{2+x} . On stoichiometric UO_2 , sodium does not seem to oxidize under our experimental conditions and the dissociation of molecular oxygen seems to be the limiting step for oxidizing sodium. This is also supported by the fact that UO_2 oxidizes into UO_{2+x} with molecular oxygen.

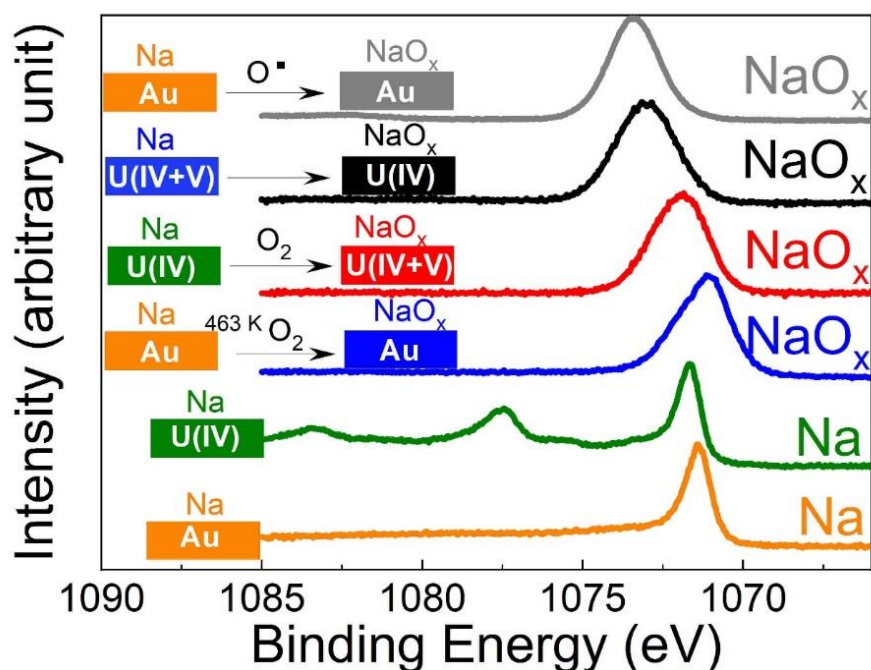


Figure 129: Na-1s spectra obtained on Au after oxidation with atomic and molecular oxygen, on stoichiometric UO_2 , on stoichiometric UO_2 with molecular oxygen and on UO_{2+x} .

Poor wetting is due to a weak interface interaction between non-reactive metallion-covalent oxides. It is not strong enough to counterbalance the metallic bond in the neighborhood of the interface [1]. To increase wettability of oxides by liquid metals, dissolution of oxygen even on the ppm level [14] is necessary. This phenomenon, explained by Naidich et al. [15], suggests that oxygen, dissolved in the metal, associates with metal atoms and forms clusters having a partially ionic character, with a charge transfer from the metal to the oxygen atoms. These clusters can develop Coulomb interactions with ionocovalent ceramics and, consequently, adsorb strongly to the metal/oxide interfaces. Compared to the Na-1s BE of metallic sodium at 1071.5, the 0.7 eV higher BE in Na/ UO_2 plus O_2 match the difference between Na_2O and metallic Na [16], suggesting that the sodium oxidizes together with UO_2 in presence of molecular oxygen resulting in the formation of an oxidic sodium compound [17]. Na-1s in ternary compounds has a BE of 1071.8 eV, close to the one of metallic sodium, but it is broader than Na-1s present in the metallic.

Annex: Heterogeneous MOX

Even following the usual external gelation process for the production of MOX powder, the technique is known to give a homogeneous solid solution, the first batch resulted in a heterogeneous composition.

The powder (referred to the compound after the sintering) was composed at least of two phases corresponding to (XRD data):

1. $\text{U}_{0.82}\text{Pu}_{0.18}\text{O}_2$
2. $\text{U}_{0.65}\text{Pu}_{0.35}\text{O}_2$

The heterogeneity of the compound was also confirmed by SEM and RAMAN analysis.

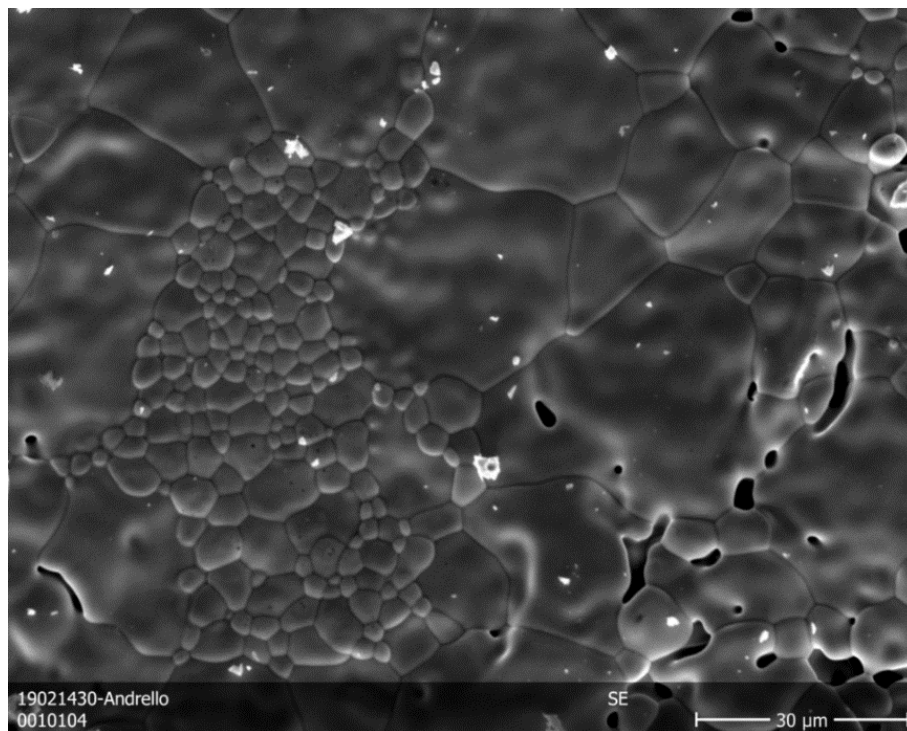


Figure 130: SEM of Heterogeneous MOX

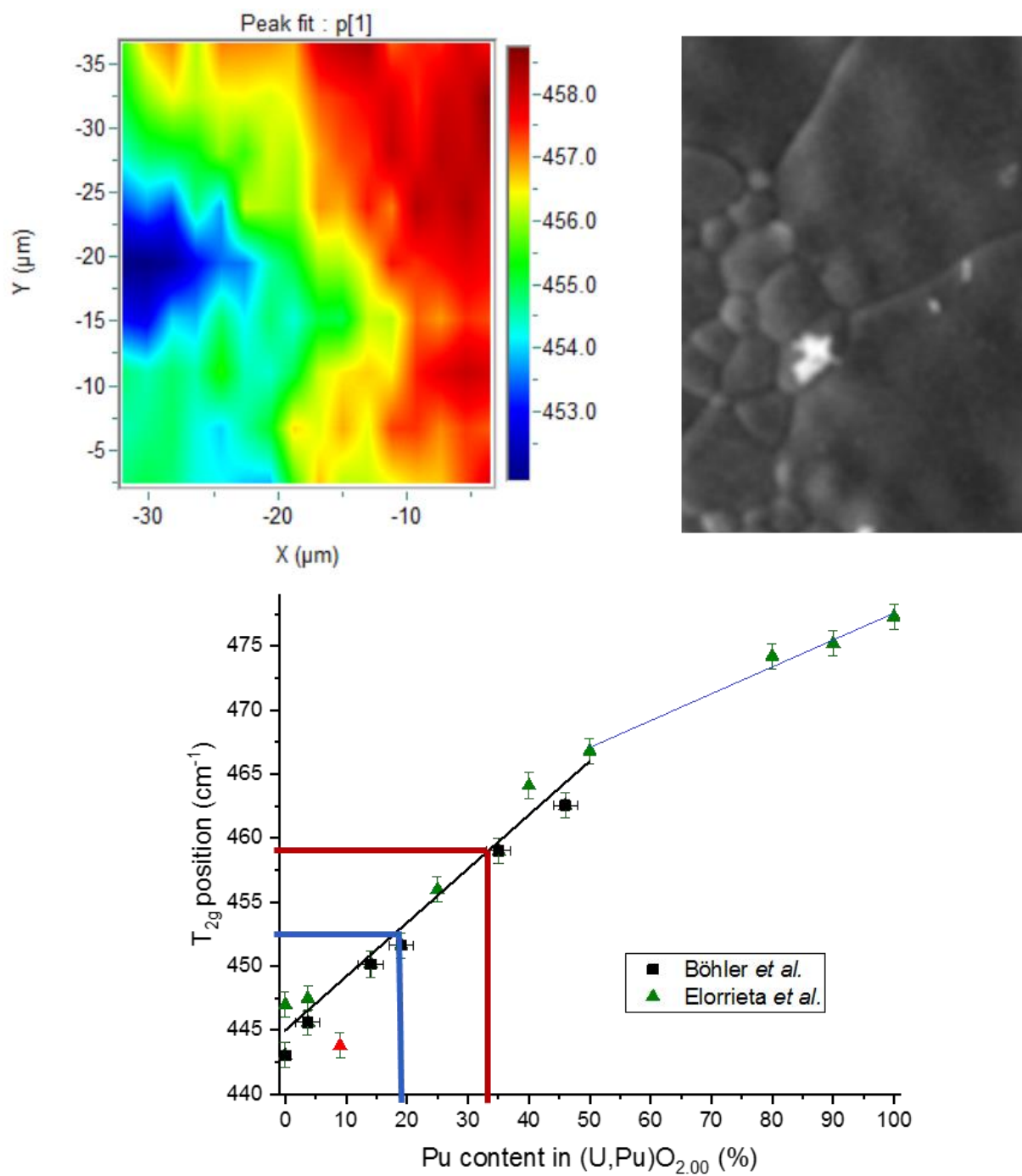


Figure 131: RAMAN Mapping heterogeneous MOX

Bibliography

- [1] "<https://www.gen-4.org>," [Online].
- [2] "<https://www.iaea.org/topics/fast-reactors>," [Online].
- [3] "4th generation sodium-cooled fast reactors the ASTRID technological demonstrator," CEA, 2012.
- [4] I. Pioro, "Introduction: Generation IV International Forum," in *Handbook of Generation IV Nuclear Reactors*, 2016.
- [5] F. Roelofs, "Introduction to liquid metal cooled reactors," in *Thermal Hydraulics Aspects of Liquid Metal Cooled Nuclear Reactors*, 2019, pp. 1-15.
- [6] C. Venard, C. Coquelet-Pascal, A. Conti, D. Gentet, P. Lamagnère, R. Lavastre, P. Gauthé, B. Bernardin, T. Beck, D. Lorenzo, A. C. Scholer, B. Perrin and D. Verrier, "The astrid core at the end of the conceptual design phase," IAEA-CN-245-288.
- [7] M. F. Dechelette, M. C. Courcier and M. J. Hirn, "The fuel Handling Route of ASTRID at the beginning of the basic design- IAEA-CN-245-395," in *Proceedings of International Conference on Fast Reactors and Related Fuel Cycles*, Yekaterinburg, Russian Federation, 2017.
- [8] F. Tete, "La réaction $\text{Cs}_2\text{MoO}_4/\text{Na}$: Application à l'interaction combustible/sodium lors d'une rupture de gaine à fort taux de combustion dans un RNR," Université de Provence- (Aix - Marseille I), 1999.
- [9] D. Costin, "SFR fuel pin evolution and implications for the internal storage safety criteria of the ADTRID reactor: A bibliographic review.," CEA internal report, 2015.
- [10] S. Jacobi, "Fuel Failure Detection and Location in LMFBRs," KfK 3203, 1982.
- [11] K. Schleisiek, J. Aberle, S. Jacobi, G. Karsten, A. Rahn, L. Schmidt, G. Vanmassenhove and A. Verwimp, "Mol 7C Experiments on local fault propagation in irradiated LMFBR fuel subassemblies," *Nuclear Engineering and Design*, vol. 100, pp. 435-445, 1987.
- [12] H. Plitz, "Failed Fuel Pin Performance in Fast Metal-Cooled Reactors," *Nuclear Technology*, vol. 37, pp. 48-58, 1978.
- [13] H. Plitz, G. Crittenden and A. Languille, "Experience with failed LMR oxide fuel element performance in European fast reactors," *Journal of Nuclear Materials*, vol. 204, pp. 238-243, 1993.
- [14] M. Adamson, M. Mignanelli, P. Potter and M. Rand, "On the oxygen thresholds for the reactions of liquid sodium with urania and urania-plutonia solid solutions," *Journal of Nuclear Materials*, vol. 97, no. 1-2, pp. 203-212, 1981.

- [15] M. A. Mignanelli and P. E. Potter, "An investigation of the reaction between sodium and hyperstoichiometric urania," *Journal of Nuclear Materials*, vol. 114, no. 2-3, pp. 168-180, 1983.
- [16] M. Mignanelli and P. E. Potter, "The reactions between sodium and plutonia, urania-plutonia and urania-plutonia containing fission product simulants," *Journal of Nuclear Materials*, vol. 125, no. 2, pp. 182-201, 1984.
- [17] M. Mignanelli and P. Potter, "The reactions of sodium with urania, plutonia and their solid solutions," *Journal of Nuclear Materials*, vol. 130, pp. 289-297, 1985.
- [18] M. Mignanelli and P. Potter, "On the chemistry of the reactions between liquid sodium and urania-plutonia fuel for fast breeder nuclear reactors," *Thermochimica Acta*, vol. 129, no. 1, pp. 143-160, 1988 .
- [19] P. Blackburn, "In International Atomic Energy Agency, Proceedings of a Panel on the Behaviour and Chemical State of Irradiated Ceramic Fuels," in *IAEA*, Vienna, 1974.
- [20] M. Housseau, G. Dean, J.-P. Marcon and J. Marin, "Report CEA-N-1588," 1973.
- [21] P. Weimar, "Experimental and theoretical evaluation of defect growth of fuel pin cladding by chemical-sodium interaction".
- [22] R. Strain, J. Bottcher, S. Ukai and Y. Arii, "Fuel-sodium reaction product and its influence on breached mixed-oxide fuel pins," *Journal of Nuclear Materials*, vol. 204, pp. 252-260, 1993.
- [23] J. Matsunaga, K. Matsushima and M. Hirai, "An investigation of kinetics reaction and decomposition of sodium uranate," *Journal of Nuclear Science and Technology*, vol. 52, pp. 1290-1295, 2015.
- [24] "Some Important Fuel Chemistry Aspects Related to the Use of MOX as a Fast Reactor Fuel," in *Nuclear Science and Engineering*, 2014, pp. 367-372.
- [25] R. W. Caputi, M. G. Adamson and S. K. Evans, in *Proc; Topl Mtg. Int. Conf. Fast Breeder Reactor Fuel Performance*, 1979.
- [26] M. G. Adamson and E. A. Aitke, *Trans. Am. Nucl. Soc.*, 1973.
- [27] D. K. Warinner, "The LMFBR Fuel-Design Environment for Endurance Testing, Primarily of Oxide Fuel Elements With Local Faults," *Journal of Engineering for Power*, vol. 105, pp. 679-689, 1983.
- [28] H. Kleykamp, "The chemical state of defective uranium-plutonium oxide fuel pins irradiated in sodium cooled reactors," *Journal of Nuclear Materials*, vol. 248, pp. 209-213, 1997.

- [29] J. D. B. Lambert, R. V. Strain, K. C. Gross, G. L. Hofman, R. P. Colburn, M. C. Adamson and S. .. Ukai, "Performance of Breached LMFBR Fuel Pins During Continued Operation".
- [30] R. V. Strain, K. C. Gross, J. D. B. Lambert, R. P. Colburn and T. Odo, "Behavior of Breached Mixed-Oxide Fuel Pins during Off-Normal High-Temperature Irradiation," *Nuclear Technology*, vol. 97, pp. 227-240, 1992.
- [31] K. Schleisiek, J. Aberle, I. Schmuck, L. Schmidt, P. Weimar and A. Verwimp, "Experimental Investigation of Role of Burn-Up for Local Fault Propagation in LMR Fuel Assemblies," *Journal of Nuclear Science and Technology*, vol. 31, pp. 1011-1022, 1994.
- [32] D. K. Warinner, "LMFBR Operational and Experimental In-Core, Local-Fault Experience, Primarily With Oxide Fuel Elements," *Journal of Engineering for Power*, vol. 105, pp. 669-678, 1983.
- [33] K. R. Kummerer, "The German Oxide Fuel Pin Irradiation Test Experience for Fast Reactors," in *Proceedings of International Conference on Fast Breeder Reactor Fuel Performance*, American Nuclear Society, 1979.
- [34] M. Tourasse, M. Boidron and B. Pasquet, "Fission product behaviour in Phenix fuel pins at high burnup," *Journal of Nuclear Materials*, vol. 188, pp. 49-57, 1992.
- [35] M. Naganuma, S. Koyama, T. Asaga, J. Noirot, D. Lespiaux, J. Rouault, G. Crittenden and C. Brown, "High burnup irradiation performance of annular fuel pins irradiated in fast reactor PFR," *IAEA-SM-358/24*, pp. 311-321.
- [36] R. Ball, W. Burns, J. Henshaw, M. Mignanelli and P. Potter, "The chemical constitution of the fuel-clad gap in oxide fuel pins for nuclear reactors," *Journal of Nuclear Materials*, vol. 167, pp. 191-204, 1989.
- [37] Y. Guerin, "Fuel performance of Fast Spectrum Oxide Fuel," in *Comprehensive Nuclear Materials*, 2012, pp. 547-578.
- [38] M. G. Adamson, E. A. Aitken and T. B. Lindemer, "Chemical thermodynamics of Cs and Te fission product interactions in irradiated LMFBR Mixed-OXide fuel pins," *Journal of Nuclear Materials*, vol. 130, pp. 375-392, 1985.
- [39] T. Ozawa and T. Abe, "Development and Verifications of Fast Reactor Fuel Design Code CEPTAR," *Nuclear Technology*, vol. 156, pp. 39-55, 2006.
- [40] A. Smith, G. Kauric, L. v. Eijck, K. Goubitz, N. Clavier, G. Wallez and R. Konings, "Structural and thermodynamic study of Cs₃Na(MoO₄)₂: Margin to the safe operation of sodium cooled fast reactors," *Journal of Solid State Chemistry*, vol. 269, p. 1–8, 2019.
- [41] M. Pijolat and L. Favergeon, "Kinetics and Mechanisms of Solid-Gas Reactions," in *Handbook of Thermal Analysis and Calorimetry*, 2018, pp. 173-212.

- [42] M. Soustelle, Handbook of Heterogenous Kinetics, 2010, Wiley.
- [43] R. J. D. Tilley, "Defects in Solids," in *Encyclopedia of Inorganic Chemistry*, 2018, pp. 1-17.
- [44] G. Brouwer, "A general asymptotic solution of reaction equations common in solid-state chemistry," *Philips Res. Rep.*, vol. 9, p. 366–376, 1954 .
- [45] I. Langmuir, "The adsorption of gases on plane surfaces of glass, mica and platinum.," *J. Am. Chem. Soc.*, vol. 40, pp. 1361-1403, 1918.
- [46] C. Keller, L. Koch and K. H. Walter, "Die Reaktion der Oxide der Transurane mit Alkalioxiden-I Ternäre Oxide der Sechswertigen Transurane mit Lithium und Natrium," *Journal Inorganic Nuclear Chemistry*, vol. 27, pp. 1205-1225, 1965.
- [47] C. Keller, L. Koch and K. H. Walter, "Die reaktion der Transuranoxide mit Alkalioxiden-II Ternäre oxide der fünfwertigen Transurane und des Proactiniums mit Lithium und Natrium," *Journal of Inorganic Nuclear Chemistry*, vol. 27, 1965.
- [48] C. Keller, " MTP International Review of Science, in Inorganic Chemistry," 1972.
- [49] S. Pillon, "Étude des diagrammes de phases U-O-Na, Pu-O-Na et U,Pu-O-Na," University of Languedoc, 1989.
- [50] A. Smith, "Structural and Thermodynamic Properties of Sodium Actinide Ternary Oxides," University of Cambridge, 2015.
- [51] A. L. Smith, P. Martin, D. Prieur, A. C. Scheinost, P. E. Raison, A. K. Cheetham and R. J. M. Konings, "Structural Properties and Charge Distribution of the Sodium Uranium, Neptunium, and Plutonium Ternary Oxides: A Combined X-ray Diffraction and XANES Study," *Inorganic Chemistry*, vol. 55, pp. 1569-1579, 2015.
- [52] A. L. Smith, P. E. Raison, A. Hen, D. Bykov, E. Colineau, J.-P. Sanchez, R. J. M. Konings and A. K. Cheetham, "Structural investigation of Na₃NpO₄ and Na₃PuO₄ using X-ray diffraction and ²³⁷Np Mössbauer spectroscopy," *Dalton Transactions*, vol. 44, p. 18370–18377, 2015.
- [53] D. Bykov, P. Raison, R. J. M. Konings, C. Apostolidis and M. Orlova, "Synthesis and crystal structure investigations of ternary oxides in the Na–Pu–O system," *Journal of Nuclear Materials* , vol. 457, p. 54–62, 2015.
- [54] A. Kovács, "Electronic structure and spectroscopic properties of mixed sodium actinide oxides Na₂AnO₄ (An = U, Np, Pu, Am)," *Journal of Molecular Structure* , vol. 1132, pp. 95-101, 2017.
- [55] K. Claxton, "Review of the solubility data for the liquid sodium-oxygen system," *Journal of Nuclear Energy* , vol. 19, pp. 849-889, 1965 .

- [56] K. Claxton, "Contribution on the solubility of oxygen in liquid sodium," *Journal of Nuclear Energy*, vol. 21, pp. 351-357, 1967.
- [57] J. Noden, "General equation for the solubility of oxygen in liquid sodium," *Journal of British Nuclear Energy Society*, vol. 12, pp. 57-62, 1973.
- [58] J.P.Maupre and J.Trouve, "Report CEA-4905," 1977.
- [59] R. L. Eichelberger, "The solubility of oxygen in liquid sodium: a recommended expression," 1968.
- [60] A. Thorley, "NRL-R-1043," 1989.
- [61] J. Hislop, R. Thompson and D. Wood, " AERE-M-3097," 1980.
- [62] H. Wriedt, "The Na-O (Sodium-Oxygen) System," *Bulletin of Alloy Phase Diagrams*, vol. 8, pp. 234-246, 1987.
- [63] J. D. Noden and K. Q. Bagley, "The Solubility of Oxygen in Sodium and Sodium-Potassium Alloy," 1954.
- [64] C. Fazio and F. Balbaud, "Corrosion phenomena induced by liquid metals in Generation IV reactors," in *Structural Materials for Generation IV Nuclear Reactors*, 2017, pp. 23-74.
- [65] H. Kleykamp, "Assessment of the physico-chemical proprieties of phases in the Na-U-Pu-O system," KfK4701, 1990.
- [66] S. F. Bartram and R. E. Fryxell, "Preparation and crystal structure of NaUO₃ and Na₁₁U₅O₁₆," *Journal of inorganic nuclear chemistry*, vol. 32, pp. 3701-3706, 1970.
- [67] R. Scholder and H. Gläser, "Über Lithium- und Natriumuranate(V) und über strukturelle Beziehungen zwischen den Verbindungstypen Li₇AO₆ und Li₈AO₆," *Anorg. Allg. Chem.*, vol. 15, 1964.
- [68] J. Marcon, O. Pesme and M. D. Franco, "Preparation et structure cristallographique du compose Na₃UO₄," *Rev. Int. Hautes Tempér. et Réfract.*, vol. 9, 1972.
- [69] S. Pillon, F. Ingold, P. Fischer, G. Andre, F. Botta and R. Stratton, "Investigation of the U-O-Na and (U,Pu)-O-Na phase diagrams -Study of Na₃UO₄ and Na₃(U,Pu)O₄ phases," *Journal of Nuclear Materials* , vol. 206 , pp. 50-56 , 1993.
- [70] E. H. P. Cordfunke and D. J. W. IJdo, "α- and β-Na₂UO₄: Structural and Thermochemical Relationships," *Journal of Solid State Chemistry* , pp. 115-299, 1995.
- [71] D. J. W. IJdo, S. Akerboom and A. Bontenbal, "Crystal structure of - and -Na₂U₂O₇: From Rietveld refinement using powder neutron diffraction data," *Journal of Solid State Chemistry*, 2015.

- [72] I. P. Roof, M. D. Smith and H.-C. z. Loye, "Crystal growth of K_2UO_4 and Na_4UO_5 using hydroxide fluxes," *Journal of Crystal Growth*, vol. 312, pp. 1240-1243, 2010.
- [73] A. L. Smith, P. E. Raison, L. Martel, D. Prieur, T. Charpentier, G. Wallez, E. Suard, A. C. Scheinost, C. Hennig, P. Martin, K. O. Kvashnina, A. K. Cheetham and R. J. M. Konings, "A New Look at the Structural Properties of Trisodium Uranate Na_3UO_4 ," *Inorganic Chemistry*, vol. 54, p. 3552–3561, 2015.
- [74] J.-H. Liu, S. V. d. Berghe and M. J. Konstantinovic, "XPS spectra of the U^{5+} compounds KUO_3 , $NaUO_3$ and $Ba_2U_2O_7$," *Journal of Solid State Chemistry*, vol. 182, p. 1105–1108, 2009.
- [75] A. Soldatov, D. Lamoen, M. Konstantinovic, S. V. d. Berghe, A. Scheinost and M. Verwerft, "Local structure and oxidation state of uranium in some ternary oxides: X-ray absorption analysis," *Journal of Solid State Chemistry*, vol. 180, p. 53–60, 2007.
- [76] S. V. d. Berghe, A. Leenaers and C. Ritter, "Antiferromagnetism in MUO_3 ($M=Na, K, Rb$) studied by neutron diffraction," *Journal of Solid State Chemistry*, vol. 177, p. 2231, 2004.
- [77] S. Azam and A. Reshak, "Theoretical calculations for MUO_3 ($M=Na, K, Rb$): DFT + U study," *Journal of Organometallic Chemistry*, vol. 766, pp. 22-33, 2014.
- [78] S. F. Matar, "Ab-initio Studies of the Electronic Structures of the Hexavalent Uranium Compounds K_2UO_4 and Na_4UO_5 ," *Journal of Chemical Science*, 2014.
- [79] R. Lorenzelli, T. Athanassiadis and R. Pascard, "Chemical reactions between sodium and (U,Pu) O_2 mixed oxides," *Journal of Nuclear Material*, vol. 130, p. 298, 1985.
- [80] A.L.Smith, C.Guéneau, J.-L.Flèche, S.Chatain, O.Beneš and R.J.M.Konings, "Thermodynamic assessment of the Na-O and Na-U-O systems: Margin to the safe operation of SFRs," *The Journal of Chemical Thermodynamics*, vol. 114, pp. 93-115, 2017.
- [81] M. Gasperin, " $Na_2U_2O_7$: Synthèse et structure d'un monocristal,," *J. Less-Common Met*, vol. 119, 1986.
- [82] C. J. Toussaint and A. Avogadro, "Concerning uranate formation in alkali nitrate melts," *Journal of Inorganic Nuclear Chemistry*, vol. 36, p. 781, 1974.
- [83] P. A. G. O'Hare, W. A. Shinn, F. C. Mrazek and A. E. Martin, "Thermodynamic investigation of trisodium uranium(V) oxide (Na_3UO_4) I. Preparation and enthalpy of formation,," *J. Chem. Thermodyn*, vol. 4, pp. 401-409, 1972.
- [84] D. R. Fredrickson and M. G. Chasanov, "Thermodynamic investigation of trisodium (V) oxide (Na_3UO_4) III. Enthalpy to 1200 K by drop calorimetry," *Journal of Chemistry Thermodynamic*, vol. 4, 1972.

- [85] D. W. Osborne and E. F. Howard, "Thermodynamic investigation of trisodium uranium (V) oxide (Na_3UO_4) II. Heat capacity, entropy, and enthalpy increment from 5 to 350 K. Gibbs energy of formation at 298.15 K," *Journal of Chemistry Thermodynamic*, 1972.
- [86] I. Grenthe, J. Fuger, R. J. M. Konings, R. J. Lemire, A. B. Muller, C. Nguyen-Trung-Cregu and H. Wanner, "Chemical thermodynamics of Uranium," Hans WANNER and Isabelle FOREST OECD Nuclear Energy Agency, Data Bank, Issy-les-Moulineaux (France), 1992.
- [87] R. Guillaumont, T. Fanghänel, J. Fuger, I. Grenthe, V. Neck, D. A. Palmer and M. H. Rand, "Update on the chemical thermodynamics of uranium, neptunium, plutonium, americium & technetium," F. J. Mompean, M. Illemassene, C. Domenech-Orti, and K. Ben Said OECD Nuclear Energy Agency, Data Bank, Issy-les-Moulineaux, France, 2003.
- [88] R. Pankajavalli, V. Chandramouli, S. Anthonysamy, K. Ananthasivan and V. Ganesan, "Thermochemical studies on the system Na-U-O," *Journal of Nuclear Material*, pp. 437-444, 2012.
- [89] C. N. Craig, "Behaviour of Failed Fuel," *Proc. Int. Conf. Engineering of Fast Reactors for Safe and Reliable Operation*, pp. 605-625, 1972.
- [90] J. P. Gatesoupe and F. Perret, "Kinetic Study of Fuel Failure Due to Manufacturing Faults," 1976.
- [91] R. Caputi and M. Adamson, in *Proc. Int. Conf. on Fast Breeder Reactor Fuel Performance*, 1979.
- [92] *QUASES-IMFP-TPP2M Ver. 3.0, Software freely available, Quases-Tougaard Cooperation 2000-2010.*
- [93] D. Magallon, H. Schins, R. Zeyen and R. Hohmann, "The FARO experimental programme: quick look on UO_2 melting and BLOKKER I results," European Commission, Joint Research Centre, Ispra, , 1989.
- [94] D. D. Sood, "The role sol-gel process for nuclear fuels-an overview," *Journal of Sol-Gel Science and Technology*, vol. 59, p. 404-416, 2011.
- [95] F. A. F. Marcelo de Assumpção Pereira-da-Silva, "Scanning Electron Microscopy".
- [96] A. Barrie and F. J. Street, "An auger and x-ray photoelectron spectroscopic study of sodium metal and sodium oxide," *Journal of Electron Spectroscopy and Related Phenomena*, pp. 1-31, 1975.
- [97] J. F. Moulder, W. F. Stickle, P. E. Sobol and K. D. Bomben, *Handbook of X-ray Photoelectron Spectroscopy*, 1992.

- [98] H. Onishi, C. Egawa, T. Aruga and Y. Iwasawa, "Adsorption of Na atoms and oxygencontaining molecules on MgO(100) and (111) surfaces," *Surface Science*, vol. 191, pp. 479 - 491, 1987.
- [99] A. P. Savintsev, Y. O. Gavasheli, Z. K. Kalazhokov and K. K. Kalazhokov, *Journal of Physics: Conference Series* 774 (2016) 012118.
- [100] T. Gouder, F. Huber, R. Eloirdi and R. Caciuffo, "U₂O₅ Film Preparation via UO₂ Deposition by Direct Current Sputtering and Successive Oxidation and Reduction with Atomic Oxygen and Atomic Hydrogen," *Journal of Chemistry*, vol. 144, 2019.
- [101] X. Feng, "PhD thesis, Interactions of Na, O₂, CO₂ and water with MnO(100): Modeling a complex mixed oxide system for thermochemical water splitting," 2015.
- [102] M. Eskandari and M. J. Asadabad, "Electron Diffraction," in *Modern Electron Microscopy in Physical and Life Sciences*.
- [103] R. T. Pepper, J. R. Stubbles and C. R. Tottle, *Appl. Mater. Rex*, 1964.
- [104] C. Wagner, "Theoretical Analysis of the Diffusion Processes Determining the Oxidation Rate of Alloys," *J. Electrochem. Soc.*, vol. 99, pp. 369-380, 1952.
- [105] C. Duriez, J.-P. Alessandri, T. Gervais and Y. Philipponneau, "Thermal conductivity of hypostoichiometric low Pu content (U,Pu)O_{2-x} mixed oxide," *Journal of Nuclear Materials*, vol. 277, no. 2-3, pp. 143-158, 2000.
- [106] M. A. Mignanelli and P. E. Potter, "Chemical reactions between liquid sodium and urania-plutonia solid solutions-the threshold plutonium valency for the reaction," *Journal of the Less-Common Metals*, vol. 121, pp. 605-613, 1986.
- [107] J.-F. Vigier, P. M. Martin, L. Martel, D. Prieur and A. C. Scheinost, "Structural Investigation of (U_{0.7}Pu_{0.3})O_{2-x} Mixed Oxides," *Inorganic Chemistry*, vol. 54, p. 5358–5365, 2015.
- [108] H. Matzke, "Atomic Mechanisms of Mass Transport in Ceramic Nuclear Fuel Materials," *Journal of Chemistry Society*, vol. 86, no. 8, pp. 1243-1256, 1990.
- [109] O. Knacke, O. Kubaschewski and K. Hesselman, *Thermochemical properties of inorganic substances*, Berlin: Springer-Verlag, 1991.
- [110] D. Fredrickson and M. Chasanov, "The enthalpy of sodium oxide Na₂O to 1300 K by drop calorimetry," *The Journal of Chemical Thermodynamics*, vol. 5, pp. 485-490, 1973.
- [111] M. Rivollier, J. L. Courouau, M. Tabarant, C. Blanc and M.-L. Giorgi, "Oxidation of 316L(N) Stainless Steel in Liquid Sodium at 650°C," *Journal of Nuclear Materials*, vol. 500, pp. 337 - 348, 2018.
- [112] T. Gnanasekaran, "Chemical behaviuor of hyrogen in sodium system-A Review of the Literature Data," Indira Gandhi Centre for Atomic Research, 1997.

- [113] "<https://www.nuclear-power.net/Sodium-melting-point-boiling-point/>," [Online].
- [114] W. Klein, K. Armbruster and M. Jansen, "Synthesis and crystal structure determination of sodium ozonide," *Chem. Commun.*, vol. 6, pp. 707-708, 1998.
- [115] R. Lemire, J. Fuger, H. Nitsche, P. Potter, M. Rand, J. Rydberg, K. Spahiu, J. Sullivan, W. Ullman, P. Vitorge and H. Wanner, *Chemical Thermodynamics of Neptunium and Plutonium*, Issy-les-Moulineaux (France): Elsevier, 2001.
- [116] C. Keller, "Report KFK225," Kernforschungszentrum Karlsruhe, 1964.
- [117] P. A. G. O'Hare, "Thermochemical and Theoretical Investigations of the SodiumOxygen System. I. The Standard Enthalpy of Formation of Sodium Oxide (Na_2O)," *The Journal of Chemical Physics*, vol. 56, pp. 4513-4516, 1972.
- [118] P. A. G. O'Hare and A. C. Wahl, "Thermochemical and Theoretical Investigations of the Sodium Oxygen System. II. Properties of NaO and Its Ions from HartreeFock Molecular Orbital Studies," *The Journal of Chemical Physics*, vol. 56, pp. 4516-4525, 1972.
- [119] A. L. Smith, P. E. Raison, L. Martel, T. Charpentier, I. Farnan, D. Prieur and C. Hennig, "A ^{23}Na Magic Angle Spinning Nuclear Magnetic Resonance, XANES, and High-Temperature X-ray Diffraction Study of NaUO_3 , Na_4UO_5 , and $\text{Na}_2\text{U}_2\text{O}_7$," *Inorganic Chemistry*, vol. 53, p. 375-382, 2014.
- [120] D. Shoesmith, S. Sunder and W. H. Hocking, "Electrochemistry of UO_2 nuclear fuel," *Electrochemistry of Novel Materials*, 1994.
- [121] X. Guo, E. Tiferet, L. Qi, J. Solomon, A. Lanzirotti, M. Newville, M. H. Engelhar, R. K. Kukkadapu, D. Wu, E. Ilton, M. Asta, S. R. Sutton, H. Xu and A. Navrotsky, "U(V) in metal uranates: a combined experimental and theoretical study of MgUO_4 , CrUO_4 , and FeUO_4 ," *Dalton Transactions*, vol. 45, p. 4622-4632, 2016.

École Nationale Supérieure des Mines
de Saint-Étienne

NNT : 2020LYSEM027

Concettina ANDRELLO

MECHANISM AND KINETICS OF THE REACTION BETWEEN LIQUID SODIUM AND
NUCLEAR FUEL OF FUTURE FAST NEUTRON REACTORS

Speciality : Process engineering

Keywords : SFR, sodium-fuel, uranium oxide, mixed oxide, mechanism, diffusion, kinetics.

Abstract :

In support of the internal storage feasibility of future sodium cooled fast reactors, the present research concerned the development of a theoretical model based on the physical mechanism of the reaction between oxide fuel and liquid sodium. Being the reaction between oxide fuel and liquid sodium a heterogeneous reaction, which involves solid-liquid phases, the model made use of the heterogeneous kinetic formalism. The required data for the proposition of a reaction mechanism were mainly extrapolated from experimental observations. The experiments confirmed that the reaction rate could be modelled through the growth process only, since the nucleation process was instantaneous. In agreement with the literature, the reaction rate followed a parabolic law, indicating that the rate-determining step could be attributed to a diffusion step. Moreover, some new and significant experimental observations were achieved through the interaction between uranium oxide and liquid sodium. Indeed, interaction tests under well controlled condition highlighted the preferential stabilization of the corrosion product as a compound with pure pentavalent uranium atoms. For the first time, the outward growth of the corrosion layer was observed, implying uranium cations as main species controlling the growth process, which was never considered before. The formation of a double phase was observed when the tests were performed under imposed oxygen potential within a value close to the one expected in the internal storage. The formation of a double phase was never assessed before and opened the question on the possibility to form more than one phase even for the mixed oxide. The proposed reaction mechanism represented a first attempt of reaction modelling. Thereby the mechanism concerned a simplified condition, in which was considered only the superficial corrosion layer. Further improvements will be needed to take into account the contribution of the potential grain boundary attack for mixed oxide.

École Nationale Supérieure des Mines
de Saint-Étienne

NNT : 2020LYSEM027

Concettina ANDRELLO

MECANISME ET CINETIQUE DE LA REACTION ENTRE LE SODIUM LIQUIDE ET LE
COMBUSTIBLE NUCLEAIRE DES FUTURS REACTEURS A NEUTRONS RAPIDES

Spécialité: Génie des procédés

Mots clefs : SFR, sodium-combustible, oxyde d'uranium, oxyde mixte, mécanisme, diffusion, cinétique

Résumé :

Pour assoir la faisabilité du stockage interne dans de futurs réacteurs à neutrons rapides refroidis au sodium, ce travail vise à développer un modèle théorique mécaniste de la réaction entre le combustible oxyde et le sodium liquide. Ce modèle utilise le formalisme de la cinétique hétérogène car elle implique une réaction entre un solide, le combustible oxyde, et un liquide, le sodium. Le modèle proposé s'appuie sur des mécanismes réactionnels qui ont été déduits de résultats expérimentaux. Ces résultats ont montré que la cinétique de réaction pouvait être modélisée avec l'étape de croissance uniquement, car l'étape de germination était instantanée. En accord avec les études précédentes, la cinétique de réaction mesurée suit une loi parabolique, ce qui permet d'identifier une étape de diffusion comme l'étape limitante de la réaction. En outre, des observations originales ont été mises en évidence lors de la réaction entre le dioxyde d'uranium et le sodium liquide. Les tests réalisés dans des conditions thermochimiques contrôlées ont montré que l'uranium avait un degré d'oxydation 5+ dans la couche de corrosion. Nous avons mis en évidence pour la première fois un mécanisme de croissance externe pour la couche de corrosion, ce qui implique que l'uranium soit l'espèce chimique qui contrôle l'étape de croissance. La formation d'une couche de corrosion biphasée a été observée dans des tests à potentiel oxygène imposé pour des valeurs de potentiels proches de celles attendues en stockage interne. L'existence d'une couche de corrosion biphasée n'avait jamais été envisagée précédemment et cela ouvre la question de son existence pour le combustible MOX. Le mécanisme de réaction proposé est une première tentative pour modéliser la réaction oxyde sodium. Il s'appuie sur des hypothèses simplificatrices où seule la couche de corrosion externe est prise en compte. Des améliorations seront nécessaires pour rendre compte de la contribution éventuelle de la corrosion des joints de grains.